Dynamical mean-field theory for disordered alloys: Effective medium theory in correlated electronic systems

Dylan Jones

Angaben zur Veröffentlichung / Publication details:

Jones, Dylan. 2026. “Dynamical mean-field theory for disordered alloys: Effective medium theory in correlated electronic systems.” Augsburg: Universität Augsburg.

Dynamical Mean-Field Theory for Disordered Alloys

Effective Medium Theory in Correlated Electronic Systems

Dissertation

zur Erlangung des akademischen Grades

Dr. rer. nat.

eingereicht an der

Mathematisch-Naturwissenschaftlich-Technischen Fakultät
der Universität Augsburg

von

Dylan Loher Jones

Augsburg, Februar 2026

Erster Gutachter:
Prof. Dr. Liviu Chioncel

Zweiter Gutachter:
Prof. Dr. Ulrich Eckern

Tag der mündlichen Prüfung:
11. Mai 2026

Preface

This thesis contains previously published material [P1–P3], which includes most of the central results and, in part, elements of the theoretical framework. Portions of these works are reproduced here either verbatim or with minor edits for clarity and consistency with the present narrative. Sections that correspond to these publications are marked in the headings with the corresponding reference. The bibliography entries are marked with a P as prefix. In addition, I also contributed as a co-author to Ref. [P4]. As the topic is not central to the aims of this thesis, the work is not included in the following chapters.

This work is mainly numerical in nature, and the calculations were performed using established software, as well as codes that I developed [C1, C2]. Software used throughout this work is referenced using a C as prefix in the bibliography.

Contents

1 Introduction

"The purpose of computation is insight, not numbers"
— R. W. Hamming [1]

Strongly correlated electron systems are among the most intriguing and challenging subjects in condensed matter physics. In these materials, electron-electron interactions are comparable to (or larger than) the characteristic kinetic energy scales, so that the electronic degrees of freedom cannot be described in terms of nearly independent quasiparticles as in conventional metals and semiconductors.

As a consequence, correlation effects drive qualitative changes in the low-energy electronic structure, giving rise to phenomena such as Mott localization, unconventional magnetism, and emergent collective states. Beyond their fundamental importance for quantum many-body physics, strongly correlated materials underpin a range of technologically relevant platforms – from transition-metal oxides and heavy-fermion compounds to high-temperature superconductors and candidate quantum spin liquids. Capturing their behavior therefore requires theoretical and computational approaches that go beyond standard band theory and explicitly account for the interplay between local Coulomb interactions, itinerancy, magnetism, and the lattice geometry.

Historically, the theory of electronic structure, i.e., the band theory of itinerant electrons, developed along two complementary directions. On the one hand, simplified many-body models were formulated to isolate and clarify the essential mechanisms of electronic correlations; on the other hand, ab-initio approaches aimed at computing energy spectra and material-specific properties of real compounds from first principles. For correlated materials, bridging these perspectives is indispensable. It has long been recognized that, in transition-metal compounds and alloys with narrow d- or f-derived bands, the local Coulomb interaction competes with kinetic delocalization on comparable energy scales. As a result, even small changes in crystal structure, stoichiometry, chemical substitution, or applied pressure can drive qualitative changes in the low-energy electronic structure.

From a computational perspective, density functional theory (DFT) is uniquely successful for ground-state properties of weakly correlated materials, yet its standard semilocal approximations underestimate correlation effects in narrow bands and are, by construction, eigenvalue theories rather than Green's function theories for spectroscopic observables. Embedding ideas that combine DFT with many-body treatments address these limitations by adding frequency-dependent self-energies to selected subspaces while retaining the material specificity of ab-initio electronic structure. Among these, dynamical mean-field theory (DMFT) has emerged as a controlled nonperturbative framework for local dynamical correlations in realistic materials. In DMFT, the lattice problem is mapped onto a quantum impurity embedded in a self-consistent electronic bath; the associated local Green's function G and self-energy Σ encode quasiparticle renormalization, spectral weight transfers, Kondo screening, and Hubbard bands. In metals, this provides a natural language for mass enhancements, lifetime effects, and the frequency dependence of response functions that are essential to a quantitative description of correlated transition metals and their alloys.

Materials of technological relevance often introduce a second, equally fundamental ingredient: configurational disorder. Even in nominally simple alloys, random occupation of lattice sites modifies scattering rates, redistributes spectral weight across the Brillouin zone, and smears fine features of the Fermi surface; at larger disorder strengths, localization tendencies may develop and qualitatively alter transport properties. On the theory side, the coherent potential approximation (CPA) offers a self-consistent effective-medium description that captures configurational averaging at the single-site level while preserving translational invariance. Combining CPA with DMFT leverages a common single-site structure and yields a natural platform to treat local dynamical correlations and substitutional disorder on equal footing, enabling realistic studies of correlated disordered metals and superconductors.

This thesis builds on these methodological pillars – charge- and self-energy self-consistent DFT+DMFT implemented with a multiple-scattering basis and its CPA extension – to elucidate correlation and disorder effects in transition-metal systems. The starting point throughout is a general multi-orbital lattice Hamiltonian that separates one-body band formation from on-site interactions, written here in second-quantized form as

$$\hat{H} = \sum_{ij} \sum_{mm'} \sum_{\sigma} t_{ij}^{mm'} \hat{c}_{im\sigma}^{\dagger} \hat{c}_{jm'\sigma} + \frac{1}{2} \sum_{i} \sum_{\{m\}} \sum_{\{\sigma\}} U_{mm'm''m'''} \hat{c}_{im\sigma}^{\dagger} \hat{c}_{im'\sigma'}^{\dagger} \hat{c}_{im'''\sigma'} \hat{c}_{im''\sigma}, \quad (1.1)$$

where $t_{ij}^{mm'}$ encodes the hopping (and crystal-field) amplitudes between orbitals m, m' on sites i, j, while the local interaction tensor $U_{mm'm''m'''}$ parameterizes intra- and inter-orbital Coulomb repulsion and Hund's exchange.

Outline

The thesis is organized as follows. The first two chapters, Ch. 2 on density functional theory and Ch. 3 on the exact muffin-tin orbitals (EMTO) method, are a concise literature synthesis: they consolidate well-established results and standard formulations from the existing literature, with the primary aim of fixing notation, conventions, and baseline assumptions used throughout the thesis. Building on this foundation, Ch. 4 introduces dynamical mean-field theory (DMFT) as an extension of DFT suitable for correlated materials. Two impurity solvers used in this work are then presented in Chs. 5 and 6, namely the spin-polarized T-matrix fluctuation-exchange (SPTF) approximation and the continuous-time quantum Monte Carlo method in the hybridization expansion, respectively. The second methodological pillar concerns substitutional disorder, discussed in Ch. 7. Its combination with local electronic correlations, DMFT+CPA, and the fully self-consistent LDA+DMFT workflow are detailed in Ch. 8. Practical aspects of analytic continuation, essential for accessing real-frequency observables, are reviewed in Ch. 9. Applications follow in the second part of the thesis. Chapter 10 analyzes superconducting transition temperatures in V and V–Ti alloys by providing LDA(CPA)+DMFT input to McMillan theory. Chapter 11 investigates quasiparticle Fermi surfaces in Nb and Nb–Ti at high pressure using the same methodology. Finally, Ch. 12 examines the emergence of correlated states at an oxide interface ($LaAlO_3$ and $SrTiO_3$), highlighting the interplay between disorder and correlations in low-dimensional settings.

2 Density functional theory

Density functional theory (DFT) provides a framework to compute ground-state equilibrium properties of an interacting many-electron system given the existence of functionals of the electron density $n(\mathbf{r})$ rather than of the many-body wave function. This shift of viewpoint traces back to early statistical models of atoms due to Thomas and Fermi, who proposed a local relation between $n(\mathbf{r})$ and the kinetic energy [2, 3]. While the Thomas–Fermi approach captured trends across the periodic table, its lack of explicit presence of quantum numbers in the functional form and leads to a poor description of bonding. Important refinements followed – Dirac's local exchange for the uniform electron gas [4] and von Weizsäcker's gradient correction to the kinetic energy [5] – but a general, exact variational principle in terms of $n(\mathbf{r})$ remained elusive.

The conceptual breakthrough was provided by Hohenberg and Kohn (1964), who established that (i) the external potential, and hence the Hamiltonian, is a unique functional of the ground-state density, and (ii) a universal energy functional attains its minimum at the true ground-state density [6]. These results, now known as the Hohenberg-Kohn (HK) theorems, recast ground-state quantum mechanics as a density-only variational problem. Shortly thereafter, Kohn and Sham (1965) introduced a practical route by mapping the interacting system onto an auxiliary system of noninteracting fermions reproducing the same $n(\boldsymbol{r})$ [7]. The price for this reduction is an *exchange-correlation* (XC) functional, $E_{\mathrm{xc}}[n]$, that must be approximated.

The first widely used approximation was the local-density approximation (LDA), which integrates the XC energy density of the uniform electron gas at the local value of $n(\boldsymbol{r})$. Modern LDA parameterizations rely on quantum Monte Carlo data for the electron gas [8, 9]. Systematic improvements followed: generalized-gradient approximations (GGAs) include ∇n information and significantly improve binding, surface energies, and chemisorption trends [10]; meta-GGAs incorporate kinetic-energy-density ingredients and can capture intermediate-range correlation improving the constraints [11]. For systems where nonlocal exchange is essential (e.g., wide-gap insulators, molecules), hybrid functionals admix a fraction of exact exchange, either globally or in a screened, short-range form [12, 13]. Long-range dispersion, missing in semilocal forms, is now routinely included via nonlocal correlation functionals and atom-pair dispersion corrections [14, 15].

These developments transformed DFT into a quantitative tool across condensed matter physics, materials science, and chemistry. It provides reliable ground-state structures, cohesive and formation energies, elastic constants, and phonon spectra for a vast class of systems at computational costs that scale favorably with system size [16, 17]. At the same time, DFT's accuracy is controlled by the XC approximation: common semilocal functionals underestimate band gaps, struggle with strongly localized d/f electrons, and historically underestimated van der Waals interactions [18]. Such limitations motivate extensions that embed additional physics, including DFT+U for static on-site correlations [19], hybrid and GW-based quasiparticle methods for excited states, and DFT+DMFT for dynamical local correlations in metals and Mott systems [20].

With this historical and methodological context in place, we now turn to a compact

statement and discussion of the Hohenberg–Kohn theorems and their implications for practical electronic-structure calculations.

Density Functional theory (DFT) is based on a series of theorems according to which physical properties of a many-particle interacting system can be described using the one-particle electron density $n(\boldsymbol{r})$. Consider N electrons subject to a local external potential $v(\boldsymbol{r})$ (typically the electron–nuclear attraction within the Born–Oppenheimer approximation). The electronic Hamiltonian in atomic units ($\hbar = e = m_e = 4\pi\varepsilon_0 = 1$) for such a system reads

$$H = T + V + U = -\sum_{i=1}^{N} \frac{\nabla_i^2}{2} + \sum_{i=1}^{N} v(\boldsymbol{r}_i) + \sum_{i<j}^{N} \frac{1}{|\boldsymbol{r}_i - \boldsymbol{r}_j|}, \tag{2.1}$$

where T is the kinetic energy of the electrons, V describes the external potential caused by the nuclei, and U describes the electron-electron repulsion energy. The one-particle electron density for a many-particle wave function Ψ is then given by

$$\begin{aligned} n(\boldsymbol{r}) &= \langle\Psi|\hat{n}|\Psi\rangle = \langle\Psi|\sum_{i=1}^{N}\delta(\boldsymbol{r}-\boldsymbol{r}_i)\,|\Psi\rangle \\ &= N\sum_{\{\sigma_i\}}\int \mathrm{d}\boldsymbol{r}_2 \cdots \int \mathrm{d}\boldsymbol{r}_N |\Psi(\boldsymbol{r},\sigma_1;\,\boldsymbol{r}_2,\sigma_2;\,\ldots;\,\boldsymbol{r}_N,\sigma_N)|^2. \end{aligned} \tag{2.2}$$

In contrast to the high-dimensional many-electron wave function (with $3N$ spatial variables plus spin coordinates), the spin-summed density $n(\boldsymbol{r})$ depends only on three spatial variables [21, 22]. Conceptually, DFT trades the full wave function for the one-body density, i.e. the diagonal of the first-order reduced density matrix. The Hohenberg–Kohn theorems state that the ground-state density uniquely determines the external potential and that there is a density-only variational principle for the ground-state energy. Consequently, DFT provides controlled access to the total energy, the density, and observables obtained as derivatives of the energy functional. This reduction is particularly advantageous for large systems, where solving the many-body Schrödinger equation directly is computationally impractical.

2.1 The Hohenberg-Kohn theorems

According to the first theorem of Hohenberg and Kohn, there is an injective correspondence between the (nondegenerate) ground state electron density n_0 and the local external potential V_{ext}. This mapping immediately leads to the fact that the Hamiltonian H as well as the ground state wave function $\Psi_0(\boldsymbol{r})$ are completely defined by knowing the one-particle density $n(\boldsymbol{r})$. The classic proof proceeds by contradiction: assume two distinct external potentials v and v' (differing by more than a constant) yield the same $n_0(\boldsymbol{r})$ with ground states $|\Psi_0\rangle$ and $|\Psi_0'\rangle$. Rayleigh–Ritz applied twice then implies

$$E_0 < \langle\Psi_0'|\hat{H}|\Psi_0'\rangle = E_0' + \int \mathrm{d}\boldsymbol{r}\,[v(\boldsymbol{r}) - v'(\boldsymbol{r})]\,n_0(\boldsymbol{r}) \tag{2.3}$$

and symmetrically

$$E_0' < E_0 + \int \mathrm{d}\boldsymbol{r}\,[v'(\boldsymbol{r}) - v(\boldsymbol{r})]\,n_0(\boldsymbol{r}), \tag{2.4}$$

which is impossible when added. Thus the mapping $n_0 \mapsto v$ is injective (modulo constants). In the case of a degenerate ground state the statement is refined using ensembles: the density still determines the set of external potentials producing it and all ground-state expectation values remain functionals of n_0 within ensemble DFT [23, 24].

The second Hohenberg and Kohn theorem states that the ground state energy E_0 is an energy functional of the ground state electron density n_0 and is defined by minimizing the energy functional [22]. Define the energy functional at fixed v as

$$E_v[n] = \langle\Psi|\hat{H}|\Psi\rangle = F[n] + V[n], \qquad F[n] \text{ universal}, \tag{2.5}$$

with the external functional

$$V[n] = \int \mathrm{d}\boldsymbol{r}\; v(\boldsymbol{r})n(\boldsymbol{r}). \tag{2.6}$$

and the universal functional $F[n]$, which collects the kinetic and interaction energies *independent* of $v(\boldsymbol{r})$. The HK variational principle states that $E_v[n]$ attains its minimum at the physical ground-state density n_0, with the ground-state energy E_0 as minimum value, i.e.

$$E_0 = E_v[n_0] = \min_n E_v[n]. \tag{2.7}$$

To turn Eqs. (2.5) to (2.7) into a mathematically precise problem one uses the constrained-search formulation due to Levy [25, 26]:

$$F[n] = \min_{\Psi\to n} \langle\Psi|\hat{T} + \hat{U}|\Psi\rangle = T[n] + U[n], \tag{2.8}$$

where the minimization is over all antisymmetric N-electron wave functions yielding the prescribed density $n(\boldsymbol{r})$. Equation (2.8) (i) bypasses the v-representability issue by working with the broader set of N-representable densities and (ii) ensures universality of F.

A complementary convex-analytic formulation due to Lieb expresses F as a Legendre–Fenchel transform [23]:

$$F[n] = \sup_v \left\{ E_v - \int \mathrm{d}\boldsymbol{r}\, v(\boldsymbol{r})\, n(\boldsymbol{r}) \right\}, \qquad E_v \equiv \inf_\Psi \langle\Psi|\hat{H}[v]|\Psi\rangle\,, \tag{2.9}$$

which makes convexity and lower semicontinuity of F explicit. In particular, the densities are nonnegative and normalized ($n(\boldsymbol{r}) \geq 0$, $\int \mathrm{d}\boldsymbol{r}\, n(\boldsymbol{r}) = N$) and are sufficient regularity to ensure finiteness of both $F[n]$ and the pairing $\int \mathrm{d}\boldsymbol{r}\, v(\boldsymbol{r})n(\boldsymbol{r})$ (precise conditions are detailed in [23]). In this setting, the subgradients of F at a given density correspond to external potentials $v(\boldsymbol{r})$ determined up to an additive constant, reflecting the irrelevance of shifting v_{ext} by a constant [23].

Imposing particle conservation via a Lagrange multiplier μ and performing a density variation of the energy functional,

$$\delta E[n] = 0, \tag{2.10}$$

with the secondary condition

$$\int \mathrm{d}\boldsymbol{r}\, n(\boldsymbol{r}) = N, \tag{2.11}$$

leads to the Lagrangian

$$\mathcal{L}[n,\,\mu] = E[n] - \mu\Big(\int \mathrm{d}\boldsymbol{r}\, n(\boldsymbol{r}) - N\Big). \tag{2.12}$$

The constrained condition $\delta E[n] = 0$ with $\int \mathrm{d}\boldsymbol{r}\, n(\boldsymbol{r}) = N$ then is equivalent to requiring stationarity of $\mathcal{L}$ with respect to independent variations of n and μ. Thus,

$$\delta\left[E[n] - \mu\Big(\int \mathrm{d}\boldsymbol{r}\, n(\boldsymbol{r}) - N\Big)\right] = 0, \tag{2.13}$$

where variation with respect to μ returns the constraint, and variation with respect to n yields the Euler equation [21]:

$$\frac{\delta F[n]}{\delta n(\boldsymbol{r})} + v(\boldsymbol{r}) = \mu, \tag{2.14}$$

The multiplier μ equals the ground-state chemical potential, $\mu = \partial E/\partial N|_v$, and controls the normalization. Equation (2.14) is exact but not directly useful unless a tractable approximation for $F[n]$ is available; this motivates the Kohn–Sham reduction.

2.2 The Kohn–Sham scheme

Kohn and Sham introduced an auxiliary system of non-interacting fermions in an effective local potential $v_{\mathrm{KS}}(\boldsymbol{r})$ chosen such that its ground-state density equals that of the interacting system [7]. The universal functional is decomposed as

$$F[n] = T_{ni}[n] + U[n] + E_{xc}[n], \tag{2.15}$$

where $T_{ni}[n]$ is the non-interacting kinetic energy,

$$U[n] = \frac{1}{2}\int \mathrm{d}\boldsymbol{r} \int \mathrm{d}\boldsymbol{r}'\, \frac{n(\boldsymbol{r})n(\boldsymbol{r}')}{|\boldsymbol{r}-\boldsymbol{r}'|} = \frac{1}{2}\int \mathrm{d}\boldsymbol{r}\; n(\boldsymbol{r})v_H([n],\boldsymbol{r}), \quad v_H([n],\boldsymbol{r}) = \int \mathrm{d}\boldsymbol{r}'\, \frac{n(\boldsymbol{r}')}{|\boldsymbol{r}-\boldsymbol{r}'|} \tag{2.16}$$

is the classical Hartree energy [22], and the (unknown) exchange–correlation functional $E_{xc}[n]$ collects both the many-body correction to the kinetic energy and the Coulomb contribution beyond Hartree. We can now rewrite the total-energy functional in terms of the Kohn-Sham decomposition as

$$E_v[n] = T_{ni}[n] + \frac{1}{2}\int \mathrm{d}\boldsymbol{r}\, n(\boldsymbol{r})v_H([n],\boldsymbol{r}) + E_{xc}[n] + \int \mathrm{d}\boldsymbol{r}\, n(\boldsymbol{r})v(\boldsymbol{r}). \tag{2.17}$$

To make Eq. (2.17) operational, we represent the density by N orthonormal single-particle orbitals $\{\psi_j\}$ of the auxiliary non-interacting system,

$$n(\boldsymbol{r}) = \sum_{\epsilon_j<\epsilon_{\mathrm{F}}} |\psi_j(\boldsymbol{r})|^2, \tag{2.18}$$

and write the non-interacting kinetic energy as

$$T_{ni}[n] = -\frac{1}{2}\sum_{\epsilon_j<\epsilon_{\mathrm{F}}} \int \mathrm{d}\boldsymbol{r}\, \psi_j^*(\boldsymbol{r})\nabla^2\psi_j(\boldsymbol{r}). \tag{2.19}$$

The ground state follows from a constrained minimization over orbitals,

$$\delta\left[E[n]-\sum_{j=1}^{N}\epsilon_j\left(\int \mathrm{d}\boldsymbol{r}\,|\psi_j(\boldsymbol{r})|^2-1\right)\right]=0, \tag{2.20}$$

where ϵ_j are Lagrange multipliers enforcing $\int \mathrm{d}\boldsymbol{r}\,|\psi_j|^2=1$ [27]. Using the expression (2.18) for the density $n(\boldsymbol{r})$ and the chain rule, functional differentiation with respect to ψ_j^* yields the single-particle Euler-Lagrange equations

$$\left[-\frac{1}{2}\nabla^2+v_{KS}([n],\,\boldsymbol{r})\right]\psi_j(\boldsymbol{r})=\epsilon_j\psi_j(\boldsymbol{r}), \tag{2.21}$$

i.e., the *Kohn-Sham* equations for non-interacting electrons in the effective local potential [7, 22]. Equation (2.21) takes the form of the Schrödinger equation for non-interacting electrons in the potential v_{KS} and the Kohn–Sham orbitals ψ_j.

Comparing the Euler equation (2.14) evaluated with the interacting functional (2.17) to the corresponding Kohn-Sham stationarity condition,

$$E_{KS}[n]=T_{ni}[n]+\int \mathrm{d}\boldsymbol{r}\,n(\boldsymbol{r})v_{KS}([n],\,\boldsymbol{r}), \tag{2.22}$$

gives an explicit expression for the effective potential. Formally,

$$\frac{\delta E_v[n]}{\delta n}=\frac{\delta T_{ni}[n]}{\delta n}+\frac{\delta U[n]}{\delta n}+\frac{\delta E_{xc}[n]}{\delta n}+\frac{\delta V[v,\,n]}{\delta n}=\mu \tag{2.23}$$

$$\frac{\delta E_{KS}[n]}{\delta n}=\frac{\delta T_{ni}[n]}{\delta n}+\frac{\delta V[v_{KS},\,n]}{\delta n}=\mu, \tag{2.24}$$

so the common kinetic term cancels and we identify

$$v_{KS}([n],\,\boldsymbol{r})=v(\boldsymbol{r})+\int \mathrm{d}\boldsymbol{r}'\,\frac{n(\boldsymbol{r}')}{|\boldsymbol{r}-\boldsymbol{r}'|}+\frac{\delta E_{xc}[n]}{\delta n} \tag{2.25}$$

using

$$\frac{\delta U[n]}{\delta n}=\int \mathrm{d}\boldsymbol{r}'\,\frac{n(\boldsymbol{r}')}{|\boldsymbol{r}-\boldsymbol{r}'|}\equiv v_H([n],\,\boldsymbol{r}),\qquad v_{xc}([n],\boldsymbol{r})\equiv\frac{\delta E_{xc}[n]}{\delta n}. \tag{2.26}$$

Equation (2.25) becomes the standard decomposition of the potential known as the *Kohn–Sham potential*

$$v_{KS}([n],\boldsymbol{r})=v(\boldsymbol{r})+v_H([n],\,\boldsymbol{r})+v_{xc}([n],\,\boldsymbol{r}). \tag{2.27}$$

The unknown object is no longer the full universal functional $F[n]$ but the exchange-correlation energy: the Kohn-Sham formulation shifts the problem to determining $E_{xc}[n]$. It gathers the many-body correction to the kinetic energy and the electron-electron interaction beyond Hartree. The associated potential is $v_{xc}([n],\boldsymbol{r})$, which enters the effective Kohn-Sham potential via Eq. (2.27). In typical ground-state calculations the absolute magnitude of $E_{xc}[n]$ is smaller than the leading pieces $T_{ni}[n]$ and $U[n]$, yet it controls chemically relevant energy differences (bonding, reaction barriers, band gaps) and therefore must be approximated with care [17, 22, 28, 29]. According to the first Hohenberg-Kohn theorem, the ground-state density $n(\boldsymbol{r})$ uniquely determines the

external potential up to an additive constant. In the auxiliary non-interacting problem this implies a one-to-one correspondence between n and v_{KS} (again up to a constant). Because v_{KS} and the orbitals ψ_j are linked by the single-particle equation (2.21), the orbitals themselves are density dependent in the self-consistent solution. Concretely, the Kohn-Sham scheme can be written as a fixed-point problem for the density and the ground state satisfies the self-consistency condition $n' = n$.

In pure Kohn–Sham DFT the Coulomb energy is partitioned as $U[n] + E_{xc}[n]$ by definition, so Eqs. (2.17) and (2.27) contain no redundancy. The term *double counting* arises when an explicit many-body interaction or self-energy is added on top of DFT (e.g., DFT+U or DFT+DMFT): part of the local electron–electron interaction is then included twice: once implicitly through $E_{xc}[n]$ and a second time in the added interaction. To compensate, one subtracts a double-counting term,

$$E^{\mathrm{DFT+MB}} = E_v[n] + E_{\mathrm{int}} - E_{dc}, \qquad v_{dc}(\boldsymbol{r}) = \frac{\delta E_{dc}}{\delta n(\boldsymbol{r})}\,, \tag{2.28}$$

where common choices for E_{dc} include the fully localized limit (FLL) and around-mean-field (AMF) forms in DFT+U; in DFT+DMFT several prescriptions exist and a unique exact form is still under debate [20, 30–32].

2.3 Approximate exchange correlation functionals

The Kohn–Sham formulation reduces the many-body problem to a one-body equation in an effective local potential, Eq. (2.27), by introducing a universal exchange–correlation energy $E_{xc}[n]$. The most crucial step in DFT is to approximate this unknown exchange-correlation energy $E_{xc}[n]$ and its functional derivative $v_{xc}([n], \boldsymbol{r})$. Over six decades a hierarchy of approximations, the so-called Perdew's "Jacob's ladder" [29], has been developed, climbing from the uniform electron gas (UEG) to fully nonlocal, many-body levels, as illustrated in Fig. 1. Each rung adds new ingredients (density gradients, kinetic-energy density, exact exchange, response functions) while striving to satisfy exact constraints (uniform scaling, sum rules, spin-scaling, Lieb–Oxford bound, correct asymptotics) and to recover the uniform electron gas limit [28, 29].

2.3.1 Local density approximation (LDA/LSDA)

The simplest and most important approximation is the local density approximation (LDA), and its spin-polarized version LSDA, which replaces the inhomogeneous electron gas locally by the UEG:

$$E_{xc}^{\mathrm{LDA}}[n] = \int \mathrm{d}\boldsymbol{r}\, n(\boldsymbol{r})\, \varepsilon_{xc}^{\mathrm{UEG}}(n(\boldsymbol{r}))\,, \qquad E_{xc}^{\mathrm{LSDA}}[n_\uparrow, n_\downarrow] = \int \mathrm{d}\boldsymbol{r}\, n(\boldsymbol{r})\, \varepsilon_{xc}^{\mathrm{UEG}}(n_\uparrow(\boldsymbol{r}), n_\downarrow(\boldsymbol{r}))\,, \tag{2.29}$$

In LDA, the XC potential is purely local,

$$v_{xc}^{\mathrm{LDA}}([n], \boldsymbol{r}) = \left.\frac{\mathrm{d}[n\, \varepsilon_{xc}^{\mathrm{UEG}}(n)]}{\mathrm{d}n}\right|_{n(\boldsymbol{r})}\,, \tag{2.30}$$

and in LSDA it depends only on the spin-resolved densities $n_\uparrow(\boldsymbol{r}), n_\downarrow(\boldsymbol{r})$ at the same point $\boldsymbol{r}$ (no gradients or orbitals enter). The exchange is taken from Dirac's uniform-gas limit, while correlation is obtained from quantum Monte Carlo parametrizations

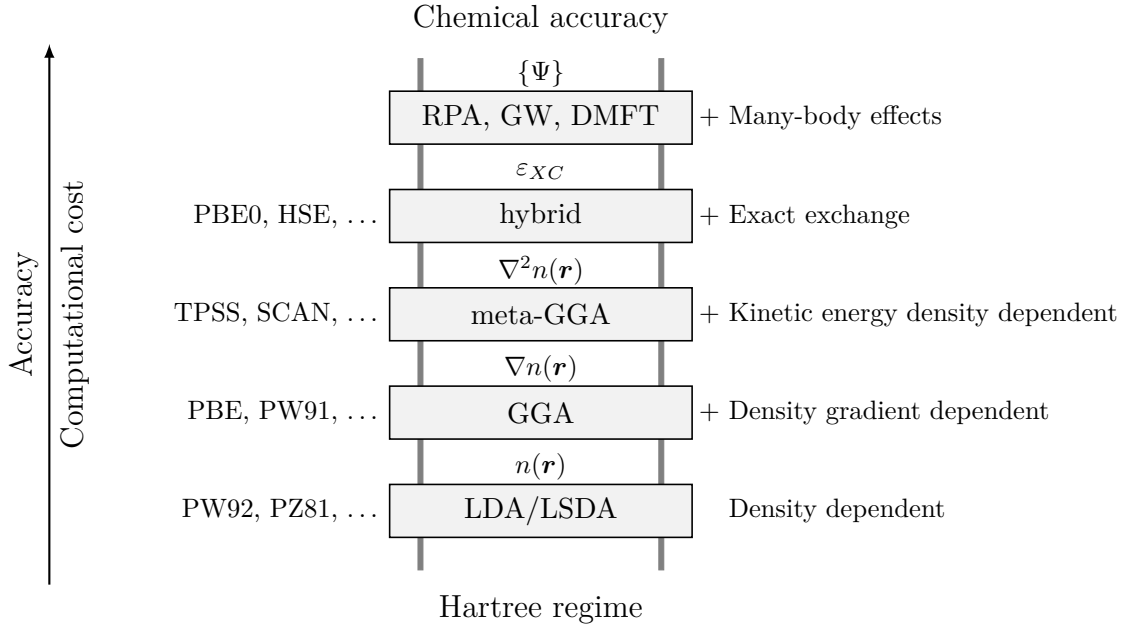

Figure 1: Schematic representation of Perdew's "Jacob's ladder" of exchange-correlation functionals [29]. The rungs represent successive improvements in the complexity and accuracy of the functionals. Each rung adds more detailed information about the electron density and its derivatives, leading to better approximations of the exchange-correlation energy.

such as PZ81 or PW92 [9, 33]. Owing to its nonempirical construction and exact uniform-gas form, LDA often yields cohesive energies and simple-metal properties that are surprisingly reasonable, and its numerical stability makes it a reliable baseline in solid-state studies [28, 29]. Nevertheless, the locality of v_{xc} leads to overbinding and underestimated lattice constants for many solids, poor reaction barriers and molecular thermochemistry, and severe underestimation of band gaps. These failures are symptomatic of self-interaction and delocalization errors as well as the absence of nonlocal correlation [9, 24, 34].

2.3.2 Generalized gradient approximations (GGA)

Generalized gradient approximations incorporate the leading effects of inhomogeneity through the reduced gradient, writing

$$E_{xc}^{\mathrm{GGA}}[n] = \int \mathrm{d}\boldsymbol{r}\, n(\boldsymbol{r})\, \varepsilon_{xc}^{\mathrm{GGA}}(n(\boldsymbol{r}), \nabla n(\boldsymbol{r})). \tag{2.31}$$

The potential remains multiplicative and semilocal: $v_{xc}^{\mathrm{GGA}}(\boldsymbol{r})$ depends on $n(\boldsymbol{r})$ and $\nabla n(\boldsymbol{r})$ but not explicitly on densities at distant points. Constraint-based designs such as PBE and PW91 are ubiquitous in both chemistry and materials, and PBEsol restores the second-order gradient expansion to improve equilibrium volumes and vibrational properties in solids [10, 35, 36]. Compared to LDA, GGAs reduce the systematic overbinding and generally improve structures and ionization energies while retaining modest computational cost. Yet the semilocal form does not eliminate self-interaction or restore the missing derivative discontinuity, so delocalization persists and long-range

dispersion (attractive part of the van der Waals interaction due to correlated instantaneous charge fluctuations) is absent. Consequently, band gaps, barrier heights, and weak interactions remain challenging [24, 34, 37].

2.3.3 Meta-GGAs

Meta-GGA functionals enrich the ingredient set with the positive kinetic-energy density

$$\tau(\boldsymbol{r}) = \frac{1}{2} \sum_{\epsilon_j < \epsilon_\mathrm{F}} |\nabla \psi_j(\boldsymbol{r})|^2 \tag{2.32}$$

and, in some cases, the Laplacian $\nabla^2 n(\boldsymbol{r})$. This additional local information allows the functional to recognize distinct bonding environments and to recover the exact exchange limit for one-electron densities. The resulting potential is still a scalar field in real space,

$$v_{xc}^{\mathrm{mGGA}}(\boldsymbol{r}) = v_{xc}\Big(n(\boldsymbol{r}), \nabla n(\boldsymbol{r}), \tau(\boldsymbol{r}), \nabla^2 n(\boldsymbol{r})\Big)\,, \tag{2.33}$$

but it is implicitly orbital dependent through $\tau(\boldsymbol{r})$. Nonempirical examples include TPSS and, more recently, SCAN, which imposes a wide set of exact constraints and can distinguish metallic, covalent, and weak bonding; when combined with a nonlocal dispersion correction such as rVV10, SCAN+rVV10 improves interlayer binding and adsorption energies in layered and molecular crystals [38–40]. In practice, meta-GGAs often refine formation energies, magnetic moments, and phase stabilities relative to GGA while remaining far cheaper than hybrids. They can, however, be numerically more sensitive to integration grids and density quality, and although band gaps are typically better than with PBE, the derivative discontinuity is still absent so fundamental gaps may remain underestimated [24, 39].

2.3.4 Hybrids and screened hybrids

To mitigate self-interaction and recover part of the derivative discontinuity, hybrid functionals admix a fraction of exact (Fock) exchange into semilocal exchange,

$$E_{xc}^{\mathrm{hyb}} = a\, E_x^{\mathrm{EXX}}[\{\psi\}] + (1-a) E_x^{\mathrm{semi}}[n, \nabla n, \ldots] + E_c^{\mathrm{semi}}[n, \nabla n, \ldots]\,. \tag{2.34}$$

Because E_x^{EXX} is orbital dependent, the exchange contribution enters as a nonlocal operator $\hat{v}_x^{\mathrm{EXX}}$ and the Kohn–Sham equations are solved in the generalized Kohn–Sham sense. PBE0 is a widely used global hybrid, whereas HSE employs range separation to screen the long-range part of Fock exchange, which is advantageous for extended systems where screening is important [13, 41, 42]. Relative to semilocal functionals, hybrids generally produce more reliable defect levels and semiconductor band gaps and reduce delocalization errors in molecules and insulators. The computational cost rises appreciably due to the nonlocal exchange, and global hybrids may overlocalize in metals, so screened forms such as HSE are often preferred for solids [13, 42]. Long-range correlation remains absent unless an explicit dispersion treatment is added [43, 44].

2.3.5 Adiabatic-connection and many-body approaches

The adiabatic-connection formalism connects the noninteracting and fully interacting systems at fixed density and, combined with the fluctuation-dissipation theorem, leads to the random phase approximation for correlation,

$$E_c^{\mathrm{RPA}} = \frac{1}{2\pi}\int_0^\infty \mathrm{d}u\ \mathrm{Tr}\Big[\ln\Big(1 - v\,\chi_0(\mathrm{i}u)\Big) + v\,\chi_0(\mathrm{i}u)\Big]\,, \tag{2.35}$$

where χ_0 is the Kohn–Sham response function [45, 46]. In practice, RPA is paired with exact exchange (EXX+RPA), capturing dispersion and improving relative phase energetics without empirical parameters, albeit at substantially higher cost than hybrids. On the same top rung of Fig. 1 one typically places post-DFT Green's-function and many-body methods: the GW family for quasiparticle excitations, with $\Sigma = \mathrm{i}GW$ yielding accurate band structures and fundamental gaps [47, 48], and DFT+DMFT, which introduces a frequency-dependent self-energy for selected localized subspaces to capture Hubbard physics and temperature-dependent spectral weights [20]. These methods are not simple functionals of $n(\boldsymbol{r})$, but they systematically add nonlocal and dynamical correlation that is inaccessible to lower rungs; their main practical limitations are computational expense and, for GW/DMFT, sensitivity to starting points, interaction choices, and double counting.

2.4 Self-consistent Kohn–Sham cycle and convergence

The Kohn–Sham ground state is obtained as the fixed point of a nonlinear map from densities to densities. Given an input density $n^{(k)}(\boldsymbol{r})$ one constructs the effective potential

$$v_{KS}[n^{(k)}](\boldsymbol{r}) = v(\boldsymbol{r}) + v_H[n^{(k)}](\boldsymbol{r}) + v_{xc}[n^{(k)}](\boldsymbol{r})\,, \tag{2.36}$$

solves the one-particle equations

$$\Big[-\nabla^2/2 + v_{KS}[n^{(k)}](\boldsymbol{r})\Big]\psi_j^{(k)}(\boldsymbol{r}) = \epsilon_j^{(k)}\,\psi_j^{(k)}(\boldsymbol{r})\,, \tag{2.37}$$

forms the output density

$$n^{(k)\prime}(\boldsymbol{r}) = \sum_{\epsilon_j^{(k)} < \epsilon_F^{(k)}} |\psi_j^{(k)}(\boldsymbol{r})|^2 \quad \text{(with partial occupancies for metals)}\,, \tag{2.38}$$

and checks for self-consistency. If $n^{(k)\prime} \approx n^{(k)}$ within a prescribed tolerance, the fixed point $n^\star$ has been reached; otherwise one updates the input via a *mixing* step and repeats. The flow of this self-consistency cycle is illustrated in Fig. 2.

It is convenient to cast the SCF fixed point as a root-finding problem for the residual

$$R[n](\boldsymbol{r}) \equiv n'(\boldsymbol{r}) - n(\boldsymbol{r})\,, \tag{2.39}$$

so convergence corresponds to $R[n^\star] = 0$. The simplest update, linear mixing,

$$n^{(k+1)}(\boldsymbol{r}) = n^{(k)}(\boldsymbol{r}) + \alpha\,R^{(k)}(\boldsymbol{r})\,, \tag{2.40}$$

with $0 < \alpha \leq 1$, is robust for small systems and wide-gap insulators but can be inefficient or unstable in metals and large supercells. The underlying difficulty, often called

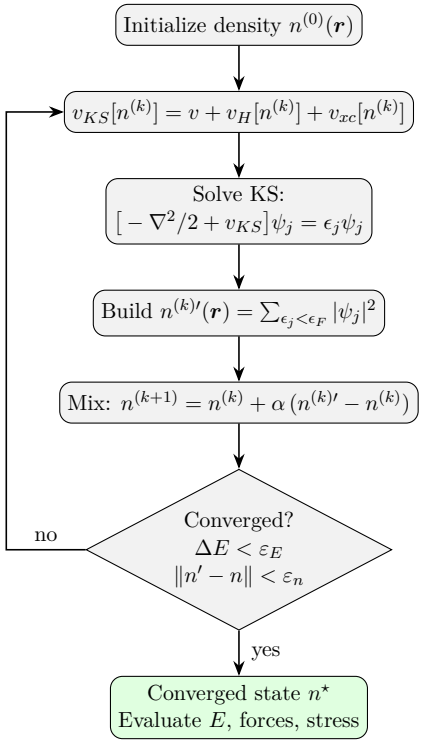

Figure 2: Self-consistent Kohn–Sham (SCF) flow. From an initial density, build v_{KS}, solve the KS equations, update the density using mixing, and iterate until simultaneous energy and density-residual criteria are met.

"charge sloshing", is the amplification of long-wavelength (small-$\boldsymbol{q}$) density modes by the metallic response, which drives oscillatory or divergent updates under naive mixing [49].

In reciprocal-space implementations, a preconditioner $M(\boldsymbol{q})$ damps these small-$\boldsymbol{q}$ components of $R(\boldsymbol{q})$. The Kerker form,

$$M(\boldsymbol{q}) \propto \frac{|\boldsymbol{q}|^2}{|\boldsymbol{q}|^2 + q_0^2}, \tag{2.41}$$

embodies Thomas-Fermi screening and dramatically stabilizes metallic SCF [50]. Consequently, modern codes perform density or potential mixing with such preconditioning by default.

Quasi-Newton and subspace-acceleration strategies further improve convergence. Anderson/Pulay mixing (DIIS) forms $n^{(k+1)}$ as an optimal linear combination of several past iterates, effectively approximating the inverse Jacobian of $R[n]$ without forming it [51–53]. Broyden-type updates make this explicit by iteratively refining a low-rank Jacobian (or inverse) using residual differences; practical variants due to Johnson are common in plane-wave codes [54, 55]. In insulating systems, where the density response is short-ranged, DIIS/Broyden mixing typically yields rapid, near-quadratic convergence once sufficiently close to the fixed point.

3 Exact muffin-tin orbitals

The *Exact Muffin-Tin Orbitals* (EMTO) method emerged at the turn of the century as a modern successor to the multiple-scattering approaches that shaped the early history of electronic-structure theory. Its lineage can be traced to the Korringa-Kohn-Rostoker (KKR) formalism, where the one-electron Green's function is built from site-centered scattering solutions and free-space propagators [56, 57]. In the decades that followed, practical implementations commonly adopted the *Muffin-Tin* (MT) in the form of the *Atomic Sphere Approximation* (ASA): the Kohn-Sham potential was assumed spherically symmetric inside nonoverlapping atomic spheres and constant in the interstitial. This spherical partition greatly simplified the scattering problem and enabled efficient band-structure calculations, but its shape approximation could be severe in open or strongly directional structures.

A major step toward accuracy at comparable cost was the development of linear methods with compact, site-centered bases. Andersen's *Linear Muffin-Tin Orbitals* (LMTO) introduced an energy-linearized, minimal basis built from partial waves and their energy derivatives, leading to the celebrated LMTO-ASA technique that dominated alloy and transition-metal studies for years [58, 59]. Linearization, however, entails a controlled but finite error tied to the chosen expansion energy, and the ASA itself remains the limiting approximation. Parallel efforts pursued *full-potential* formalisms such as LAPW and full-potential KKR/LMTO, which improved transferability at a higher computational cost.

During the 1990s, a second pivotal idea reshaped multiple scattering: *screening*. In the screened KKR (SKKR) formulation, the long-ranged free-space propagators are computed in basis of *screened* spherical waves, and the lattice geometry enters through short-ranged, rapidly convergent *screened structure constants*. This recasting leads to well-conditioned equations, faster k-space convergence, and an efficient real-space description [60, 61]. Screening thus provided a numerically robust backbone on which new basis constructions could be built.

EMTO unifies these streams by combining an *optimized, overlapping* muffin-tin representation of the Kohn-Sham potential with the screened multiple-scattering machinery. Instead of strictly nonoverlapping spheres and a sizable interstitial, large spheres are allowed to overlap so that the interstitial potential becomes nearly constant while the intra-sphere part remains close to spherical. On this optimized partition one constructs *energy-dependent* exact single-site solutions inside each sphere and matches them to screened spherical waves in the (reduced) interstitial. The resulting EMTO basis $\{\phi_{RL}(\varepsilon, \boldsymbol{r})\}$ is free of the linearization error intrinsic to LMTO, yet inherits the sparse, short-ranged algebra of SKKR. Band structures follow from solving a *kink-cancellation* condition: a generalized secular equation for the energy- and k-dependent *kink matrix* assembled from single-site scattering matrices (phase shifts) and screened structure constants; eigenvalues satisfy $\det K(\varepsilon, \boldsymbol{k}) = 0$, and the Green's function needed for densities and moments is obtained by energy-contour integration [62, 63].

A remaining historical challenge for all spherical-potential schemes concerned total energies. While ASA/MT band structures were often reliable, quantitative energetics demanded a reconstruction of the all-electron charge density, including nonspherical

multipoles omitted by the shape approximation. EMTO addressed this with the *full charge-density* (FCD) technique: the site-resolved density extracted from the EMTO Green's function is augmented by multipole corrections so that the total $n(\boldsymbol{r})$ reproduces the correct Coulomb and exchange-correlation contributions when inserted into the standard Kohn-Sham energy functional [64]. In practice, the combination of overlapping MT spheres, screened structure constants, energy-dependent orbitals, and FCD evaluation yields near-full-potential accuracy for close-packed and moderately open metals at a computational effort comparable to traditional ASA methods.

3.1 Overlapping muffin-tin wells

The classical muffin-tin (MT) construction partitions space into atom-centered spheres and an interstitial, and replaces the true Kohn-Sham potential $v_{\mathrm{KS}}(\boldsymbol{r})$ by spherical wells inside the spheres and a constant in the interstitial [56–59, 65]. While this greatly simplifies multiple scattering, its accuracy degrades when nonoverlapping spheres leave a large, structured interstitial. The *overlapping* muffin-tin (OMT) strategy resolves this tension by admitting judicious sphere overlaps and by *optimizing* both the spherical wells and the background level so that the composite model potential reproduces $v_{\mathrm{KS}}(\boldsymbol{r})$ as closely as possible in a least-squares sense [63, 66]. Concretely, one writes the model potential as

$$v(\boldsymbol{r}) \approx v_{\mathrm{mt}}(\boldsymbol{r}) \equiv v_0 + \sum_R \Big[v_R(r_R) - v_0 \Big], \qquad \boldsymbol{r}_R \equiv r_R \hat{r}_R = \boldsymbol{r} - \boldsymbol{R}, \tag{3.1}$$

with *spherical* wells $v_R(r_R)$ that, by construction, *equal* the constant level v_0 outside a chosen *potential sphere* of radius s_R, i.e. $v_R(r_R \geq s_R) = v_0$. Equation (3.1) is equivalent to assembling the crystal potential from overlapping spherical contributions plus a constant background; when two spheres overlap both contributions are present, and their sum is arranged to mimic the true $v_{\mathrm{KS}}(\boldsymbol{r})$ in the overlap region. The overlap of these radii can be as large as 30-40 % [67]. In practice one suppresses the density-dependence in the notation (all quantities are evaluated self-consistently) and uses the shorthand $\boldsymbol{r}_R = r_R \hat{\boldsymbol{r}}_R \equiv \boldsymbol{r} - \boldsymbol{R}$ for the local spherical coordinate. The *optimized* OMT (OOMT) potential follows by determining $\{v_R(r)\}$ and v_0 variationally for a *fixed* set of potential spheres $\{s_R\}$. The target is to minimize the mean-squared deviation between $v_{\mathrm{mt}}(\boldsymbol{r})$ and the actual effective potential over a chosen region Ω (typically the unit cell),

$$F_v\Big[\{v_R\},\, v_0\Big] \equiv \int_\Omega \Big[v_{\mathrm{KS}}(\boldsymbol{r}) - v_0 - \sum_R \Big(v_R(r_R) - v_0 \Big) \Big]^2 \mathrm{d}\boldsymbol{r}, \tag{3.2}$$

leading to the Euler conditions

$$\int_\Omega \frac{\delta F_v}{\delta v_R(r)} \delta v_R(r) \mathrm{d}\boldsymbol{r} = 0 \quad \text{for all } R, \qquad \frac{\partial F_v}{\partial v_0} = 0. \tag{3.3}$$

Solving Eqs. (3.2) to (3.3) yields the optimal set of spherical wells and the background level, i.e. the OOMT potential [63]. In words: the overlaps are not artefacts but *degrees of freedom* that allow the constant part to absorb most of the interstitial structure while the spherical parts reproduce the near-atomic features within the potential spheres. A

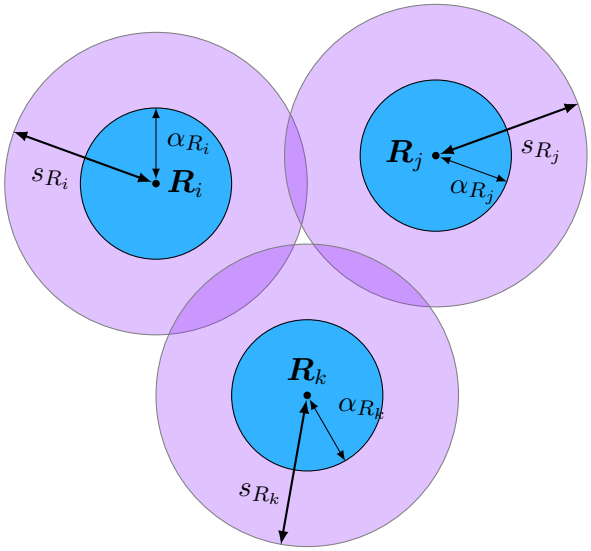

Figure 3: Illustration of the muffin-tin approximation, showing atom-centered spheres with radii s_R, as well as their inner non-overlapping regions with radii α_{R_i}, centered at lattice sites $\boldsymbol{R}_i$. The schematic highlights the partitioning of space into overlapping spheres and interstitial regions, which is central to the EMTO method.

visual illustration of the OOMT partition is shown in Fig. 3. In the limit of vanishing overlaps Eqs. (3.2) and (3.3) reduce to the spherical average of the full potential within a sphere:

$$v_R(r_R) = \frac{1}{4\pi}\int v(\boldsymbol{r})\mathrm{d}\hat{r} \quad \text{for } r_R \leq s_R \tag{3.4}$$

and the average potential in the interstitial for v_0

$$v_0 = \frac{1}{\Omega_s}\int_{I_s} v(\boldsymbol{r})\mathrm{d}\boldsymbol{r}, \tag{3.5}$$

where I_s is the s-interstitial region outside all potential spheres and $\Omega_s = \Omega\sum_R \frac{4\pi s_R^3}{3}$ is its volume.

3.2 Exact muffin-tin orbitals

To solve the Kohn-Sham equations (2.21) for the muffin-tin potential (3.1), we expand the Kohn-Sham orbitals $\Psi_j(\boldsymbol{r})$ in terms of the *exact muffin-tin orbitals* $\bar{\psi}^a_{RL}(\epsilon_j, \boldsymbol{r}_R)$:

$$\Psi_j(\boldsymbol{r}) = \sum_{RL} \bar{\psi}^a_{RL}(\epsilon_j, \boldsymbol{r}_R) v^a_{RL,j}, \tag{3.6}$$

which form a complete basis set for the Kohn-Sham scheme. The exact muffin-tin orbitals are defined for each lattice site $\boldsymbol{R}$ and angular momentum channel $L = (l,m)$, denoting the set of orbital (l) and magnetic (m) quantum numbers. In practice, the angular momentum expansion is truncated at a maximum $l_{\max} = 3$, including s, p, d, and f muffin-tin orbitals. The expansion coefficients $v^a_{RL,j}$ are determined by the requirement that the orbitals $\Psi_j(\boldsymbol{r})$ satisfy the Kohn-Sham equations in the entire space. This matching condition leads to the *kink-cancellation* equation, i.e., the discontinuities

of the radial derivatives at the screening spheres are required to vanish, which yields the screened multiple-scattering secular problem [62, 63]. Formally, this is the *screened* counterpart of the classic Korringa-Kohn-Rostoker *tail-cancellation* condition [56, 57], obtained within the screened-KKR representation of the structure constants [60, 61].

3.2.1 Screened spherical waves

The exact muffin-tin orbitals are constructed by different basis functions inside the potential spheres and in the interstitial region. In the interstitial region, where the potential is approximated by the constant level $v(\boldsymbol{r}) \approx v_0$, a convenient basis is provided by the *screened spherical waves* $\psi^a_{RL}(\kappa^2, \boldsymbol{r}_R)$ [63], defined as the solutions of the Helmholtz equation,

$$\left[\nabla^2 + \kappa^2\right] \psi^a_{RL}(\kappa^2, \boldsymbol{r}_R) = 0, \qquad \kappa^2 \equiv \varepsilon - v_0, \tag{3.7}$$

where ε is the energy [66]. These solutions are subject to energy-independent boundary conditions imposed on a set of nonoverlapping *screening spheres* of radii $\{a_R\}$ centered at the lattice sites R [63]. For simplicity, we take a_R site dependent but l independent. The boundary conditions enforce a pure real harmonic $Y_L(\hat{\boldsymbol{r}}_R)$ on the own a-sphere and vanishing $Y_{L'}(\hat{\boldsymbol{r}}_{R'})$ projections on all other a-spheres, $R' \neq R$. With these conditions, and for κ^2 below the onset of the a-sphere continuum, ψ^a_{RL} are short-ranged and only weakly energy-dependent. They form a complete basis in the a-interstitial and can be expanded in terms of real harmonics centered at any site R'

$$\begin{aligned}\psi^a_{RL}(\kappa^2, \boldsymbol{r}_R) = {} & f^a_{Rl}(\kappa^2, r_R) Y_L(\hat{r}_R) \delta_{RR'} \delta_{LL'} \\ & + \sum_{L'} g^a_{R'l'}(\kappa^2, r_{R'}) Y_{L'}(\hat{r}_{R'}) S^a_{R'L',RL}(\kappa^2),\end{aligned} \tag{3.8}$$

where f^a_{Rl} and g^a_{Rl} are the *value* (head) and *slope* (tail) functions, and the expansion coefficients $S^a(\kappa^2)$ are the elements of *slope matrix*. The latter plays the role of (screened) structure constants and is related to the bare KKR structure-constant matrix through an inhomogeneous Dyson-like equation [61]. The boundary conditions require each screened spherical wave to be a pure real harmonic on its own screening sphere and to have no harmonic content on any other sphere. Explicitly,

$$\psi^a_{RL}(\kappa^2, \boldsymbol{r}_R)\Big|_{r_R = a_R} = Y_L(\hat{r}_R), \qquad \text{for} \quad R' \neq R \quad \text{and all } L'. \tag{3.9}$$

Equivalently, the $Y_{L'}$ projection equals $\delta_{RR'}\delta_{LL'}$ at $r_{R'} = a_{R'}$ and vanishes otherwise. This leads to the conditions

$$f^a_{Rl}(\kappa^2, r)\Big|_{r_R = a_R} = 1, \qquad g^a_{Rl}(\kappa^2, r)\Big|_{r_R = a_R} = 0, \tag{3.10}$$

at the α-spheres with the fixed slopes

$$\left.\frac{\partial f^a_{Rl}(\kappa^2, r)}{\partial r}\right|_{r_R = a_R} = 0, \qquad \left.\frac{\partial g^a_{Rl}(\kappa^2, r)}{\partial r}\right|_{r_R = a_R} = \frac{1}{a_R}. \tag{3.11}$$

Using spherical Bessel and Neumann functions, $j_l(\kappa r)$ and $n_l(\kappa r)$, the value and slope functions can be written as

$$f^a_{Rl}(\kappa^2, r) = \quad t^{(1)}_{Rl}(\kappa^2) n_l(\kappa r) + t^{(2)}_{Rl}(\kappa^2) j_l(\kappa r), \tag{3.12}$$

$$g^a_{Rl}(\kappa^2, r) = -t^{(3)}_{Rl}(\kappa^2) n_l(\kappa r) - t^{(4)}_{Rl}(\kappa^2) j_l(\kappa r), \tag{3.13}$$

with *screening parameters* $t^{(i)}_{Rl}(\kappa^2)$ fixed by the boundary conditions (3.10)-(3.11). Collecting the terms, one finds the linear system

$$\begin{bmatrix} t^{(1)}_{Rl}(\kappa^2) & t^{(2)}_{Rl}(\kappa^2) \\ t^{(3)}_{Rl}(\kappa^2) & t^{(4)}_{Rl}(\kappa^2) \end{bmatrix} = 2\frac{a_R^2}{\omega} \begin{bmatrix} \frac{\partial j_l(\kappa^2, a_R)}{\partial r_R} & -\frac{\partial n_l(\kappa^2, a_R)}{\partial r_R} \\ \frac{1}{a_R} j_l(\kappa^2, a_R) & -\frac{1}{a_R} n_l(\kappa^2, a_R) \end{bmatrix}, \tag{3.14}$$

where w is the average Wigner-Seitz radius, defined by the atomic Volume V

$$\frac{4\pi\omega^3}{3} \equiv V = \frac{\text{unit cell volume}}{\text{number of atoms in unit cell}}. \tag{3.15}$$

The Bessel and Neumann functions satisfy the Wronskian relation,

$$\mathcal{W}_r(n_l,\, j_l) = r_R^2 \left[n_l(\kappa^2,\, r_R) \frac{\partial j_l(\kappa^2,\, a_R)}{\partial r_R} - \frac{\partial n_l(\kappa^2,\, a_R)}{\partial r_R} j_l(\kappa^2,\, a_R) \right] = \frac{\kappa}{2}, \tag{3.16}$$

which ensures that the value and slope functions also satisfy the Wronskian relation [63]:

$$\mathcal{W}_r\left(f^a_{Rl}, g^a_{Rl}\right) = a_R, \tag{3.17}$$

leading to the determinant of the screening matrix in Eq. (3.14) being

$$d^a_{Rl}(\kappa^2) \equiv t^{(1)}_{Rl}(\kappa^2) t^{(4)}_{Rl}(\kappa^2) - t^{(2)}_{Rl}(\kappa^2) t^{(3)}_{Rl}(\kappa^2) = \frac{2a_R^2}{\omega}\frac{\kappa}{2}. \tag{3.18}$$

Because ψ^a_{RL} solve the Helmholtz equation, they are irregular at the origin and carry no pure $(l,\, m)$ character in general. This problem can be remedied by replacing the irregular heads inside the potential spheres with regular partial waves.

3.2.2 Partial waves

Inside each potential sphere $r_R \leq s_R$, the EMTO basis is built from the *partial waves* $\phi_{Rl}(\varepsilon, r_R)$, defined as the regular, energy-dependent radial solutions of the radial Schrödinger equation in the spherical well $v_R(r_R)$. Writing $u_{Rl}(\varepsilon, r_R) \equiv r_R \phi_{Rl}(\varepsilon,\, r_R)$, the radial equation takes the standard form

$$\left[-\frac{1}{2}\frac{\partial^2}{\partial r_R^2} + \frac{l(l+1)}{2r_R^2} + v_R(r_R) - \varepsilon \right] u_{Rl}(\varepsilon, r_R) = 0, \tag{3.19}$$

or, equivalently, for the reduced radial function ϕ_{Rl},

$$\frac{\partial^2 \Big\{ r_R \phi_{Rl}(\varepsilon, r_R) \Big\}}{\partial r_R^2} = \left[\frac{l(l+1)}{r_R^2} + v_R(r_R) - \varepsilon \right] r_R \phi_{Rl}(\varepsilon, r_R). \tag{3.20}$$

The corresponding real, site-centered functions are

$$\phi^a_{Rl}(\varepsilon, \boldsymbol{r}_R) = N^a_{Rl}(\varepsilon) \phi_{Rl}(\varepsilon, r_R) Y_L(\hat{r}_R), \tag{3.21}$$

where $Y_L(\hat{r}_R)$ are real harmonics and $N^a_{Rl}(\varepsilon)$ is an energy-dependent normalization fixed by the matching condition at the screening radius $r_R = a_R$.

In the screened multiple-scattering formulation, a screened spherical wave carries a pure angular character $Y_L(\hat{\boldsymbol{r}}_R)$ only on its own screening (or a-) sphere. Hence, the natural place to impose matching between a site-centered screened spherical wave and a site-resolved radial solution is the sphere of radius a_R. At the same time, an accurate representation of the single-electron potential requires overlapping potential spheres in EMTO, so one typically chooses $s_R > a_R$ (as discussed in Sec. 3.1). These two radii introduce a gap between the screening sphere (where the screened spherical wave has the pure Y_L form) and the potential sphere (where the true partial wave is defined).

To bridge this gap, EMTO introduces a *free-electron* solution with pure (lm) character that connects the screened spherical wave at $r_R = a_R$ to the (energy-dependent) partial wave at $r_R = s_R$. This connection function is chosen to join continuously and differentiably to the partial wave at s_R, and continuously to the screened spherical wave at a_R [63, 66]. The radial part of the corresponding backward-extrapolated free-electron solution is written as

$$\varphi^a_{Rl}(\varepsilon, r_R) = f^a_{Rl}(\kappa^2, r_R) + g^a_{Rl}(\kappa^2, r_R) D^a_{Rl}(\varepsilon), \tag{3.22}$$

where κ^2 is the energy parameter of the free-electron Helmholtz equation in the interstitial (Eq. (3.7)), and $D^a_{Rl}(\varepsilon) \equiv \mathcal{D}\{\varphi^a_{Rl}(\varepsilon, r_R)\}$ is the (dimensionless) logarithmic derivative at the screening radius $r_R = a_R$ [63, 66]. Explicitly, the logarithmic derivative of a function $f(r_R)$ in the radial mesh point r^0_R is defined as

$$\mathcal{D}\left\{f(r^0_R)\right\} \equiv \frac{r^0_R}{f(r^0_R)} \left.\frac{\partial f(r_R)}{\partial r_R}\right|_{r_R = r^0_R}, \tag{3.23}$$

which leads to

$$D^a_{Rl}(\varepsilon) = \mathcal{D}\left\{\varphi^a_{Rl}(\varepsilon,\, r_R)\right\} = \left.\frac{r_R\, \varphi^{a\prime}_{Rl}(\varepsilon, r_R)}{\varphi^a_{Rl}(\varepsilon,\, r_R)}\right|_{r_R = a_R}. \tag{3.24}$$

The pair $\left(f^a_{Rl},\, g^a_{Rl}\right)$ are linearly independent free-electron radial solutions (linear combinations of spherical Bessel/Neumann functions for the chosen κ) that are fixed by the canonical normalization at $r_R = a_R$,

$$f^a_{Rl}(a_R) = 1, \quad a_R f^{a\prime}_{Rl}(a_R) = 0, \qquad g^a_{Rl}(a_R) = 0, \quad a_R g^{a\prime}_{Rl}(a_R) = 1, \tag{3.25}$$

so that Eq. (3.22) enforces $\phi^a_{Rl}(a_R) = 1$ and $D\{\varphi^a_{Rl}\}(a_R) = D^a_{Rl}(\varepsilon)$ by construction.

The normalization $N^a_{Rl}(\varepsilon)$ in Eq. (3.21) and the logarithmic derivative $D^a_{Rl}(\varepsilon)$ in Eq. (3.22) are determined by imposing the matching conditions on the partial wave and the backward-extrapolated free-electron

$$N^a_{Rl}(\varepsilon)\phi_{Rl}(\varepsilon, s_R) = \varphi^a_{Rl}(\varepsilon, s_R), \tag{3.26}$$

$$N^a_{Rl}(\varepsilon) \left.\frac{\partial \phi_{Rl}(\varepsilon,\, r_R)}{\partial r_R}\right|_{r_R = s_R} = \left.\frac{\partial \varphi^a_{Rl}(\varepsilon,\, r_R)}{\partial r_R}\right|_{r_R = s_R}. \tag{3.27}$$

Equivalently, Eqs. (3.26) to (3.27) can be written in terms of logarithmic derivatives at s_R:

$$N^a_{Rl}(\varepsilon)\phi_{Rl}(\varepsilon,\, s_R) = \varphi^a_{Rl}(\varepsilon,\, s_R), \qquad \mathcal{D}\{\phi_{Rl}(\varepsilon,\, s_R)\} = \mathcal{D}\{\varphi_{Rl}(\varepsilon,\, s_R)\}. \tag{3.28}$$

Using the representation (3.22) and the shorthand

$$D_s\{\cdot\} \equiv D\{\cdot\}\Big|_{r_R=s_R}, \qquad \phi_s \equiv \phi_{Rl}(\varepsilon,\, s_R), \quad f_s \equiv f^a_{Rl}(\kappa^2,\, s_R), \quad g_s \equiv g^a_{Rl}(\kappa^2,\, s_R), \tag{3.29}$$

the matching conditions yield, after straightforward algebra, the explicit formulas

$$\frac{1}{N^a_{Rl}(\varepsilon)} = \frac{\phi_s f_s D_s\{\phi_{Rl}\} - D_s\{g^a_{Rl}\}}{D_s\{f^a_{Rl}\} - D_s\{g^a_{Rl}\}}, \tag{3.30}$$

$$D^a_{Rl}(\varepsilon) = -\frac{f_s D_s\{\phi_{Rl}\} - D_s\{f^a_{Rl}\}}{g_s D_s\{\phi_{Rl}\} - D_s\{g^a_{Rl}\}}. \tag{3.31}$$

In Eqs. (3.30) to (3.31), all logarithmic derivatives are understood at $r_R = s_R$ in the sense of $D\{f\} = r_R f'(r_R)/f(r_R)$.

Finally, the *exact muffin-tin orbital* at site R is assembled as a superposition of (i) the screened spherical wave (of unit amplitude at a_R), (ii) the normalized partial wave inside the potential sphere, and (iii) the backward-extrapolated free-electron connector that removes the double counting:

$$\bar{\psi}^a_{RL}(\varepsilon,\, \boldsymbol{r}_R) = \psi^a_{RL}(\kappa^2,\, \boldsymbol{r}_R) + N^a_{Rl}(\varepsilon)\phi_{Rl}(\varepsilon,\, r_R)Y_L(\hat{r}_R) - \varphi^a_{Rl}(\varepsilon,\, r_R)Y_L(\hat{r}_R), \tag{3.32}$$

with the last two terms truncated outside the s-spheres $r_R = s_R$. This function is also named the *kinked partial wave* [68], as it generally has a radial-derivative discontinuity (kink) at the screening sphere $r_R = a_R$, which will become clear in the next section. The composite function (3.32) matches the screened boundary conditions at a_R, carries the correct single-site physics inside s_R, and is the building block from which the EMTO kink matrix and secular equation are constructed [63].

3.2.3 Kink cancellation equation

With the exact muffin-tin orbitals at site R, defined in Eq. (3.32), the Kohn-Sham orbitals are expanded as in Eq. (3.6) and can be expressed as

$$\begin{aligned}\Psi(\boldsymbol{r}_R) = &\sum_L N^a_{Rl}(\varepsilon)\phi_{Rl}(\varepsilon,\, r_R)Y_L(\hat{r}_R)\, v^a_{RL} \\ &+ \sum_L \left[f^a_{Rl}(\kappa^2,\, r_R)v^a_{RL} + g^a_{Rl}(\kappa^2,\, r_R) \sum_{R'L'} S^a_{RLR'L'}(\kappa^2) v^a_{R'L'} \right] Y_L(\hat{r}_R) \\ &- \sum_L \left[f^a_{Rl}(\kappa^2,\, r_R) + g^a_{Rl}(\kappa^2,\, r_R) D^a_{Rl}(\varepsilon) \right] Y_L(\hat{r}_R)\, v^a_{RL}.\end{aligned} \tag{3.33}$$

The head part $f^a_{Rl}(\kappa^2,\, r_R)$ of the screened spherical wave (3.8) in the second term exactly cancels out the corresponding piece of the backward-extrapolated free-electron solution (3.22) in the third term. Only the g^a_{Rl} "tail" survives explicitly, leading to

$$\begin{aligned}\Psi(\boldsymbol{r}_R) = &\sum_L N^a_{Rl}(\varepsilon)\phi_{Rl}(\varepsilon,\, r_R)Y_L(\hat{r}_R)v^a_{RL} \\ &+ \sum_L g^a_{Rl}(\kappa^2,\, r_R)Y_L(\hat{r}_R) \sum_{R'L'} \left[S^a_{RLR'L'}(\kappa^2) - \delta_{RR'}\delta_{LL'} D^a_{Rl}(\varepsilon) \right] v^a_{R'L'}.\end{aligned} \tag{3.34}$$

Equation (3.34) separates the trial state into a regular partial-wave piece (first line) and a piece proportional to g^a_{Rl} (second line).

The trial function Ψ will satisfy the single-particle Schrödinger equation (2.21) for the OOMT potential (3.1) provided that, inside every potential s-sphere $r_R \leq s_R$, the part of the second line of Eq. (3.34) spanned by the retained angular momenta $l \leq l_{\max}$ vanishes for all radii r_R. In other words, the $l \leq l_{\max}$ components of the screened spherical waves, when combined with the expansion coefficients, must be canceled exactly by the backward-extrapolated free-electron connector, i.e. by $\phi^a_{Rl}(\varepsilon, r_R)Y_L(\hat{r}_R)v^a_{RL}$. This requirement enforces smoothness (no radial-derivative "kink") of Ψ across the screening sphere for the whole set of channels actually used in the basis. The residual ($l > l_{\max}$) tails, if present, are free-electron in character and do not contribute inside $r_R \leq s_R$. Concretely, the vanishing of the bracket in Eq. (3.34) for every (R, L) yields the *kink-cancellation equation*

$$\sum_{RL} a_{R'} \left[S^a_{RLR'L'}(\kappa^2) - \delta_{RR'}\delta_{LL'} D^a_{Rl}(\varepsilon) \right] v^a_{RL} = 0, \tag{3.35}$$

which must be satisfied for all $l' \leq l_{\max}$ at each site R'. The difference between the slope matrix and the logarithmic derivative matrix defines the *kink matrix*

$$K^a_{RLR'L'}(\varepsilon) \equiv a_{R'} S^a_{RLR'L'}(\kappa^2) - \delta_{RR'}\delta_{LL'} a_R D^a_{Rl}(\varepsilon). \tag{3.36}$$

With the kink matrix, the kink-cancellation equation (3.35) takes the compact form

$$\sum_{RL} K^a_{RLR'L'}(\varepsilon) v^a_{RL} = 0, \tag{3.37}$$

and we can write the trial wave functions (3.34) as

$$\begin{aligned} \Psi(\boldsymbol{r}_R) = &\sum_L N^a_{Rl}(\varepsilon)\phi_{Rl}(\varepsilon,\, r_R)Y_L(\hat{r}_R)v^a_{RL} \\ &+ \sum_L g^a_{Rl}(\kappa^2,\, r_R)Y_L(\hat{r}_R) \sum_{R'L'} \frac{1}{a_{R'}} K^a_{RLR'L'}(\varepsilon) v^a_{R'L'}. \end{aligned} \tag{3.38}$$

For periodic crystals one introduces the Bloch vector $\boldsymbol{k}$ from the first Brillouin zone, replacing $\boldsymbol{S}^a(\kappa^2) \to \boldsymbol{S}^a(\kappa^2,\, \boldsymbol{k})$ via a lattice Fourier transform (Bloch sum)

$$S^a_{RL,R'L'}(\kappa^2,\, \boldsymbol{k}) = \sum_{\boldsymbol{T}} e^{\mathrm{i}\boldsymbol{k}\cdot\boldsymbol{T}} S^a_{RL,(R'+T)L'}(\kappa^2), \tag{3.39}$$

where R and R' now are two sites from the primitive cell and $\boldsymbol{T}$ is a lattice translation vector. Accordingly, the kink matrix becomes $\boldsymbol{k}$-dependent

$$K^a_{RL,R'L'}(\varepsilon,\, \boldsymbol{k}) = S^a_{RL,R'L'}(\kappa^2,\, \boldsymbol{k}) - \delta_{RR'}\delta_{LL'} D^a_{Rl}(\varepsilon). \tag{3.40}$$

The eigenvalue problem defined by the kink-cancellation matrix,

$$K^a_{RL,R'L'}(\varepsilon,\, \boldsymbol{k}) v^a_{R'L'} = 0, \qquad \det \boldsymbol{K}^a(\varepsilon,\, \boldsymbol{k}) = 0, \tag{3.41}$$

yields the single-electron band energies $\varepsilon_{n\boldsymbol{k}}$ and their expansion coefficients $v^a_{RL}(n,\, \boldsymbol{k})$. The same spectrum is obtained from the poles of the path operator $\boldsymbol{g}^a(z,\, \boldsymbol{k})$ (the

site- and channel-resolved Green's function in the screened representation), defined for complex energy z by the resolvent relation

$$\sum_{R'L'} K^a_{R'L',R''L''}(z,\,\boldsymbol{k}) g^a_{R'L',R''L''}(z,\,\boldsymbol{k}) = \delta_{RR'}\delta_{LL'}. \tag{3.42}$$

Thus $\boldsymbol{g}^a(z,\,\boldsymbol{k}) = [\boldsymbol{K}^a(z,\,\boldsymbol{k})]^{-1}$, and its poles on the real axis locate the eigenenergies, while the corresponding residues reconstruct the wave-function amplitudes in the EMTO basis.

3.2.4 Overlap matrix

The overlap of two EMTO basis functions separates naturally into contributions from the partial waves inside the potential spheres ($r_R \le s_R$), the backward-extrapolated free-electron connectors in the shell $a_R \le r_R \le s_R$, and the screened spherical waves in the a-interstitial I^a. The overlap integral of the partial waves inside s_R is the norm

$$\int \phi^{a\,*}_{Rl}(\varepsilon,\,\boldsymbol{r}_R)\phi^a_{Rl}(\varepsilon,\,\boldsymbol{r}_R)\mathrm{d}\boldsymbol{r}_R = \left[N^a_{Rl}(\varepsilon)\right]^2 \int_0^{s_R} \phi_{Rl}(\varepsilon,\,r_R)^2 r_R^2 \mathrm{d}r_R, \tag{3.43}$$

which recasts the volume integration into the radial norm. The latter can be evaluated by combining the radial Schrödinger equation. (3.20) with Green's second identity (see also Ref. [63], App. B), yielding the standard relation

$$\int_0^{s_R} \phi_{Rl}(\varepsilon,\,r_R)^2 r_R^2 \mathrm{d}r_R = -s_R \dot{\mathcal{D}}\{\phi_{Rl}(\varepsilon,\,s_R)\}\phi_{Rl}(\varepsilon,\,s_R)^2 \tag{3.44}$$

with the energy derivative of the logarithmic derivative

$$\dot{\mathcal{D}}\{\phi_{Rl}(\varepsilon,\,s_R)\} \equiv \frac{\partial \mathcal{D}\{\phi_{Rl}(\varepsilon,\,s_R)\}}{\partial \varepsilon}. \tag{3.45}$$

Analogously, the overlap integral of the backward-extrapolated free-electron $\phi^a_{Rl}(\varepsilon,r_R)$, defined in Eq. (3.22), between the s- and a-sphere $a_R \le r_R \le s_R$, can be written as

$$\begin{aligned}\int_{a_R}^{s_R} \varphi^{a\,*}_{Rl}(\varepsilon,\,r_R)\varphi^a_{Rl}(\varepsilon,\,r_R) r_R^2 \mathrm{d}r_R &= \int_0^{s_R} \varphi^a_{Rl}(\varepsilon,\,r_R)^2 r_R^2 \mathrm{d}r_R - \int_0^{a_R} \varphi^a_{Rl}(\varepsilon,\,r_R)^2 r_R^2 \mathrm{d}r_R \\ &= -s_R \dot{\mathcal{D}}\{\varphi^a_{Rl}(\varepsilon,\,s_R)\}\varphi^a_{Rl}(\varepsilon,\,s_R)^2 + a_R \dot{D}^a_{Rl}(\varepsilon),\end{aligned} \tag{3.46}$$

where $\varphi^a_{Rl}(\varepsilon,\,a_R) = 1$ was used at the screening sphere. The matching condition of the logarithmic derivatives at s_R (Eq. (3.28)) ensures that the energy derivatives in Eqs. (3.44) and (3.46) are equal,

$$\dot{\mathcal{D}}\{\phi_{Rl}(\varepsilon,\,s_R)\} = \dot{\mathcal{D}}\{\varphi^a_{Rl}(\varepsilon,\,s_R)\}, \tag{3.47}$$

and thus the first term on the right-hand side of Eq. (3.46) is equal to the overlap integral of the partial waves in Eq. (3.44).

The overlap of screened spherical waves over the a-interstitial follows similarly from the screened Helmholtz equation and Green's theorem. Denoting the a-interstitial by I^a, one finds the compact result

$$\int_{I^a} \psi^{a*}_{R'L'}(\kappa^2,\,\boldsymbol{r}_{R'})\psi^a_{RL}(\kappa^2,\,\boldsymbol{r}_R)\mathrm{d}\boldsymbol{r} = a_R \dot{S}^a_{R'L',RL}(\kappa^2), \tag{3.48}$$

where $\dot{S}^a(\kappa^2) \equiv \partial S^a(\kappa^2)/\partial\varepsilon$. We recall that only the low-l components of ψ^a_{RL} are truncated outside I^a, so high-l components extend throughout space and their contribution is included in Eq. (3.48).

Collecting the three pieces, the total overlap of two EMTO basis functions over all space can be established most transparently for nonoverlapping s-spheres that lie inside the corresponding a-spheres ($s_R < a_R$). In that case the overlap integral $\int \bar{\psi}^{a\,*}_{R'L'}(\varepsilon, \boldsymbol{r})\bar{\psi}^a_{RL}(\varepsilon, \boldsymbol{r})\,\mathrm{d}\boldsymbol{r}$ splits into the sum of the partial-wave norm inside s_R (Eq. (3.44)), the connector contribution in the shell $a_R \le r_R \le s_R$ (Eq. (3.44)), and the screened-wave term over I^a:

$$\int \bar{\psi}^{a\,*}_{R'L'}(\varepsilon, \boldsymbol{r})\bar{\psi}^a_{RL}(\varepsilon, \boldsymbol{r})\mathrm{d}\boldsymbol{r} = a_R\dot{S}^a_{R'L',RL}(\kappa^2) - a_R\dot{D}^a_{Rl}(\varepsilon)\delta_{RR'}\delta_{LL'} \equiv \dot{K}^a_{R'L',RL}(\varepsilon), \quad (3.49)$$

i.e. the overlap matrix equals the energy derivative of the kink matrix (3.36). When s-spheres overlap, additional small terms appear from the overlap regions; for modest overlaps these corrections are negligible and Eq. (3.49) remains an excellent approximation. A detailed discussion of the overlap corrections can be found in Andersen and co-workers [59, 69] (see also Refs. [63]).

3.2.5 Green's function and Fermi level

In each self-consistency step for solving the self-consistent Kohn-Sham equations (2.21), described in Section 2.4, the Fermi energy ε_F is fixed by enforcing charge neutrality:

$$N(\varepsilon_\mathrm{F}) = N_e, \quad (3.50)$$

i.e. the total number of occupied one-electron states below ε_F equals the number of electrons N_e in the cell. Practically, one evaluates $N(\varepsilon)$ for a sequence of trial ε and updates ε_F until Eq. (3.50) is satisfied to the prescribed tolerance. Within EMTO it is advantageous to compute $N(\varepsilon)$ from a contour integral of the normalized Green's function in the complex-energy plane (residue theorem). Since the overlap matrix of the EMTO basis equals the energy derivative of the kink matrix, $\dot{K}^a(z) \equiv \partial K^a(z)/\partial z$ the matrix elements of the properly normalized Green's function can be written as [67, 70]

$$G_{RLR'L'}(z) \equiv \sum_{R''L''} g^a_{R''L'',RL}(z)\dot{K}^a_{R'L'}(z) - \delta_{RR'}\delta_{LL'}I^a_{RL}(z), \quad (3.51)$$

where the subtraction term $I^a_{RL}(z)$ removes unphysical poles originating from the energy derivative of the screened logarithmic derivative $D^a_{Rl}(z)$. These spurious poles occur because $D^a_{Rl}(z)$ contains the screening denominator $D\{\phi_{Rl}\} - D\{g^a_{Rl}\}$. Whenever this denominator vanishes, D^a_{Rl} diverges although no physical state is present [66]. Practical schemes for constructing $I^a_{RL}(z)$ are described in Refs. [63, 69].

With the normalized $G(z)$, the integrated number of states below the Fermi level follows directly from a contour integral,

$$N(\varepsilon_\mathrm{F}) = \frac{1}{2\pi}\sum_{RLR'L'}\oint_{\mathcal{C}(\varepsilon_\mathrm{F})} \mathrm{Im}\, G_{RLR'L'}(z)\mathrm{d}z, \quad (3.52)$$

where $\mathcal{C}(\varepsilon_\mathrm{F})$ is a contour in the complex plane that starts below the bottom of the valence band on the real axis and returns at $z = \varepsilon_\mathrm{F}$ (for periodic systems one uses the

$\boldsymbol{k}$-resolved form and sums over the Brillouin zone). Near a physical eigenvalue $z \to \varepsilon_{n\boldsymbol{k}}$ the path operator behaves as

$$\boldsymbol{g}^a(z,\,\boldsymbol{k}) \simeq \frac{\left[\dot{\boldsymbol{K}}^a(\varepsilon_{n\boldsymbol{k}},\,\boldsymbol{k})\right]^{-1}}{z-\varepsilon_{n\boldsymbol{k}}}, \tag{3.53}$$

so that the first term in (3.51) contributes a unit residue per enclosed state, while I^a contributes zero once the spurious poles are removed. Thus (3.52) is the EMTO analogue of Lloyd's formula and yields the correct state counting when combined with the overlap identity [63, 71].

3.3 Self-consistency in EMTO: slope matrix, Poisson equation, and full charge density

The self-consistent solution of the Kohn–Sham equations using the EMTO basis follows the general scheme outlined in Section 2.4, while exploiting the screened multiple-scattering formalism.

At a given iteration one has an optimized overlapping muffin-tin (OOMT) potential $v_{\rm mt}(\boldsymbol{r})$, introduced in Eq. (3.1), and the associated single-site scatterers $\{\phi_{Rl}(z,r), D^a_{Rl}(z)\}$. The update then proceeds through two tightly coupled ingredients: the *slope matrix* (lattice coupling) and the *Poisson problem* for the Coulomb potential generated by the current charge. After convergence, the *full charge-density* (FCD) reconstruction can be used to obtain accurate energies and forces. The overall self-consistency flow is summarized in Fig. 4.

Single-site scattering is embedded into the crystal through the screened (short-ranged) structure constants. For complex energy $z = \kappa^2 + v_0$ and Bloch vector $\boldsymbol{k}$, the Bloch-summed slope matrix reads

$$S^a_{RL,R'L'}(\kappa^2,\ \boldsymbol{k}) = \sum_{\boldsymbol{T}} \mathrm{e}^{\mathrm{i}\boldsymbol{k}\cdot\boldsymbol{T}} S^a_{RL,(R'+T)L'}(\kappa^2), \tag{3.54}$$

with R, R' restricted to the sites in the primitive cell and $L \equiv (lm)$, as discussed in Section 3.2.3. The screened kink matrix and the path operator follow as

$$K^a_{RL,R'L'}(z,\,\boldsymbol{k}) = S^a_{RL,R'L'}(\kappa^2,\,\boldsymbol{k}) - \delta_{RR'}\delta_{LL'} D^a_{Rl}(z), \qquad \boldsymbol{g}^a(z,\boldsymbol{k}) = \left[\boldsymbol{K}^a(z,\boldsymbol{k})\right]^{-1}. \tag{3.55}$$

The band energies $\varepsilon_{n\boldsymbol{k}}$ are obtained from the secular condition $\det \boldsymbol{K}^a(\varepsilon_{n\boldsymbol{k}},\boldsymbol{k}) = 0$. The Fermi level is fixed by charge neutrality using a contour integral of the properly normalized Green's function,

$$N(\varepsilon_{\rm F}) = \frac{1}{2\pi} \sum_{RLR'L'} \oint_{\mathcal{C}(\varepsilon_{\rm F})} \mathrm{Im}\, G_{RLR'L'}(z)\mathrm{d}z, \qquad \dot{\boldsymbol{K}}^a \equiv \partial \boldsymbol{K}^a/\partial z, \tag{3.56}$$

which counts states exactly (Lloyd-type formula) when spurious poles from the screened logarithmic derivative are removed channel by channel [63, 69, 71]. On the same contour one accumulates site- and energy-resolved densities needed for the Coulomb problem.

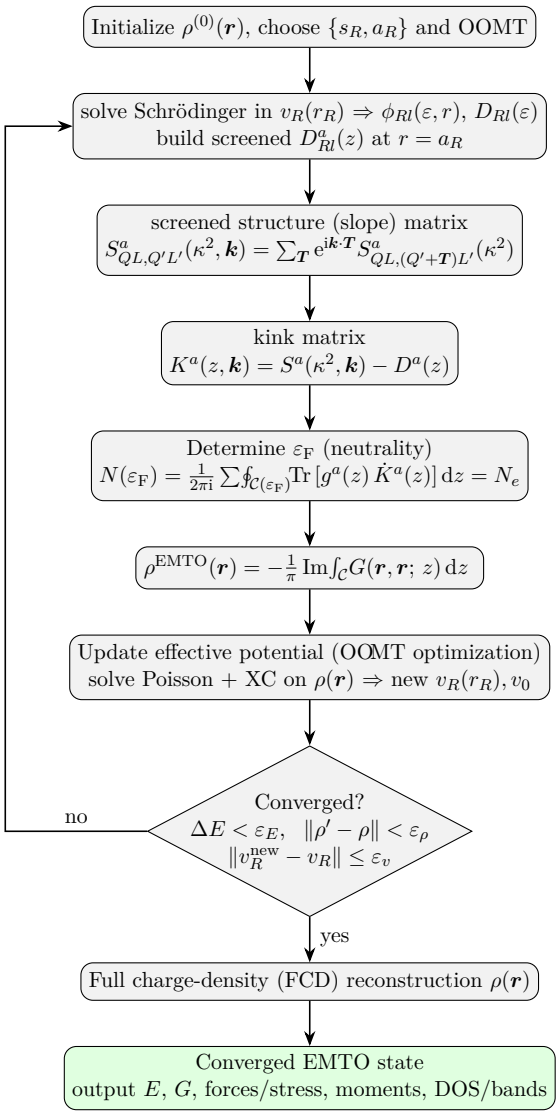

Figure 4: Self-consistency loop for the EMTO method: starting from an initial charge density and OOMT potential, the Kohn-Sham equations are solved in the EMTO basis via the slope matrix and kink matrix formalism. Upon convergence the full charge-density reconstruction can be performed.

Because the single-site problem is solved with spherical wells, an accurate total energy after obtaining self-consistency in the OOMT potential requires a nonspherical reconstruction of the charge density. EMTO-FCD expands the charge in each potential sphere in real spherical harmonics,

$$\rho(\boldsymbol{r}_R) = \sum_L \rho_L^R(r_R)\, Y_L(\hat{r}_R), \qquad r_R \le s_R, \tag{3.57}$$

with radial multipoles $\rho_L^R(r_R)$ obtained from the site-diagonal Green's function built out of $\{\phi_{Rl}\}$ and the path operator $g^{\,a}$ (energy integration along $\mathcal{C}$). In the a-interstitial I^a one retains a smooth representation consistent with the screened spherical waves (typically via Fourier components or a real-space grid). The FCD step ensures that all low-order multipoles (not only the spherical average) enter the electrostatics and

exchange-correlation, which is essential for quantitative total energies and forces [63, 64].

Given $\rho(\boldsymbol{r})$ computed from the normalized Green's function and the screened path operator, the Hartree potential v_H solves

$$\nabla^2 v_H(\boldsymbol{r}) = -4\pi\Big[\rho(\boldsymbol{r}) - \rho_{\mathrm{nuc}}(\boldsymbol{r})\Big], \qquad \rho_{\mathrm{nuc}}(\boldsymbol{r}) = \sum_R Z_R\,\delta(\boldsymbol{r}-\boldsymbol{R}), \tag{3.58}$$

with a partitioned solution. Inside each sphere $r_R \le s_R$ one employs the multipole expansion

$$v_H(\boldsymbol{r}_R) = 4\pi \sum_L \left[\frac{r_R^l}{2l+1}\,A_L^R + \frac{1}{r_R^{l+1}}\,B_L^R\right] Y_L(\hat{r}_R), \tag{3.59}$$

where the *internal* moments A_L^R are functionals of $\rho_L^R(r)$ and the *external* moments B_L^R embed the electrostatic influence of all other sites and the interstitial (Ewald- or screened-lattice sums in practice) [63, 72]. In the interstitial one then solves the Poisson-equation $\nabla^2 v_H = -4\pi\,\rho(\boldsymbol{r})$ with periodic boundary conditions, and continuity of v_H and its normal derivative is enforced at $r_R = s_R$ for every L up to a chosen $l_{\max}^{\mathrm{Coul}}$. The exchange-correlation $v_{xc}[\rho]$ is assembled from the reconstructed $\rho(\boldsymbol{r})$ (LDA/GGA/meta-GGA as chosen), and the updated OOMT potential is re-optimized: new $v_R(r_R)$ and v_0 minimize the least-squares deviation to $v_{\mathrm{KS}}(\boldsymbol{r}) = v_{ext}(\boldsymbol{r}) + v_H(\boldsymbol{r}) + v_{xc}(\boldsymbol{r})$ for the fixed set $\{s_R,a_R\}$ [63, 69].

The cycle is closed by mixing the charge or the effective potential (site radial wells v_R, background v_0). The same mixing schemes as described in Section 2.4 are applicable. Convergence is monitored through simultaneous thresholds on total-energy changes, norms of charge/potential residuals, and – when relaxing structures – Hellmann-Feynman forces. Upon convergence one evaluates total energies, stresses, and response properties from the reconstructed $\rho(\boldsymbol{r})$ and the EMTO Green's function $G(z)$.

In summary, the slope matrix provides the short-ranged lattice embedding for screened multiple scattering; the FCD step lifts the spherical approximation by restoring non-spherical charge moments; and the multipole Poisson solver couples both pieces into an updated OOMT potential. Together they deliver near-full-potential accuracy at the computational cost characteristic of spherical multiple-scattering methods [60, 61, 63, 64].

4 Dynamical mean-field theory

Density-functional theory in the Kohn-Sham formulation provides an efficient, ground-state framework that replaces the many-electron problem by noninteracting particles in an effective local potential. Along Perdew's "Jacob's ladder" of exchange-correlation approximations, depicted in Fig. 1, ever richer ingredients are added, culminating in approaches that incorporate nonlocal correlation or many-body screening (RPA, GW). Yet these extensions remain essentially static: they produce a time- (or frequency-) independent potential, and thus cannot generate dynamical signatures of strong correlations such as Hubbard sidebands, temperature-dependent quasiparticle coherence, or lifetime broadening. Precisely here, dynamical mean-field theory (DMFT) enters as a complementary, explicitly many-body approach: it keeps the full local time dependence of electron-electron interactions through a frequency-dependent self-energy while neglecting nonlocal correlations.

Building on this motivation, a decisive conceptual step was the observation that on lattices with large coordination number Z the many-body self-energy becomes predominantly local. In the corresponding large-Z (or $d \to \infty$) limit the problem acquires a nontrivial mean-field structure in which spatial fluctuations are suppressed while temporal (quantum) fluctuations at a given site remain fully dynamical. This insight, due to *Metzner* and *Vollhardt*, provided a small parameter ($1/Z$) and a controlled route to a solvable limit for correlated lattice fermions [73]. Shortly thereafter, *Georges et al.* formulated the self-consistency mapping that defines dynamical mean-field theory: the lattice model is replaced by a quantum impurity embedded in a self-consistent electronic bath (see Fig. 5), and the mapping is iterated until the local observables of the impurity and the lattice coincide [74].

This impurity perspective is physically transparent. It captures the local competition between kinetic delocalization and on-site interactions responsible for correlation phenomena. Numerically, the required impurity problems are solved with a growing toolbox of solvers: from early Hirsch-Fye quantum Monte Carlo and exact diagonalization to modern continuous-time Monte Carlo methods that handle multi-orbital

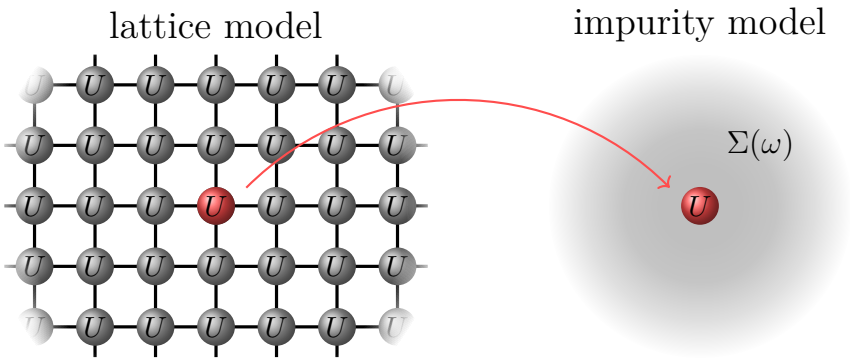

Figure 5: Illustration of the concept of dynamical mean-field theory (DMFT). The lattice model is mapped onto an impurity model, where a single interacting site is coupled to an effective bath.

Hubbard-Hund interactions with high accuracy at finite temperature [20, 75]. The result is a frequency-dependent local self-energy that endows the one-electron spectrum with lifetimes, temperature evolution, and high-/low-energy features inaccessible to static functionals.

The most predominant limitation of single-site DMFT is the missing nonlocal (momentum-dependent) components of the self-energy. Long-wavelength collective modes and intersite exchange processes are then only partially or statically represented. Cluster extensions – formulated either in real space or in momentum space – mitigate this by introducing short-range spatial correlations while retaining the dynamical treatment on the cluster, enabling, for example, studies of pseudogap physics and short-range singlets [76].

4.1 Essentials of the Hubbard model

The central difficulty of correlated-electron physics is the competition between kinetic delocalization and local Coulomb repulsion. When the characteristic interaction scale competes with the electronic bandwidth, there is no obvious small parameter and perturbative expansions around a noninteracting band picture may fail – precisely the regime that motivates DMFT. To set the stage, we start from a general, normal-ordered many-body Hamiltonian written in a localized one-particle basis (e.g. tight-binding/Wannier functions)

$$\hat{H} = \sum_{ij} h_{ij}\, \hat{c}_i^\dagger \hat{c}_j + \frac{1}{2} \sum_{ijkl} U_{ijkl}\, \hat{c}_i^\dagger \hat{c}_j^\dagger \hat{c}_l \hat{c}_k, \tag{4.1}$$

where h_{ij} collects kinetic hoppings and one-body potentials (including, by convention, the chemical potential via $h_{ij} \to h_{ij} - \mu\delta_{ij}$), and U_{ijkl} are the Coulomb matrix elements in this basis. Creation/annihilation operators $\hat{c}_{i\sigma}^\dagger$, $\hat{c}_{i\sigma}$ carry composite indices $i \equiv (R, m)$ for site R and orbital m; they define the particle number operator $\hat{n}_{i\sigma} = \hat{c}_{i\sigma}^\dagger \hat{c}_{i\sigma}$. Equation (4.1) is exact once the basis is specified (e.g. Wannier functions) and will later provide the bridge between material-specific DFT/EMTO bandstructures and low-energy many-body models.

A widely used reduction of (4.1) is the (single-band) *Hubbard model*, which retains only the dominant contributions: short-range hopping and on-site interaction [77–79]. For one orbital per site, nearest-neighbor hopping, and a site-diagonal on-site energy, the Hamiltonian reads

$$\hat{H} = \sum_{i,\sigma} \epsilon_i\, \hat{n}_{i\sigma} + \sum_{\langle i,j\rangle,\sigma} t_{ij}\, \hat{c}_{i\sigma}^\dagger \hat{c}_{j\sigma} + \sum_i U_i\, \hat{n}_{i\uparrow} \hat{n}_{i\downarrow}. \tag{4.2}$$

Here t_{ij} are hopping amplitudes between nearest neighbors $\langle i,j\rangle$, ϵ_i are on-site levels, and $U_i = U_{iiii}$ is the on-site (Hubbard) repulsion penalizing double occupancy. Despite its minimal form,Eq. (4.2) captures the metal-insulator transition driven by interactions (Mott physics), the emergence of local moments, and strong mass renormalization.

In realistic materials, crystal fields and Hund's exchange act within degenerate d/f shells, calling for a multi-orbital generalization of (4.2). The interaction tensor is then often parameterized in the Slater-Kanamori form with intra-orbital U, inter-orbital U', Hund's coupling J, and pair hopping – parameters that can be linked to screened Slater integrals or constrained-first-principles estimates [20, 74, 79].

4.2 The DMFT effective action

To derive the DMFT equations we employ the "cavity method" following [74, 80, 81], a method borrowed from classical statistical mechanics, which explicitly constructs a local, dynamical mean field in the large-coordination limit. The general idea of the cavity method is to remove a reference site (say, $i = o$) from the lattice, solve the remaining system (the *cavity*) and then couple the site back to this environment. Integrating out the cavity degrees of freedom generates an *effective local action* on site o that contains the original local interaction and a retarded, frequency-dependent hybridization that encodes virtual hopping to and from the environment. This hybridization defines the Weiss field $\mathcal{G}$ and turns the on-site problem into a quantum impurity embedded in a self-consistent bath. In the limit of large coordination $Z \to \infty$, the self-energy becomes purely local, so the impurity Green's function equals the local component of the lattice Green's function, closing the self-consistency loop. Operationally, the cavity construction thus provides a clean path from the lattice Hamiltonian (4.1) (or its Hubbard reduction (4.2)) to the impurity action used in DMFT, while making transparent the role of the Weiss field and the locality assumption [73, 74].

The cavity method is most conveniently formulated in the field integral representation [82]. For the lattice Hamiltonian in Eq. (4.2), the grand-canonical partition function can be written as a functional integral over Grassmann fields:

$$\mathcal{Z} = \int \prod_{i,\sigma} \mathcal{D}[c^+_{i\sigma}(\tau), c_{i\sigma}(\tau)] \mathrm{e}^{-S_{\mathrm{latt}}[\boldsymbol{c}^+, \boldsymbol{c}]}, \tag{4.3}$$

with the lattice action

$$S_{\mathrm{latt}}[\boldsymbol{c}^+, \boldsymbol{c}] = \int_0^\beta \mathrm{d}\tau \left(\sum_{ij,\sigma} c^+_{i\sigma}(\tau) \big[\partial_\tau \delta_{ij} + h_{ij} \big] c_{j\sigma}(\tau) + \sum_i U_i n_{i\uparrow}(\tau) n_{i\downarrow}(\tau) \right), \tag{4.4}$$

where $\beta = 1/T$, h_{ij} includes the chemical potential shift $h_{ij} \to h_{ij} - \mu\, \delta_{ij}$, and $(c^+_{i\sigma}, c_{i\sigma})$ are Grassmann fields corresponding to the fermionic operators $(\hat{c}^\dagger_{i\sigma}, \hat{c}_{i\sigma})$ with $n_{i\sigma} \equiv c^+_{i\sigma} c_{i\sigma}$. The vector notation of the Grassmann fields abbreviates the set of all space and spin indices, e.g. $\boldsymbol{c}(\tau) = \{c_{i\sigma}(\tau)\}_{i,\sigma}$. The representation of the partition function (4.3) and the action (4.4) will allow us to excise a reference site, integrate out the cavity, and derive the local impurity action and Weiss field used in DMFT.

We now derive the effective local action by selecting the reference site $i = o$ and integrating out all other degrees of freedom:

$$\frac{1}{\mathcal{Z}_{\mathrm{eff}}} \mathrm{e}^{-S_{\mathrm{eff}}[\boldsymbol{c}^+_o, \boldsymbol{c}_o]} \equiv \frac{1}{\mathcal{Z}} \int \prod_{i \neq o, \sigma} \mathcal{D}[c^+_{i\sigma}(\tau), c_{i\sigma}(\tau)] \mathrm{e}^{-S_{\mathrm{latt}}[\boldsymbol{c}^+, \boldsymbol{c}]}. \tag{4.5}$$

The effective action S_{eff} contains the original local interaction on site o plus a dynamical hybridization term arising from virtual hopping to and from the cavity. It defines the effective single-site problem at the heart of DMFT, which needs to be solved. The expectation values of local observables (e.g. the impurity Green's function) with respect to S_{eff} are equal to the local observables of the original lattice problem. This condition closes the DMFT self-consistency loop, letting us determine all local quantities via the impurity problem. In general, the Grassmann numbers are functions of imaginary

time $\tau \in [0, \beta]$. For notational simplicity, we suppress this dependence in the following unless otherwise noted.

To derive S_{eff}, we split the full lattice action S_{latt} (4.4) into three parts: the on-site action of the chosen site S_o, the action of the cavity $S^{(o)}$ (the lattice with site o removed), and the coupling between site o and the cavity ΔS:

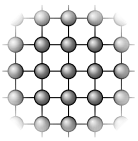

$$S_{\text{latt}} = S_o + S^{(o)} + \Delta S \tag{4.6}$$

$$S_o = \int_0^\beta \mathrm{d}\tau \left(\sum_\sigma c^+_{o\sigma} \big(\partial_\tau + \epsilon_o - \mu \big) c_{o\sigma} + U_o n_{o\uparrow} n_{o\downarrow} \right) \tag{4.7}$$

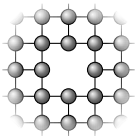

$$S^{(o)} = \int_0^\beta \mathrm{d}\tau \left(\sum_{i,j\neq o,\sigma} c^+_{i\sigma} \Big[\big(\partial_\tau + \varepsilon_i - \mu \big) + t_{ij} \Big] c_{j\sigma} + \sum_{i\neq o} U_i n_{i\uparrow} n_{i\downarrow} \right) \tag{4.8}$$

$$\Delta S = \int_0^\beta \mathrm{d}\tau \sum_{i\neq o,\sigma} \left(t_{io} c^+_{i\sigma} c_{o\sigma} + t_{oi} c^+_{o\sigma} c_{i\sigma} \right) \tag{4.9}$$

Expectation values with respect to the cavity action $S^{(o)}$ are denoted by $\langle \cdot \rangle_{S^{(o)}}$. Since the local action S_o is independent of all other sites and the cavity fields, we can factor it out of the path integral. Starting from the full partition function,

$$\mathcal{Z} = \int \mathcal{D}[\boldsymbol{c}^+_o,\, \boldsymbol{c}_o] \exp(-S_o) \int \prod_{i\neq o,\sigma} \mathcal{D}[c^+_{i\sigma},\, c_{i\sigma}] \exp\Big(-S^{(o)} - \Delta S \Big), \tag{4.10}$$

we integrate out only the cavity fields to obtain the (unnormalized) weight of a fixed local configuration $(\boldsymbol{c}^+_o,\, \boldsymbol{c}_o)$:

$$\mathcal{W}[\boldsymbol{c}^+_o, \boldsymbol{c}_o] \coloneqq \int \prod_{i\neq o,\sigma} \mathcal{D}[c^+_{i\sigma},\, c_{i\sigma}] \exp\Big(-S^{(o)} - \Delta S \Big) = \mathcal{Z}^{(o)} \left\langle \mathrm{e}^{-\Delta S} \right\rangle_{S^{(o)}}, \tag{4.11}$$

where the last equality is just the definition of the cavity expectation value. The quantity we are actually interested in is the normalized probability density over $(\boldsymbol{c}^+_o, \boldsymbol{c}_o)$, induced by the full lattice measure

$$\mathcal{P}[\boldsymbol{c}^+_o, \boldsymbol{c}_o] \coloneqq \frac{1}{\mathcal{Z}} \mathrm{e}^{-S_o[\boldsymbol{c}^+_o, \boldsymbol{c}_o]} \mathcal{W}[\boldsymbol{c}^+_o,\, \boldsymbol{c}_o] = \frac{\mathcal{Z}^{(o)}}{\mathcal{Z}} \mathrm{e}^{-S_o[\boldsymbol{c}^+_o, \boldsymbol{c}_o]} \left\langle \mathrm{e}^{-\Delta S} \right\rangle_{S^{(o)}}. \tag{4.12}$$

By construction, $\int \mathcal{D}[\boldsymbol{c}^+_o,\, \boldsymbol{c}_o]\, \mathcal{P}[\boldsymbol{c}^+_o,\, \boldsymbol{c}_o] = 1$. We now define the local effective action S_{eff} and its normalizing partition function $\mathcal{Z}_{\text{eff}}$ by writing this normalized measure in Boltzmann form:

$$\mathcal{P}[\boldsymbol{c}^+_o, \boldsymbol{c}_o] \equiv \frac{1}{\mathcal{Z}_{\text{eff}}} \mathrm{e}^{-S_{\text{eff}}[\boldsymbol{c}^+_o, \boldsymbol{c}_o]}, \qquad \mathcal{Z}_{\text{eff}} \coloneqq \int \mathcal{D}[\boldsymbol{c}^+_o, \boldsymbol{c}_o] \mathrm{e}^{-S_{\text{eff}}[\boldsymbol{c}^+_o, \boldsymbol{c}_o]}. \tag{4.13}$$

Equating (4.12) with (4.13) we can express the integral as the expectation value of the coupling term ΔS with respect to the cavity action:

$$\frac{1}{\mathcal{Z}_{\text{eff}}}\mathrm{e}^{-S_{\text{eff}}} = \frac{1}{\mathcal{Z}}\mathrm{e}^{-S_o[\boldsymbol{c}_o^+,\boldsymbol{c}_o]}\int\prod_{i\neq o,\sigma}\mathcal{D}\left[c_{i\sigma}^+,c_{i\sigma}\right]\mathrm{e}^{-S^{(o)}}\mathrm{e}^{-\Delta S} = \frac{\mathcal{Z}^{(o)}}{\mathcal{Z}}\mathrm{e}^{-S_o}\left\langle\mathrm{e}^{-\Delta S}\right\rangle_{S^{(o)}} \tag{4.14}$$

The average $\langle\mathrm{e}^{-\Delta S}\rangle_{S^{(o)}}$ in (4.14) is a generating functional for cavity Green's functions [74, 82, 83]. To make this explicit, we couple Grassmann sources linearly to the cavity fields $\{c_{i\sigma}(\tau), c_{i\sigma}^+(\tau)\}_{i\neq o}$ and identify those sources with operators built from the local fields at site o:

$$\eta_{i\sigma}(\tau) \coloneqq t_{io}c_{o\sigma}(\tau), \qquad \eta_{i\sigma}^+(\tau) \coloneqq c_{o\sigma}^+(\tau)t_{oi}. \tag{4.15}$$

With this choice we rewrite the coupling as

$$\Delta S = \int_0^\beta \mathrm{d}\tau \sum_{i\neq o,\sigma}\left[c_{i\sigma}^+(\tau)\eta_{i\sigma}(\tau) + \eta_{i\sigma}^+(\tau)c_{i\sigma}(\tau)\right], \tag{4.16}$$

leading to

$$\mathrm{e}^{-S_{\text{eff}}[\boldsymbol{\eta}^+,\boldsymbol{\eta}]} = \frac{\mathcal{Z}_{\text{eff}}\mathcal{Z}^{(o)}}{\mathcal{Z}}\mathrm{e}^{-S_o}\left\langle\exp\left(-\int_0^\beta \mathrm{d}\tau\sum_{i\neq o,\sigma}\left[c_{i\sigma}^+\eta_{i\sigma}+\eta_{i\sigma}^+c_{i\sigma}\right]\right)\right\rangle_{S^{(o)}} \tag{4.17}$$

Using left Grassmann functional derivatives with respect to the explicit sources, the unconnected cavity Green's functions are generated by derivatives of $\mathrm{e}^{-S_{\text{eff}}[\boldsymbol{\eta}^+,\boldsymbol{\eta}]}$ [83]. In particular, the two-point function reads

$$G^{(o)}_{i\sigma,j\sigma'}(\tau,\tau') = -\frac{\delta^2}{\delta\eta_{i\sigma}^+(\tau)\delta\eta_{j\sigma'}(\tau')}\mathrm{e}^{-S_{\text{eff}}[\boldsymbol{\eta}^+,\boldsymbol{\eta}]}\bigg|_{\eta=\eta^+=0} = -\left\langle c_{i\sigma}(\tau)c_{j\sigma'}^+(\tau')\right\rangle_{S^{(o)}}, \tag{4.18}$$

and, more generally, the n-particle unconnected cavity Green's function is obtained as

$$\begin{aligned} &G^{(o)}_{i_1\sigma_1,\ldots,i_n\sigma_n,j_1\sigma_1',\ldots,j_n\sigma_n'}(\tau_1,\ldots,\tau_n,\tau_1',\ldots,\tau_n') \\ &\quad= (-1)^{n+1}\frac{\delta^{2n}}{\delta\eta_{i_1\sigma_1}^+(\tau_1)\cdots\delta\eta_{i_n\sigma_n}^+(\tau_n)\delta\eta_{j_1\sigma_1'}(\tau_1')\cdots\delta\eta_{j_n\sigma_n'}(\tau_n')}\mathrm{e}^{-S_{\text{eff}}[\boldsymbol{\eta}^+,\boldsymbol{\eta}]}\bigg|_{\eta=\eta^+=0} \\ &\quad= -\left\langle c_{i_1\sigma_1}(\tau_1)\cdots c_{i_n\sigma_n}(\tau_n)c_{j_1\sigma_1'}^+(\tau_1')\cdots c_{j_n\sigma_n'}^+(\tau_n')\right\rangle_{S^{(o)}}. \end{aligned} \tag{4.19}$$

The additional factor $(-1)^n$ in Eq. (4.19) results from the fact that Grassmann numbers and derivatives anticommute: for each pair of indices, we need to move the derivative $\delta/\delta\eta$ past c^+ to act on η, leading to one additional minus sign. We can avoid additional sign changes by following the standard convention of applying all η^+-derivatives first, then all η-derivatives (as written) [83].

Equation (4.17) shows that $\mathrm{e}^{-S_{\text{eff}}[\boldsymbol{\eta}^+,\boldsymbol{\eta}]}$ is proportional to the cavity average of a source-coupled exponential. Taking the logarithm isolates the source-dependent part:

$$-S_{\text{eff}}[\boldsymbol{\eta}^+,\boldsymbol{\eta}] = \ln\left(\tfrac{\mathcal{Z}_{\text{eff}}\mathcal{Z}^{(o)}}{\mathcal{Z}}\right) - S_o[\boldsymbol{c}_o^+,\boldsymbol{c}_o] + \ln\left\langle\mathrm{e}^{-\Delta S}\right\rangle_{S^{(o)}}, \tag{4.20}$$

The first two terms on the right-hand side are independent of the sources and thus irrelevant for functional differentiation.

Since S_{eff} is the logarithm of the source-coupled average, its functional derivatives generate *connected* cavity green's functions $G_c^{(o)}$ [82, 83]:

$$\begin{aligned} &G^{(o)}_{c;\, i_1\sigma_1,\ldots,i_n\sigma_n,j_1\sigma_1',\ldots,j_n\sigma_n'}(\tau_1,\,\ldots,\tau_n,\tau_1',\,\ldots,\tau_n') \\ &\quad= \frac{\delta^{2n}}{\delta\eta^+_{i_1\sigma_1}(\tau_1)\cdots\delta\eta^+_{i_n\sigma_n}(\tau_n)\delta\eta_{j_1\sigma_1'}(\tau_1')\cdots\delta\eta_{j_n\sigma_n'}(\tau_n')} S_{\text{eff}}[\boldsymbol{\eta}^+,\,\boldsymbol{\eta}]\Big|_{\eta=\eta^+=0} \end{aligned} \tag{4.21}$$

For the particle-number-conserving lattice action S_{latt}, averages with an unbalanced number of c^+ and c vanish. Expanding the effective action S_{eff} in powers of the sources yields the linked-cluster series in connected cavity Green's functions

$$\begin{aligned} S_{\text{eff}} = -\ln\Big(\tfrac{\mathcal{Z}_{\text{eff}}\mathcal{Z}^{(o)}}{\mathcal{Z}}\Big) + S_o + \sum_{n=1}^{\infty}\frac{1}{(n!)^2}\sum_{\substack{i_1,\ldots,j_n\neq o\\ \sigma_1,\ldots\sigma_n'}}\int_0^\beta \mathrm{d}\tau_1\ldots\mathrm{d}\tau_n'\;\eta^+_{i_1\sigma_1}(\tau_1)\ldots\eta^+_{i_n\sigma_n}(\tau_n) \\ \times G^{(o)}_{c;\, i_1,\ldots,j_n,\sigma_1,\ldots\sigma_n'}(\tau_1,\,\ldots,\tau_n')\eta_{j_1\sigma_1'}(\tau_1')\ldots\eta_{j_n\sigma_n'}(\tau_n'). \end{aligned} \tag{4.22}$$

The factor $1/(n!)^2$ in Eq. (4.22) accounts for the symmetry of the connected cavity Green's function under permutations of the n incoming and n outgoing legs separately. Note that the first nontrivial term in the expansion is quadratic in the sources, since the one-point cavity Green's function vanishes for a particle-number-conserving action. In the non-interacting case $U_i = 0$, all connected cavity Green's functions of order $n \geq 2$ vanish, so only the term with $n = 1$ remains [84] [1] . Therefore the effective action becomes quadratic in the sources (i.e. bilinear in the local fields), and in imaginary time it reads

$$\begin{aligned} S_{\text{eff}}[\boldsymbol{c}_o^+,\,\boldsymbol{c}_o] = \int_0^\beta \mathrm{d}\tau\sum_\sigma c^+_{o\sigma}(\tau)\Big(\partial_\tau + \epsilon_o - \mu\Big)c_{o\sigma}(\tau) + \int_0^\beta \mathrm{d}\tau\, U_o n_{o\uparrow}(\tau)n_{o\downarrow}(\tau) \\ + \int_0^\beta \mathrm{d}\tau\int_0^\beta \mathrm{d}\tau'\sum_{i,j\neq o,\sigma} t_{oi}c^+_{o\sigma}(\tau)G^{(o)}_{ij,\sigma}(\tau-\tau')t_{jo}c_{o\sigma}(\tau'). \end{aligned} \tag{4.23}$$

The effective action can also be represented by introducing the *Weiss field*

$$\mathcal{G}_0^{-1}(\tau-\tau') \coloneqq -\Big(\partial_\tau + \epsilon_o - \mu\Big)\delta(\tau-\tau') - \sum_{i,j\neq o} t_{oi}G^{(o)}_{ij}(\tau-\tau')t_{jo}, \tag{4.24}$$

which encodes the dynamical hybridization of the impurity site o to the cavity:

$$S_{\text{eff}}[\boldsymbol{c}_o^+,\boldsymbol{c}_o] = -\int_0^\beta \mathrm{d}\tau\int_0^\beta \mathrm{d}\tau'\sum_\sigma c^+_{o\sigma}(\tau)\mathcal{G}^{-1}_{0,\sigma}(\tau-\tau')c_{o\sigma}(\tau') + \int_0^\beta \mathrm{d}\tau\, U_o n_{o\uparrow}(\tau)n_{o\downarrow}(\tau) \tag{4.25}$$

To close the equations we relate the *cavity* Green's function $G_{ij}^{(o)}$ to the full-lattice Green's function G_{ij} for the example of the Bethe lattice: Removing site o corresponds

[1] In the limit of infinite coordination number $Z \to \infty$, the cavity expansion simplifies drastically. To obtain a nontrivial limit in which kinetic and interaction energies remain comparable, the hopping elements must be scaled as $t_{ij} \to \frac{t_{ij}}{Z^{\|i-j\|_1/2}}$, where $\|i-j\|_1$ is the Manhattan distance [73, 74, 85]. Under this scaling, only the *one-particle* connected cavity Green's function survives.

to taking the Schur complement of the local block in the resolvent. In Matsubara frequency space this yields the classical Hubbard identity [74, 77]

$$G_{ij}^{(o)}(i\omega_n) = G_{ij}(i\omega_n) - \frac{G_{io}(i\omega_n)G_{oj}(i\omega_n)}{G_{oo}(i\omega_n)}. \tag{4.26}$$

The relation (4.26) can be understood heuristically by interpreting the Green's functions as propagators on the lattice. The Green's function G_{ij} sums amplitudes for all paths from i to j on the full lattice. The cavity propagator $G_{ij}^{(o)}$ omits those paths that traverse site o. The difference $G_{ij} - G_{ij}^{(o)}$ therefore collects precisely the contributions of paths that reach o and leave it again. Such contributions factor into an amplitude to go from i to o (G_{io}), from o to j (G_{oj}), and a renormalization at o that removes overcounting of multiple excursions through the intermediate site. This renormalization is exactly G_{oo}^{-1}, which counts paths that leave and return to o only once [77]. Summing these processes reproduces Eq. (4.26). A similar expression to Eq. (4.26) can be formulated for more general lattices, requiring additional terms involving the Fourier transform of the hopping terms.

4.3 Single impurity Anderson model

In the $Z \to \infty$ limit the effective action S_{eff} of the distinguished lattice site o becomes local apart from a quadratic nonlocal-in-time term that encodes virtual hops into the rest of the lattice [cf. Eq. (4.23)]. This structure is precisely that of a quantum impurity (the local interacting site) hybridized with a noninteracting fermionic bath. The canonical realization is the *single impurity Anderson model* (SIAM), a model proposed by *P. W. Anderson* in 1961 to describe magnetic impurities in nonmagnetic host metals [86].

The SIAM Hamiltonian reads

$$\hat{H}_{\text{imp}} = \sum_{\sigma} \epsilon_\sigma \hat{d}_\sigma^\dagger \hat{d}_\sigma + U \hat{d}_\uparrow^\dagger \hat{d}_\uparrow \hat{d}_\downarrow^\dagger \hat{d}_\downarrow + \sum_{k,\sigma} \epsilon_{k\sigma} \hat{c}_{k\sigma}^\dagger \hat{c}_{k\sigma} + \sum_{k,\sigma} \left(V_{k\sigma} \hat{c}_{k\sigma}^\dagger \hat{d}_\sigma + V_{k\sigma}^* \hat{d}_\sigma^\dagger \hat{c}_{k\sigma} \right), \tag{4.27}$$

where $\hat{d}_\sigma^\dagger$ and $\hat{d}_\sigma$ are the creation and annihilation operators for an electron with spin σ on the impurity orbital, while, $\hat{c}_{k\sigma}^\dagger$ and $\hat{c}_{k\sigma}$ are the corresponding operators for the free conduction electrons in the host metal, the bath. The original model assumed d-orbital impurities hybridizing with an s-band conduction electron bath, but the model is more generally applicable. The first two terms in Eq. (4.27) describe the impurity with on-site energy ϵ_d and Coulomb repulsion U, while the last two terms describe the bath dispersion ϵ_k and its hybridization V_k with the impurity.

Since the bath of the SIAM is noninteracting, it can be integrated out similar to the cavity fields in the previous section. Splitting the SIAM action into impurity S_{imp}, bath S_{bath}, and hybridization S_{hyb} parts,

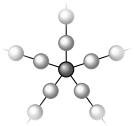

$$S_{\mathrm{imp}} = S_{\mathrm{loc}} + S_{\mathrm{bath}} + S_{\mathrm{hyb}}, \tag{4.28}$$

$$S_{\mathrm{loc}} = \int_0^\beta \mathrm{d}\tau \left(\sum_\sigma d_\sigma^+ \big(\partial_\tau + \epsilon_\sigma\big) d_\sigma + U d_\uparrow^+ d_\uparrow d_\downarrow^+ d_\downarrow \right), \tag{4.29}$$

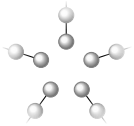

$$S_{\mathrm{bath}} = \int_0^\beta \mathrm{d}\tau \sum_{k,\sigma} c_{k\sigma}^+ \big(\partial_\tau + \varepsilon_{k\sigma}\big) c_{k\sigma}, \tag{4.30}$$

$$S_{\mathrm{hyb}} = \int_0^\beta \mathrm{d}\tau \sum_{k,\sigma} \Big(V_{k\sigma} c_{k\sigma}^+ d_\sigma + V_{k\sigma}^* d_\sigma^+ c_{k\sigma} \Big), \tag{4.31}$$

where $(d_\sigma^+,\, d_\sigma)$ and $(c_{k\sigma}^+,\, c_{k\sigma})$ again are the Grassmann fields corresponding to the fermionic operators of the impurity $(\hat{d}_\sigma^\dagger,\, \hat{d}_\sigma)$ and the bath $(\hat{c}_{k\sigma}^\dagger,\, \hat{c}_{k\sigma})$. The grand-canonical partition function of the SIAM is given by the path integral

$$\mathcal{Z}_{\mathrm{imp}} = \int \prod_\sigma \mathcal{D}[d_\sigma^+,\, d_\sigma] \mathrm{e}^{-S_{\mathrm{loc}}} \int \prod_{k,\sigma} \mathcal{D}[c_{k\sigma}^+,\, c_{k\sigma}] \mathrm{e}^{-S_{\mathrm{bath}} - S_{\mathrm{hyb}}}. \tag{4.32}$$

The SIAM action is quadratic in the noninteracting bath degrees of freedom $\{c_{k\sigma},\, c_{k\sigma}^+\}$. Fourier transforming from imaginary time to Matsubara frequencies replaces $\partial_\tau \to -\mathrm{i}\omega_n$, where $\omega_n = (2n+1)\pi/\beta$ are fermionic Matsubara frequencies. The fields are accordingly transform as $c_{k\sigma}(\tau) \to c_{k\sigma}(\mathrm{i}\omega_n) \equiv c_{k\sigma n}$, introducing the frequency-labeled Grassmann fields $c_{k\sigma n}$, $c_{k\sigma n}^+$ and $d_{\sigma n}$, $d_{\sigma n}^+$. The bath degrees of the action then reads

$$S_{\mathrm{bath}} + S_{\mathrm{hyb}} = \sum_{k\sigma n} c_{k\sigma n}^+ \big(i\omega_n - \varepsilon_{k\sigma}\big) c_{k\sigma n} - \sum_{k\sigma n} \Big(c_{k\sigma n}^+ V_{k\sigma} d_{\sigma n} + d_{\sigma n}^+ V_{k\sigma}^* c_{k\sigma n} \Big). \tag{4.33}$$

The functional integral over the bath Grassmann variables is Gaussian[83]. Performing the integration yields

$$\int \prod_{k\sigma n} \mathcal{D}[c_{k\sigma n}^+, c_{k\sigma n}] \mathrm{e}^{-S_{\mathrm{bath}} - S_{\mathrm{hyb}}} = \mathcal{Z}_{\mathrm{bath}} \exp\Big(\sum_{\sigma n} d_{\sigma n}^+ \underbrace{\Big[\sum_k V_{k\sigma}^* \frac{1}{\mathrm{i}\omega_n - \varepsilon_{k\sigma}} V_{k\sigma} \Big]}_{\Delta_\sigma(\mathrm{i}\omega_n)} d_{\sigma n} \Big), \tag{4.34}$$

i.e. the bath generates the *hybridization function* $\Delta_\sigma(\mathrm{i}\omega_n)$:

$$\Delta_\sigma(\mathrm{i}\omega_n) = \sum_k \frac{|V_{k\sigma}|^2}{\mathrm{i}\omega_n - \varepsilon_{k\sigma}} = \sum_k |V_{k\sigma}|^2 g_{k\sigma}(\mathrm{i}\omega_n), \qquad g_{k\sigma}(\mathrm{i}\omega_n) \equiv \frac{1}{\mathrm{i}\omega_n - \varepsilon_{k\sigma}}, \tag{4.35}$$

where $g_{k\sigma}(\mathrm{i}\omega_n)$ is the free Green's function of an isolated bath level $k\sigma$. The prefactor $\mathcal{Z}_{\mathrm{bath}}$ in Eq. (4.34) is a field-independent normalization, affecting only the absolute

magnitude of the partition function but not observables. Fourier transforming (4.35) gives

$$\Delta_\sigma(\tau) = \frac{1}{\beta}\sum_n \mathrm{e}^{-\mathrm{i}\omega_n\tau}\Delta_\sigma(\mathrm{i}\omega_n) \tag{4.36}$$

which evaluates to the familiar piecewise form (antiperiodic on $\tau \in (-\beta,\, \beta)$):

$$\Delta_\sigma(\tau) = \sum_k |V_{k\sigma}|^2 \times \begin{cases} f(\varepsilon_{k\sigma})\mathrm{e}^{-\varepsilon_{k\sigma}\tau}, & \tau \in (-\beta,\, 0), \\ -\Big[1 - f(\varepsilon_{k\sigma})\Big]\mathrm{e}^{-\varepsilon_{k\sigma}\tau}, & \tau \in (\ \ 0,\, \beta), \end{cases} \tag{4.37}$$

where $f(\varepsilon)$ is the Fermi function. The impurity site is described by an effective action that is quadratic in the noninteracting (bath-induced) part and local in the interaction:

$$\begin{aligned} S_{\mathrm{eff}}[\boldsymbol{d}^+,\, \boldsymbol{d},\, \Delta] = \int_0^\beta \mathrm{d}\tau \left[\sum_\sigma d_\sigma^+(\tau)\Big(\partial_\tau + \varepsilon_\sigma\Big)d_\sigma(\tau) + U d_\uparrow^+(\tau)d_\uparrow(\tau)d_\downarrow^+(\tau)d_\downarrow(\tau)\right] \\ + \int_0^\beta \mathrm{d}\tau \int_0^\beta \mathrm{d}\tau' \sum_\sigma d_\sigma^+(\tau)\Delta_\sigma(\tau-\tau')d_\sigma(\tau'), \end{aligned} \tag{4.38}$$

Fourier transforming to Matsubara frequencies, the quadratic kernel defines the inverse of the noninteracting impurity Green's function:

$$G_{0,\sigma}^{-1}(\mathrm{i}\omega_n) = \mathrm{i}\omega_n - \varepsilon_\sigma - \Delta_\sigma(\mathrm{i}\omega_n), \tag{4.39}$$

so that the effective action can be written compactly as

$$S_{\mathrm{eff}}[\boldsymbol{d}^+, \boldsymbol{d}, \Delta] = \sum_{\sigma n} d_{\sigma n}^+ G_{0,\sigma}^{-1}(\mathrm{i}\omega_n) d_{\sigma n} + S_U, \qquad S_U = U\int_0^\beta \mathrm{d}\tau\, n_\uparrow(\tau) n_\downarrow(\tau), \tag{4.40}$$

with $n_\sigma(\tau) = d_\sigma^+(\tau)d_\sigma(\tau)$.

4.4 Equivalence of lattice and impurity effective actions

The cavity construction discussed in Section 4.2 yields a local effective lattice action $S_{\mathrm{eff}}[\boldsymbol{c}_o^+,\, \boldsymbol{c}_o]$, Eq. (4.25), for the distinguished site o that is interacting only on-site and coupled to the rest of the lattice through the Weiss field $\mathcal{G}_0^{-1}$, which encodes the dynamical hybridization of the impurity site o to the cavity. The single-impurity Anderson model (SIAM), upon integrating out its noninteracting bath, produces an impurity action $S_{\mathrm{imp}}[\boldsymbol{d}^+,\, \boldsymbol{d},\, \Delta] \equiv S_{\mathrm{eff}}[\boldsymbol{d}^+,\, \boldsymbol{d},\, \Delta]$, Eq. (4.38), of the same structure, fully characterized by the hybridization function $\Delta(\mathrm{i}\omega_n)$ (see Sec. 4.3). Thus, there is a one-to-one correspondence

$$\Delta \Longleftrightarrow \mathcal{G} \Longleftrightarrow S_{\mathrm{eff}} \Longleftrightarrow S_{\mathrm{imp}}\,,$$

up to a field-independent normalization that does not affect observables. In the limit of infinite coordination ($Z \to \infty$) the cavity cumulant expansion truncates at the two-point level, so that all higher connected terms vanish and S_{eff} becomes *exactly* quadratic in the bath coupling [73, 74]. Identifying the local fields as $d_\sigma \equiv c_{o\sigma}$ then makes S_{eff} and S_{imp} identical provided they share the same Δ (or $\mathcal{G}$). DMFT turns this structural equivalence into a closed theory by fixing Δ through the self-consistency

condition $G_{\mathrm{imp}}(\mathrm{i}\omega_n) = G_{\mathrm{loc}}(\mathrm{i}\omega_n)$, which enforces that the impurity reproduces the local physics of the lattice [74].

For a single impurity Anderson model with a bath chosen such that

$$\Delta(\mathrm{i}\omega_n) = \sum_{ij\neq o} t_{oi} G^{(o)}_{ij}(\mathrm{i}\omega_n) t_{jo} \tag{4.41}$$

and identical on-site energies to the lattice model, the effective actions of the lattice site o and the impurity coincide, $S_{\mathrm{eff}}[\boldsymbol{c}^+_o, \boldsymbol{c}_o] = S_{\mathrm{imp}}[\boldsymbol{d}^+, \boldsymbol{d}, \Delta]$. For the non-interacting Green's function of the impurity this implies

$$G^{-1}_{0,\mathrm{imp}}(\mathrm{i}\omega_n) = \mathrm{i}\omega_n + \mu - \varepsilon_o - \sum_{ij\neq o} t_{oi} G^{(o)}_{ij}(\mathrm{i}\omega_n) t_{jo} =: \mathcal{G}^{-1}_0(\mathrm{i}\omega_n). \tag{4.42}$$

We now can substitute the Hubbard identity (4.26) into equations (4.41) and (4.42). After some algebraic manipulations this yields the important DMFT self-consistency condition

$$\Delta(\mathrm{i}\omega_n) = \mathrm{i}\omega_n + \mu - \varepsilon_o - \Sigma(\mathrm{i}\omega_n) - G^{-1}_{oo}(\mathrm{i}\omega_n). \tag{4.43}$$

For a homogeneous system, where all sites are equivalent, the self-energy is site-independent, and thus $\Sigma_i(\mathrm{i}\omega_n) = \Sigma(\mathrm{i}\omega_n)$. In the limit of infinite coordination number $Z \to \infty$, the lattice self-energy is k-independent and coincides with the impurity self-energy, $\Sigma(\mathrm{i}\omega_n) = \Sigma_{\mathrm{imp}}(\mathrm{i}\omega_n)$ [73, 74]. The local lattice Green's function can then be expressed via the non-interacting DOS

$$\rho(\varepsilon) = \frac{1}{N} \sum_{\boldsymbol{k}} \delta(\varepsilon - \varepsilon_{\boldsymbol{k}}) \tag{4.44}$$

leading to

$$G_{\mathrm{loc}}(\mathrm{i}\omega_n) \equiv G_{oo}(\mathrm{i}\omega_n) = \int \mathrm{d}\varepsilon \, \frac{\rho(\varepsilon)}{\mathrm{i}\omega_n + \mu - \varepsilon_o - \Sigma(\mathrm{i}\omega_n) - \varepsilon}. \tag{4.45}$$

For single-orbital models, the Hilbert transform can be simplified to

$$G_{\mathrm{loc}}(\mathrm{i}\omega_n) = G_{0,\mathrm{loc}}\Big(\mathrm{i}\omega_n - \Sigma(\mathrm{i}\omega_n)\Big), \tag{4.46}$$

where $G_{0,oo}$ is the non-interacting local lattice Green's function.

4.5 Self-consistent DMFT cycle and convergence

Having established the formal equivalence between the effective lattice action and the SIAM, we now turn to the practical realization of the DMFT self-consistency. The task is to determine the hybridization Δ (or equivalently the Weiss field $\mathcal{G}^{-1}_0$) such that the impurity Green's function G_{imp} reproduces the local lattice Green's function $G_{\mathrm{loc}} \equiv G_{oo}$ while the self-energies coincide, $\Sigma_{\mathrm{imp}} = \Sigma$.

In practice, one proceeds iteratively:

1. Start from an initial guess for the self-energy $\Sigma(\mathrm{i}\omega_n)$ (or equivalently for the hybridization function $\Delta(\mathrm{i}\omega_n)$). A reasonable initial guess is the noninteracting limit $\Sigma(\mathrm{i}\omega_n) = 0$ or the Hartree approximation.

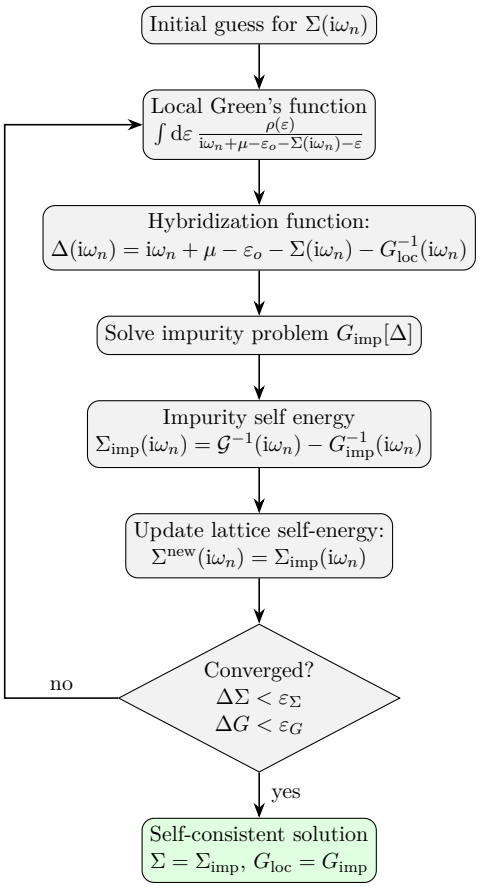

Figure 6: Single-site DMFT self-consistency loop. Starting from an initial self-energy (or hybridization), compute the local lattice Green's function, update the hybridization (equivalently the Weiss field), solve the impurity problem, and iterate until $G_{\mathrm{imp}} = G_{\mathrm{loc}}$ and $\Sigma_{\mathrm{imp}} = \Sigma$.

2. With the current self-energy, compute the local lattice Green's function from the lattice dispersion or the non-interacting DOS (4.45):

$$G_{\mathrm{loc}}(\mathrm{i}\omega_n) = \int \mathrm{d}\varepsilon \, \frac{\rho(\varepsilon)}{\mathrm{i}\omega_n + \mu - \varepsilon_o - \Sigma(\mathrm{i}\omega_n) - \varepsilon}. \tag{4.47}$$

3. Construct the hybridization function Δ (4.43) (or equivalently the Weiss field $\mathcal{G}_0$) defining the impurity problem:

$$\Delta(\mathrm{i}\omega_n) = \mathrm{i}\omega_n + \mu - \varepsilon_o - \Sigma(\mathrm{i}\omega_n) - G^{-1}_{\mathrm{loc}}(\mathrm{i}\omega_n). \tag{4.48}$$

4. Solve the impurity problem $G[\Delta]$ using an appropriate impurity solver for the single-impurity Anderson model.

5. Compute the impurity self-energy via the Dyson equation:

$$\Sigma_{\mathrm{imp}}(\mathrm{i}\omega_n) = \mathcal{G}^{-1}(\mathrm{i}\omega_n) - G^{-1}_{\mathrm{imp}}(\mathrm{i}\omega_n). \tag{4.49}$$

6. Update the lattice self-energy with the impurity self-energy:

$$\Sigma^{\text{new}}(\mathrm{i}\omega_n) = \Sigma_{\text{imp}}(\mathrm{i}\omega_n). \tag{4.50}$$

   As described in the previous self-consistent methods, one may optionally employ mixing schemes to stabilize convergence.

7. Check for convergence of the self-energy and/or Green's function

$$\Delta\Sigma = \frac{1}{N_\omega}\sum_n |\Sigma^{\text{new}}(\mathrm{i}\omega_n) - \Sigma(\mathrm{i}\omega_n)|, \quad \Delta G = \frac{1}{N_\omega}\sum_n |G_{\text{imp}}(\mathrm{i}\omega_n) - G_{\text{loc}}(\mathrm{i}\omega_n)|. \tag{4.51}$$

   If not converged, return to step 2 with the updated self-energy.

After convergence is reached, the self-consistent solution $\Sigma(\mathrm{i}\omega_n) = \Sigma_{\text{imp}}(\mathrm{i}\omega_n)$ and $G_{\text{loc}}(\mathrm{i}\omega_n) = G_{\text{imp}}(\mathrm{i}\omega_n)$ can be used to compute observables of interest. A schematic representation of the DMFT self-consistency loop is shown in Fig. 6.

The DMFT self-consistency becomes *exact* only in the limit of infinite coordination ($Z \to \infty$), where the self-energy is purely local and the cavity construction closes without error [73, 74]. For real lattices with finite Z, DMFT is an approximation that neglects nonlocal (spatial) correlations while retaining the full local quantum dynamics. Its leading corrections scale with inverse coordination and with the strength/range of spatial fluctuations. Two important *exact* limits persist at finite Z: the atomic limit ($t_{ij} = 0$), where the impurity decouples from the lattice and DMFT reduces to the exact local problem, and the noninteracting limit ($U = 0$), where $\Sigma = 0$ and the DMFT loop reproduces the exact band Green's function. Between these limits, DMFT is most reliable on high-coordination lattices or in regimes dominated by local physics. Systematic improvements are available via cluster extensions (CDMFT/DCA) when short-range spatial correlations matter [74].

To close the DMFT loop one needs an impurity solver that maps a given Weiss field $\mathcal{G}$ (or hybridization Δ) to the interacting impurity Green's function G_{imp} and self-energy Σ_{imp}. In the next chapters, we briefly discuss two widely used classes. The spin-polarized T-matrix fluctuation-exchange (SPTF/FLEX) approximation is a self-consistent, diagrammatic (Baym-Kadanoff conserving) approach that resums particle-particle ladders into a T matrix and incorporates particle-hole spin/charge fluctuations; its spin-polarized formulation treats broken-symmetry states and generates a frequency-dependent, spin-resolved Σ_{imp} at relatively low cost, making it suitable for weak-to-intermediate interactions and multi-orbital settings [87–89]. By contrast, continuous-time quantum Monte Carlo (CT-QMC) solvers are numerically exact (up to statistical noise): the interaction-expansion (CT-INT), auxiliary-field (CT-AUX), and hybridization-expansion (CT-HYB) algorithms stochastically sample the perturbation series implied by S_{imp} and return unbiased Matsubara Green's functions and vertex data; they handle strong coupling and complex local interactions but are limited by sign problems and by the need for analytic continuation to real frequencies [90–92].

5 Spin polarized T-matrix FLEX approximation

5.1 Fluctuation exchange approximation (FLEX)

The fluctuation-exchange (FLEX) formalism is a self-consistent, *conserving* approximation designed for systems with intermediate to moderately strong correlations. It builds on the Baym-Kadanoff framework of Φ-derivable functionals [93, 94], which guarantees the microscopic conservation of particle number, momentum, and energy. In practice, FLEX goes beyond mean-field (Hartree-Fock) theory by resumming classes of diagrams associated with interparticle scattering: particle-particle ladders (the T-matrix channel) and particle-hole bubbles/ladders (spin and charge fluctuation channels), treated on equal footing and closed self-consistently for both the self-energy and susceptibilities [87]. Because these collective fluctuation channels are included, FLEX captures the feedback of charge and spin fluctuations that is essential for analyzing competing ordering tendencies in correlated metals and multi-orbital systems.

The fluctuation-exchange (FLEX) formalism treats both instantaneous and retarded two-particle interactions on equal footing. A convenient starting point is an effective action of the lattice model [87, 93, 94]

$$\begin{aligned} S &= S_0 + S_V, \\ S_0 &= \sum_{x,x',\sigma} c^+_\sigma(x)\Big(\partial_\tau + h_0\Big)_{xx'} c_\sigma(x'), \\ S_V &= \frac{1}{2}\sum_{x,x',\sigma,\sigma'} v(x-x') c^+_\sigma(x) c^+_{\sigma'}(x') c_{\sigma'}(x') c_\sigma(x), \end{aligned} \tag{5.1}$$

similar to the derivation of DMFT in Section 4.2. Here, $x = (\boldsymbol{r}, \tau)$ combines lattice position and imaginary time, and $\sum_x \equiv \sum_{\boldsymbol{r}} \int_0^\beta \mathrm{d}\tau$. We abbreviate $x_1 \equiv 1$, etc. The Grassmann fields c_σ, c^+_σ represent fermions, and $v(x-x')$ is a general two-body interaction depending only on coordinate differences. For the (single-band) Hubbard model one has $v(x-x') = U\ \delta_{xx'}$, i.e. in shorthand $v(1-2) = U\ \delta_{12}$. In the one-band case it is convenient to rewrite the action using the Fourier transformed quantities

$$c_\sigma(x) = \frac{1}{\sqrt{N}}\sum_k c_\sigma(k)\mathrm{e}^{\mathrm{i}k\cdot x}, \quad c^+_\sigma(x) = \frac{1}{\sqrt{N}}\sum_k c^+_\sigma(k)\mathrm{e}^{-\mathrm{i}k\cdot x}, \quad v(x) = \frac{1}{\sqrt{N}}\sum_q v(q)\mathrm{e}^{\mathrm{i}q\cdot x},$$

with N the number of lattice sites, Brillouin-zone momentum sums, and $k = (\boldsymbol{k}, \omega_n)$, $q = (\boldsymbol{q}, \Omega_m)$ composed of crystal momentum and Matsubara frequency:

$$\omega_n = (2n+1)\pi T \quad \text{(fermionic)}, \qquad \Omega_m = 2m\pi T \quad \text{(bosonic)}. \tag{5.2}$$

The action (5.1) can then be expressed in momentum space as

$$S_0 = \sum_{k,\sigma}\Big(-\mathrm{i}\omega_n + \varepsilon_{\boldsymbol{k}}\Big) c^+_\sigma(k) c_\sigma(k), \tag{5.3}$$

$$S_V = \frac{1}{2}\sum_{k,k',q}\sum_{\sigma,\sigma'} v(q) c^+_\sigma(k+q) c^+_{\sigma'}(k'-q) c_{\sigma'}(k') c_\sigma(k), \tag{5.4}$$

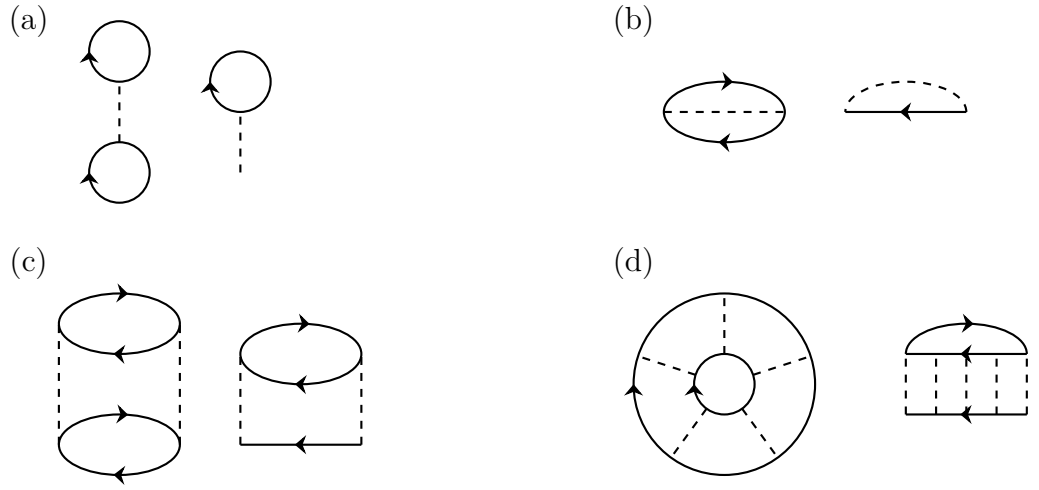

Figure 7: Schematic correspondence between Luttinger-Ward Φ diagrams (left) and the self-energy $\Sigma = \delta\Phi/\delta G$ (right). Cutting a G line in a Φ diagram produces the associated Σ term. Shown are (a) Hartree, (b) Fock, (c) second order particle-hole, and (d) particle-particle ladder (T-matrix) contributions [93].

where $\varepsilon_{\boldsymbol{k}}$ is determined by the non-interacting Haniltonian h_0. In a general self-consistent (not necessarily conserving) approximation, the two-particle interaction v is replaced by an effective one-particle medium: fermions propagate in a space- and time-dependent field represented by the self-energy $\Sigma_\sigma(x,\, x')$, to be determined within a given approximation. FLEX is obtained by constructing Σ from a Φ-derivable functional that self-consistently resums particle-particle ladders (the T-matrix channel) and particle-hole spin/charge fluctuations, thereby retaining microscopic conservation laws and capturing the feedback of collective modes on single-particle properties [87, 94].

A sufficient condition for an approximation to be conserving is that its self-energy be Φ-*derivable* in the sense of Baym and Kadanoff [93, 94]. That is, there exists a Luttinger-Ward functional $\Phi[G,\, v]$ such that

$$\Sigma_\sigma(x,\, x') = \frac{\delta\Phi[G,\, v]}{\delta G_\sigma(x',\, x)}. \tag{5.5}$$

Diagrammatically, the functional derivative "cuts a Green's-function line" in a Φ-diagram to produce the corresponding self-energy diagram; the resulting Σ is automatically consistent with macroscopic conservation laws (particle number, momentum, and energy) and with thermodynamic consistency, as shown schematically in Fig. 7.

The one-particle Green's function G not only encodes single-particle excitations, but as shown by Luttinger and Ward, it also generates the equilibrium thermodynamics of an interacting Fermi system through a functional of G [95]. In Matsubara formalism, the (grand-potential) free-energy functional can be written as

$$\mathcal{F}[G] = -\operatorname{Tr}\ln(-G) + \operatorname{Tr}(\Sigma G) - \Phi[G], \tag{5.6}$$

where Tr denotes the full functional trace over space, spin/orbital indices, and imaginary time (or momentum and Matsubara frequency). The self-energy is related to the interacting and noninteracting propagators by

$$\Sigma = G_0^{-1} - G^{-1}, \tag{5.7}$$

and $\Phi[G]$ is the Luttinger-Ward (or Baym-Kadanoff) functional, defined as the sum of all two-particle-irreducible skeleton diagrams built with G and the bare interaction.

A central result of Luttinger and Ward is that $\mathcal{F}[G]$ is *stationary* at the physical Green's function provided the self-energy is Φ-derivable,

$$\frac{\delta \mathcal{F}}{\delta G} = 0 \qquad \Longleftrightarrow \qquad \Sigma = \frac{\delta \Phi[G]}{\delta G}, \tag{5.8}$$

and, together with Eq. (5.7), this yields Dyson's equation $G^{-1} = G_0^{-1} - \Sigma$. Approximations constructed from a truncated (but explicit) $\Phi[G]$ are therefore *stationary* and *conserving*: by varying G they satisfy the macroscopic conservation laws and remain thermodynamically consistent [94].

5.2 Spin-polarized T-matrix FLEX

Following Refs. [89, 96], we adopt a Hamiltonian formulation of the spin-polarized FLEX (SPTF): instantaneous one-body terms can be supplied by the spin-polarized LDA (LSDA) Hamiltonian, while dynamical two-particle fluctuations are treated within DMFT via the spin-polarized T-matrix FLEX (SPTF) self-energy. The fluctuating effective fields (charge and spin channels) will be generated by generalized susceptibilities constructed from the interacting Green's functions. We begin by defining the multi-orbital model Hamiltonian and the correlated subspace.

$$H = \sum_{ij\sigma} \sum_{\{m\}} t^{ij}_{m_1 m_2} \hat{c}^\dagger_{im_1\sigma} \hat{c}_{jm_2\sigma} + \frac{1}{2} \sum_{i\sigma\sigma'} \sum_{\{m\}} U^i_{m_1 m_2 m_1' m_2'} \hat{c}^\dagger_{im_1\sigma} \hat{c}^\dagger_{im_2\sigma'} \hat{c}_{im_2'\sigma'} \hat{c}_{im_1'\sigma}, \tag{5.9}$$

where i, j label lattice sites, m enumerate localized orbitals (e.g. d or f within a chosen projector/subspace), and σ is the spin index. The one-electron parameters $t^{ij}_{m_1 m_2}$ come from the spin-polarized Kohn-Sham Hamiltonian represented in the correlated Wannier (or projector) basis. The on-site Coulomb tensor is

$$U^i_{m_1 m_2 m_1' m_2'} = \int \mathrm{d}^3\boldsymbol{r} \int \mathrm{d}^3 r' \Psi^*_{im_1}(\boldsymbol{r}) \Psi^*_{im_2}(\boldsymbol{r}') V_{ee}(\boldsymbol{r} - \boldsymbol{r}') \Psi_{im_1'}(\boldsymbol{r}) \Psi_{im_2'}(\boldsymbol{r}'), \tag{5.10}$$

with V_{ee} the (screened) Coulomb interaction and $\{\Psi_{im}\}$ localized orbitals spanning the interacting subspace. If LDA one-electron terms are used for the non-interacting Hamiltonian, we subtract a double-counting (dc) term from the one-body part and write

$$H^{\mathrm{dc}}_{\mathrm{LDA}} = \sum_{ij\sigma} \sum_{\{m\}} h^{ij}_{m_1 m_2} \hat{c}^\dagger_{im_1\sigma} \hat{c}_{jm_2\sigma} - E^{\mathrm{dc}}, \tag{5.11}$$

$$H = H^{\mathrm{dc}}_{\mathrm{LDA}} + \frac{1}{2} \sum_{i\sigma\sigma'} \sum_{\{m\}} U^i_{m_1 m_2 m_1' m_2'} \hat{c}^\dagger_{im_1\sigma} \hat{c}^\dagger_{im_2\sigma'} \hat{c}_{im_2'\sigma'} \hat{c}_{im_1'\sigma}. \tag{5.12}$$

Here $h^{ij}_{m_1 m_2}$ are spin-dependent one-particle matrix elements obtained from LSDA and projected to the correlated basis; E^{dc} compensates the static mean-field part of interactions already included in LSDA (double-counting). The interaction tensor U^i is nonzero only on correlated sites i and within the correlated orbitals $\{m\}$.

Contrary to FLEX implementations that retain explicit momentum dependence, here we adopt the DMFT locality assumption and work with a purely local, frequency-dependent self-energy $\Sigma(\mathrm{i}\omega_n)$. Following the spin-polarized T-matrix FLEX (SPTF) scheme of Lichtenstein and Katsnelson [89, 96], we improve upon the original FLEX formulation by treating particle-particle (pp) and particle-hole (ph) channels asymmetrically: the pp channel is summed to all ladder orders to form a T matrix, which renormalizes the effective interaction, and this *renormalized* interaction is then used explicitly in the ph channel for spin and charge fluctuations. This separation captures short-range pairing-type correlations via the pp ladders while preserving a conserving description of spin/charge dynamics in the ph sector.

To organize the interacting channels we symmetrize the on-site Coulomb tensor over ph and pp combinations. For a correlated site i with localized orbitals $\{m\}$ we define

$$U^d_{m_1m_1'm_2m_2'} = 2U^i_{m_1m_2m_1'm_2'} - U^i_{m_1m_2\,m_2'm_1'}, \tag{5.13}$$

$$U^m_{m_1m_1'm_2m_2'} = -U^i_{m_1m_2m_2'm_1'}, \tag{5.14}$$

$$U^s_{m_1m_1'm_2m_2'} = \tfrac{1}{2}\left(U^i_{m_1m_1'm_2m_2'} + U^i_{m_1m_1'm_2'm_2}\right), \tag{5.15}$$

$$U^t_{m_1m_1'm_2'm_2} = \tfrac{1}{2}\left(U^i_{m_1m_1'm_2'm_2} - U^i_{m_1m_1'm_2m_2'}\right), \tag{5.16}$$

which act, respectively, in the ph density (d) and magnetic (m) channels, and in the pp singlet (s) and triplet (t) channels. These combinations are most transparently obtained by projecting the bare interaction onto pair operators that generate correlated particle-hole and particle-particle fluctuations.

Let $1 \equiv (m_1, \sigma_1)$ and $2 \equiv (m_2, \sigma_2)$ denote orbital-spin indices on the same site, and write $\hat{c}_1$ for $\hat{c}_{m_1\sigma_1}$, etc. The ph density and spin operators are

$$d_{12} = \frac{1}{\sqrt{2}}\left(\hat{c}^\dagger_{m_1\uparrow}\hat{c}_{m_2\uparrow} + \hat{c}^\dagger_{m_1\downarrow}\hat{c}_{m_2\downarrow}\right), \tag{5.17}$$

$$m^0_{12} = \frac{1}{\sqrt{2}}\left(\hat{c}^\dagger_{m_1\uparrow}\hat{c}_{m_2\uparrow} - \hat{c}^\dagger_{m_1\downarrow}\hat{c}_{m_2\downarrow}\right), \qquad m^+_{12} = \hat{c}^\dagger_{m_1\uparrow}\hat{c}_{m_2\downarrow}, \qquad m^-_{12} = \hat{c}^\dagger_{m_1\downarrow}\hat{c}_{m_2\uparrow}, \tag{5.18}$$

while the pp singlet and triplet pair operators are

$$s_{12} = \frac{1}{\sqrt{2}}\left(\hat{c}_{m_1\downarrow}\hat{c}_{m_2\uparrow} - \hat{c}_{m_1\uparrow}\hat{c}_{m_2\downarrow}\right), \qquad s^+_{12} = \frac{1}{\sqrt{2}}\left(\hat{c}^\dagger_{m_1\downarrow}\hat{c}^\dagger_{m_2\uparrow} - \hat{c}^\dagger_{m_1\uparrow}\hat{c}^\dagger_{m_2\downarrow}\right), \tag{5.19}$$

$$t^+_{12} = \hat{c}_{m_1\uparrow}\hat{c}_{m_2\uparrow}, \qquad t^0_{12} = \frac{1}{\sqrt{2}}\left(\hat{c}_{m_1\downarrow}\hat{c}_{m_2\uparrow} + \hat{c}_{m_1\uparrow}\hat{c}_{m_2\downarrow}\right), \qquad t^-_{12} = \hat{c}_{m_1\downarrow}\hat{c}_{m_2\downarrow}, \tag{5.20}$$

and their Hermitian conjugates create the corresponding pairs. Projecting the bare interaction onto these operators produces the matrix elements in Eqs. (5.13) to (5.16), which then serve as input to the SPTF construction of the spin-dependent effective interactions $W^{\sigma\sigma'}_{m_1m_2m_3m_4}$. In SPTF, the pp ladders built with U^s and U^t define a dynamic T matrix that renormalizes the short-range vertex; the resulting effective interaction is subsequently used in the ph density and magnetic channels (with U^d and U^m) to compute generalized susceptibilities and the spin-resolved, local self-energy $\Sigma_\sigma(\mathrm{i}\omega_n)$ self-consistently within DMFT [89, 96].

5.3 Green's function

Within DMFT we neglect any explicit momentum dependence of the self-energy and work with a purely local, frequency-dependent $\Sigma(\mathrm{i}\omega_n)$. As in standard many-body practice, the self-energy is decomposed into a static (Hartree-Fock-like) contribution, Σ^U, obtained from the instantaneous on-site interaction, and a dynamical part that incorporates fluctuation effects beyond mean field. In the present spin-polarized T-matrix FLEX (SPTF) implementation the dynamical part is constructed in a GW-type fashion from renormalized effective interactions (see below). The resulting orbital- and spin-resolved Green's function reads

$$G^{-1}_{mm'\sigma}(\mathrm{i}\omega_n) = (\mathrm{i}\omega_n + \mu)\delta_{mm'} - h_{mm'\sigma} - \Sigma^U_{mm'\sigma} - \Sigma_{mm'\sigma}(\mathrm{i}\omega_n), \tag{5.21}$$

where μ is the chemical potential, $\omega_n = (2n+1)\pi/\beta$ are fermionic Matsubara frequencies, and h^σ are the LSDA one-body matrix elements projected to the correlated subspace. Unless stated otherwise, all quantities are local (site index suppressed) and matrices act in the orbital indices $\{m\}$.

In the spirit of Kanamori's idea, we treat particle-particle (pp) and particle-hole (ph) channels asymmetrically: the pp ladders are summed first to form a T matrix that *renormalizes* the local interaction; this dynamic effective vertex is then used explicitly in the ph channel to describe spin and charge fluctuations. Concretely, the Kanamori T matrix satisfies a Dyson-like ladder equation in the pp channel,

$$\langle 13|T^{\sigma\sigma'}(\mathrm{i}\Omega_m)|24\rangle = \langle 13|v|24\rangle - \frac{1}{\beta}\sum_{\omega_n}\sum_{56,78} G^{\sigma}_{56}(\mathrm{i}\omega_n)G^{\sigma'}_{78}(\mathrm{i}\Omega_m - \mathrm{i}\omega_n)\,\langle 58|T^{\sigma\sigma'}(\mathrm{i}\Omega_m)|76\rangle\,, \tag{5.22}$$

where v denotes the bare on-site interaction tensor. Hartree and Fock contributions are obtained by replacing the bare vertex by T:

$$\Sigma^{(\mathrm{TH})}_{12\sigma}(\mathrm{i}\omega_n) = \frac{1}{\beta}\sum_{\Omega_m}\sum_{34\sigma'} \langle 13|T^{\sigma\sigma'}(\mathrm{i}\Omega_m)|24\rangle\, G^{\sigma'}_{43}(\mathrm{i}\Omega_m - \mathrm{i}\omega_n), \tag{5.23}$$

$$\Sigma^{(\mathrm{TF})}_{12\sigma}(\mathrm{i}\omega_n) = -\frac{1}{\beta}\sum_{\Omega_m}\sum_{34} \langle 14|T^{\sigma\sigma}(\mathrm{i}\Omega_m)|32\rangle\, G^{\sigma}_{34}(\mathrm{i}\Omega_m - \mathrm{i}\omega_n). \tag{5.24}$$

This construction is exact in the dilute limit (small hole or electron density in the correlated shell), where the pp ladders dominate and the T matrix sums the leading scattering processes.

Beyond the dilute limit, ph fluctuations renormalize quasiparticles and generate additional structure in the self-energy. We therefore supplement Eqs. (5.23) to (5.24) by a ph contribution built from generalized susceptibilities and spin-dependent effective potentials $W^{\sigma\sigma'}$. Combining density and longitudinal-spin channels into $D \equiv (d,\, m^0)$ and transverse channels into $m^\pm$, the interaction part of the (local) Hamiltonian can be recast in compact form

$$H_U = \frac{1}{2}\,\mathrm{Tr}\left(D^\dagger * V^\parallel * D + m^+ * V^\perp_m * m^- + m^- * V^\perp_m * m^+\right), \tag{5.25}$$

where $*$ denotes matrix multiplication in the paired orbital indices $(m_1 m_2)$, and

$$V^\parallel = \frac{1}{2}\begin{pmatrix} V^{dd} & V^{dm} \\ V^{md} & V^{mm}\end{pmatrix}, \qquad \left(V^\perp_m\right)_{1234} = \langle 13|T^{\uparrow\downarrow}|42\rangle\,. \tag{5.26}$$

The longitudinal (z)-channel matrix elements are obtained from the spin-resolved T matrix as

$$V^{dd}_{1234} = \frac{1}{2}\sum_{\sigma}\left(\sum_{\sigma'}\langle 13|T^{\sigma\sigma'}|42\rangle - \langle 13|T^{\sigma'\sigma'}|42\rangle\right), \tag{5.27}$$

$$V^{dm}_{1234} = \frac{1}{2}\sum_{\sigma\sigma'}\sigma\left(\langle 13|T^{\sigma\sigma}|42\rangle - \langle 13|T^{\sigma\sigma}|24\rangle + \langle 13|T^{\sigma'\sigma}|42\rangle\right) = V^{md}_{1234}, \tag{5.28}$$

$$V^{mm}_{1234} = \frac{1}{2}\sum_{\sigma}\left(\sum_{\sigma'}\sigma\sigma'\,\langle 13|T^{\sigma\sigma'}|42\rangle - \langle 13|T^{\sigma'\sigma'}|42\rangle\right). \tag{5.29}$$

5.4 Bubbles, susceptibilities, and fluctuation potentials

The building block for susceptibilities is the empty loop (bubble)

$$\Gamma^{\sigma\sigma'}_{m_1m_2m_3m_4}(\tau) = -G_{m_2m_3\sigma}(\tau)G_{m_4m_1\sigma'}(-\tau), \tag{5.30}$$

with $\Gamma(\mathrm{i}\omega_n)$ its Matsubara transform. We define the bare longitudinal susceptibility matrix

$$\chi_0^{\parallel}(\mathrm{i}\omega_n) = \frac{1}{2}\begin{pmatrix}\Gamma^{\uparrow\uparrow}+\Gamma^{\downarrow\downarrow} & \Gamma^{\uparrow\uparrow}-\Gamma^{\downarrow\downarrow}\\ \Gamma^{\uparrow\uparrow}-\Gamma^{\downarrow\downarrow} & \Gamma^{\uparrow\uparrow}+\Gamma^{\downarrow\downarrow}\end{pmatrix}, \tag{5.31}$$

whose entries correspond to (dd), (dm^0), (m^0d), and (m^0m^0) channels, respectively. The RPA-like resummations in transverse and longitudinal sectors then give

$$\chi^{\perp}(\mathrm{i}\omega_n) = \frac{\Gamma^{\uparrow\downarrow}(\mathrm{i}\omega_n)}{\mathbb{1} + V_m^{\perp} * \Gamma^{\uparrow\downarrow}(\mathrm{i}\omega_n)}, \tag{5.32}$$

$$\chi^{\parallel}(\mathrm{i}\omega_n) = \frac{\chi_0^{\parallel}(\mathrm{i}\omega_n)}{\mathbb{1} + V^{\parallel} * \chi_0^{\parallel}(\mathrm{i}\omega_n)}. \tag{5.33}$$

The spin-resolved fluctuation potentials follow as

$$W_{\uparrow\uparrow}(\mathrm{i}\omega_n) = \tfrac{1}{2}V^{\parallel} * \left(\chi^{\parallel} - \chi_0^{\parallel}\right) * V^{\parallel}, \tag{5.34}$$

$$W_{\downarrow\downarrow}(\mathrm{i}\omega_n) = \tfrac{1}{2}V^{\parallel} * \left(\tilde{\chi}^{\parallel} - \tilde{\chi}_0^{\parallel}\right) * V^{\parallel}, \tag{5.35}$$

$$W_{\uparrow\downarrow}(\mathrm{i}\omega_n) = \tfrac{1}{2}V_m^{\perp} * \left(\chi^{+-} - \chi_0^{+-}\right) * V_m^{\perp}, \tag{5.36}$$

$$W_{\downarrow\uparrow}(\mathrm{i}\omega_n) = \tfrac{1}{2}V_m^{\perp} * \left(\chi^{-+} - \chi_0^{-+}\right) * V_m^{\perp}, \tag{5.37}$$

where $\tilde{\chi}^{\parallel}$ is obtained from $\chi^{\parallel}$ by interchanging $\uparrow\uparrow$ and $\downarrow\downarrow$ in Eq. (5.31). The particle-hole contribution to the self-energy is then

$$\Sigma^{(\mathrm{ph})}_{12\sigma}(\tau) = \sum_{34,\sigma'} W^{\sigma\sigma'}_{1342}(\tau)G_{34\sigma'}(\tau). \tag{5.38}$$

Collecting the pieces, the local dynamical self-energy entering Eq. (5.21) is

$$\Sigma_{\sigma}(\mathrm{i}\omega_n) = \Sigma^{(\mathrm{TH})}_{\sigma}(\mathrm{i}\omega_n) + \Sigma^{(\mathrm{TF})}_{\sigma}(\mathrm{i}\omega_n) + \Sigma^{(\mathrm{ph})}_{\sigma}(\mathrm{i}\omega_n), \tag{5.39}$$

which is evaluated self-consistently together with Eqs. (5.22) to (5.38) inside the DMFT loop. Physically, the T-matrix ladders renormalize short-range scattering in the pp channel (exact in the dilute limit), while $W^{\sigma\sigma'}$ accounts for dynamical spin and charge fluctuations in the ph channel, generating the characteristic frequency dependence of $\Sigma_{\sigma}(\mathrm{i}\omega_n)$.

6 Continuous-time quantum Monte Carlo

Continuous-time quantum Monte Carlo (CT-QMC) emerged in the mid-2000s as the decisive step beyond discrete-time Hirsch-Fye QMC [97] for solving quantum impurity problems at the heart of DMFT. The key innovation was to abandon imaginary-time Trotter discretization and to formulate diagrammatic expansions directly in continuous time, which removed systematic Trotter errors and unlocked access to lower temperatures and larger local Hilbert spaces. Three complementary implementations crystallized almost simultaneously and have since defined the field: the weak-coupling interaction expansion (CT-INT), introduced by Rubtsov, Savkin, and Lichtenstein [90], provided a continuous-time determinant framework built around an expansion in the local interaction and quickly became a reference for benchmark studies and cluster extensions. The hybridization expansion (CT-HYB), introduced by Werner, Comanac, de' Medici, Troyer, and Millis [98], shifted perspective by treating the local Hamiltonian exactly and expanding the hybridization, which proved especially powerful for multi-orbital d- and f-shell problems and set the standard in realistic LDA/GGA+DMFT. The auxiliary-field variant (CT-AUX), developed by Gull, Werner, Parcollet, Troyer, and Millis [99], adapted continuous-time ideas to a discrete Hubbard-Stratonovich formulation and offered a scalable weak-coupling route that connected naturally to determinant-QMC techniques. Within a few years these solvers replaced Hirsch-Fye across DMFT applications, and a comprehensive synthesis by Gull *et al.* in a 2011 review [92] defined best practices, clarified performance envelopes, and established shared terminology. Since then, CT-QMC has underpinned advances ranging from realistic materials studies to two-particle response functions and diagrammatic extensions, with CT-HYB dominating strongly correlated multiorbital physics, CT-INT and CT-AUX playing central roles in weak-to-intermediate regimes and cluster calculations, and all three implementations becoming the canonical numerical workhorses of modern DMFT.

In this chapter, we focus on the hybridization expansion (CT-HYB) and restrict the discussion to density-density interactions, which can be efficiently treated using the segment picture [92, 98]. In this picture configurations are visualized as occupied time intervals on the imaginary-time axis for each spin flavor.

The computations presented in this chapter were performed within the `TRIQS` framework [C3] using the `TRIQS/cthyb` solver [C4], which implements the segment algorithm with state-of-the-art optimizations.

6.1 Hybridization expansion

The starting point of CT-HYB is a decomposition of the action S into a solvable part S_0 and a remainder ΔS, such that the partition function can be expressed as

$$\mathcal{Z}_{\text{imp}} = \int \mathcal{D}[\hat{d}^\dagger(\tau),\, \hat{d}(\tau)] \mathrm{e}^{-S_0 - \Delta S} = \mathcal{Z}_0 \left\langle \mathrm{e}^{-\Delta S} \right\rangle_{S_0} . \tag{6.1}$$

Overall constants such as $\mathcal{Z}_0$ cancel in normalized estimators and thus do not affect Monte Carlo measurements. Expanding the exponential yields the diagrammatic series

$$\mathcal{Z}_{\mathrm{imp}}/\mathcal{Z}_0 = \sum_{n=0}^{\infty} \frac{(-1)^n}{n!} \langle (\Delta S)^n \rangle_{S_0} \,, \tag{6.2}$$

which is sampled stochastically over contributions of all expansion orders n with configuration weights given by the functional averages in (6.2) [90, 92]. The average expansion order $\langle n \rangle$ of the sampled diagrams is then given by

$$\langle n \rangle = \frac{\mathcal{Z}_0}{\mathcal{Z}_{\mathrm{imp}}} \sum_{n=0}^{\infty} n \cdot \frac{(-1)^n}{n!} \langle (\Delta S)^n \rangle_{S_0} = - \langle \Delta S \rangle_S \,, \tag{6.3}$$

where $\langle \cdot \rangle_S$ denotes the expectation value with respect to the full action. The last equality follows from the identity $\frac{\mathrm{d} \ln \mathcal{Z}}{\mathrm{d}\lambda} = -\langle \Delta S \rangle_{S,\lambda}$ [92] by introducing a coupling parameter λ via $\mathcal{Z}(\lambda) = \mathcal{Z}_0 \langle e^{-\lambda \Delta S} \rangle_{S_0}$.

In the case of the Single Impurity Anderson Model (SIAM) with density-density interactions, as described in Section 4.3, a natural choice is to take the effective action (4.38) and expand the impurity-bath hybridization, i.e. $\Delta_\sigma(\tau)$ (4.36), while keeping the local impurity part in $S_0 = S_{\mathrm{loc}}$:

$$\begin{aligned} \mathcal{Z}_{\mathrm{imp}}/\mathcal{Z}_{\mathrm{bath}} &= \int \mathcal{D}[\hat{d}^\dagger(\tau),\, \hat{d}(\tau)] \exp\left(-S_{\mathrm{loc}} - \int_0^\beta \mathrm{d}\tau \int_0^\beta \mathrm{d}\tau' \sum_\sigma d_\sigma^+(\tau) \Delta_\sigma(\tau - \tau') d_\sigma(\tau') \right) \\ &= \mathcal{Z}_{\mathrm{loc}} \left\langle \exp\left(- \int_0^\beta \mathrm{d}\tau \int_0^\beta \mathrm{d}\tau' \sum_\sigma d_\sigma^+(\tau) \Delta_\sigma(\tau - \tau') d_\sigma(\tau') \right) \right\rangle_{S_{\mathrm{loc}}} . \end{aligned} \tag{6.4}$$

The impurity partition function $\mathcal{Z}_{\mathrm{imp}}[\Delta]$ is a generating functional for n-particle Green's functions: functional derivatives with respect to the hybridization function $\Delta_\sigma(\tau - \tau')$ generate connected correlators up to the usual normalization by $\mathcal{Z}_{\mathrm{imp}}$. In particular, the single-particle Green's function follows as the functional derivative of the logarithm,

$$G_\sigma(\tau' - \tau) = -\frac{\delta \ln \mathcal{Z}_{\mathrm{imp}}}{\delta \Delta_\sigma(\tau - \tau')}, \tag{6.5}$$

which is the CT-HYB analogue of standard source-functional identities [83, 91, 92, 98]. Expanding the exponential in (6.4) yields

$$\begin{aligned} \mathcal{Z}_{\mathrm{imp}} = & \mathcal{Z}_{\mathrm{loc}} \mathcal{Z}_{\mathrm{bath}} \sum_{n=0}^{\infty} \frac{(-1)^n}{n!} \int_0^\beta \mathrm{d}\tau_1 \int_0^\beta \mathrm{d}\tau_1' \cdots \int_0^\beta \mathrm{d}\tau_n \int_0^\beta \mathrm{d}\tau_n' \\ & \times \left\langle \sum_{\{\sigma\}} d_{\sigma_1}^+(\tau_1) d_{\sigma_1}(\tau_1') \ldots d_{\sigma_n}^+(\tau_n) d_{\sigma_n}(\tau_n') \right\rangle_{S_{\mathrm{loc}}} \\ & \times \Delta_{\sigma_1}(\tau_1 - \tau_1') \ldots \Delta_{\sigma_n}(\tau_n - \tau_n'). \end{aligned} \tag{6.6}$$

This is equivalent to writing the partition function as a sum over all possible Monte Carlo configurations

$$\mathfrak{c} = \mathfrak{c}_\uparrow \cup \mathfrak{c}_\downarrow, \qquad \mathfrak{c}_\sigma = \{\tau_1, \ldots, \tau_n; \tau_1', \ldots, \tau_n'\}, \tag{6.7}$$

which represent operator insertions at imaginary times τ_i (creation) and τ_i' (annihilation) on the impurity for each spin channel. As written, (6.6) is not yet convenient for Monte Carlo sampling, because different permutations of the primed imaginary times $\{\tau_1', \ldots, \tau_n'\}$ yield the same local operator string but appear with different hybridization kernels and, crucially, with alternating signs from Grassmann reordering. For example, the second-order contribution contains the two terms [91, 92]

$$\begin{aligned} &\left\langle d^+(\tau_1)d(\tau_2')d^+(\tau_2)d(\tau_1')\right\rangle_{S_{\mathrm{loc}}} \Delta(\tau_1-\tau_2')\Delta(\tau_2-\tau_1') \\ =&-\left\langle d^+(\tau_1)d(\tau_1')d^+(\tau_2)d(\tau_2')\right\rangle_{S_{\mathrm{loc}}} \Delta(\tau_1-\tau_2')\Delta(\tau_2-\tau_1') \end{aligned} \tag{6.8}$$

where the minus sign arises from exchanging Grassmann numbers. While the hybridization function $\Delta(\tau)$ obeys fermionic antiperiodicity $\Delta(\tau) = -\Delta(\tau-\beta)$ and is typically negative for $\tau \in [0, \beta)$ in standard conventions, individual terms still come with alternating algebraic signs due to permutations. Naive sampling of such alternating sums leads to large cancellations and noise [92].

The remedy, already emphasized in the original CT-HYB work [91, 98], is to collect all permutations of primed indices at fixed unprimed indices and use the identity

$$\det(\boldsymbol{A}) = \sum_{\tilde{s}\in\mathcal{S}_n} \mathrm{sign}(\tilde{s}) \prod_{i=1}^{n} a_{i\tilde{s}_i} \tag{6.9}$$

where $\mathcal{S}_n$ is the symmetric group of order n. This exactly mirrors the Grassmann reordering signs. Since there are $|\mathcal{S}_n| = n!$ permutations, the expansion can be reorganized into a single determinant of the $n \times n$ hybridization matrix $\boldsymbol{\Delta}_n$ with entries $(\boldsymbol{\Delta}_n)_{ij} = \Delta(\tau_i - \tau_j')$, yielding the standard CT-HYB form

$$\begin{aligned} \mathcal{Z}_{\mathrm{imp}} =& \mathcal{Z}_{\mathrm{bath}}\mathcal{Z}_{\mathrm{loc}} \sum_{n=0}^{\infty} \frac{(-1)^n}{(n!)^2} \int_0^\beta \mathrm{d}\tau_1 \int_0^\beta \mathrm{d}\tau_1' \cdots \int_0^\beta \mathrm{d}\tau_n \int_0^\beta \mathrm{d}\tau_n' \\ &\times \left\langle \sum_{\{\sigma\}} d^+_{\sigma_1}(\tau_1) d_{\sigma_1}(\tau_1') \ldots d^+_{\sigma_n}(\tau_n) d_{\sigma_n}(\tau_n') \right\rangle_{S_{\mathrm{loc}}} \det \boldsymbol{\Delta}_n. \end{aligned} \tag{6.10}$$

In practice one compensates the combinatorial factor $1/(n!)^2$ by restricting the τ_i and τ_j' sums to ordered sets, so that each configuration is counted once. The Monte Carlo weight then factorizes into a local trace and a hybridization determinant, which are both computed efficiently in modern implementations.

To proceed, we evaluate the expectation values in (6.10). For density-density interactions (single-band Anderson impurity)

$$\hat{H}_{\mathrm{loc}} = \sum_{\sigma} (\varepsilon_\sigma - \mu)\hat{n}_\sigma + U\hat{n}_\uparrow\hat{n}_\downarrow, \tag{6.11}$$

the local operator average factorizes into a purely local trace and a hybridization determinant that is block-diagonal in spin thus, the segment picture applies [92, 98].

6.2 Segment picture

For density-density interactions the local trace in (6.10) is diagonal in the occupation basis and each configuration can be represented by *segments* on the imaginary-time axis.

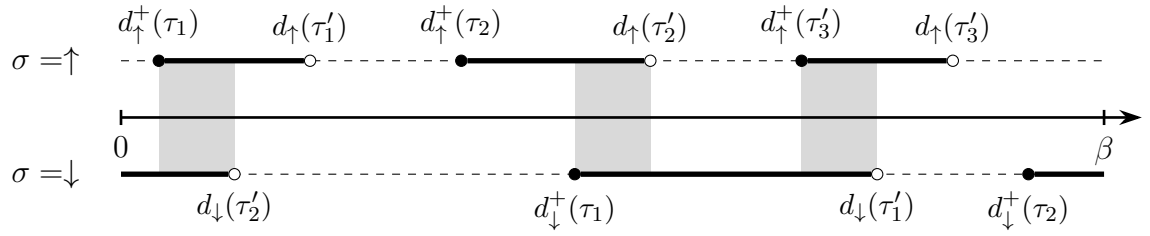

Figure 8: Example of a CT-HYB segment configuration $\mathfrak{c}$ with three spin-up segments $n_\uparrow = 3$ and two spin-down segments $n_\downarrow = 2$ on the imaginary-time interval $[0, \beta)$. Creation (annihilation) operators are indicated by filled (empty) circles. Each segment (line) represents an occupied time interval for the corresponding spin. The shaded areas indicate the overlap intervals where both spins are present.

A contribution of order n consists of $n_\uparrow \leq n$ pairs of creation/annihilation operators for spin $\sigma =\uparrow$ and $n_\downarrow = n - n_\uparrow$ pairs for spin $\sigma =\downarrow$. We collect the imaginary times at which the operators act as ordered sets

$$\{\tau_i\}^{n_\sigma}, \qquad \{\tau'_i\}^{n_\sigma}, \tag{6.12}$$

where $\hat{d}^\dagger_\sigma(\tau_i)$ is the i-th creation and $\hat{d}_\sigma(\tau'_i)$ the i-th annihilation. Time ordering on the imaginary-time interval enforces an alternation of creation and annihilation for fixed σ, up to the cyclic boundary at β:

$$\tau_1 < \tau'_1 < \tau_2 < \tau'_2 < \cdots < \tau_n < \tau'_n \pmod{\beta}, \tag{6.13}$$

with the understanding that the last annihilation $\tau'_{k_\sigma\sigma}$ may wrap around and precede $\tau_{1\sigma}$ in $[0, \beta)$, reflecting the cyclic trace. The *segment picture* is a geometric way to visualize such a configuration: we draw the impurity time axis on the interval $\tau \in [0, \beta)$. For each spin σ, every creation $\hat{d}^\dagger_\sigma(\tau)$ begins a time interval of occupancy that ends at the next annihilation $\hat{d}_\sigma(\tau')$ with $\tau < \tau'$ understood modulo β. An example of a segment configuration is shown in Fig. 8.

We represent each occupied interval by a line segment $[\tau_{i\sigma}, \tau'_{i\sigma})$. If the impurity is already occupied at $\tau = 0$, the corresponding segment *wraps* across the boundary: it begins at some $\tau_{i\sigma} < \beta$, continues through β, and closes at $\tau'_{j\sigma} \in [0, \tau_{i\sigma})$, producing an *open* line that connects across the endpoints of the interval.

For bookkeeping it is convenient to define, for each configuration c, the piecewise-constant occupation $n_\sigma(\tau) \in \{0, 1\}$ that equals 1 precisely on the union of all σ-segments, the total occupied length

$$L_\sigma(\mathfrak{c}) \equiv \sum_{i=1}^{n_\sigma} l_{i\sigma}, \qquad l_{i\sigma} = (\tau' - \tau)_\beta = \begin{cases} \tau' - \tau + \beta, & \text{if the segment crosses } \beta\,, \\ \tau' - \tau, & \text{else} \end{cases} \tag{6.14}$$

where $l_{i\sigma}$ is the length of segment i of the σ-channel, and the total overlap length where both spins are present,

$$O_{\uparrow\downarrow}(\mathfrak{c}) \equiv \int_0^\beta \mathrm{d}\tau\, n_\uparrow(\tau)\, n_\downarrow(\tau)\,. \tag{6.15}$$

For convenience we switch to the Hamiltonian formalism to evaluate the local action contribution S_{loc}. The local expectation values in (6.10) can then be expressed as

traces in the impurity (Fock) space. For a single-band impurity the local basis is $\{|0\rangle, |\uparrow\rangle, |\downarrow\rangle, |\uparrow\downarrow\rangle\}$, and for density-density interactions the Hamiltonian is diagonal. The local weight entering (6.10) for a single configuration $\mathfrak{c}$ then reads

$$W_{\mathrm{loc}}^{(n)}(\mathfrak{c}) = \mathrm{Tr}_{\mathrm{loc}}\left[e^{-\beta H_{\mathrm{loc}}}\mathcal{T}_\tau \prod_\sigma \hat{d}_\sigma^\dagger(\tau_1)\hat{d}_\sigma(\tau_1')\cdots\hat{d}_\sigma^\dagger(\tau_k)\hat{d}_\sigma(\tau_k')\right], \tag{6.16}$$

with $\mathcal{T}_\tau$ the time-ordering operator to arrange operators along the imaginary-time contour. Because H_{loc} is diagonal in the occupation basis and creation/annihilation operators only flip occupations by ± 1 within a spin sector, the time-ordered product fixes a *single* sequence of local basis states along the imaginary-time contour once the first segment is chosen (for $n_\uparrow > 0$ and $n_\downarrow > 0$). In particular, segments contribute only if the numbers of creation and annihilation operators match for each spin; hence it suffices to consider operator strings where the multiset $\{\sigma_i'\}$ is a permutation of $\{\sigma_i\}$ [91, 92, 98].

Moving the diagonal H_{loc} through the time-ordered operator string yields a purely geometric local factor that depends only on the total lengths of segments $L_\sigma(\mathfrak{c})$ and overlaps $O_{\uparrow\downarrow}(\mathfrak{c})$ of the configuration $\mathfrak{c}$. Then,

$$W_{\mathrm{loc}}^{(n)}(\mathfrak{c}) = s(\mathfrak{c}) \exp\Big(-\varepsilon_\uparrow L_\uparrow - \varepsilon_\downarrow L_\downarrow - U O_{\uparrow\downarrow}\Big). \tag{6.17}$$

The sign s originates from time ordering in the Hamiltonian formalism. For density-density interactions in the segment algorithm, one can choose the operator convention so that $s(\mathfrak{c}) = +1$ and all fermionic signs are captured by the hybridization determinants [92, 98]. Consequently, the total configuration weight factorizes as

$$w(\mathfrak{c}) = W_{\mathrm{loc}}^{(n)}(\mathfrak{c}) \prod_\sigma \det \mathbf{\Delta}_{\mathfrak{c}}^{(\sigma)}, \qquad \left[\mathbf{\Delta}_{\mathfrak{c}}^{(\sigma)}\right]_{ij} = \Delta_\sigma\Big(\tau_i - \tau_j'\Big), \tag{6.18}$$

which is the working expression used for Monte Carlo sampling in the segment picture. The special cases $k_\uparrow = 0$ or $k_\downarrow = 0$ are covered by (6.17) with the corresponding $L_\sigma = 0$. If only one spin sector appears, the trace still reduces to a single path through $\{|0\rangle, |\sigma\rangle\}$ and the same exponential form applies. Practically, (6.17) implies immediate estimators for local observables, $\langle \hat{n}_\sigma \rangle = \langle L_\sigma \rangle / \beta$ and $\langle \hat{n}_\uparrow \hat{n}_\downarrow \rangle = \langle O_{\uparrow\downarrow} \rangle / \beta$, while (6.18) provides the Metropolis ratios via fast rank-1 updates of $\mathbf{\Delta}^{-1}$ under segment insertion/removal and endpoint shifts. These are the standard building blocks of the CT-HYB segment algorithm [91, 92, 98].

6.3 Monte Carlo sampling

We sample the configuration sum with a Markov-chain Monte Carlo process that proposes local updates of the segment configuration c and accepts them with Metropolis probabilities. To guarantee that ensemble averages reproduce the path-integral expectation values, the set of updates must be *ergodic*: starting from any admissible configuration, repeated application of the moves can reach any other admissible configuration in a finite number of steps. In the single-band, density-density (segment) algorithm it is sufficient to insert and remove *pairs* of creation/annihilation operators,

or equivalently, segments (occupied intervals) and anti-segments (empty intervals), independently in the spin-up and spin-down sectors [92, 98]. Another requirement for Monte Carlo sampling is that the chain converges to a *stationary* probability distribution $p(\mathfrak{c}_n)$. A simple sufficient condition is *detailed balance*:

$$p(\mathfrak{c}_n)T_{\mathfrak{c}_n\to\mathfrak{c}'_m} = p(\mathfrak{c}'_m)\,T_{\mathfrak{c}'_m\to\mathfrak{c}_n}, \tag{6.19}$$

where $T_{c\to c'}$ is the one-step transition probability between configurations $\mathfrak{c}$ and $\mathfrak{c}'$. If (6.19) holds, then summing over all predecessors yields stationarity,

$$\sum_{\mathfrak{c}'_m} p(\mathfrak{c}'_m)T_{\mathfrak{c}'_m\to\mathfrak{c}_n} = p(\mathfrak{c}_n)\sum_{\mathfrak{c}'_m} T_{\mathfrak{c}_n\to\mathfrak{c}'_m} = p(\mathfrak{c}_n), \tag{6.20}$$

using normalization $\sum_{\mathfrak{c}'} T_{\mathfrak{c}\to\mathfrak{c}'} = 1$. We implement T in two stages: propose $\mathfrak{c}\to\mathfrak{c}'$ with probability $P_{\mathfrak{c}\to\mathfrak{c}'}$ and accept it with probability $A_{\mathfrak{c}\to\mathfrak{c}'}$,

$$T_{\mathfrak{c}\to\mathfrak{c}'} = P_{\mathfrak{c}\to\mathfrak{c}'}\,A_{\mathfrak{c}\to\mathfrak{c}'}\,. \tag{6.21}$$

The Metropolis-Hastings choice enforces (6.19) by

$$A_{\mathfrak{c}\to\mathfrak{c}'} = \min\left\{1,\,\frac{p(\mathfrak{c}')P_{\mathfrak{c}'\to\mathfrak{c}}}{p(\mathfrak{c})P_{\mathfrak{c}\to\mathfrak{c}'}}\right\}. \tag{6.22}$$

With this, any proposal kernel P (together with ergodic moves) produces a stationary chain sampling $p(\mathfrak{c})$ [100, 101].

6.3.1 Configuration updates

An (anti-)segment insertion proposes to add a new occupied (empty) time interval, i.e. a pair of creation and annihilation operators-for spin σ to the current configuration, thereby increasing the expansion order $n_\sigma \to n_\sigma+1$. For the segment insertion, we first draw a time $\tau \in [0,\,\beta)$ with the uniform probability density $\mathrm{d}\tau/\beta$ for spin σ, where $\mathrm{d}\tau$ is an infinitesimal time interval. If the imaginary time τ falls within an empty σ-segment, the impurity is unoccupied and we propose to add a new creation operator $\hat{d}^\dagger_\sigma(\tau)$, inserting a new electron (segment). Next, we define $l_{\max}$ as the distance, along increasing imaginary time with wrap-around at β, from τ to the next start of a σ-segment. If no σ-segments are present, we set $l_{\max} = \beta$. We then choose the time τ' uniformly within the available window,

$$\tau' \in (\tau,\,\tau + l_{\max}) \pmod{\beta}, \qquad \text{with probability } \frac{\mathrm{d}\tau}{l_{\max}}, \tag{6.23}$$

so that the proposed segment has length $l_{\mathrm{new}} \equiv (\tau'-\tau)_\beta \in (0,\,l_{\max})$ (see Fig. 9). For the anti-segment insertion, the method is similar: We pick a time $\tau' \in [0,\,\beta)$, check if τ' falls within an occupied σ-segment, define $l_{\max}$ as the distance to the next end of the σ-segment, and choose τ uniformly in the interval $(\tau'-l_{\max},\,\tau')$ (mod β).

The total proposal probability for an (anti-)segment insertion is therefore

$$P_{\mathfrak{c}_n\to\mathfrak{c}_{n+1}} = \frac{\mathrm{d}\tau}{\beta}\cdot\frac{\mathrm{d}\tau}{l_{\max}}. \tag{6.24}$$

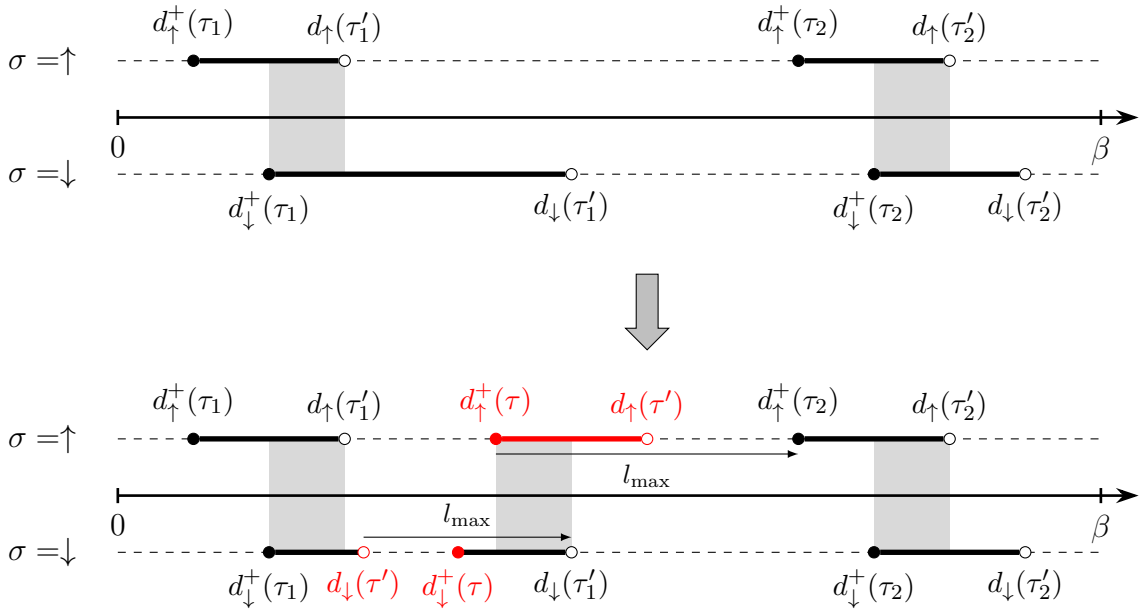

Figure 9: Example of a segment insertion move in the spin-up channel and an anti-segment insertion move in the spin-down channel. Note that these are two separate updates that change the configuration independently. The lengths $l_{\max}$ indicate the maximal allowed lengths for the new (anti-)segments. In both examples, the expansion order is increased by one, $n_\sigma \to n_\sigma + 1$.

A special case of inserting an anti-segment is the removal of a complete segment, i.e. removing a pair of creation/annihilation operators that form a full occupied interval (segment), reducing the expansion order $n_\sigma \to n_\sigma - 1$ for spin σ by one. In this case, the proposal probability is simply

$$P_{\mathfrak{c}_n \to \mathfrak{c}_{n-1}} = \frac{1}{n_\sigma}, \tag{6.25}$$

since we choose one of the n_σ existing segments uniformly for removal [102].

The probability for a configuration $\mathfrak{c}_n$ can be identified from the partition function (6.10) and the local weight (6.16):

$$\begin{aligned} \mathcal{Z}_{\text{imp}} &= \mathcal{Z}_{\text{bath}} \mathcal{Z}_{\text{loc}} \sum_{n=0}^{\infty} \sum_{\{\sigma\}} \int_0^\beta \mathrm{d}\tau_1 \int_0^\beta \mathrm{d}\tau_1' \cdots \int_0^\beta \mathrm{d}\tau_n \int_0^\beta \mathrm{d}\tau_n' \frac{1}{(n!)^2} W_{\text{loc}}^{(n)}(\mathfrak{c}) \det \mathbf{\Delta}_n \\ &= \mathcal{Z}_{\text{bath}} \mathcal{Z}_{\text{loc}} \sum_{n=0}^{\infty} \int \mathrm{d}\mathfrak{c}_n \frac{1}{(n!)^2} W_{\text{loc}}^{(n)}(\mathfrak{c}) \det \mathbf{\Delta}_n, \end{aligned} \tag{6.26}$$

where we have introduced the shorthand notation $\int \mathrm{d}\mathfrak{c}_n$ for the multiple integrals over imaginary times and the sum over spin configurations at fixed order n_σ. Thus, the probability density for a configuration $\mathfrak{c}_n$ is

$$p(\mathfrak{c}_n) \sim \frac{1}{(n!)^2} W_{\text{loc}}^{(n)}(\mathfrak{c}) \det \mathbf{\Delta}_n. \tag{6.27}$$

Using this in the Metropolis-Hastings acceptance ratio (6.22) together with the proposal probabilities for (anti-)segment insertion (6.24) and removal (6.25) yields the

acceptance ratio

$$A_{\mathfrak{c}_n \to \mathfrak{c}_{n+1}} = \min\left(1,\ \frac{p(\mathfrak{c}_{n+1})}{p(\mathfrak{c}_n)} \frac{P_{\mathfrak{c}_{n+1}\to\mathfrak{c}_n}}{P_{\mathfrak{c}_n\to\mathfrak{c}_{n+1}}}\right) = \min\left(1,\ \frac{\beta l_{\max}}{(\mathrm{d}\tau)^2(n_\sigma+1)^3} \frac{W_{\mathrm{loc}}^{(n+1)}}{W_{\mathrm{loc}}^{(n)}} \frac{\det \boldsymbol{\Delta}_{n+1}}{\det \boldsymbol{\Delta}_n}\right) \tag{6.28}$$

for an insertion move and the acceptance ratio

$$A_{c_{n+1} \to c_n} = \min\left(1,\ \frac{p(\mathfrak{c}_n)}{p(\mathfrak{c}_{n+1})} \frac{P_{\mathfrak{c}_n\to\mathfrak{c}_{n+1}}}{P_{\mathfrak{c}_{n+1}\to\mathfrak{c}_n}}\right) = \min\left(1,\ \frac{(\mathrm{d}\tau)^2(n_\sigma+1)^3}{\beta l_{\max}} \frac{W_{\mathrm{loc}}^{(n)}}{W_{\mathrm{loc}}^{(n+1)}} \frac{\det \boldsymbol{\Delta}_n}{\det \boldsymbol{\Delta}_{n+1}}\right) \tag{6.29}$$

for a removal move.

Beyond single (anti-)segment insertions/removals, modern CTHYB implementations employ several higher-order or cross-spin moves that improve ergodicity and reduce autocorrelation, especially in multi-orbital problems with off-diagonal hybridization.

A move update transfers a segment (or antisegment) from one spin/orbital to another, increasing the expansion order of one channel and decreasing it of the other channel while keeping the total expansion order fixed. This is done by choosing an existing segment in one channel and proposing to insert it into a different channel, provided that the hybridization between the two channels is non-zero. Other common complex updates include all variations of double (anti-)segment insertions and removals. These moves change the expansion order in two channels simultaneously, improving sampling efficiency in the presence of inter-orbital hybridizations. Such coupled moves preserve detailed balance with Metropolis-Hastings acceptance based on the corresponding local-trace and hybridization-determinant ratios, and are standard in state-of-the-art solvers to ensure efficient sampling in the presence of inter-orbital couplings and complex $\boldsymbol{\Delta}(\tau)$. If inter-orbital interactions beyond density-density terms are present, additional updates such as spin-insertions, spin-swaps and spin segment splits are required to ensure ergodicity [91, 103].

6.3.2 Determinant ratios and fast matrix updates

The acceptance ratios (6.28) and (6.29) require the evaluation of determinant ratios $\det \boldsymbol{\Delta}_{n+1}/\det \boldsymbol{\Delta}_n$ and $\det \boldsymbol{\Delta}_n/\det \boldsymbol{\Delta}_{n+1}$ upon (anti-)segment insertion and removal. A naive computation of determinants scales as $\mathcal{O}(n^3)$ (LU decomposition), which would make the algorithm prohibitively expensive at large expansion orders n. However, inserting or removing an (anti-)segment corresponds to rank-1 updates of the hybridization matrix $\boldsymbol{\Delta}_n$, adding or removing a single row and column for the new creation/annihilation operator pair. It is therefore possible to evaluate the determinant ratios in $\mathcal{O}(n^2)$ for insertions and $\mathcal{O}(1)$ for removals [102].

Let us first consider an (anti-)segment insertion that adds a new pair of operators at times (τ, τ') to a configuration $\mathfrak{c}_n$, yielding $\mathfrak{c}_{n+1}$. The new hybridization matrix $\boldsymbol{\Delta}_{n+1}$ can be written in block form as

$$\boldsymbol{\Delta}_{n+1} = \begin{pmatrix} \boldsymbol{\Delta}_n & \boldsymbol{u} \\ \boldsymbol{v}^\top & \alpha \end{pmatrix}, \tag{6.30}$$

adding a new row and column to $\boldsymbol{\Delta}_n$. Here, $\boldsymbol{u} \equiv \boldsymbol{\Delta}_{n+1}^{[:,n+1]}$ is a $n+1 \times 1$ column vector, $\boldsymbol{v}^\top \equiv \boldsymbol{\Delta}_{n+1}^{[n+1,:]}$ is a $1 \times n+1$ row vector, and $\alpha \equiv \Delta_{n+1}^{[n+1,n+1]}$ is a scalar[1].

Using the determinant formula for partitioned matrices,

$$\det \begin{pmatrix} \boldsymbol{A} & \boldsymbol{B} \\ \boldsymbol{C} & \boldsymbol{D} \end{pmatrix} = \det \boldsymbol{A} \cdot \det\bigl(\boldsymbol{D} - \boldsymbol{C}\boldsymbol{A}^{-1}\boldsymbol{B}\bigr), \tag{6.31}$$

the ratio of determinants upon insertion becomes

$$\frac{\det \boldsymbol{\Delta}_{n+1}}{\det \boldsymbol{\Delta}_n} = \frac{\det \boldsymbol{\Delta}_n \cdot \det\bigl(\alpha - \boldsymbol{v}^\top \boldsymbol{\Delta}_n^{-1} \boldsymbol{u}\bigr)}{\det \boldsymbol{\Delta}_n} = \alpha - \boldsymbol{v}^\top \boldsymbol{\Delta}_n^{-1} \boldsymbol{u} = \alpha - \boldsymbol{v}^\top \boldsymbol{M}_n \boldsymbol{u}, \tag{6.32}$$

where we have introduced the inverse hybridization matrix $\boldsymbol{M}_n \equiv \boldsymbol{\Delta}_n^{-1}$. To compute the inverse matrix $\boldsymbol{M}_n$, we can express $\boldsymbol{\Delta}_n$ as a rank-two update of a block-diagonal, easily invertible matrix:

$$\boldsymbol{A} \equiv \begin{pmatrix} \boldsymbol{\Delta}_{n-1} & \boldsymbol{0} \\ \boldsymbol{0}^\top & 1 \end{pmatrix}, \qquad \boldsymbol{U} \equiv \begin{pmatrix} \boldsymbol{u} & \boldsymbol{0} \\ \alpha - 1 & 1 \end{pmatrix}, \qquad \boldsymbol{V} \equiv \begin{pmatrix} \boldsymbol{0}^\top & 1 \\ \boldsymbol{v}^\top & 0 \end{pmatrix}, \tag{6.33}$$

so that

$$\boldsymbol{\Delta}_n = \boldsymbol{A} + \boldsymbol{U}\boldsymbol{V}. \tag{6.34}$$

The "1" in the lower-right corner of $\boldsymbol{A}$ is inserted precisely so that $\boldsymbol{A}$ is invertible; it is subtracted back by $\boldsymbol{U}\boldsymbol{V}$ so that $\boldsymbol{A} + \boldsymbol{U}\boldsymbol{V}$ matches the original 1×1 block α. This precisely matches the setup of the Sherman-Morrison-Woodbury formula [104, p. 65],

$$(\boldsymbol{A} + \boldsymbol{U}\boldsymbol{V})^{-1} = \boldsymbol{A}^{-1} - \boldsymbol{A}^{-1}\boldsymbol{U}(\mathbb{1}_k + \boldsymbol{V}\boldsymbol{A}^{-1}\boldsymbol{U})^{-1}\boldsymbol{V}\boldsymbol{A}^{-1}. \tag{6.35}$$

Since $\boldsymbol{A}^{-1} = \operatorname{diag}(\boldsymbol{M}_{n-1}, 1)$ is trivial to compute, the only nontrivial piece is the 2×2 block matrix

$$\boldsymbol{S} \equiv \mathbb{1}_2 + \boldsymbol{V}\boldsymbol{A}^{-1}\boldsymbol{U} = \begin{pmatrix} \alpha & 1 \\ \boldsymbol{v}^\top \boldsymbol{M}_{n-1} \boldsymbol{u} & 1 \end{pmatrix}. \tag{6.36}$$

Its determinant is the Schur complement

$$s \equiv \det \boldsymbol{S} = \alpha - \boldsymbol{v}^\top \boldsymbol{M}_{n-1} \boldsymbol{u}, \tag{6.37}$$

and its inverse is

$$\boldsymbol{S}^{-1} = \frac{1}{s} \begin{pmatrix} 1 & -1 \\ -\boldsymbol{v}^\top \boldsymbol{M}_{n-1} \boldsymbol{u} & \alpha \end{pmatrix}. \tag{6.38}$$

Multiplying out the matrix product in (6.35) leads to

$$\begin{aligned} \boldsymbol{A}^{-1}\boldsymbol{U} \cdot \boldsymbol{S}^{-1} \cdot \boldsymbol{V}\boldsymbol{A}^{-1} &= \frac{1}{s} \begin{pmatrix} \boldsymbol{M}_{n-1}\boldsymbol{u} & \boldsymbol{0} \\ \alpha - 1 & 1 \end{pmatrix} \begin{pmatrix} 1 & -1 \\ -\boldsymbol{v}^\top \boldsymbol{M}_{n-1} \boldsymbol{u} & \alpha \end{pmatrix} \begin{pmatrix} \boldsymbol{0} & 1 \\ \boldsymbol{v}^\top \boldsymbol{M}_{n-1} & 0 \end{pmatrix} \\ &= \frac{1}{s} \begin{pmatrix} -\boldsymbol{M}_{n-1}\boldsymbol{u}\boldsymbol{v}^\top \boldsymbol{M}_{n-1} & \boldsymbol{M}_{n-1}\boldsymbol{u} \\ \boldsymbol{v}^\top \boldsymbol{M}_{n-1} & \alpha - 1 - \boldsymbol{v}^\top \boldsymbol{M}_{n-1} \boldsymbol{u} \end{pmatrix}. \end{aligned} \tag{6.39}$$

[1]The notation $\boldsymbol{A}_{[i,:]}$ and $\boldsymbol{A}_{[:,j]}$ denotes the i-th row and j-th column of the matrix $\boldsymbol{A}$. The : symbol indicates all indices in that dimension. Similarly, $\boldsymbol{A}_{[i:j,\,k:l]}$ denotes the submatrix of $\boldsymbol{A}$ with rows i to $j-1$ and columns k to $l-1$ [104, pp. 19–20].

Finally, we can express the updated inverse matrix $\boldsymbol{M}_n \equiv \boldsymbol{\Delta}_n^{-1}$ as

$$\boldsymbol{M}_n = \begin{pmatrix} \boldsymbol{M}_{n-1} & \boldsymbol{0} \\ \boldsymbol{0}^\top & 1 \end{pmatrix} - \frac{1}{s} \begin{pmatrix} -\boldsymbol{M}_{n-1}\boldsymbol{u}\boldsymbol{v}^\top\boldsymbol{M}_{n-1} & \boldsymbol{M}_{n-1}\boldsymbol{u} \\ \boldsymbol{v}^\top\boldsymbol{M}_{n-1} & \alpha - 1 - \boldsymbol{v}^\top\boldsymbol{M}_{n-1}\boldsymbol{u} \end{pmatrix}. \tag{6.40}$$

Using the definition of s, the lower-right entry simplifies to $1/s$, yielding the standard rank-one outer-product update formula:

$$\boldsymbol{M}_n = \begin{pmatrix} \boldsymbol{M}_{n-1} & \boldsymbol{0} \\ \boldsymbol{0}^\top & 0 \end{pmatrix} - \frac{1}{s} \begin{pmatrix} -\boldsymbol{M}_{n-1}\boldsymbol{u}\boldsymbol{v}^\top\boldsymbol{M}_{n-1} & \boldsymbol{M}_{n-1}\boldsymbol{u} \\ \boldsymbol{v}^\top\boldsymbol{M}_{n-1} & -1 \end{pmatrix}. \tag{6.41}$$

For the removal of a full segment, we can use a similar approach to derive the determinant ratio and the updated inverse matrix. We assume the segment to be removed corresponds to the last row/column of the current hybridization matrix[2]. We can then write the current hybridization matrix $\boldsymbol{\Delta}_n$ in block form as in (6.30), with $\boldsymbol{\Delta}_{n-1}$ the hybridization matrix after removal,

$$\boldsymbol{\Delta}_n = \begin{pmatrix} \boldsymbol{\Delta}_{n-1} & \boldsymbol{u} \\ \boldsymbol{v}^\top & \alpha \end{pmatrix}, \tag{6.42}$$

and denote its inverse by

$$\boldsymbol{M}_n \equiv \boldsymbol{\Delta}_n^{-1} = \begin{pmatrix} \boldsymbol{E} & \boldsymbol{f} \\ \boldsymbol{g}^\top & \gamma \end{pmatrix}, \tag{6.43}$$

where

$$\boldsymbol{E} = \boldsymbol{M}_{n-1} + \frac{1}{s}\boldsymbol{M}_{n-1}\boldsymbol{u}\boldsymbol{v}^\top\boldsymbol{M}_{n-1}, \quad \boldsymbol{f} = -\frac{1}{s}\boldsymbol{M}_{n-1}\boldsymbol{u}, \quad \boldsymbol{g}^\top = -\frac{1}{s}\boldsymbol{v}^\top\boldsymbol{M}_{n-1}, \quad \gamma = \frac{1}{s}, \tag{6.44}$$

For a removal we need the new inverse $\boldsymbol{M}_{n-1} = \boldsymbol{\Delta}^{-1}$ given the known blocks $\boldsymbol{E}, \boldsymbol{f}, \boldsymbol{g}, \gamma$ of $\boldsymbol{M}_n$. Eliminating $\boldsymbol{u}, \boldsymbol{v}, \alpha$ and s, we obtain directly

$$\boldsymbol{M}_{n-1} = \boldsymbol{E} - \boldsymbol{f}\gamma^{-1}\boldsymbol{g}^\top = \boldsymbol{M}_n^{[1:n-1,\,1:n-1]} - \frac{\boldsymbol{M}_n^{[1:n-1,\,n]}\,\boldsymbol{M}_n^{[n,\,1:n-1]}}{\boldsymbol{M}_n^{[n,\,n]}}. \tag{6.45}$$

This is a rank-one downdate: the $(n-1)\times(n-1)$ top-left block of $\boldsymbol{M}_n$ is taken and an outer product divided by the scalar $\boldsymbol{M}_n^{[n,\,n]}$ is subtracted. Applying the determinant formula for partitioned matrices (6.31) to the ratio of determinants upon removal yields

$$\frac{\det \boldsymbol{\Delta}_{n-1}}{\det \boldsymbol{\Delta}_n} = \frac{1}{s} = \gamma = \boldsymbol{M}_n^{[n,\,n]}. \tag{6.46}$$

The determinant ratio for a removal is therefore given directly by the lower-right entry of the current inverse hybridization matrix $\boldsymbol{M}_n$.

With these formulas, the acceptance ratios (6.28) and (6.29) can be evaluated in $\mathcal{O}(n^2)$ time for insertions and $\mathcal{O}(1)$ time for removals, making the segment CT-HYB algorithm efficient even at large expansion orders.

[2]If it is the r-th one, first permute indices so that row/column r is moved to position n; apply the formulas below; then unpermute. Permutations are orthogonal and do not change determinants.

6.3.3 Green's function sampling

The Green's function $G_\sigma(\tau - \tau')$ can be sampled directly in imaginary time during the Monte Carlo process. We recall the definition of the imaginary-time Green's function,

$$G_\sigma(\tau - \tau') = -\left\langle \mathcal{T}_\tau \hat{d}_\sigma(\tau)\hat{d}^\dagger_\sigma(\tau')\right\rangle = -\left\langle d_\sigma(\tau)d^+_\sigma(\tau')\right\rangle_{S_{\text{imp}}}, \tag{6.47}$$

and the CT-HYB generating-functional identity

$$G_\sigma(\tau - \tau') = -\frac{\delta \ln \mathcal{Z}_{\text{imp}}}{\delta \Delta_\sigma(\tau' - \tau)}, \tag{6.48}$$

which follows from differentiating the action with respect to the hybridization kernel. Applying the logarithmic derivative, the Green's function can be expressed as

$$G_\sigma(\tau - \tau') = -\frac{\delta \ln \mathcal{Z}_{\text{imp}}}{\delta \Delta_\sigma(\tau' - \tau)} = -\frac{1}{\mathcal{Z}_{\text{imp}}}\frac{\delta \mathcal{Z}_{\text{imp}}}{\delta \Delta_\sigma(\tau' - \tau)}. \tag{6.49}$$

Inserting the configuration expansion of the partition function (Eq. (6.26)),

$$\mathcal{Z}_{\text{imp}} = \mathcal{Z}_{\text{bath}}\mathcal{Z}_{\text{loc}} \sum_{n=0}^{\infty} \int \mathrm{d}\mathfrak{c}_n \, \frac{1}{(n!)^2} W^{(n)}_{\text{loc}}(\mathfrak{c}) \det \mathbf{\Delta}_n, \tag{6.50}$$

we obtain

$$G_\sigma(\tau - \tau') = -\frac{\mathcal{Z}_{\text{bath}}\mathcal{Z}_{\text{loc}}}{\mathcal{Z}_{\text{imp}}} \sum_{n=0}^{\infty} \int \mathrm{d}\mathfrak{c}_n \, \frac{1}{(n!)^2} \, W^{(n)}_{\text{loc}}(\mathfrak{c}) \, \frac{\delta \det \Delta_n}{\delta \Delta_\sigma(\tau' - \tau)} \, . \tag{6.51}$$

Differentiating $\ln \mathcal{Z}_{\text{imp}}$ with respect to the hybridization kernel replaces one hybridization line by the inverse hybridization matrix on each configuration, i.e removing one row and one column from the hybridization matrix $\mathbf{\Delta}_n$ [91, 92, 102]. This can also be seen via the Green's function definition and equation (6.6):

$$\begin{aligned} G_\sigma(\tau - \tau') &= -\left\langle d_\sigma(\tau)d^+_\sigma(\tau')\right\rangle_{S_{\text{imp}}} = -\frac{\mathcal{Z}_{\text{bath}}\mathcal{Z}_{\text{loc}}}{\mathcal{Z}_{\text{imp}}} \sum_n \frac{(-1)^n}{n!} \left\langle d_\sigma(\tau)d^+_\sigma(\tau')(\Delta S)^n\right\rangle_{S_{\text{loc}}} \\ &= -\frac{\mathcal{Z}_{\text{bath}}\mathcal{Z}_{\text{loc}}}{\mathcal{Z}_{\text{imp}}} \sum_{n=0}^{\infty} \frac{(-1)^n}{n!} \int_0^\beta \mathrm{d}\tau_1 \int_0^\beta \mathrm{d}\tau_1' \cdots \int_0^\beta \mathrm{d}\tau_n \int_0^\beta \mathrm{d}\tau_n' \\ &\quad \times \left\langle d_\sigma(\tau)d^+_\sigma(\tau') \sum_{\{\sigma\}} d^+_{\sigma_1}(\tau_1)d_{\sigma_1}(\tau_1') \ldots d^+_{\sigma_n}(\tau_n)d_{\sigma_n}(\tau_n') \right\rangle_{S_{\text{loc}}} \\ &\quad \times \Delta_{\sigma_1}(\tau_1 - \tau_1') \ldots \Delta_{\sigma_n}(\tau_n - \tau_n'). \end{aligned} \tag{6.52}$$

The expectation value over the local action contains a free pair of Grassmann numbers $d_\sigma(\tau)d^+_\sigma(\tau')$. All other pairs of Grassmann numbers $d^+_{\sigma_i}(\tau_i)d_{\sigma_i}(\tau_i')$ are connected by hybridization lines $\Delta_{\sigma_i}(\tau_i - \tau_i')$. This lets us use the determinant ratio of a segment removal, i.e. removing a row and column from the hybridization matrix:

$$G_\sigma(\tau - \tau') = -\frac{\mathcal{Z}_{\text{bath}}\mathcal{Z}_{\text{loc}}}{\mathcal{Z}_{\text{imp}}} \sum_{n=0}^{\infty} \int \mathrm{d}\mathfrak{c}_n \, \frac{1}{(n!)^2} W^{(n)}_{\text{loc}}(\mathfrak{c}) \det \mathbf{\Delta}_n \frac{\det \mathbf{\Delta}_{n-1}}{\det \mathbf{\Delta}_n}. \tag{6.53}$$

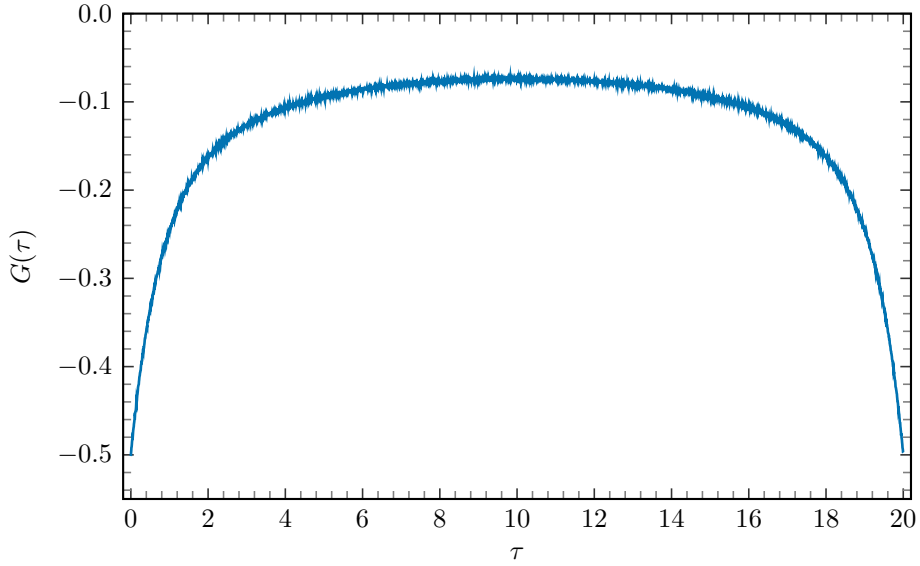

Figure 10: Imaginary-time Green's function $G(\tau)$ sampled with CT-HYB for the single-orbital Anderson impurity model with Hubbard interaction $U = 2$ and $\beta = 20$ at half-filling ($\mu = U/2$) for a semi-circular bath (Bethe lattice) with half bandwidth $D = 1$. The data was obtained with $N_{\text{sample}} = 10^6$ Monte Carlo measurements and cycle length $N_{\text{step}} = 200$ after $N_{\text{warmup}} = 10^5$ thermalization steps.

As shown in the previous section, the ratio of determinants for a segment removal is simply given by the corresponding entry of the inverse hybridization matrix (Eq. (6.46)):

$$G_\sigma(\tau - \tau') = -\frac{\mathcal{Z}_{\text{bath}}\mathcal{Z}_{\text{loc}}}{\mathcal{Z}_{\text{imp}}} \sum_{n=0}^{\infty} \int \mathrm{d}\mathfrak{c}_n \, \frac{1}{(n!)^2} W_{\text{loc}}^{(n)}(\mathfrak{c}) \det \boldsymbol{\Delta}_n \boldsymbol{M}_n^{[n,n]}. \tag{6.54}$$

The remaining factors in the integral of (6.54) are precisely the configuration weights sampled in the Monte Carlo process in the calculation of the partition function (6.26):

$$G_\sigma(\tau - \tau') = -\frac{\mathcal{Z}_{\text{bath}}\mathcal{Z}_{\text{loc}}}{\mathcal{Z}_{\text{imp}}} \sum_{n=0}^{\infty} \int \mathrm{d}\mathfrak{c}_n \, W_{\text{MC}}^{(n)} \boldsymbol{M}_n^{[n,n]} =: \mathbb{E}(\boldsymbol{M}_n^{[n,n]}), \tag{6.55}$$

where $\mathbb{E}$ denotes the Monte Carlo expectation value.

An example of the imaginary-time Green's function $G_\sigma(\tau)$ of the single-orbital Anderson impurity model with a semi-circular bath (Bethe lattice) sampled with CT-HYB is shown in Fig. 10. Equation (6.55) can also be written in terms of the Monte Carlo average $\langle\cdot\rangle_{\text{MC}}$ with weights $W_{\text{MC}}^{(n)}$:

$$\langle\cdot\rangle_{\text{MC}} = \sum_{n=0}^{\infty} \int \mathrm{d}\mathfrak{c}_n \, W_{\text{MC}}^{(n)}(\cdot), \tag{6.56}$$

For any test function $\varphi(\tau)$, we have

$$\int_0^\beta \mathrm{d}\tau \, \varphi(\tau) \, G_\sigma(\tau) = -\left\langle \sum_{i,j=1}^{n_\sigma(\mathfrak{c})} \boldsymbol{M}_{n\sigma}^{[i,j]} \varphi\Big((\tau'_{i\sigma} - \tau_{j\sigma})_\beta\Big) \right\rangle_{\text{MC}}, \tag{6.57}$$

where $(\cdot)_\beta$ denotes wrapping into $[0, \beta)$. Since (6.57) holds for all smooth φ, the corresponding kernel is

$$G_\sigma^{(\mathfrak{c})}(\tau) = -\sum_{i,j=1}^{n_\sigma(\mathfrak{c})} \boldsymbol{M}_{n\sigma}^{[i,j]}\, \delta\Big(\tau - (\tau'_{i\sigma} - \tau_{j\sigma})_\beta\Big), \tag{6.58}$$

and $G_\sigma(\tau) = \Big\langle G_\sigma^{(\mathfrak{c})}(\tau)\Big\rangle_{\mathrm{MC}} = \mathbb{E}(\boldsymbol{M}_n^{[n,n]})$. To see the equivalence of (6.58) with (6.55), pick any pair (i_0, j_0) and permute creation/annihilation indices so that it becomes the last row/column; then the determinant ratio for removing that pair equals the bottom-right inverse element $\boldsymbol{M}_n^{[n,n]}$, and the average over uniformly chosen pairs reproduces the full sum in (6.58). Thus (6.55) and (6.58) are the same estimator written, respectively, in compressed "selected-pair" form and in fully expanded delta-sum form.

In the segment formulation, local observables follow directly from segment geometry. Using the total length of spin-σ segments $L_\sigma(\mathfrak{c})$ (Eq. (6.14)) and the total overlap length $O_{\uparrow\downarrow}(\mathfrak{c})$ (Eq. (6.15)), one obtains the Monte Carlo estimators

$$\langle \hat{n}_\sigma \rangle \;=\; \frac{\langle L_\sigma \rangle_{MC}}{\beta}\,, \qquad \langle \hat{n}_\uparrow \hat{n}_\downarrow \rangle \;=\; \frac{\langle O_{\uparrow\downarrow} \rangle_{MC}}{\beta}\,, \tag{6.59}$$

where $\langle\cdot\rangle_{MC}$ denotes the Monte Carlo average over configurations with the usual CT-HYB weights. Equivalently, writing the expectation explicitly as $\mathbb{E}[\cdot]$ for the sampled ensemble used in (6.55),

$$\langle \hat{n}_\sigma \rangle \;=\; \mathbb{E}\left[\frac{L_\sigma(\mathfrak{c})}{\beta}\right], \qquad \langle \hat{n}_\uparrow \hat{n}_\downarrow \rangle \;=\; \mathbb{E}\left[\frac{O_{\uparrow\downarrow}(\mathfrak{c})}{\beta}\right]. \tag{6.60}$$

These estimators are $O(1)$ to accumulate per configuration and require no additional matrix operations: L_σ and $O_{\uparrow\downarrow}$ are updated incrementally whenever a segment is inserted/removed. Spin-resolved densities $n_\uparrow$,$n_\downarrow$ and their combinations, e.g. $n = n_\uparrow + n_\downarrow$ and $m = n_\uparrow - n_\downarrow$, are obtained directly from (6.59). These relations hold for any density-density local interaction in CT-HYB and are standard in the segment algorithm [91, 92, 98].

6.4 Sign problem

In Monte Carlo sampling with potentially negative (or complex) configuration weights $w(\mathfrak{c})$, one rewrites averages as

$$\langle \mathcal{O} \rangle = \frac{\sum_{\mathfrak{c}} w(\mathfrak{c})\mathcal{O}(\mathfrak{c})}{\sum_{\mathfrak{c}} w(\mathfrak{c})} = \frac{\sum_{\mathfrak{c}} |w(\mathfrak{c})|\,\mathrm{sign}(\mathfrak{c})\mathcal{O}(\mathfrak{c})}{\sum_{\mathfrak{c}} |w(\mathfrak{c})|\,\mathrm{sign}(\mathfrak{c})} = \frac{\langle \mathrm{sign}\cdot\mathcal{O}\rangle_{\mathrm{MC}}}{\langle \mathrm{sign}\rangle_{\mathrm{MC}}}, \tag{6.61}$$

with $\mathrm{sign}(\mathfrak{c}) = w(\mathfrak{c})/|w(\mathfrak{c})|$ and $\langle\cdot\rangle_{\mathrm{MC}}$ the average in the $|w|$-ensemble. The variance of such reweighted estimators scales as $\mathrm{Var}(\langle\mathcal{O}\rangle) \propto [\langle \mathrm{sign}\rangle_{\mathrm{MC}}^2 N]^{-1}$, so an average sign $\langle \mathrm{sign}\rangle_{\mathrm{MC}} \ll 1$ inflates errors and can render simulations exponentially hard in β and system size [92, 105]. This is the infamous fermionic *sign problem* [106]. In CT-HYB with density-density interactions and diagonal (spin/orbital) hybridization, the segment algorithm yields nonnegative weights and thus $\langle \mathrm{sign}\rangle_{\mathrm{MC}} = 1$ by construction [91,

92]. A sign problem reappears when rotationally invariant interactions (spin-flip, pair hopping), off-diagonal/complex hybridization (spin-orbit, crystal-field mixing, broken time-reversal), or cluster/multiorbital couplings introduce additional fermionic permutations. In those cases $\langle \mathrm{sign} \rangle_{\mathrm{MC}}$ typically decreases as temperature is lowered or correlations are strengthened. Mitigations are model- and solver-specific (choice of basis to diagonalize hybridization, symmetry points, gauge choices), but no general cure exists [105, 106].

6.5 Error estimates of observables

Monte Carlo measurements form a correlated time series. Consequently, naive $1/\sqrt{N}$ error bars underestimate uncertainties when autocorrelations are present. For an observable $\mathcal{O}$ with Monte Carlo average $\bar{\mathcal{O}} = \langle \mathcal{O} \rangle_{\mathrm{MC}}$ over N_{sample} samples and variance $\sigma^2_{\mathcal{O}} = \langle \mathcal{O}^2 \rangle_{\mathrm{MC}} - \bar{\mathcal{O}}^2$, the *integrated autocorrelation time* [107] is defined as

$$\mathcal{T}_{\mathcal{O}} = 1 + 2 \sum_{i=1}^{N_{\mathrm{sample}}} \frac{\mathcal{C}_{\mathcal{O}}(\tau_i)}{\mathcal{C}_{\mathcal{O}}(0)}, \tag{6.62}$$

where

$$\mathcal{C}_{\mathcal{O}}(\tau_i) = \frac{1}{N_{\mathrm{sample}} - i} \sum_{j=1}^{N_{\mathrm{sample}}-i} (\mathcal{O}_j - \bar{\mathcal{O}})(\mathcal{O}_{j+i} - \bar{\mathcal{O}}) \tag{6.63}$$

is the autocorrelation function of $\mathcal{O}$ at lag τ_i. The integrated autocorrelation time scales the effective number of independent samples, $N_{\mathrm{eff}} = N_{\mathrm{sample}} / \left(2\mathcal{T}_{\mathcal{O}}\right)$, and the standard error becomes

$$\mathrm{SE}(\bar{O}) = \sqrt{\frac{\sigma^2_{\mathcal{O}}}{N_{\mathrm{eff}}}} = \sqrt{\frac{\mathcal{T}_{\mathcal{O}} \sigma^2_{\mathcal{O}}}{N_{\mathrm{sample}}}}\,. \tag{6.64}$$

Thus, truly independent measurements can only be performed every $\mathcal{T}_{\mathcal{O}}$ MC update steps. In practice, observables are measured by binning/blocking: Between measurements, one performs N_{step} Monte Carlo update moves to ensure the measured configurations are approximately decorrelated, requiring $N = N_{\mathrm{sample}} N_{\mathrm{step}}$ total update moves for N_{sample} measurements. The bin size N_{step} should be larger than the largest integrated autocorrelation time among all observables of interest, $\max_{\mathcal{O}} \mathcal{T}_{\mathcal{O}}$.

Before recording measurements, it is important that the Markov chain has reached stationarity and has equilibrated to the target distribution. The initial segment pattern, inverse matrices, and proposal scales imprint a transient drift in observables. Sampling during this nonstationary phase would bias averages. Warm-up (or thermalization) cycles are therefore discarded: One runs N_{warmup} update moves without measuring until key observables exhibit stationary running means and fluctuations. The required warm-up length depends on the slowest autocorrelated mode of the chain and thus on temperature, interaction strength, and move set. In practice one chooses a conservative number of warm-up cycles (often many times the estimated integrated autocorrelation time) and verifies stationarity by comparing early/late segments of the run.

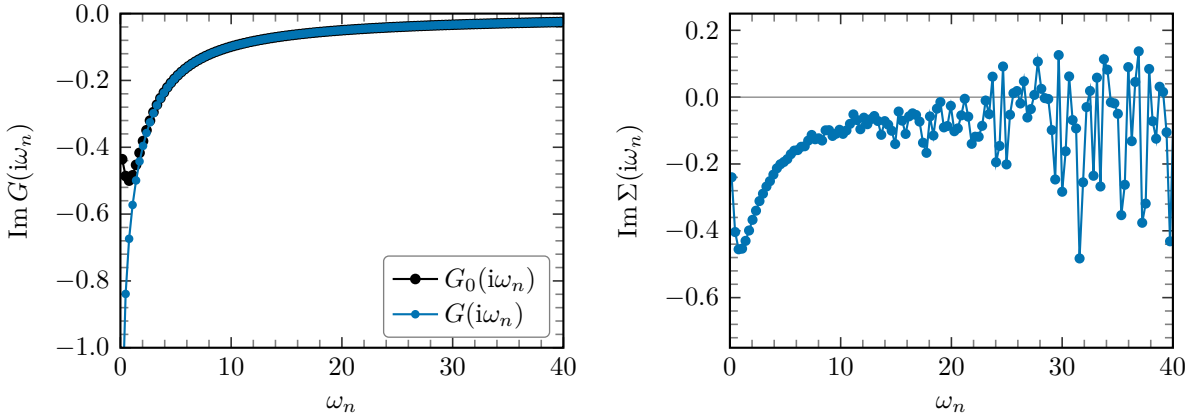

Figure 11: Example of the non-interacting and interacting Matsubara Green's functions $G_0(\mathrm{i}\omega_n)$ and $G(\mathrm{i}\omega_n)$ (left) and the noisy self-energy $\Sigma(\mathrm{i}\omega_n)$ from direct Dyson inversion (right). The model is a single-orbital Anderson impurity with $U = 2$, $\beta = 20$, and a semi-circular bath (Bethe lattice) with half-bandwidth $D = 1$ at half-filling.

6.6 Self-energy stabilization

The self-energy $\Sigma_\sigma(i\omega_n)$ is obtained from the Dyson equation

$$G_\sigma(\mathrm{i}\omega_n) = G_{0,\sigma}(\mathrm{i}\omega_n) + G_{0,\sigma}(\mathrm{i}\omega_n)\Sigma_\sigma(\mathrm{i}\omega_n)G_\sigma(\mathrm{i}\omega_n), \tag{6.65}$$

or equivalently after rearrangement,

$$\Sigma_\sigma(\mathrm{i}\omega_n) = G^{-1}_{0,\sigma}(\mathrm{i}\omega_n) - G^{-1}_\sigma(\mathrm{i}\omega_n), \tag{6.66}$$

where $G_{0,\sigma}$ is the noninteracting impurity Green's function and G_σ the interacting impurity Green's function (sampled in CT-HYB). At large ω_n, the Dyson inversion amplifies Monte Carlo noise in $G_\sigma(\mathrm{i}\omega_n)$, causing erratic self-energies in the high-frequency tail, as shown in Fig. 11 (right panel). In order to use CT-HYB solvers in combination with algorithms that require accurate self-energies and analytic continuation, it is crucial to stabilize the self-energy tails at large frequencies.

To obtain reliable $\Sigma_\sigma(\mathrm{i}\omega_n)$ at high frequencies, one can enforce the correct asymptotics rather than inverting raw, noisy $G_\sigma(\mathrm{i}\omega_n)$. Below we outline three complementary strategies: simple tail fitting constrained by exact high-frequency moments (from equal-time commutators/sum rules), measuring G in an orthogonal-polynomial (Legendre) basis to compress noise before transforming to Matsubara frequencies and the constraint renormalization method (CRM) that reduces noise by projecting onto known moments.

6.6.1 Tail fitting with high-frequency moments

The Green's function and self-energy have known asymptotic expansions at large frequencies:

$$G_\sigma(\mathrm{i}\omega_n) = \sum_{j=1}^{N} \frac{G^\sigma_j}{(\mathrm{i}\omega_n)^j}, \qquad \Sigma_\sigma(\mathrm{i}\omega_n) = \Sigma^\sigma_0 + \sum_{j=1}^{N} \frac{\Sigma^\sigma_j}{(\mathrm{i}\omega_n)^j}. \tag{6.67}$$

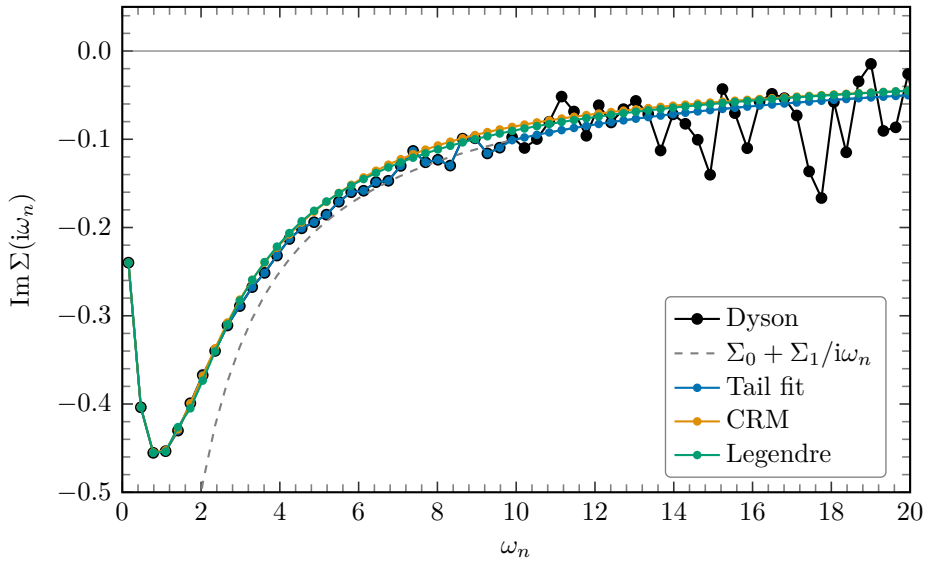

Figure 12: Comparison of self-energy stabilization methods for the single-orbital Anderson impurity model with $U = 2$, $\beta = 20$, and a semi-circular bath (Bethe lattice) with half-bandwidth $D = 1$ at half-filling. The raw Dyson self-energy (black solid) is noisy at high frequencies. The dashed line shows the exact asymptotic form $\Sigma_0 + \Sigma_1/\mathrm{i}\omega_n$. The stabilized self-energies obtained from tail fitting (blue), CRM (orange), and Legendre basis measurement (green) all recover the correct high-frequency behavior. For intermediate frequencies, the methods yield slightly different results due to varying trade-offs between noise reduction, bias and accuracy.

The expansion coefficients (moments) G_j^σ and Σ_j^σ can be computed exactly from equal-time expectation values of nested commutators of the Hamiltonian with creation/annihilation operators [92]. The coefficient Σ_0^σ is the Hartree shift, while higher-order coefficients encode correlation effects. For the single-orbital Anderson impurity model with density-density interaction U and on-site energy ϵ_σ, the first two Green's function moments are

$$G_1^\sigma = \left\langle \left\{ \hat{d}_\sigma,\, \hat{d}_\sigma^\dagger \right\} \right\rangle = 1, \tag{6.68a}$$

$$G_2^\sigma = \left\langle \left\{ [H_{\mathrm{imp}},\, \hat{d}_\sigma],\, \hat{d}_\sigma^\dagger \right\} \right\rangle = \epsilon_\sigma + U \left\langle n_{\bar{\sigma}} \right\rangle . \tag{6.68b}$$

Here, $\bar{\sigma}$ denotes the spin opposite to σ. Higher-order moments can be derived similarly, but become increasingly cumbersome. In practice, the first two moments of G and Σ are often sufficient to stabilize self-energy tails. To this end, one fits the high-frequency part of the sampled $G_\sigma(\mathrm{i}\omega_n)$ to the asymptotic form, constraining the fit to reproduce the exact moments. The fitted $G_\sigma(\mathrm{i}\omega_n)$ is then used in the Dyson equation to obtain a stabilized self-energy $\Sigma_\sigma(\mathrm{i}\omega_n)$.

The central difficulty of high-frequency tail fitting is the transition between measured data Σ^{MC} and the fitted asymptotics Σ^{tail}. Using the fit alone is invalid at intermediate $|\omega_n|$, while a sharp switch produces kinks and violates smoothness, which can pollute analytic continuation and self-consistency. A robust workflow to handle this transition is to determine a data-driven splice window where measurements have acceptable signal-to-noise yet the asymptotics already dominate, and blend rather than switch.

Let $n_1 < n_2$ be Matsubara indices defining the window. We choose them by monitoring the relative error $\mathrm{SE}[\Sigma(\mathrm{i}\omega_n)]/|\Sigma(\mathrm{i}\omega_n)|$ or a χ^2 goodness-of-fit of the tail form. Using a smooth transition function w_n that interpolates from 0 at n_1 to 1 at n_2, the stabilized self-energy can be formed as a weighted average of the Monte Carlo measurement $\Sigma_\sigma^{\mathrm{MC}}(\mathrm{i}\omega_n)$ and the fitted tail $\Sigma_\sigma^{\mathrm{tail}}(\mathrm{i}\omega_n)$:

$$\Sigma_\sigma^{\mathrm{stab}}(\mathrm{i}\omega_n) = \Big(1 - w_n\Big)\Sigma_\sigma^{\mathrm{MC}}(\mathrm{i}\omega_n) + w_n\Sigma_\sigma^{\mathrm{tail}}(\mathrm{i}\omega_n), \tag{6.69}$$

Requiring continuity of value and first discrete derivative at n_1 further suppresses splice artifacts. We have found that the tails themselves are reliable once moments are anchored, but the blend window must be chosen conservatively: too small and residual noise leaks in; too large and the fit intrudes into the mid-frequency structure.

The example in Fig. 12 shows the self-energy of a single-orbital Anderson impurity model stabilized by tail fitting using $N = 2$ exact high frequency moments (blue curve). The transition region is smoothly blended over a few Matsubara points to avoid artifacts, centered around $\omega_n = 10$. As can be seen, the stabilized self-energy recovers the correct high-frequency behavior and is significantly less noisy than the direct Dyson inversion. However, some residual noise remains at intermediate frequencies around $\omega_n = 5 - 10$. Choosing the transition between measured data and fitted tail at lower frequencies would introduce wrong self-energy features, since the asymptotic form $\Sigma_0 + \Sigma_1/\mathrm{i}\omega_n$ (dashed line) differs significantly from the true self-energy for low frequencies.

6.6.2 Orthogonal polynomial (Legendre) representation

A convenient way to reduce statistical noise and enforce short-time structure is to use an orthogonal polynomial representation of the imaginary-time Green's function. One such basis is provided by Legendre polynomials $P_\ell(x)$, which form a complete orthogonal set on the interval $x \in [-1, 1]$, but other polynomial bases (Chebyshev, Jacobi) can also be used. Some basic properties of Legendre polynomials are summarized in Appendix A. Following Ref. [108], we map $\tau \mapsto x = 2\tau/\beta - 1 \in [-1, 1]$ and expand $G(\tau)$ in Legendre polynomials $P_\ell(x)$,

$$G(\tau) = \sum_{\ell \geq 0} \frac{\sqrt{2\ell + 1}}{\beta} P_\ell\Big(x(\tau)\Big) G_\ell, \tag{6.70}$$

where the expansion coefficients in the Legendre basis are given by

$$G_\ell = \sqrt{2\ell + 1} \int_0^\beta \mathrm{d}\tau \, P_\ell\Big(x(\tau)\Big) G(\tau). \tag{6.71}$$

The coefficients G_ℓ are *directly* measurable in CT-HYB and decay rapidly with ℓ because Monte Carlo noise is predominantly high-frequency in τ but projects onto large-ℓ components. Truncating at a modest $\ell_{\max}$ thus yields a compact, denoised representation.

In the CT-HYB segment formulation the time-domain Green's function estimator on configuration $\mathfrak{c}$ in the delta-sum form (6.58) is

$$G_\sigma(\tau) = \Big\langle G_\sigma^{(\mathfrak{c})}(\tau) \Big\rangle_{\mathrm{MC}} = \left\langle - \sum_{i,j=1}^{n_\sigma(\mathfrak{c})} \boldsymbol{M}_{n\sigma}^{[i,j]} \, \delta\Big(\tau - (\tau'_{i\sigma} - \tau_{j\sigma})_\beta\Big) \right\rangle_{\mathrm{MC}}. \tag{6.72}$$

This can be transformed directly to the Legendre basis according to (6.71):

$$\begin{aligned} G_{\sigma\ell} &= \sqrt{2\ell+1}\int_0^\beta \mathrm{d}\tau\, P_\ell\Big(x(\tau)\Big)G_\sigma(\tau) \\ &= \sqrt{2\ell+1}\left\langle -\sum_{i,j=1}^{n_\sigma(\mathfrak{c})} \boldsymbol{M}_{n\sigma}^{[i,j]} \int_0^\beta \mathrm{d}\tau\, P_\ell\Big(2\tau/\beta-1\Big)\delta\Big(\tau-(\tau'_{i\sigma}-\tau_{j\sigma})_\beta\Big)\right\rangle_{\mathrm{MC}} \\ &= -\sqrt{2\ell+1}\left\langle \sum_{i,j=1}^{n_\sigma(\mathfrak{c})} \boldsymbol{M}_{n\sigma}^{[i,j]}\, \tilde{P}_\ell\Big(2(\tau'_{i\sigma}-\tau_{j\sigma})_\beta/\beta\Big)\right\rangle_{\mathrm{MC}} . \end{aligned} \tag{6.73}$$

In contrast to other stabilization methods, this allows direct accumulation of Legendre coefficients during the Monte Carlo process by adding the contribution of each annihilation-creation pair $(\tau'_{i\sigma},\, \tau_{j\sigma})$ to all $0 \le \ell \le \ell_{\max}$ using the pretabulated $P_\ell(x)$ values. Equation (6.73) is the Legendre-basis analogue of (6.72). It replaces the Dirac delta by the test function $P_\ell(x)$ and averages with the same Monte Carlo weights $W_{\mathrm{MC}}^{(n)}$.

For codes that maintain only the matrix element used in (6.55) (i.e. a specific removal index), first permute the chosen pair to the last row/column (as in the fast-update formulas) and then apply (6.73) with $(i,\, j) = (n_\sigma,\, n_\sigma)$. Averaging over uniformly sampled pairs restores the full sum.

Once the expansion coefficients $G_{\ell,\sigma}$ are accumulated, the Matusbara Green's function can be efficiently reconstructed via

$$G_\sigma(\mathrm{i}\omega_n) = \sum_{\ell=0}^{\ell_{\max}} G_{\sigma\ell}\frac{\sqrt{2\ell+1}}{\beta}\int_0^\beta \mathrm{d}\tau\, \mathrm{e}^{\mathrm{i}\omega_n\tau}P_\ell\Big(x(\tau)\Big) = \sum_{\ell=0}^{\ell_{\max}} T_{n\ell}\, G_{\sigma\ell}, \tag{6.74}$$

where the unitary transformation matrix is given by

$$T_{n\ell} = \frac{\sqrt{2\ell+1}}{\beta}\int_0^\beta \mathrm{d}\tau\, \mathrm{e}^{\mathrm{i}\omega_n\tau}P_\ell\Big(2\tau/\beta-1\Big). \tag{6.75}$$

Using the general expression of the Fourier transform of Legendre polynomials restricted to $[-1,\, 1]$,

$$\int_{-1}^{1} \mathrm{d}x\, \mathrm{e}^{\mathrm{i}kx}P_\ell(x) = \mathrm{i}^\ell\sqrt{\frac{2\pi}{k}}J_{\ell+\frac{1}{2}}(k) = 2\mathrm{i}^\ell j_\ell(k), \tag{6.76}$$

where $J_\nu(k)$ is the Bessel function of the first kind and $j_\ell(k)$ the spherical Bessel function of order ℓ [108], we find

$$T_{n\ell} = (-1)^\ell \mathrm{i}^{\ell+1}\sqrt{2\ell+1}\, j_\ell\left(\frac{(2n+1)\pi}{2}\right). \tag{6.77}$$

Note that the transformation elements $T_{n\ell}$ are independent of β and only depend on the reduced Matsubara frequencies $\omega_n/\beta = (2n+1)\pi$. Expanding the Green's function at large Matsubara frequency as described in Sec. 6.6.1,

$$G(\mathrm{i}\omega_n) = \sum_{j=1}^{\infty}\frac{G_j}{(\mathrm{i}\omega_n)^j}, \tag{6.78}$$

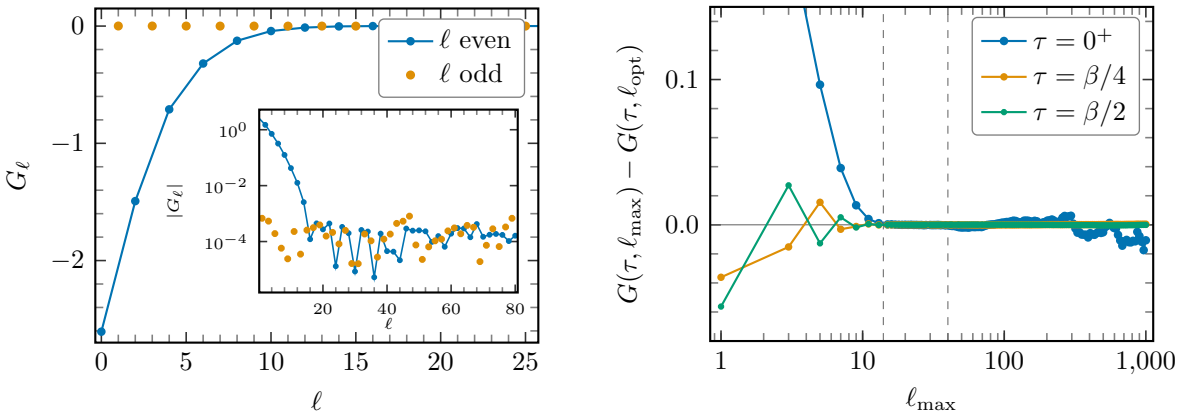

Figure 13: The sampled Legendre coefficients G_ℓ of the Green's function (left) and the convergence of the reconstructed imaginary-time Green's function $G(\tau, \ell_{\max})$ to the optimal cutoff ℓ_{opt} as a function of the Legendre cutoff $\ell_{\max}$ at different imaginary times τ (right). The vertical dashed lines indicate the approximate location of the plateau region used to determine ℓ_{opt}. The data corresponds to the model discussed in Fig. 12.

and using the high-frequency expansion of the transformation matrix,

$$T_{n\ell} = \sum_{i=j}^{\infty} \frac{T_j^{(n\ell)}}{(\mathrm{i}\omega_n \beta)^j}, \tag{6.79}$$

yields a direct, linear relation between tail moments and Legendre coefficients:

$$G_j = \beta^{-j} \sum_{\ell \geq 0} T_j^{(n\ell)} G_\ell. \tag{6.80}$$

The coefficients $T_j^{(n\ell)}$ can be computed by expanding the spherical Bessel functions at large arguments. A general expression for $T_j^{(n\ell)}$ is derived in Appendix E of Ref. [108], leading to the explicit formula

$$T_j^{(n\ell)} = (-1)^j 2\sqrt{2\ell+1} \frac{(\ell+j-1)!}{(j-1)!(\ell-j+1)!} \delta_{\ell+1,\text{odd}}. \tag{6.81}$$

Because $T_j^{(n\ell)} \sim \ell^{2j-3/2}$ while G_ℓ decays rapidly with ℓ, the series for the Green's function expansion coefficients G_j converges stably versus the Legendre cutoff $\ell_{\max}$.

However, higher j amplify large-ℓ coefficients and require larger $\ell_{\max}$ and cleaner data. The choice of $\ell_{\max}$ must therefore ensure that the quantity of interest is accurately represented: if $\ell_{\max}$ is too small, relevant information is truncated and G_ℓ does not capture all contributions to the observable being computed; if it is too large, one starts to include coefficients whose error bars are comparable to or larger than their values, which eventually pollutes the result and introduces a new source of noise. One procedure to determine the cutoff $\ell_{\max}$ is to examine the observable as a function of the cutoff $\ell_{\max}$: The observable typically reaches a plateau where it is well converged, indicating that higher-order coefficients are negligible. For larger $\ell_{\max}$, statistical noise in G_ℓ destabilizes this plateau. The existence of such a plateau provides a controlled way to determine an adequate $\ell_{\max}$ [108].

Figure 12 shows the self-energy stabilized by an orthogonal polynomial representation using Legendre polynomials (green curve) for the same model as before. The Legendre Green's function is measured directly in the Legendre basis during the same Monte Carlo simulation that produced the raw Dyson self-energy. Figure 13 (left) shows the sampled Legendre coefficients G_ℓ of the Green's function, which decay rapidly with increasing ℓ. The right panel of Fig. 13 shows the convergence of the reconstructed imaginary-time Green's function $G(\tau, \ell_{\max}) - G(\tau, \ell_{\text{opt}})$ to the optimal cutoff ℓ_{opt} as a function of the Legendre cutoff $\ell_{\max}$ at different imaginary times τ. The plateau region used to determine ℓ_{opt} is indicated by the vertical dashed lines. As can be seen, the Green's function converges well and forms a plateau region in the range $\ell_{\max} \approx 14-40$, before larger errors in the higher-order Legendre coefficients starts to destabilize the result. This destabilization is most pronounced for $\beta = 0^+$, where $G(\tau)$ first decreases slightly before increasing again for larger $\ell_{\max}$. For the self-energy in Fig. 12, we therefore choose $\ell_{\max} = 14$ to ensure a stable and accurate representation. The high-frequency behavior is correctly recovered, matching the exact asymptotic form. In contrast to the tail-fitting method, the Legendre self-energy matches the Dyson self-energy very well at intermediate and low frequencies, while still being significantly less noisy than the direct Dyson result. However, for small Matsubara frequencies of around $\omega_n = 1 - 3$, the self-energy deviates slightly from the Dyson result, which is presumed very accurate for these low frequencies. This deviation arises because the Legendre representation smooths the Green's function over the entire imaginary-time interval $[0, \beta)$, and thus cannot perfectly reproduce all Matsubara frequencies simultaneously.

6.6.3 Constrained residual minimization

The CRM-Dyson (constrained residual minimization) approach stabilizes the extraction of the self-energy from Monte-Carlo data by posing Dyson's equation as a constrained optimization problem in a compact basis. Instead of directly inverting noisy Green's functions using the Dyson equation, CRM parameterizes Σ_σ in a low-rank representation (e.g. discrete Lehmann or similar compact bases) and determines its coefficients by minimizing the mismatch between measured and reconstructed Green's function over a chosen Matsubara set.

The spectral Lehmann representation of the imaginary-time Green's function is defined as

$$G_\sigma(\tau) = \int_{-\infty}^{\infty} \mathrm{d}\omega \; K(\tau, \omega)\rho_\sigma(\omega), \tag{6.82}$$

relating the Green's function to the density $\rho_\sigma(\omega)$ [109], where

$$K(\tau, \omega) = -\frac{\mathrm{e}^{-\tau\omega}}{1 + \mathrm{e}^{-\beta\omega}} \tag{6.83}$$

is the analytic continuation kernel (see Sec. 9.1 for details). The same kernel appears in the discrete Lehmann representation (DLR),

$$G_\sigma(\tau) \approx \sum_{i=1}^{N} K(\tau, \nu_i)\hat{g}_{i,\sigma}, \tag{6.84}$$

with the DLR frequencies ν_i and coefficients $\hat{g}_{i,\sigma}$. Equation (6.84) approximates $G(\tau)$ by a short expansion in the analytically known kernel. The DLR frequencies ν_i are chosen

by a rank-revealing (pivoted) Gram-Schmidt factorization of the analytic-continuation kernel (6.83) [110], and depend only on the target accuracy ϵ of the DLR expansion and on the dimensionless cutoff $\Lambda = \beta\,\omega_{\max}$ (with $\rho(\omega) = 0$ for $|\omega| > \omega_{\max}$), not on the particular Green's function. For any fermionic G obeying the cutoff, there exists a set of coefficients $\{\hat{g}_i\}$ such that (6.84) holds to accuracy ϵ. The number of terms required for an accurate representation of G is small, scaling as

$$N = \mathcal{O}\Big(\log\Lambda \log\epsilon^{-1}\Big)\,, \tag{6.85}$$

which underlies the compactness of the representation. The coefficients can be determined either by a least-squares fit or, more robustly, by interpolation at N DLR time nodes τ_k, also generated by the same factorization. Evaluating (6.84) at $\tau = \tau_k$ yields an $N \times N$ linear system that is well conditioned at the prescribed ϵ. A fully analogous expansion holds in the Matsubara domain,

$$G_\sigma(\mathrm{i}\omega_n) \approx \sum_{i=1}^{N} K(\mathrm{i}\omega_n,\, \nu_i)\,\hat{g}_{i,\sigma}, \qquad K(\mathrm{i}\omega_n, \omega) = \frac{1}{\mathrm{i}\omega_n - \omega}\,, \tag{6.86}$$

with coefficients determined by interpolation at N DLR Matsubara nodes ω_{n_k}. Once the coefficients $\hat{g}_i$ are known, Eqs. (6.84) and (6.86) evaluate G in imaginary time and frequency without numerical Fourier transforms, and the same framework applies to self-energies and hybridization functions. The DLR is closely related to the intermediate representation (IR) [111], which uses an SVD of the kernel to build an orthogonal numerical basis rather than the DLR's non-orthogonal analytic kernels. The expansion sizes are comparable (IR often slightly smaller), and both can be obtained either by fitting or by interpolation using carefully chosen nodes.

To avoid the numerically unstable inversion, we start from the Dyson's equation (6.65) and define its residual

$$R_\sigma(\mathrm{i}\omega_n) = G_\sigma(\mathrm{i}\omega_n) - G_{0,\sigma}(\mathrm{i}\omega_n) - G_{0,\sigma}(\mathrm{i}\omega_n)\Sigma_\sigma(\mathrm{i}\omega_n)G_\sigma(\mathrm{i}\omega_n), \tag{6.87}$$

which would vanish if the (noise-free) Dyson equation were satisfied. Given the leading high-frequency coefficients, as described in Sec. 6.6.1, of the self-energy,

$$\Sigma(\mathrm{i}\omega_n) = \Sigma_0 + \frac{\Sigma_1}{\mathrm{i}\omega_n} + \mathcal{O}(\omega_n^{-2})\,, \tag{6.88}$$

we determine Σ by minimizing $\|R\|$ subject to physically exact constraints on the high-frequency tail and symmetry. Equation (6.87) can be discretized over the DLR Matsubara nodes $\mathrm{i}\omega_{n_k}$, yielding a small set of nonlinear equations. Defining the sampled quantities

$$r_k \equiv R(\mathrm{i}\omega_{n_k}), \qquad g_k \equiv G(\mathrm{i}\omega_{n_k}), \qquad g_k^0 \equiv G_0(\mathrm{i}\omega_{n_k}), \qquad \sigma_k \equiv \Sigma(\mathrm{i}\omega_{n_k}), \tag{6.89}$$

the discretized residual (6.87) reads:

$$r_k = g_k - g_k^0\sigma_k g_k - g_k^0 = d_k - a_k\sigma_k, \qquad d_k \equiv g_k - g_k^0, \quad a_k \equiv g_k^0 g_k. \tag{6.90}$$

With the definitions (6.89), the DLR expansion of G_0 and G can be recovered directly from g_k and g_k^0 via (6.86). For the self-energy, the constant (Hartree) term Σ_0 first has to be separated out. Defining

$$\tilde{\Sigma} = \Sigma - \Sigma_0, \tag{6.91}$$

the correct self-energy Σ can be reconstructed from $\tilde{\Sigma} = \sigma_k - \Sigma_0$, which also defines the constraint on the constant term of the high-frequency tail of Σ. The shifted self-energy $\tilde{\Sigma}$ is then represented in the DLR basis,

$$\tilde{\Sigma}_\sigma(\mathrm{i}\omega_n) = \sum_{i=1}^{N} K(\mathrm{i}\omega_n, \nu_i)\hat{\sigma}_{i,\sigma} = \Sigma_\sigma(\mathrm{i}\omega_n) - \Sigma_0^\sigma = \frac{\Sigma_1^\sigma}{\mathrm{i}\omega_n} + \mathcal{O}(\omega_n^{-2}). \tag{6.92}$$

The constraint on the leading decaying moment Σ_1 of the self-energy follows from multiplying both sides by $\mathrm{i}\omega_n$ and taking the limit $\omega_n \to \infty$:

$$\sum_{i=1}^{N} \hat{\sigma}_{i,\sigma} = \Sigma_1^\sigma. \tag{6.93}$$

The residual (6.87) is measured with the imaginary-time L^2 norm,

$$\|R_\sigma\|_{L^2}^2 \equiv \frac{1}{\beta}\int_0^\beta \mathrm{d}\tau R_\sigma^2(\tau). \tag{6.94}$$

For matrix-valued Green's functions and consequently matrix-valued residuals, $R^2(\tau)$ generalizes to the Frobenius norm $\|R(\tau)\|_F^2$ [110]. The norm (6.94) reduces to a quadratic form in the DLR coefficients of R:

$$\|R_\sigma\|_{L^2}^2 \equiv \frac{1}{\beta}\int_0^\beta \mathrm{d}\tau R_\sigma^2(\tau) = \frac{1}{\beta}\sum_{i,j=1}^{N} \hat{r}_i\hat{r}_j \int_0^\beta \mathrm{d}\tau K(\tau, \nu_i)K(\tau, \nu_j) \equiv \sum_{i,j=1}^{N} \hat{r}_i M_{ij}\hat{r}_j. \tag{6.95}$$

The squared norm therefore reduces to a quadratic form in the DLR coefficients $\hat{r}_i$, which can be evaluated from the discretized residuals r_k by interpolation at the DLR Matsubara nodes, and the matrix M_{ij}:

$$M_{ij} = K(0, \nu_i)K(0, \nu_j)\frac{1 - \mathrm{e}^{-\beta(\nu_i+\nu_j)}}{\beta(\nu_i + \nu_j)} \tag{6.96a}$$

$$= \frac{K(0, \nu_i)K(0, \nu_j) - K(\beta, \nu_i)K(\beta, \nu_j)}{\beta(\nu_i + \nu_j)}. \tag{6.96b}$$

Both expressions are equivalent, but suffer from numerical instabilities in different regimes. If $\nu_i \approx -\nu_j$, both formulas involve cancellation of nearly equal terms. Equation (6.96a) can remy this with very accurate numerical computation of $\mathrm{e}^{-\beta(\nu_i+\nu_j)} - 1$, which typically can be done in a stable manner using special functions in numerical libraries. However, in the case of $\beta(\nu_i + \nu_j) \ll 0$, Eq. (6.96a) suffers from numerical overflow, while Eq. (6.96b) remains stable.

In total, the discretized constrained residual minimization problem is given by

$$\arg\min_{\sigma_k} \|R\|_{L^2}^2 \quad \text{subject to} \quad \sum_{i=1}^{N} \tilde{\sigma}_i = \Sigma_1. \tag{6.97}$$

After solving (6.97) for the σ_k at the DLR Matsubara nodes and interpolating to obtain the DLR coefficients $\hat{\sigma}_i$, the self-energy can be reconstructed in the DLR basis and evaluated at any Matsubara frequency via

$$\Sigma_\sigma(\mathrm{i}\omega_n) = \Sigma_0^\sigma + \sum_{i=1}^{N} K(\mathrm{i}\omega_n, \nu_i)\hat{\sigma}_{i,\sigma}. \tag{6.98}$$

Since the CRM formulation poses Dyson's equation as a minimization problem, it naturally smooths out high-frequency noise while exactly enforcing known high-frequency moments. However, particularly at low temperatures, the self-energy might exhibit larger errors at intermediate frequencies due to the limited number of DLR basis functions.

Figure 12 shows the self-energy stabilized by CRM (orange curve) for the same single-orbital Anderson impurity model as in the tail-fitting example. The error tolerance for the DLR basis is set to $\epsilon = 10^{-6}$, and $\omega_{\max} = 4$ is used as frequency cutoff to ensure $\rho(\omega) \approx 0$ for $|\omega| > \omega_{\max}$ for the given model parameters. The CRM-stabilized self-energy recovers the correct high-frequency behavior and is significantly less noisy than the direct Dyson inversion. It also matches the Dyson self-energy very well at low and intermediate frequencies.

Similar to the choice of $\ell_{\max}$ of the Legendre representation, the choice of the frequency cutoff $\omega_{\max}$ (or dimensionless $\Lambda = \beta\omega_{\max}$) influences the CRM results. Since for interacting systems the spectral support is not known *a priori*, the choice of $\omega_{\max}$ can be subtle and requires care. In practice, the DLR cutoff parameter can be determined by self-convergence of the CRM solution with respect to $\omega_{\max}$. Concretely, we begin from a physically motivated initial guess – anchored by an estimate of the spectral support – and sweep $\omega_{\max}$ upward while monitoring a self-convergence error of the resulting Green's function or self-energy. We then choose the smallest cutoff for which the CRM solution reaches a clear plateau (below a prescribed tolerance) across several consecutive steps.

In our experience, choosing $\omega_{\max}$ too large (even if it lies outside the bands) can introduce spurious features in the solution. Increasing the cutoff enlarges the admissible function space and typically worsens conditioning by adding directions that are only weakly constrained by the Matsubara/imaginary-time data. This is well documented for analytic-continuation kernels, whose singular values decay faster as the "problem size" grows [112]. As a result, solutions may drift with $\omega_{\max}$ due to amplified null-space components, not because of genuine physical weight outside the bands. A closely related effect occurs when the high-frequency tail is not constrained (e.g., by moment/sum-rule information): different $\omega_{\max}$ choices redistribute tiny amounts of spectral weight at large ω that nonetheless feed back into the least-squares fit [113].

7 Substitutional disorder: Multicomponent alloys

The physical properties of structurally disordered materials remain a central theme in contemporary solid-state physics. Random substitutions, vacancies, stacking faults, or site-to-site variations in atomic environments disrupt the perfect translational symmetry that underpins Bloch's theorem, thereby introducing additional scattering channels which profoundly influence electronic, magnetic, and vibrational degrees of freedom [114, 115]. Understanding how such disorder affects, for example, electrical resistivity, localization phenomena, or even the robustness of superconductivity therefore requires theoretical tools capable of treating randomness on equal footing with the underlying electronic structure. Over the past decades a variety of techniques have been proposed to meet this challenge, ranging from real-space supercell approaches and diagrammatic perturbation theory to cluster extensions of dynamical mean-field theory.

The coherent potential approximation (CPA) emerged in the late 1960s as a non-perturbative, single-site effective-medium theory that restores translational invariance in substitutionally disordered alloys while retaining the chemical identity of each component at the level of local scattering. In its modern form it can be traced back to the independent works of Soven and of Taylor, who formalized the self-consistent embedding of a randomly chosen atom into a translationally invariant host such that the configuration-averaged single-site scattering matrix vanishes [116, 117]. Closely related diagrammatic and multiple-scattering derivations by Velický and by Györffy clarified the connection to locator expansions and to Korringa-Kohn-Rostoker (KKR) multiple scattering, respectively [118, 119]. Classic reviews by Elliott, Krumhansl, and Leath, and by Yonezawa and Morigaki, cemented the CPA as the standard reference point for electronic transport and spectral properties in random alloys [120, 121].

7.1 Disorder configurations

We consider a crystalline solid with an underlying Bravais lattice and a fixed basis (for notational simplicity, a single orbital per site will be used first and generalized below). In a substitutionally disordered alloy the geometric lattice is intact, while each lattice site i is occupied by exactly one of M chemical components, indexed by α:

$$i \mapsto \alpha \equiv \text{site } i \text{ occupied by species } \alpha \in \{1, \ldots, M\}. \tag{7.1}$$

The microscopic realization of the alloy is specified by a configuration map

$$\text{conf} \,:\, \{i\} \to \{\alpha\}\,, \tag{7.2}$$

where mathematically a configuration is a function

$$i \mapsto \text{conf}(i) \equiv \alpha(i), \tag{7.3}$$

so that α_i is the species residing on site i. The set of all possible configurations is the configuration space $\Omega \equiv \{\text{conf}\}$.

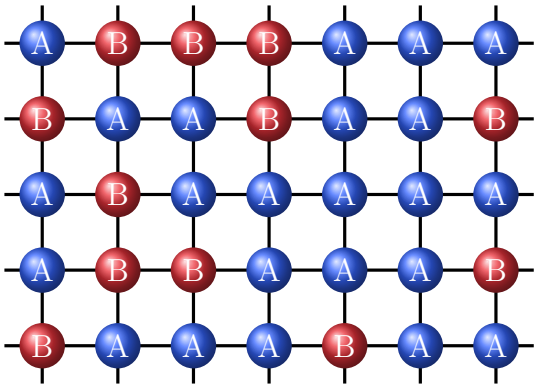

Figure 14: Example of a single configuration for a disordered binary alloy with two components A and B.

In reality, the configuration of a given sample is unobservable. Therefore, theoretical analyses replace the unknown sample-specific configuration by an ensemble average over all admissible disorder configurations. The macroscopic composition is encoded by concentrations $c_\alpha \in [0,1]$ with $\sum_{\alpha=1}^{M} c_\alpha = 1$. The probability of a specific lattice site i being occupied by species α is therefore the concentration of that component $P(i \mapsto \alpha) = c_\alpha$. The standard random substitutional ensemble assumes independent site occupations drawn from a product measure,

$$\mathbb{P}(\text{conf}) = \prod_{i=1}^{N} c_{\alpha(i)}\,, \tag{7.4}$$

which is translationally invariant in distribution. This description enforces the concentrations on average. In finite systems one may instead restrict to the multinomial subset with exactly $N_\alpha = c_\alpha N$ sites of type α (a "canonical" ensemble), which becomes equivalent to (7.4) in the thermodynamic limit $N \to \infty$. For any configuration-dependent observable $\mathcal{O}[\text{conf}]$, the configurational average is

$$\langle \mathcal{O} \rangle \equiv \sum_{\text{conf}\in\Omega} \mathbb{P}(\text{conf})\mathcal{O}[\text{conf}]\,. \tag{7.5}$$

We use $\langle\cdot\rangle$ for averages over disorder in this chapter. In practice, physical samples are assumed to be *self-averaging*, so that macroscopic observables coincide with their configurational averages in the thermodynamic limit.

Given a fixed configuration conf, a minimal single-band tight-binding description reads

$$\hat{H}[\text{conf}] = \sum_{i,j} t_{ij}\hat{c}_i^\dagger \hat{c}_j + \sum_i v_{\alpha(i)}\hat{n}_i, \tag{7.6}$$

where t_{ij} are configuration-independent hopping integrals on the Bravais lattice and $v_{\alpha(i)}$ is the on-site potential associated with the species $\alpha(i)$ occupying site i. For a binary alloy one frequently writes $v_A = +\Delta/2$ and $v_B = -\Delta/2$, with Δ the on-site disorder strength. Equation (7.6) embodies diagonal (on-site) disorder. More generally, one may allow off-diagonal disorder in which the hopping itself depends on the adjacent species, however this is not considered further in this thesis.

For a fixed configuration conf we define the single-particle Green's function as the resolvent

$$\boldsymbol{G}[\mathrm{conf}](z) = \Big[z\mathbb{1} - \boldsymbol{H}[\mathrm{conf}]\Big]^{-1}, \tag{7.7}$$

with site (and orbital) matrix elements $G_{ij}(z)$ and the single-particle Hamiltonian matrix $\boldsymbol{H}$ defined by $\hat{H} = \hat{\boldsymbol{c}}^\dagger \boldsymbol{H} \hat{\boldsymbol{c}}$. The complex frequency $z \in \mathbb{C}$ parametrizes both imaginary- and real-frequency formulations as Matsubara or retarded/advanced Green's functions,

$$\text{Matsubara:}\quad z = \mathrm{i}\omega_n\,, \qquad \text{Retarded:}\quad z = \omega + \mathrm{i}0^+, \tag{7.8}$$

and, when needed, the advanced function follows from $z = \omega - \mathrm{i}0^+$. Analyticity of $G(z)$ in the upper (retarded) or lower (advanced) half-plane ensures that the Matsubara and real-frequency objects are related by analytic continuation. While $G_{ij}[\mathrm{conf}](z)$ is not translationally invariant for a given configuration, the ensemble implies translation invariance after configurational averaging:

$$\langle G_{ij}(z)\rangle = \bar{G}(\boldsymbol{r}_i - \boldsymbol{r}_j,\, z), \qquad \bar{G}(\boldsymbol{k}, z) = \sum_{\boldsymbol{r}} \mathrm{e}^{-\mathrm{i}\boldsymbol{k}\cdot\boldsymbol{r}} \bar{G}(\boldsymbol{r},\, z)\,, \tag{7.9}$$

so that a lattice Fourier transform exists for any z in the domains (7.8). In particular, $\langle G(\mathrm{i}\omega_n)\rangle$ provides the imaginary-frequency description used in finite-temperature many-body calculations, while $\langle G(\omega + \mathrm{i}0^+)\rangle$ yields the retarded Green's function and associated spectral information, $A(\omega) = -\frac{1}{\pi}\,\mathrm{Im}\,\langle G(\omega + \mathrm{i}0^+)\rangle$.

Throughout this chapter we consider *quenched* disorder: the configuration conf is frozen on electronic time scales and averaging is performed over the probability measure (7.4). Thermodynamic or transport observables computed from $\langle G\rangle$ thus represent disorder-averaged properties of the alloy.

The definitions above fix notation for the subsequent sections. We next introduce the hierarchy of effective-medium approximations, beginning with the virtual crystal approximation (VCA), proceeding to the average T-matrix approximation (ATA), and culminating in the coherent potential approximation (CPA), each formulated in terms of the averaged Green's function $\langle G\rangle$ and single-site scattering on a translationally invariant host. There are various derivations of these approximations in the literature. Here we follow the *propagator formalism* with diagrammatic visualizations, but alternative routes based on *multiple scattering theory* or pure *diagrammatic perturbation theory* are also common [122].

7.2 Propagator formalism and scattering matrix

The Hamiltonian introduced in (7.6) can be partitioned into a periodic reference and a random potential,

$$\boldsymbol{H}[\mathrm{conf}] = \boldsymbol{H_0} + \boldsymbol{V}, \tag{7.10}$$

where $\boldsymbol{H}_0$ is the homogeneous configuration-independent contribution and $\boldsymbol{V} \equiv \boldsymbol{V}[\mathrm{conf}]$ describes the site-diagonal random potential. Here, $\boldsymbol{V}$ is considered as a perturbation to the reference system $\boldsymbol{H}_0$. Similar to the full Green's function (7.7), the reference Green's function of the non-random system is defined as the resolvent

$$\boldsymbol{G}_0(z) = \Big[z\mathbb{1} - \boldsymbol{H}_0\Big]^{-1}, \tag{7.11}$$

which is also called the propagator of the unperturbed system, as $\boldsymbol{H}_0$ typically contains only kinetic (hopping) terms. The full Green's function $\boldsymbol{G}(z)$ can be expressed in terms of the propagator $\boldsymbol{G}_0(z)$,

$$\boldsymbol{G}(z) = \Big[z\mathbb{1} - \boldsymbol{H}_0 - \boldsymbol{V}\Big]^{-1} = \Big[\boldsymbol{G}_0(z)^{-1} - \boldsymbol{V}\Big]^{-1} = \boldsymbol{G}_0(z)\Big[\mathbb{1} - \boldsymbol{V}\boldsymbol{G}_0(z)\Big]^{-1}. \tag{7.12}$$

By rearranging (7.12) one obtains,

$$\boldsymbol{G}(z) = \boldsymbol{G}_0(z) + \boldsymbol{G}_0(z)\boldsymbol{V}\boldsymbol{G}(z), \tag{7.13}$$

and, by iteratively inserting $\boldsymbol{G}$ back into the r.h.s of (7.13), the Born series

$$\boldsymbol{G} = \boldsymbol{G}_0 + \boldsymbol{G}_0\boldsymbol{V}\boldsymbol{G}_0 + \boldsymbol{G}_0\boldsymbol{V}\boldsymbol{G}_0\boldsymbol{V}\boldsymbol{G}_0 + \dots . \tag{7.14}$$

The Green's function can thus be viewed as a perturbation expansion in powers of the random potential $\boldsymbol{V}$,

$$\boldsymbol{G}(z) = \boldsymbol{G}_0(z)\sum_{n=0}^{\infty}\Big[\boldsymbol{V}\boldsymbol{G}_0(z)\Big]^n. \tag{7.15}$$

This expression represents the propagation of a particle in a perfect lattice, represented by $\boldsymbol{H}_0$, with scattering events taking place at the random potentials $\boldsymbol{V}$. The terms of the series represent multiple scattering off the random potentials, with increasing order in $\boldsymbol{V}$ corresponding to an increasing number of scattering events. The propagator $\boldsymbol{G}_0(z)$ describes the propagation between successive events.

It is often advantageous to rewrite (7.15) into

$$\boldsymbol{G}(z) = \boldsymbol{G}_0(z) + \boldsymbol{G}_0(z)\sum_{n=0}^{\infty}\Big[\boldsymbol{V}\boldsymbol{G}_0(z)\Big]^n\boldsymbol{V}\boldsymbol{G}_0(z), \tag{7.16}$$

which is also known as the Lippmann-Schwinger form. Equation (7.16) defines the scattering operator

$$\boldsymbol{T}(z) \coloneqq \boldsymbol{V}\sum_{n=0}^{\infty}\Big[\boldsymbol{V}\boldsymbol{G}_0(z)\Big]^n = \boldsymbol{V} + \boldsymbol{V}\boldsymbol{G}_0(z)\boldsymbol{V} + \boldsymbol{V}\boldsymbol{G}_0(z)\boldsymbol{V}\boldsymbol{G}_0(z)\boldsymbol{V} + \dots \tag{7.17}$$

which collects all multiple scattering events off the potential $\boldsymbol{V}$. The scattering operator $\boldsymbol{T}(z)$ is also called the T-matrix, and can be written as

$$\boldsymbol{T}(z) = \boldsymbol{V} + \boldsymbol{V}\boldsymbol{G}_0(z)\boldsymbol{T}(z) = \boldsymbol{V}\Big[\mathbb{1} - \boldsymbol{V}\boldsymbol{G}_0(z)\Big]^{-1}, \tag{7.18}$$

by contracting the series in (7.17) back into itself. With this definition, the Green's function can be compactly written as

$$\boldsymbol{G}(z) = \boldsymbol{G}_0(z) + \boldsymbol{G}_0(z)\boldsymbol{T}(z)\boldsymbol{G}_0(z). \tag{7.19}$$

The last two equalities of (7.18) are only valid if all scattering paths are considered and the Born series of the scattering operator is not truncated.

In real space, $\boldsymbol{T}$ organizes multiple scattering paths into on-site and intersite events. Using $\boldsymbol{V} = \sum_{ij} v_i\delta_{ij}$, where we have introduced the shorthand notation $v_i \equiv v_{\alpha(i)}$, the T-matrix elements can be decomposed as

$$T_{ij} = v_i\delta_{ij} + v_iG^{(0)}_{ij}v_j + \sum_n v_iG^{(0)}_{in}v_nG^{(0)}_{nj}v_j + \sum_{n,m} v_iG^{(0)}_{in}v_nG^{(0)}_{nm}v_mG^{(0)}_{mj}v_j + \dots . \tag{7.20}$$

Diagrammatically, G_0 are propagator lines and v_i are impurity insertions. Equation (7.18) is the exact resummation of all such insertions. Similarly, we can write the Born series of the Green's function (7.15) as sum over multiple paths connecting different sites via the components of the random potential $\boldsymbol{V}$:

$$G_{ij} = G_{ij}^{(0)} + \sum_n G_{in}^{(0)} v_n G_{nj}^{(0)} + \sum_{n,m} G_{in}^{(0)} v_n G_{nm}^{(0)} v_m G_{mj}^{(0)} + \dots . \tag{7.21}$$

Since the perturbation $\boldsymbol{V}$ is assumed to be diagonal, the propagator $\boldsymbol{G}_0$ can be separated into its local (diagonal) $\boldsymbol{g}_0$ and non-local (off-diagonal) parts $\tilde{\boldsymbol{G}}_0$,

$$\boldsymbol{G}_0(z) = \boldsymbol{g}_0(z) + \tilde{\boldsymbol{G}}_0(z), \tag{7.22}$$

with

$$g_{ij}^{(0)}(z) = G_{ii}^{(0)}(z)\delta_{ij}, \quad \text{and} \quad \tilde{G}_{ij}^{(0)}(z) = (1-\delta_{ij})G_{ij}^{(0)}(z). \tag{7.23}$$

Accordingly, the T-matrix (7.18) can be rewritten in terms of local and non-local propagators as

$$\begin{aligned} \boldsymbol{T}(z) &= \boldsymbol{V} + \boldsymbol{V}\left[\boldsymbol{g}_0(z) + \tilde{\boldsymbol{G}}_0(z)\right]\boldsymbol{T}(z) \\ &= \boldsymbol{V}\boldsymbol{g}_0(z)\boldsymbol{T}(z) + \boldsymbol{V}\left[\mathbb{1} + \tilde{\boldsymbol{G}}_0(z)\boldsymbol{T}(z)\right] \\ &= \left[\mathbb{1} - \boldsymbol{V}\boldsymbol{g}_0(z)\right]^{-1}\boldsymbol{V}\left[\mathbb{1} + \tilde{\boldsymbol{G}}_0(z)\boldsymbol{T}(z)\right], \end{aligned} \tag{7.24}$$

where the first term describes the local or atomic t-matrix:

$$\boldsymbol{t}(z) \equiv \left[\mathbb{1} - \boldsymbol{V}\boldsymbol{g}_0(z)\right]^{-1}\boldsymbol{V}. \tag{7.25}$$

The local t-matrix sums all multiple scattering events taking place on the same site and therefore is diagonal in the site representation. The full T-matrix then collects all processes in which local scattering events are connected by non-local propagation via $\tilde{\boldsymbol{G}}_0$:

$$\boldsymbol{T}(z) = \boldsymbol{t}(z) + \boldsymbol{t}(z)\tilde{\boldsymbol{G}}_0(z)\boldsymbol{T}(z). \tag{7.26}$$

Scattering processes off a single site i can be isolated by considering the diagonal elements of the local t-matrix:

$$t_i(z) = v_i + v_i G_{ii}^{(0)}(z) v_i + v_i G_{ii}^{(0)}(z) v_i G_{ii}^{(0)}(z) v_i + \dots , \tag{7.27}$$

or, assuming that the product $G_{ii}^{(0)}(z)v_i$ is small,

$$t_i(z) = v_i\left[1 - G_{ii}^{(0)}(z)v_i\right]^{-1} = \left[1 - v_i G_{ii}^{(0)}(z)\right]^{-1} v_i. \tag{7.28}$$

In all practical applications of multiple scattering theory, (7.28) is assumed to be valid [122].

7.3 Configuration averages and the effective medium

We are ultimately interested in disorder-averaged one-particle properties, i.e. the configurational average of the resolvent

$$\langle G(z)\rangle = \left\langle \left[z\mathbb{1} - \boldsymbol{H}_0 - \boldsymbol{V}[\mathrm{conf}]\right]^{-1} \right\rangle, \tag{7.29}$$

In general, averaging must be performed at the level of Green's functions (resolvents), not Hamiltonians. An expression for the ensemble-averaged propagator $\langle G\rangle$ can be obtained, in principle, by averaging the Born series (7.15) term by term. In the site representation (7.21), this yields

$$\langle G_{ij}\rangle = G^{(0)}_{ij} + \sum_n G^{(0)}_{in}\,\langle v_n\rangle\, G^{(0)}_{nj} + \sum_{n,m} G^{(0)}_{in}\left\langle v_n G^{(0)}_{nm} v_m\right\rangle G^{(0)}_{mj} + \dots. \tag{7.30}$$

The propagators $G^{(0)}_{ij}$ are configuration-independent and thus factor out of the averages, leaving terms of the form $\langle v_i v_j \dots v_n\rangle$. These are nontrivial to evaluate depending on the distance between the involved sites, concentrations, and other statistical properties of the disorder ensemble. Additionally, the series can in general not be truncated at finite order, as multiple scattering events of arbitrary order contribute to the average, and no truncation scheme can be trusted to lead to convergence of the series [122].

It is therefore convenient to define a translationally invariant, energy-dependent effective Hamiltonian

$$\boldsymbol{H}_{\mathrm{eff}}(z) \equiv \boldsymbol{H}_0 + \boldsymbol{\Sigma}(z), \tag{7.31}$$

such that the ensemble-averaged Green's function is given by

$$\langle \boldsymbol{G}(z)\rangle = \left[z\mathbb{1} - \boldsymbol{H}_{\mathrm{eff}}(z)\right]^{-1}. \tag{7.32}$$

The self-energy $\boldsymbol{\Sigma}(z)$ encodes all effects of the random potential and is defined via the Dyson equation:

$$\langle \boldsymbol{G}(z)\rangle = \boldsymbol{G}_0(z) + \boldsymbol{G}_0(z)\boldsymbol{\Sigma}(z)\,\langle \boldsymbol{G}(z)\rangle = \left[\boldsymbol{G}_0^{-1}(z) - \boldsymbol{\Sigma}(z)\right]^{-1}, \tag{7.33}$$

The self-energy $\Sigma(z)$ is non-Hermitian and must be translationally invariant. Similarly, the ensemble-averaged Green's function can also be written by averaging the Schwinger equation (7.19), relating $\langle \boldsymbol{G}\rangle$ to the averaged T-matrix $\langle \boldsymbol{T}\rangle$:

$$\langle \boldsymbol{G}(z)\rangle = \boldsymbol{G}_0(z) + \boldsymbol{G}_0(z)\,\langle \boldsymbol{T}(z)\rangle\,\boldsymbol{G}_0(z). \tag{7.34}$$

The naive ensemble average of the Born series (7.30) can be visualized using the diagrammatic representations shown in Fig. 15, with propagator lines representing G_0

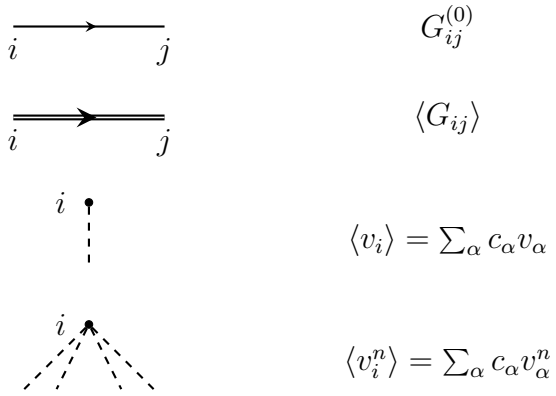

Figure 15: Diagrammatic representation of propagators and scattering events.

and dashed lines representing scattering events off the random potentials v_i:

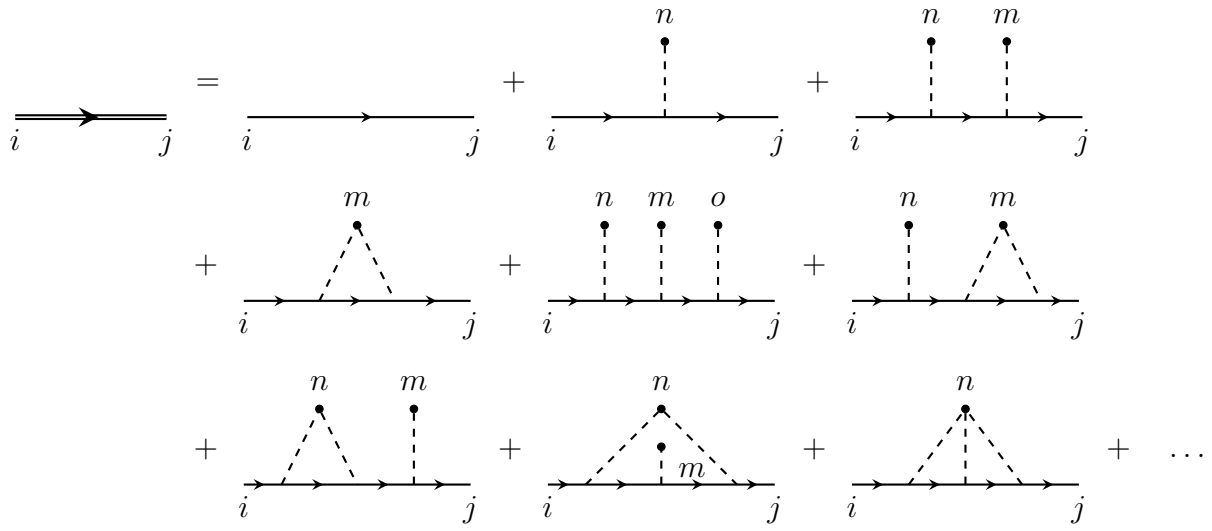

Here, all diagrams up to the fourth order are shown. Similarly, the Dyson equation (7.33) can be represented as

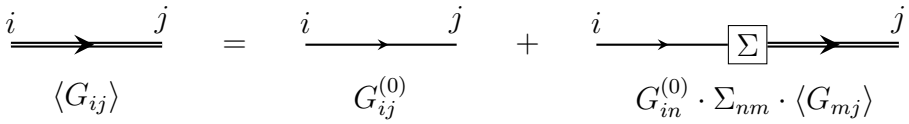

7.4 Virtual crystal approximation

The Virtual Crystal Approximation (VCA) replaces the random on-site potentials by their composition average, thereby restoring exact translational invariance and yielding a simple, Bloch-like propagator. As the zeroth term in a cumulant (moment) expansion of the disorder, VCA retains only the first moment of the potential distribution and discards all higher moments. It is therefore exact for small enough perturbations $\boldsymbol{V}$ and often adequate when disorder is weak compared to the bandwidth or when one is

interested primarily in band filling and long-wavelength properties that are insensitive to phase-coherent multiple scattering [120, 122].

Assuming that $\boldsymbol{V}$ is small, the naive average (7.30) can be decoupled into a random phase approximation (RPA) by neglecting correlations between different scattering events:

$$\langle G_{ij}\rangle \simeq G^{(0)}_{ij} + \sum_n G^{(0)}_{in}\,\langle v_n\rangle\, G^{(0)}_{nj} + \sum_{n,m} G^{(0)}_{in}\,\langle v_n\rangle\, G^{(0)}_{nm}\,\langle v_m\rangle\, G^{(0)}_{mj} + \dots . \tag{7.35}$$

With $\langle v_i v_j \dots v_n\rangle \simeq \langle v_i\rangle\,\langle v_j\rangle \dots \langle v_n\rangle$ the Green's function then immediately follows as

$$\langle \boldsymbol{G}(z)\rangle = \boldsymbol{G}_0(z) + \boldsymbol{G}_0(z)\,\langle \boldsymbol{V}\rangle\,\langle \boldsymbol{G}(z)\rangle = \left[z\mathbb{1} - \boldsymbol{H}_0 - \langle \boldsymbol{V}\rangle\right]^{-1}, \tag{7.36}$$

which is equivalent to the Green's function of a perfect crystal with a simple potential shift $\langle \boldsymbol{V}\rangle$. The self energy in this approximation is the lowest-order term,

$$\boldsymbol{\Sigma}_{\mathrm{VCA}} = \langle \boldsymbol{V}\rangle\,, \tag{7.37}$$

which is real, and independent of z and the wavevector $\boldsymbol{k}$, leading to a local self energy:

$$\Sigma_{\mathrm{VCA}} = \langle v_i\rangle = \sum_{\alpha=1}^{M} c_\alpha v_\alpha. \tag{7.38}$$

Consequently, VCA captures band filling but not broadening, lifetime effects, or multiple scattering events. For binary alloys, the virtual crystal approximation only gives reasonable results near the limit of where v_A and v_B are equal, or in the limit of $c \to 0$ of one species. Diagrammatically, VCA amounts to retaining only the disconnected (tadpole) contribution and discarding all fluctuation effects:

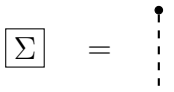

(7.39)

7.5 Average T-matrix approximation

The VCA captures only the mean of the random on-site potentials and therefore misses all fluctuation effects. A natural next step is to keep the medium translationally invariant while explicitly incorporating single-site multiple scattering from the fluctuations around a chosen reference. To this end we split the random potential into a uniform energy independent "coherent" part $\bar{v}$ and a fluctuation, defining the effective medium as

$$\hat{H}_{\mathrm{eff}} = \sum_{i,j} t_{ij}\hat{c}_i^\dagger \hat{c}_j + \sum_i \bar{v}\,\hat{n}_i. \tag{7.40}$$

The parameter $\bar{v}$ is the coherent on-site potential that shifts every site equally. The total Hamiltonian then reads

$$\hat{H} = \hat{H}_{\mathrm{eff}} + \hat{V} = \sum_{i,j} t_{ij}\hat{c}_i^\dagger \hat{c}_j + \sum_i \bar{v}\,\hat{n}_i + \sum_i (v_{\alpha(i)} - \bar{v})\,\hat{n}_i. \tag{7.41}$$

where $\hat{V}$ is the perturbation with respect to the effective medium:

$$\hat{V} = \sum_i (v_{\alpha(i)} - \bar{v})\, \hat{n}_i = \sum_i \tilde{v}_{\alpha(i)}\, \hat{n}_i, \tag{7.42}$$

or in matrix notation, $\boldsymbol{V} = \sum_{ij} \tilde{v}_i \delta_{ij}$.

In the remaining of the chapter, we distinguish between the bare-lattice Green's function $\boldsymbol{G}_0(z)$ corresponding to the kinetic part of the Hamiltonian $\hat{H}_0$, the coherent Green's function $\boldsymbol{G}_{\text{coh}}(z)$ associated with $\hat{H}_{\text{eff}}$, and the full disorder-averaged propagator $\langle \boldsymbol{G}(z) \rangle$. Since $\hat{H}_{\text{eff}}$ is translationally invariant, $G_{\text{coh}}(\boldsymbol{k}, z)$ is diagonal in $\boldsymbol{k}$-space and the local coherent Green's function is given by:

$$G_{\text{coh}}(z) = \frac{1}{N_k} \sum_{\boldsymbol{k}} G_{\text{coh}}(\boldsymbol{k}, z) = \frac{1}{N} \sum_{\boldsymbol{k}} \frac{1}{z - \varepsilon_{\boldsymbol{k}} - \bar{v}}. \tag{7.43}$$

Comparing the two expressions for the ensemble-averaged Green's function, Eqs. (7.33) and (7.34), now with respect to the reference propagator $\boldsymbol{G}_{\text{coh}}$

$$\langle \boldsymbol{G} \rangle = \boldsymbol{G}_{\text{coh}} + \boldsymbol{G}_{\text{coh}} \boldsymbol{\Sigma} \langle \boldsymbol{G} \rangle\,, \tag{7.44a}$$

$$\langle \boldsymbol{G} \rangle = \boldsymbol{G}_{\text{coh}} + \boldsymbol{G}_{\text{coh}} \langle \boldsymbol{T} \rangle \boldsymbol{G}_{\text{coh}}, \tag{7.44b}$$

the self-energy can be expressed in terms of the exact averaged T-matrix as

$$\boldsymbol{\Sigma}(z) = \langle \boldsymbol{T}(z) \rangle \left[\mathbb{1} + \boldsymbol{G}_{\text{coh}}(z) \langle \boldsymbol{T}(z) \rangle \right]^{-1}. \tag{7.45}$$

To this point, no approximations have been made and the expression (7.45) for the self-energy is exact. Note that the T-matrix is now defined with respect to the reference propagator $\boldsymbol{G}_{\text{coh}}$ instead of the bare lattice Green's function $\boldsymbol{G}_0$. Using equation (7.20) for the T-matrix elements and the atomic t-matrices from (7.28), we can eliminate terms of scattering events off the same site:

$$T_{ij} = t_i \delta_{ij} + t_i \tilde{G}^{\text{coh}}_{ij} t_j + \sum_{k \neq i,j} t_i \tilde{G}^{\text{coh}}_{ik} t_k \tilde{G}^{\text{coh}}_{kj} t_j + \dots. \tag{7.46}$$

As was the case for the VCA, we can use the random phase approximation to neglect correlations between scattering events on different sites. The averaged T-matrix elements can then be approximated as

$$\langle T_{ij} \rangle \simeq \langle t_i \rangle \delta_{ij} + \langle t_i \rangle \tilde{G}^{\text{coh}}_{ij} \langle t_j \rangle + \sum_{k \neq i,j} \langle t_i \rangle \tilde{G}^{\text{coh}}_{ik} \langle t_k \rangle \tilde{G}^{\text{coh}}_{kj} \langle t_j \rangle + \dots \tag{7.47}$$

using the decoupling $\langle t_i t_j \dots t_n \rangle \simeq \langle t_i \rangle \langle t_j \rangle \dots \langle t_n \rangle$. This is known as the Average T-matrix Approximation (ATA). Since the atomic scattering matrices t must be site-independent after performing the configuration average in a translationally invariant effective medium, they can be expressed as

$$\langle \boldsymbol{t}_i \rangle = \langle t \rangle \mathbb{1}_i, \tag{7.48}$$

where $\mathbb{1}_i$ is the identity operator on site i, consisting of a single 1 as diagonal element in the i-th row and column, and zeros elsewhere. The ensemble-averaged local t-matrix elements are given by

$$\langle t(z) \rangle = \sum_{\alpha=1}^{M} c_\alpha t_\alpha(z), \tag{7.49}$$

where t_α is the atomic t-matrix for a site occupied by species α, defined by Eq. (7.28) with the shifted potential $\tilde{v}_\alpha = v_\alpha - \bar{v}$,

$$t_\alpha(z) = \frac{\tilde{v}_\alpha}{1 - \tilde{v}_\alpha G_{\mathrm{coh}}(z)} = \frac{v_\alpha - \bar{v}}{1 - (v_\alpha - \bar{v}) G_{\mathrm{coh}}(z)}, \tag{7.50}$$

Using these definitions, the averaged T-matrix can be written as

$$\langle \boldsymbol{T} \rangle \simeq \langle \boldsymbol{t} \rangle + \langle \boldsymbol{t} \rangle \, \tilde{\boldsymbol{G}}_{\mathrm{coh}} \, \langle \boldsymbol{T} \rangle \tag{7.51}$$

or, equivalently, by expanding into the Born series,

$$\langle \boldsymbol{T} \rangle \simeq \langle \boldsymbol{t} \rangle + \langle \boldsymbol{t} \rangle \, \tilde{\boldsymbol{G}}_{\mathrm{coh}} \, \langle \boldsymbol{t} \rangle + \langle \boldsymbol{t} \rangle \, \tilde{\boldsymbol{G}}_{\mathrm{coh}} \, \langle \boldsymbol{t} \rangle \, \tilde{\boldsymbol{G}}_{\mathrm{coh}} \, \langle \boldsymbol{t} \rangle + \cdots = \langle \boldsymbol{t}(z) \rangle \left[\mathbb{1} - \tilde{\boldsymbol{G}}_{\mathrm{coh}}(z) \, \langle \boldsymbol{t}(z) \rangle \right]^{-1}. \tag{7.52}$$

Inserting this expression into Eq. (7.45) then yields the self-energy in the average T-matrix approximation. Within the ATA decoupling (neglect of correlations between different sites), only single-site contributions enter the local self-energy, thus terms involving off-diagonal elements of $\tilde{\boldsymbol{G}}_{\mathrm{coh}}$ do not contribute. This gives

$$\boldsymbol{\Sigma}_{\mathrm{ATA}}(z) = \langle \boldsymbol{t}(z) \rangle \left[\mathbb{1} + \boldsymbol{G}_{\mathrm{coh}}(z) \, \langle \boldsymbol{t}(z) \rangle \right]^{-1}. \tag{7.53}$$

Because both $\langle \boldsymbol{t} \rangle$ and $\boldsymbol{G}_{\mathrm{coh}}$ are local and translationally invariant, the self-energy is also local and translationally invariant:

$$\Sigma_{\mathrm{ATA}}(z) = \langle t(z) \rangle \left[1 + G_{\mathrm{coh}}(z) \, \langle t(z) \rangle \right]^{-1}. \tag{7.54}$$

Diagrammatically, the ATA self-energy is the sum of all one-particle-irreducible diagrams, that cannot be split into two disconnected pieces by cutting a single propagator line:

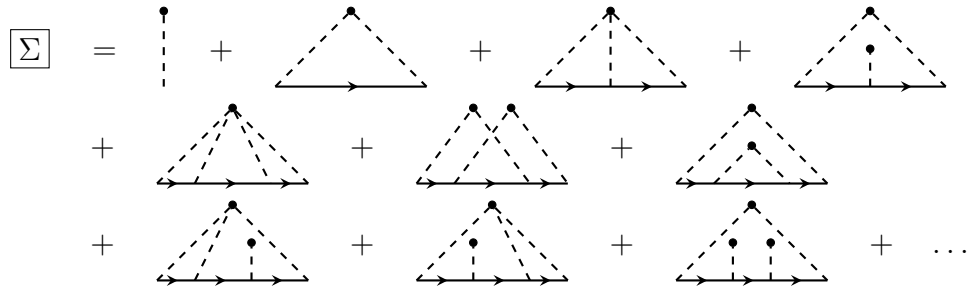

The ATA captures single-site multiple scattering with respect to the coherent potential $\bar{v}$ and thereby includes lifetime effects and band broadening, but neglects interference between different sites and depends on the choice of the coherent potential $\bar{v}$. As a result, the ATA is not self-consistent and does not enforce any specific physical condition on the effective medium. In practice, the coherent potential $\bar{v}$ is chosen as the VCA average potential,

$$\bar{v} = \Sigma_{\mathrm{VCA}} = \langle v_i \rangle = \sum_{\alpha=1}^{M} c_\alpha v_\alpha, \tag{7.55}$$

which ensures a symmetric expression for $\langle t \rangle$ and therefore for $\langle G \rangle$. This symmetry is required to correctly interpolate between the two pure limits of a binary alloy. The perturbation potentials $\tilde{v}_i$ then simply become the deviations from the average potential, $v_i - \langle V \rangle$.

7.6 Coherent potential approximation

The average T-matrix approximation (ATA) improves on VCA by resumming all *single-site* multiple scatterings on a fixed coherent background, but it does not let the effective medium "react" to those scatterings. The coherent potential approximation (CPA) improves on this idea by promoting the coherent on-site potential to a complex, energy-dependent function $\Sigma(z)$ and by determining it such that, when a randomly chosen site is embedded back into the effective medium, there is no net scattering on average. In other words, the effective medium is "coherent" with respect to the ensemble of local environments. This self-consistency enforces translational invariance of the averaged propagator while capturing disorder-induced lifetime effects and band broadening [116, 119, 122].

We impose the condition that the average scattering of a site embedded in the effective medium vanishes, i.e., the average T-matrix describing the scattering off impurity sites embedded in the effective medium defined by the yet unknown coherent potential $\Sigma_{\mathrm{CPA}}(z)$ (the reference system) vanishes:

$$\langle \boldsymbol{T} \rangle = 0. \tag{7.56}$$

Using the same approximation as before to neglect correlations between different sites this condition is fulfilled when the average local t-matrices vanish in

$$\langle T_{ij} \rangle \simeq \langle t_i \rangle \, \delta_{ij} + \langle t_i \rangle \, \tilde{G}^{\mathrm{coh}}_{ij} \, \langle t_j \rangle + \sum_{k \neq i,j} \langle t_i \rangle \, \tilde{G}^{\mathrm{coh}}_{ik} \, \langle t_k \rangle \, \tilde{G}^{\mathrm{coh}}_{kj} \, \langle t_j \rangle + \ldots . \tag{7.57}$$

Therefore, for any lattice site i, we impose the condition of vanishing average scattering when the site is replaced by any of the physical species α with on-site potential v_α:

$$\langle t_i \rangle = 0. \tag{7.58}$$

This condition determines the coherent potential $\Sigma_{\mathrm{CPA}}(z)$ self-consistently. Similar to ATA, the local t-matrix for a site occupied by species α is given by

$$t_\alpha(z) = \frac{v_\alpha - \Sigma_{\mathrm{CPA}}(z)}{1 - (v_\alpha - \Sigma_{\mathrm{CPA}}(z)) G_{\mathrm{coh}}(z,\, \Sigma_{\mathrm{CPA}})}, \tag{7.59}$$

Note that now the local coherent Green's function G_{coh} itself depends on the yet unknown coherent potential Σ_{CPA} defining the translationally invariant effective medium. In the following, we will omit this dependence for brevity. Taking the concentration average over species α, we have

$$\sum_{\alpha=1}^{M} c_\alpha \, t_\alpha(z) = \sum_{\alpha=1}^{M} c_\alpha \, \frac{v_\alpha - \Sigma_{\mathrm{CPA}}(z)}{1 - (v_\alpha - \Sigma_{\mathrm{CPA}}(z)) G_{\mathrm{coh}}(z)} = 0. \tag{7.60}$$

Equation (7.59) is the same algebra seen in ATA, but now evaluated in the dynamic host defined by $\Sigma_{\mathrm{CPA}}(z)$ via (7.60). The vanishing of the average t-matrix in (7.60) ensures that when a randomly chosen site is replaced by any of the physical species α inside the coherent medium $G_{\mathrm{coh}}(z)$, the configuration-averaged single-site scattering vanishes; i.e., the embedded site is on average indistinguishable from the medium. This

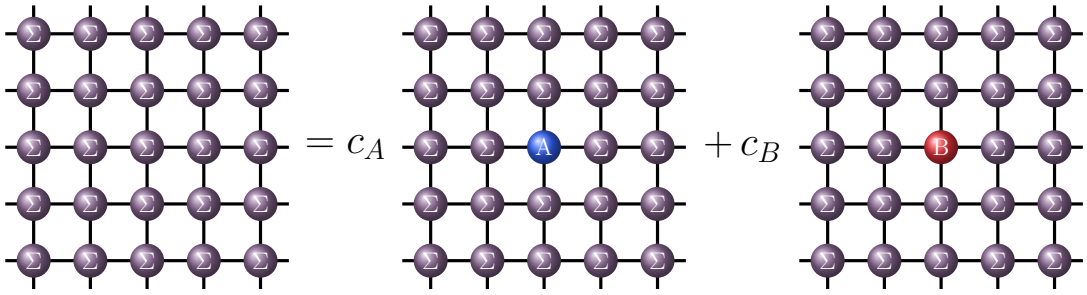

Figure 16: Self consistency condition of the coherent potential approximation (CPA). The local average Green's function of the effective medium is equal to the concentration-weighted average of the local component Green's functions, when a site of the effective medium with coherent potential Σ is replaced by an atom of species A or B with potentials v_A or v_B, respectively.

also enforces that the local propagator of the medium equals the concentration average over impurity-embedded local propagators (see Fig. 16):

$$\langle G(z)\rangle = \sum_{\alpha=1}^{M} c_\alpha \, G_\alpha(z), \tag{7.61}$$

where the impurity Green's function of an atom of species α embedded into the effective medium is given by the Dyson equation with the perturbation $v_\alpha - \Sigma_{\mathrm{CPA}}$:

$$G_\alpha(z) = \left[G_{\mathrm{coh}}^{-1}(z) - (v_\alpha - \Sigma_{\mathrm{CPA}}(z))\right]^{-1} = \frac{G_{\mathrm{coh}}(z)}{1 - (v_\alpha - \Sigma_{\mathrm{CPA}}(z))G_{\mathrm{coh}}(z)}. \tag{7.62}$$

Both statements guarantee that re-embedding a random site does not disturb the effective medium.

Once the coherent potential (CPA self-energy) $\Sigma_{\mathrm{CPA}}(z)$ has been obtained from the self-consistency condition (7.60), the disorder problem is mapped onto the effective translationally invariant medium with a purely local (site-diagonal) self-energy. By definition, the average T-matrix vanishes, $\langle \boldsymbol{T}\rangle = 0$, and Eq. (7.44b) guarantees that the ensemble-averaged Green's function in CPA equals the coherent Green's function of the effective medium,

$$\langle \boldsymbol{G}\rangle = \boldsymbol{G}_{\mathrm{coh}} + \boldsymbol{G}_{\mathrm{coh}} \langle \boldsymbol{T}\rangle \boldsymbol{G}_{\mathrm{coh}} \approx \boldsymbol{G}_{\mathrm{coh}}. \tag{7.63}$$

The ensemble-averaged Green's function then also follows from the Dyson equation with respect to the *bare* lattice,

$$\langle \boldsymbol{G}(z)\rangle \approx \boldsymbol{G}_{\mathrm{coh}}(z) = \left[\boldsymbol{G}_0^{-1}(z) - \Sigma_{\mathrm{CPA}}(z)\mathbb{1}\right]^{-1}. \tag{7.64}$$

The CPA furnishes a translationally invariant, causal effective medium: the configuration-averaged propagator $\langle G(z)\rangle$ is analytic in the upper half-plane, with $\mathrm{Im}\ \Sigma(\omega + \mathrm{i}0^+) \leq 0$ ensuring a positive spectral density and conservation of single-particle spectral weight (state-counting sum rules). It reproduces the correct pure limits, reduces to VCA when fluctuations vanish, and captures disorder-induced lifetime effects and band broadening through the self-consistent $\Sigma(z)$. In multiple-scattering implementations

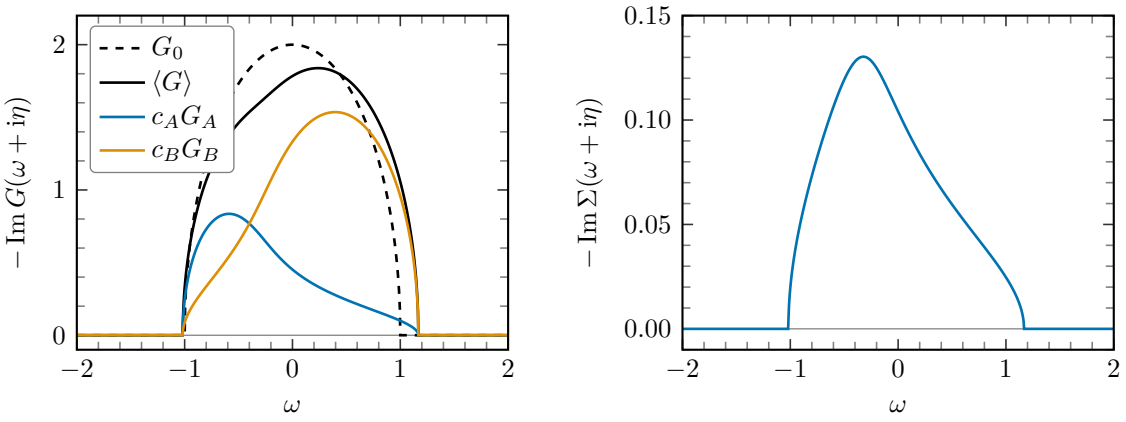

Figure 17: Self-consistent CPA results for a binary alloy with concentrations $c_A = 0.3$, $c_B = 0.7$ and disorder strengths $\Delta = 0.5$ on a Bethe lattice with half-bandwidth $D = 1$. Left: Spectral functions $-\operatorname{Im} G(\omega+i\eta)$ of the averaged Green's function $\langle G \rangle$ and the concentration-weighted component Green's functions $c_\alpha G_\alpha$. Right: Imaginary part of the CPA self-energy $\Sigma(\omega + i\eta)$. The complex broadening parameter is set to $\eta = 0.01$.

(KKR/EMTO) it is numerically efficient and for certain models it is even exact (e.g. the Lloyd model). Its principal limitation is the single-site nature of the effective medium: short-range order and multi-site (nonlocal) scattering correlations are neglected. Anderson localization and Lifshitz-tail phenomena are not captured (requiring typical-medium or cluster extensions), and off-diagonal (hopping) disorder lies outside the basic formalism unless one adopts the Blackman-Esterling-Berk generalization [120, 122]. For transport, single-site CPA supplies the disorder-broadened single-particle input but vertex corrections beyond the local approximation may be needed to capture coherent backscattering and related nonlocal effects [120, 122].

All formulas above generalize immediately to the case where each lattice site carries spin degrees of freedom and possibly n_{orb} orbitals. One simply promotes the local scalars to matrices acting in the combined local Hilbert space (orbital $\otimes$ spin). The coherent potential $\boldsymbol{\Sigma}(z)$ and the species potentials $\boldsymbol{V}_\alpha$ become matrices. In collinear spin calculations with spin-diagonal disorder one often has a block structure (independent $\uparrow$ / $\downarrow$ channels) and the CPA condition (7.60) applies separately to each spin channel.

Figure 17 shows typical CPA results for a binary alloy on a Bethe lattice with semicircular DOS with half-bandwidth $D = 1$. The disorder strength $\Delta = 0.5$, defining the difference between the two on-site potentials $v_a = -\Delta/2$ and $v_b = +\Delta/2$, is moderate compared to the bandwidth $W = 2D$, leading to band broadening and lifetime effects, but no splitting into separate impurity bands. The left panel shows the spectral functions (imaginary parts of the retarded Green's functions) of the coherent Green's function $\langle G \rangle$ and the concentration-weighted component Green's functions $c_\alpha G_\alpha$, which together sum up to the total average. The right panel shows the imaginary part of the CPA self-energy $\Sigma(\omega + i0^+)$, which defines the local effective medium and encodes the disorder-induced broadening and lifetime effects. The results presented in Fig. 17 were obtained using the iterative Green's function scheme in `TRIQS/CPA` [C1], a library I have developed for the `TRIQS` framework [C3]. It implements both root-finding and iterative CPA solvers, which we will discuss next.

7.7 Numerical solution of the CPA equations

The CPA condition (7.60) is a non-linear residual equation for the coherent potential $\Sigma(z) \equiv \Sigma_{\mathrm{CPA}}(z)$ at each complex energy z that must be solved numerically:

$$R[\Sigma] \equiv \sum_{\alpha=1}^{M} c_\alpha \frac{v_\alpha - \Sigma(z)}{1 - \Big(v_\alpha - \Sigma(z)\Big) G_{\mathrm{coh}}(z,\, \Sigma)} = 0. \tag{7.65}$$

Below we outline two practical and complementary approaches that have been found to be robust in alloy calculations [120, 122]: direct complex root-finding for $R[\Sigma] = 0$, and fixed-point iterations. Both require repeated evaluations of the local Green's function representing the unperturbed lattice. This involves performing a Brillouin-zone sum, which can be done by k-meshes, or a Hilbert transform of the unperturbed DOS $\rho_0(\varepsilon)$.

7.7.1 Root finding and Newton's method

To find the self-consistent CPA self-energy $\Sigma(z)$, the root of the residual function $R[\Sigma]$ from (7.65) must be located for every complex energy z of interest. For this, the Newton-Raphson method (or other modern alternatives) is very effective, which is a generalization of the well-known Newton's method for finding the roots of polynomial equations.

Consider the general problem of finding the roots of a scalar function: Given a continuous and differentiable function $f(x)$, we want to find x^* such that $f(x^*) = 0$. Assuming we have an initial guess x_0 close to the root, we can expand $f(x)$ in a Taylor series around x_0. Using the expansion up to first order, we have

$$f(x) \approx f(x_0) + f'(x_0)(x - x_0) = 0, \tag{7.66}$$

or equivalently,

$$x \approx x_0 - \frac{f(x_0)}{f'(x_0)}. \tag{7.67}$$

This gives us an iterative scheme to refine our guess for the root:

$$x_{n+1} = x_n - \frac{f(x_n)}{f'(x_n)}. \tag{7.68}$$

This process is repeated until convergence, i.e., until $|x_{n+1} - x_n|$ is smaller than a predefined tolerance. This method converges quadratically near the root if the initial guess is sufficiently close to avoid getting trapped in local minima, and if $f'(x)$ is non-zero at the root. Applying this to our CPA problem, we identify $f(x)$ with the residual function $R[\Sigma]$. An appropriate initial guess for $\Sigma(z)$ can be obtained from the VCA self-energy or from the converged Σ at nearby frequencies z.

In practice one can use any modern nonlinear solver on $\Sigma \in \mathbb{C} \simeq \mathbb{R}^2$: derivative-free methods like Nelder-Mead on $|R|^2$, quasi-Newton/trust-region (BFGS, TR), or secant methods all work well if supplied with a good initial guess [123–127]. When minimizing $|R|^2$, enforcing causality on the real axis as an inequality constraint $\mathrm{Im}\,\Sigma(\omega + \mathrm{i}0^+) \leq 0$ (e.g. via projection after each step) improves stability. Root finding methods are generally fast and robust, provided a good initial guess is available. However, they may

struggle with convergence if the initial guess is poor or if the function has multiple roots or is ill-conditioned. In our experience, for CPA calculations root-finding methods are very robust for moderate disorder strengths and concentrations away from the pure limits. However, close to the pure limits (e.g. $c_\alpha \to 0$ or 1) or for very strong disorder, the CPA equations become stiff and root-finding methods may struggle to converge.

7.7.2 Iterative Green's function scheme

Alternatively, the CPA self-consistency can be solved as a fixed-point problem for the coherent potential (self-energy) $\Sigma(z)$. A numerically robust realization closely parallels single-site DMFT: one alternates between constructing the translationally invariant coherent medium from a trial Σ and re-embedding physical atoms into that medium to update Σ. The scheme is outlined in Fig. 18. Starting from an initial guess $\Sigma^{(0)}(z)$ (e.g. Σ_{VCA}), we iterate the following steps. For a given $\Sigma^{(n)}(z)$, the coherent-medium Green's function is computed as

$$G_{\mathrm{coh}}(z,\, \Sigma^{(n)}) = \frac{1}{N_k} \sum_{\boldsymbol{k}} \frac{1}{z - \varepsilon_{\boldsymbol{k}} - \Sigma^{(n)}(z)}, \tag{7.69}$$

or via a Hilbert transform of the bare lattice DOS ρ_0:

$$G_{\mathrm{coh}}(z,\, \Sigma^{(n)}) = \int \mathrm{d}\varepsilon\, \frac{\rho_0(\varepsilon)}{z - \varepsilon - \Sigma^{(n)}(z)}. \tag{7.70}$$

Next, we define the Weiss (cavity) Green's function of the effective medium via the Dyson equation

$$\mathcal{G}_0^{-1}(z,\, \Sigma^{(n)}) \equiv G_{\mathrm{coh}}^{-1}(z,\, \Sigma^{(n)}) + \Sigma^{(n)}(z). \tag{7.71}$$

The Weiss (cavity) Green's function $\mathcal{G}_0(z)$ represents the propagator of the translationally invariant host as seen by a single embedded site, i.e. the "bare" propagator of the associated single-site impurity problem. Physically, $\mathcal{G}_0$ describes the propagation on a chosen site when the rest of the lattice is replaced by the translationally invariant effective medium (the "bath"); it thus contains all information about hybridization with the surrounding host, but no explicit on-site potential of the embedded atom. Inserting a real species α corresponds to adding the local perturbation v_α on top of this bath. With the local propagator of the effective medium at hand, we can proceed to embed the physical species α with on-site potential v_α into the host $\mathcal{G}_0$:

$$G_\alpha(z,\, \Sigma^{(n)}) = \Big[\mathcal{G}_0^{-1}(z,\, \Sigma^{(n)}) - v_\alpha\Big]^{-1} = \Big[G_{\mathrm{coh}}^{-1}(z,\, \Sigma^{(n)}) - (v_\alpha - \Sigma^{(n)}(z))\Big]^{-1}, \tag{7.72}$$

which is identical to the Dyson form used in Eq. (7.62), now evaluated in the host defined by $\Sigma^{(n)}$. The ensemble-averaged Green's function follows from the concentration average over species α:

$$\Big\langle G(z,\, \Sigma^{(n)}) \Big\rangle = \sum_\alpha c_\alpha\, G_\alpha(z,\, \Sigma^{(n)}). \tag{7.73}$$

Since the CPA fixed point is characterized by $\langle G \rangle = G_{\mathrm{coh}}$, we use the ensemble-averaged Green's function $\langle G \rangle$ as the new coherent Green's function to update the self-energy Σ via the inverse Dyson equation,

$$\Sigma^{(n+1)}(z) = \mathcal{G}_0^{-1}(z,\, \Sigma^{(n)}) - G_{\mathrm{coh}}^{-1}(z,\, \Sigma^{(n)}) = \mathcal{G}_0^{-1}(z,\, \Sigma^{(n)}) - \Big\langle G(z,\, \Sigma^{(n)}) \Big\rangle^{-1}. \tag{7.74}$$

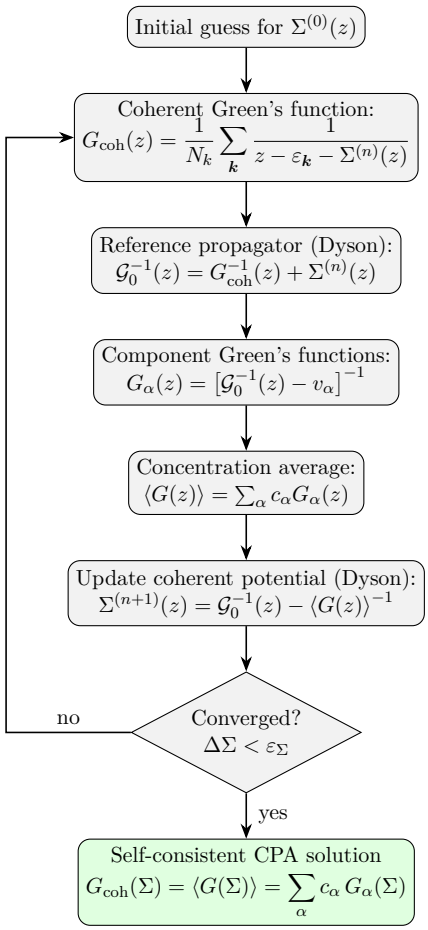

Figure 18: Iterative Green's-function scheme for the single-site CPA. Starting from $\Sigma^{(0)}(z)$, compute the medium Green's function, construct the reference propagator via Dyson, embed each component to obtain $G_\alpha(z)$, average over species, update Σ, (optionally mix), and iterate until the CPA condition $\langle G(\Sigma)\rangle = \sum_\alpha c_\alpha G_\alpha(\Sigma)$ is satisfied.

At this point one can also apply mixing schemes (e.g. simple linear mixing, Broyden, Anderson) to the update of the self-energy to improve convergence, as described in previous iterative methods. The new self-energy $\Sigma^{(n+1)}$ is then again inserted into Eq. (7.69) to recompute the coherent Green's function, and the process is repeated until convergence. When the iteration converges, the CPA condition (7.61),

$$\langle G(\Sigma)\rangle = G_{\mathrm{coh}}(\Sigma) = \sum_\alpha c_\alpha G_\alpha(\Sigma) \tag{7.75}$$

is satisfied.

The iterative Green's function scheme is generally robust and simple to implement. However, it may converge slowly, especially near critical points or phase transitions, and can be sensitive to the choice of initial guess and mixing parameters. Systems that converge poorly benefit from strong mixing, however this slows down convergence. In our experience, for CPA calculations the iterative Green's function scheme is very robust even for strong disorder and concentrations close to the pure limits, where root-finding methods may struggle.

8 Combining Electronic Correlations and Substitutional Disorder

The preceding sections have developed the separate pillars needed to address correlated, chemically disordered metals: density functional theory (DFT) as a first-principles baseline, the exact muffin-tin orbitals (EMTO) formalism as an efficient Green's-function-based realization of DFT for alloys, dynamical mean-field theory (DMFT) for local electronic correlations, and the coherent potential approximation (CPA) for substitutional disorder. What remains is to marry these ingredients into a single, operational framework capable of capturing both dynamical on-site self-energies and configurational averaging on equal footing. This chapter introduces and systematizes that merger in two steps: a model-level DMFT+CPA formulation, followed by its materials-realistic embedding, LDA(CPA)+DMFT.

8.1 DMFT+CPA: Local correlations and disorder

The aim of DMFT+CPA is to treat, on equal footing, two ubiquitous sources of complexity in real metals and alloys: local, dynamical electron-electron correlations and substitutional disorder. Historically, these ingredients were developed along largely independent tracks. The recognition that both CPA and DMFT are local, single-site, self-consistent theories made their merger natural for the Anderson-Hubbard problem: treat substitutional disorder at the CPA level while computing the species-resolved, dynamical on-site self-energies via DMFT. Early formulations along these lines established DMFT for interacting electrons in random media and charted the competition between interaction- and disorder-driven effects in infinite dimensions [128, 129]. In modern language, DMFT+CPA lets the CPA coherent medium act as the DMFT Weiss field for a set of species-resolved impurity problems. The resulting $\Sigma_\alpha(\mathrm{i}\omega_n)$ are fed back into the CPA condition (e.g., vanishing concentration-weighted T-matrix) to update the medium, closing a single, linked self-consistency. A parallel strand extended disordered DMFT to address Anderson localization physics that is not captured by arithmetic averaging: statistical DMFT and typical-medium ideas replace averages by geometric ("typical") quantities to build an order-parameter description of localization, and can be coupled to DMFT to study Mott-Anderson transitions [130–132]. While our work here adopts the conventional single-site DMFT+CPA level (local Σ, single-site disorder, no short-range order), this historical context clarifies the scope and natural extensions of the formalism.

8.1.1 Notation and basic definitions

We consider a substitutionally disordered lattice composed of alloy components (species) $\alpha \in \{A, B, \dots\}$ with concentrations c_α satisfying $\sum_\alpha c_\alpha = 1$. The approximation level is single-site for both correlation and disorder: the electronic self-energy is purely local and site-diagonal, and disorder is treated as single-site substitutional disorder without short-range order (conventional CPA). In this representation, the problem of interacting

disordered electrons can be viewed as a system of non-interacting electrons moving in a coherent medium with an additional, energy and species-dependent on-site potential given by the local DMFT self-energy $\Sigma_\alpha(z)$ of each species. The coherent self-energy $\Sigma_{\text{coh}}(z)$ can be interpreted as an effective local potential that captures both the average effect of disorder and the dynamical correlations through DMFT

$$\Sigma_{\text{coh}} \equiv \Sigma_{\text{coh}}[G_{\text{coh}}, \Sigma_\alpha], \tag{8.1}$$

where the ensemble averaged coherent Green's function G_{coh} depends on Σ_{coh} itself, as well as on the set of local self-energies Σ_α:

$$G_{\text{coh}} = \langle G(\Sigma_{\text{coh}}) \rangle \,. \tag{8.2}$$

An important difference to CPA is that the coherent self-energy $\Sigma_{\text{coh}}(z)$ and Green's function G_{coh} in DMFT+CPA encodes not only the configurational averaging of disorder but also incorporates the dynamical correlations through the DMFT self-energies. It should not be confused with the "plain" CPA effective medium.

The impurity problem for each species α is defined by embedding a site of that species into the effective medium and is given by the hybridization function (or equivalently the Weiss field) of the corresponding species α

$$\Delta_\alpha(z) = z + \mu - v_\alpha - \Sigma_{\text{coh}}(z) - G_\alpha^{-1}(z). \tag{8.3}$$

In comparison to plain DMFT discussed in Ch. 4, the key difference to Eq. (4.48) is that the lattice Green's function entering the hybridization is now the component-resolved propagator G_α. Solving the impurity problem for each species α yields the DMFT self-energy $\Sigma_\alpha(z)$ and the impurity Green's function $G_\alpha^{\text{imp}}(z)$, related by the impurity Dyson equation. The self-energies $\Sigma_\alpha(z)$ are then fed back into the CPA condition by including the DMFT self-energies $\Sigma_\alpha(z)$ for component α in the on-site potentials, resulting in the effective, energy dependent potentials

$$v_\alpha \to v_\alpha(z) = v_\alpha + \Sigma_\alpha(z). \tag{8.4}$$

The single-site scattering t-matrix for embedding a site of species α into the coherent medium, defined in Eq. (7.59), are then given by

$$t_\alpha(z) = \frac{v_\alpha(z) - \Sigma_{\text{coh}}(z)}{1 - (v_\alpha(z) - \Sigma_{\text{coh}}(z)) G_{\text{coh}}(z)} \tag{8.5}$$

with the CPA condition (7.60) now reading

$$\sum_\alpha c_\alpha \, t_\alpha(z) = \sum_\alpha c_\alpha \, \frac{v_\alpha(z) - \Sigma_{\text{coh}}(z)}{1 - (v_\alpha(z) - \Sigma_{\text{coh}}(z)) G_{\text{coh}}(z)} = 0 \,. \tag{8.6}$$

After convergence of CPA, the coherent Green's function is then given by

$$G_{\text{coh}}(z) = \langle G(\Sigma_{\text{coh}}) \rangle = \sum_\alpha c_\alpha \, G_\alpha(z) = \left[G_0^{-1}(z) - \Sigma_{\text{coh}}(z) \right]^{-1} , \tag{8.7}$$

with the component Green's functions introduced in Eq. (7.62) reading

$$G_\alpha(z) = \frac{G_{\text{coh}}(z)}{1 - (v_\alpha(z) - \Sigma_{\text{coh}}(z)) G_{\text{coh}}(z)}. \tag{8.8}$$

The propagator $G_0(z)$ defines the non-interacting and disorder-free reference system, given by the underlying lattice structure and the kinetic part of the Hamiltonian.

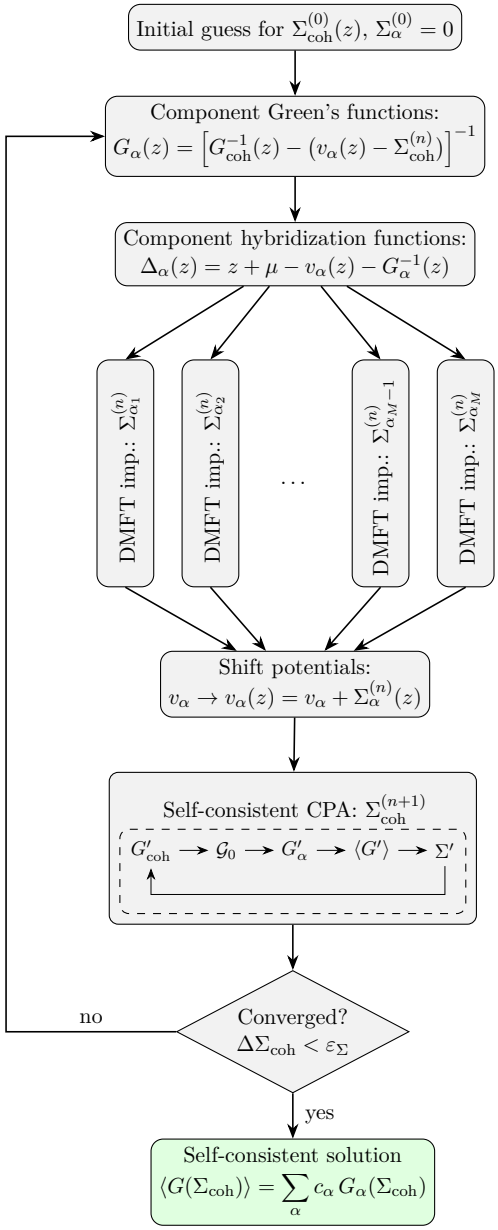

Figure 19: Self-consistency flow diagram for the combined DMFT+CPA scheme. The DMFT iterations for each component α run in parallel and yield the respective impurity self-energies Σ_α. These are used to shift the random potentials v_α before entering the CPA loop to obtain an updated coherent self-energy Σ_{coh}. The process is repeated until convergence is reached.

8.1.2 Combined self-consistency

The DMFT+CPA method links the two self-consistency loops of DMFT and CPA into a single, coupled cycle, as illustrated in Fig. 19. In practice, one solves the impurity problem defined by DMFT once per species α and iteration. The full DMFT self-consistency is considered as "outer" loop, while the CPA self-consistency is nested as an "inner" loop and solved for each main iteration. One could also compute a full self-consistent DMFT solution for each species α in every DMFT+CPA iteration, but

this would be computationally much more expensive: In general the time complexity for a single DMFT iteration is of the order of tens of minutes to hours, while the full CPA loop typically converges within seconds to minutes. Thus, we solve the CPA loop for each DMFT+CPA iteration until convergence to find the self-consistent coherent medium for the current set of impurity self-energies Σ_α and then update the hybridization functions Δ_α accordingly, solving the impurity problems once per iteration.

Depending on the specific impurity solver used, the axis of complex frequencies z can be either the imaginary Matsubara axis $z = \mathrm{i}\omega_n$ or the real-frequency axis $z = \omega + \mathrm{i}0^+$. In general, all quantities are computed on the chosen frequency axis throughout the DMFT+CPA loop. If needed, analytic continuation techniques can be applied to obtain real-frequency data from imaginary-axis results after convergence from the self-consistent solution is reached.

The DMFT+CPA iteration scheme can be summarized as follows:

1. An initial guess for the coherent self-energy $\Sigma_{\mathrm{coh}}^{(0)}(z)$ and for the impurity self-energies $\Sigma_\alpha^{(0)}(z) = 0$ is provided. The coherent self-energy typically is set to zero, while the impurity self-energies are initialized as in standard DMFT.

2. For each species α, the component Green's function is computed as

$$G_\alpha(z) = \left[G_{\mathrm{coh}}^{-1}(z) - \left(v_\alpha(z) - \Sigma_{\mathrm{coh}}^{(n)}(z) \right) \right]^{-1} .$$

3. The hybridization function for each species α is constructed via

$$\Delta_\alpha(z) = z + \mu - v_\alpha(z) - G_\alpha^{-1}(z) \,,$$

   defining the impurity problem for that species.

4. The impurity problem for each species α is solved to obtain the impurity self-energy $\Sigma_\alpha^{(n)}(z)$. In practice, this can be done in parallel for all species to reduce the wall-clock time.

5. After obtaining the component DMFT self-energies $\Sigma_\alpha^{(n)}(z)$, the on-site potentials are updated according to

$$v_\alpha \to v_\alpha(z) = v_\alpha + \Sigma_\alpha^{(n)}(z) \,.$$

6. The CPA problem is solved self-consistently for the current set of impurity self-energies $\Sigma_\alpha^{(n)}(z)$ embedded in the on-site potentials to obtain an updated coherent self-energy $\Sigma_{\mathrm{coh}}^{(n+1)}(z)$. This involves computing the single-site scattering t-matrices and enforcing the CPA condition

$$t_\alpha(z) = \frac{v_\alpha(z) - \Sigma_{\mathrm{coh}}^{(n)}(z)}{1 - (v_\alpha(z) - \Sigma_{\mathrm{coh}}^{(n)}(z)) G_{\mathrm{coh}}(z)}, \qquad \sum_\alpha c_\alpha \, t_\alpha(z) = 0 \,.$$

   The coherent self-energy can be optionally mixed with the previous iteration to improve convergence.

7. Check for convergence of the coherent self-energy $\Sigma_{\mathrm{coh}}^{(n+1)}(z)$. If the change with respect to the previous iteration is below a chosen threshold , i.e. $\Delta\Sigma_{\mathrm{coh}} < \varepsilon_\Sigma$, the self-consistent solution is reached. Otherwise, return to step 2 and repeat the process with the updated coherent self-energy $\Sigma_{\mathrm{coh}}^{(n+1)}(z)$.

After convergence, the coherent Green's function as well as the component Green's functions can be computed from the converged coherent self-energy $\Sigma_{\mathrm{coh}}(z)$.

The single-site DMFT+CPA construction is deliberately minimal: it captures frequency-dependent on-site renormalizations from interactions together with coherent configurational averaging from disorder, while discarding nonlocal self-energy effects and short-range order.

In the non-disordered limit, $c_A \to 1$ (or, equivalently, when all v_α and Σ_α coincide), the CPA constraint becomes trivial and the scheme reduces to standard single-site DMFT with hybridization $\Delta(z)$ determined solely by the lattice Hilbert transform. This is the $d \to \infty$ fixed point of local Fermi-liquid theory and obeys the familiar DMFT sum rules and causality constraints [74]. In the noninteracting limit, $U \to 0 \Rightarrow \Sigma_\alpha(z) \to 0$, Eq. (8.5) collapses to the conventional (dynamic) CPA t-matrix and the coherent propagator $G_{\mathrm{coh}}(z)$ coincides with the Herglotz analytic function fixed by the CPA condition [118].

A second set of constraints follows from analyticity and spectral sum rules. Because the impurity problems are causal and the CPA average preserves the Herglotz property, the local objects must satisfy $\mathrm{Im}\,\Delta(\mathrm{i}\omega_n) \leq 0$ and $\mathrm{Im}\,\Sigma_\alpha(\mathrm{i}\omega_n) \leq 0$ on the Matsubara axis, which guarantees a positive spectral function $A_\alpha(\omega) = -\,\mathrm{Im}\,G_\alpha(\omega + \mathrm{i}0^+)$. Numerically, violations of these inequalities indicate insufficient impurity convergence, inconsistent bath updates, or an unstable CPA solution. Enforcing monotone mixing in Δ and in Σ_{coh} typically restores causality. A further concentration sum rule follows from the definition $G_{\mathrm{coh}} = \sum_\alpha c_\alpha G_\alpha$: the coherent spectral function must equal the concentration-weighted sum of component spectra at every frequency.

8.2 The DFT(EMTO)+DMFT approach

We now turn to the materials-realistic embedding of DMFT+CPA within ab initio DFT methods. A natural choice for this purpose is the exact muffin-tin orbitals (EMTO) method, discussed in Chapter 3. The advantage of EMTO in a DMFT+CPA context is that EMTO is a Green's-function multiple-scattering method: All central objects of DMFT+CPA are native to the EMTO formalism and need no downfolding or Wannierization. In practice this removes an entire layer of approximation and workflow complexity. The correlated subspace is defined directly in the EMTO single-site basis, the local impurity self-energy is embedded as a purely on-site, energy-dependent term in the same basis, and the CPA step is just the standard single-site scattering problem with the on-site potential shifted by the DMFT self-energy. Because EMTO already computes $\boldsymbol{k}$-resolved and on-site Green's functions on a complex-energy contour, the construction of local propagators, coherent Green's functions, and concentration averages proceeds without auxiliary projections, disentanglement windows, or gauge choices that are otherwise required by Wannier methods.

This tight fit has concrete numerical benefits. First, species resolution and configurational averaging are intrinsic: single-site scattering and the coherent potential function

are the native language of EMTO-CPA, so the CPA condition $\sum_\alpha c_\alpha t_\alpha(z) = 0$ is solved in the same basis in which the self-energy acts. Second, locality is guaranteed by construction: the path operator provides site-diagonal Green's functions, ensuring that the DMFT impurity problem is exactly matched to the lattice object it must reproduce at self-consistency. Third, charge self-consistency is straightforward: the densities and total energies are already formulated from the scattering path operator, so incorporating correlations modifies these quantities without changing the underlying EMTO machinery. Analytic continuation is confined to the impurity step.

Conceptually, EMTO avoids two common pitfalls of projector-based embeddings in plane-wave or localized-orbital DFT. There is no ambiguity associated with band disentanglement or the spread/gauge of Wannier functions, the correlated orbitals coincide with the single-site scattering channels used to build the one-electron Green's function. Likewise, the double-counting term is defined in the same local block that enters the EMTO single-site problem, simplifying both its implementation. These features explain why the earliest ab initio DMFT embeddings for disordered metals were developed within EMTO/KKR, and why modern EMTO(CPA)+DMFT studies can operate with a compact, reproducible self-consistency loop that stays entirely within the Green's-function language [63, 133–135].

In the EMTO formalism the many-body/disorder embedding is most transparent when one starts from the spin-resolved DFT Green's function matrix $G^\sigma_{RL,R'L'}(\boldsymbol{k}, z)$ expressed in the EMTO basis, introduced in Eq. (3.51), and adds correlation and disorder effects as strictly local on-site terms. The EMTO(CPA)+DMFT lattice Green's function is connected to the one-electron propagator by a Dyson equation written in the EMTO indices,

$$\Big[G^\sigma_{RL,R'L'}(\boldsymbol{k}, z)\Big]^{-1} = \Big[G^{\sigma,\mathrm{DFT}}_{RL,R'L'}(\boldsymbol{k},\, z)\Big]^{-1} - \tilde{\Sigma}^\sigma_{RL,RL'}(z)\,\delta_{RR'}\,, \tag{8.9}$$

where $\tilde{\Sigma}^\sigma_{RL,RL'}(z)$ acts in the chosen correlated subspace (typically a block of d-orbitals) and is taken site-diagonal in the single-site scheme. The corresponding bath Green's function $G^{\sigma,R}_{LL'}(z)$ is obtained from the k-integrated interacting propagator,

$$\Big[G^{\sigma,R}_{LL'}(z)\Big]^{-1} = \Big[G^\sigma_{LL'}(z)\Big]^{-1} + \tilde{\Sigma}^\sigma_{LL'}(z)\,, \tag{8.10}$$

with $G^\sigma_{LL'}(z) \equiv \int_{\mathrm{BZ}} G^\sigma_{RL,R'L'}(\boldsymbol{k},\, z)\,\mathrm{d}\boldsymbol{k}$ the site-diagonal part. Equations (8.9) to (8.10) define the impurity problem seen by the local correlated orbitals. In practice, the many-body problem for $\tilde{\Sigma}^\sigma$ is solved on the Matsubara axis $\omega_n = (2n+1)\pi T$ and mapped to the complex contour used in EMTO by Padé continuation, as in the standard EMTO+DMFT workflow [133]. Since here the continuation between Matsubara frequencies and the real axis has to be computed in each DMFT+CPA iteration, it is crucial to use a robust and efficient continuation method with preferably a non-stochastic impurity solver, such as the spin-polarized T-matrix fluctuation-exchange (SPTF) approximation discussed in Ch. 5, to avoid noisy data [134, 135].

To include substitutional disorder at the single-site level, we formulate the coherent-medium condition of CPA in the same EMTO basis. Let $v^\sigma_{\alpha;LL'}$ denote the static on-site term of species α (from the EMTO single-site potential) and $\tilde{\Sigma}^\sigma_{\alpha;LL'}(z)$ the species-resolved local DMFT self-energy obtained from the impurity problem defined by the

effective medium. The coherent medium is represented by a site-diagonal, energy-dependent on-site term $\Sigma^{\sigma}_{\mathrm{coh};LL'}(z)$ that, together with the EMTO Hilbert transform, generates the on-site locator of the medium,

$$\bar{G}^{\sigma}_{LL'}(z) = \int_{\mathrm{BZ}} \left[\left(G^{\sigma,\mathrm{DFT}}(\boldsymbol{k},\, z) \right)^{-1} - \Sigma^{\sigma}_{\mathrm{coh}}(z) \right]^{-1}_{LL'} \mathrm{d}\boldsymbol{k} = \left[G^{\sigma}_{0}(z)^{-1} - \Sigma^{\sigma}_{\mathrm{coh}}(z) \right]^{-1}, \quad (8.11)$$

where $G^{\sigma}_{0}(z)$ is the site-diagonal locator of the disorder-free DFT reference delivered by EMTO. Embedding a site of species α into the coherent medium produces the single-site scattering matrix (now including dynamical on-site terms),

$$t^{\sigma}_{\alpha}(z) = \left[\mathbb{1} - \left(v^{\sigma}_{\alpha}(z) - \Sigma^{\sigma}_{\mathrm{coh}}(z) \right) G^{\sigma}_{0}(z) \right]^{-1} \left(v^{\sigma}_{\alpha}(z) - \Sigma^{\sigma}_{\mathrm{coh}}(z) \right), \quad (8.12)$$

and the CPA condition again demands vanishing concentration-weighted scattering,

$$\sum_{\alpha} c_{\alpha} t^{\sigma}_{\alpha}(z) = 0. \quad (8.13)$$

Equations (8.11) to (8.13) determine $\Sigma^{\sigma}_{\mathrm{coh}}(z)$ for a given set of impurity self-energies $\{\tilde{\Sigma}^{\sigma}_{\alpha}(z)\}$, which are added to the static on-site potentials $v^{\sigma}_{\alpha;LL'}$ to form the effective, energy-dependent potentials $v^{\sigma}_{\alpha}(z) = v^{\sigma}_{\alpha} + \tilde{\Sigma}^{\sigma}_{\alpha}(z)$. The component Green's functions that enter both CPA averaging and the impurity update are then computed site-diagonally as

$$G^{\sigma}_{\alpha}(z) = \left[G^{\sigma}_{\mathrm{coh}}(z)^{-1} - \left(v^{\sigma}_{\alpha}(z) - \Sigma^{\sigma}_{\mathrm{coh}}(z) \right) \right]^{-1}, \qquad G^{\sigma}_{\mathrm{coh}}(z) = \sum_{\alpha} c_{\alpha}\, G^{\sigma}_{\alpha}(z)\,, \quad (8.14)$$

and the species-resolved impurity problems are defined so that $G^{\mathrm{imp},\sigma}_{\alpha}(z) \equiv G^{\sigma}_{\alpha}(z)$ at self-consistency. This keeps the clear separation of roles already emphasized: CPA averages lattice objects in the EMTO basis, while DMFT is solved per species and supplies $\tilde{\Sigma}^{\sigma}_{\alpha}$.

The formulation above mirrors established EMTO/KKR realizations of CPA+DMFT: the multiple-scattering embedding of the dynamical self-energy and its interplay with the single-site CPA condition were set out in early EMTO+DMFT and KKR+DMFT papers [133, 134]. Explicit EMTO(CPA)+DMFT implementations and practical self-consistency strategies (separate mixing of the coherent medium and impurity self-energies, shared bath structure) were documented in later work [135].

In the appropriate limits the EMTO-embedded scheme reduces to well-known baselines, providing immediate consistency checks analogous to Sec. 8.1.

9 Analytical continuation

Many numerical approaches in condensed matter physics natively produce data on the imaginary Matsubara frequency axis, $z = \mathrm{i}\omega_n$, due to difficulties of performing correlated finite-temperature calculations directly on the real-frequency axis. This, for example, includes quantum Monte Carlo methods, which sample imaginary-time correlation functions that are then Fourier-transformed to imaginary frequencies, or many other impurity solvers used in dynamical mean-field theory. Spectral and transport observables, however, require real frequencies via the retarded Green's function $G(\omega + \mathrm{i}0^+)$ and the spectral function $A(\omega) = -\frac{1}{\pi}\operatorname{Im} G(\omega + \mathrm{i}0^+)$.

Originating from the mathematical field of complex analysis, the formal goal of analytical continuation is the extension of the domain of definition of a given analytical function. In condensed matter physics, analytical continuation typically refers to the numerical transformation between the imaginary-frequency Green's function and the real-frequency Green's function or spectral function. However, other quantities, such as self-energies or response functions, can also be analytically continued. Analytical continuation is fundamentally an *ill-posed* problem: small fluctuations (round-off, Monte-Carlo noise, etc.) on one axis can produce arbitrarily large changes on the other axis. As a result, the solution also may be non-unique without additional constraints (e.g., positivity, sum rules, smoothness), and, even when a solution exists in the exact, noiseless limit, numerical formulations do not guarantee that a unique solution can be found.

In the following, we will briefly review the mathematical foundations of analytical continuation and discuss two widely used numerical techniques: Padé approximants [136, 137] and the Maximum Entropy Method [138–140].

9.1 Cauchy formula and contour transforms

For imaginary times $\tau \in [0, \beta)$ one may express the fermionic Green's function as a contour integral that encircles the Matsubara poles of the thermal distribution, which is a form of Cauchy's integral formula,

$$G(\tau) = \frac{1}{\beta}\sum_{n=-\infty}^{\infty} G(\mathrm{i}\omega_n)\mathrm{e}^{-\mathrm{i}\omega_n\tau} = \frac{1}{2\pi\mathrm{i}}\oint_{\mathcal{C}} \mathrm{d}z\, G(z)\,[1 - f(z)]\,\mathrm{e}^{-z\tau}, \tag{9.1}$$

where $f(z) = 1/[\mathrm{e}^{\beta z}+1]$ is the Fermi function, with the fermionic Matsubara frequencies $\omega_n = (2n+1)\pi/\beta$. A similar expression holds for bosonic Green's functions, with the Bose function $b(z) = 1/[\mathrm{e}^{\beta z} - 1]$ and bosonic Matsubara frequencies $\nu_n = 2n\pi/\beta$. We will only discuss the fermionic case; the bosonic case is analogous. For the imaginary Matsubara frequencies the natural singularities lie on the imaginary axis: the Fermi distributions have simple poles at $z = \mathrm{i}\omega_n$, and $G(\mathrm{i}\omega_n)$ is analytic away from the real axis.

To turn the Matsubara sum in (9.1) into a contour integral by residues it is therefore convenient to take the contour $\mathcal{C}$ to run parallel to the imaginary axis, enclosing the thermal poles at $z = \mathrm{i}\omega_n$. Since $G(z)$ is analytic off the real axis but has its branch cut

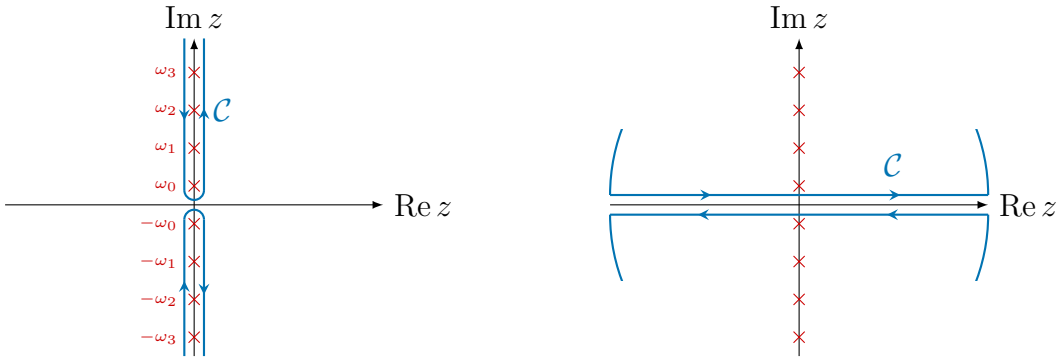

Figure 20: Contour deformation for analytical continuation. The original contour (left) encloses Matsubara poles along the imaginary axis. It is cut into two pieces $\mathcal{C}_+$ and $\mathcal{C}_-$ to avoid the branch cut on the real axis. The contour is then deformed (right) to run parallel to the real axis, enclosing all Matsubara poles in half circles in the upper and lower half planes. In the limit $R \to \infty$, the contributions from the arcs vanish, leaving only the boundary values on the real axis.

on the real line, we cut this vertical contour at $\mathrm{Re}\, z = 0$ and write it as the union of two pieces,

$$\mathcal{C} = \mathcal{C}_+ \cup \mathcal{C}_-, \qquad \mathcal{C}_+ : \ \mathrm{Im}\, z \in (0^+, \infty), \quad \mathcal{C}_- : \ \mathrm{Im}\, z \in (-\infty, -0^+), \tag{9.2}$$

so that each segment can be closed without crossing the real-axis cut, as shown on the left of Fig. 20.

Both pieces of the contour can now be deformed into paths that run parallel to the real axis plus a large half-circle of radius R in the upper/lower half plane connecting the endpoints at $\pm\infty \pm \mathrm{i}0^+$, while ensuring that all Matsubara poles remain enclosed (Fig. 20, right). The contributions from the arcs vanish as $R \to \infty$ under the standard conditions that the Green's function decays as $G(z) \sim 1/z$ for $|z| \to \infty$ and that the time-domain kernel $\mathrm{e}^{-z\tau}$ with $\tau \in [0, \beta)$ provides exponential damping whenever $\mathrm{Re}\, z > 0$. Thus, only the two straight legs along $\mathbb{R} \pm \mathrm{i}0^+$ survive, producing the boundary values $G(\omega \pm \mathrm{i}0^+)$ over the real axis:

$$G(\tau) = \int_{-\infty}^{\infty} \mathrm{d}\omega\, [1 - f(\omega)]\, \mathrm{e}^{-\omega\tau} \frac{G(\omega + \mathrm{i}0^+) - G(\omega - \mathrm{i}0^+)}{2\pi\mathrm{i}}, \tag{9.3}$$

where the negative sign arises from the clockwise orientation of the lower contour piece. The boundary values $G(\omega + \mathrm{i}0^+)$ and $G(\omega - \mathrm{i}0^+)$ are called the retarded and advanced Green's functions, respectively, and their difference across the branch cut defines the spectral function,

$$A(\omega) = \frac{G(\omega - \mathrm{i}0^+) - G(\omega + \mathrm{i}0^+)}{2\pi\mathrm{i}}. \tag{9.4}$$

Introducing the analytical continuation kernel

$$K(\tau, \omega) = [1 - f(\omega)]\, \mathrm{e}^{-\omega\tau} = \frac{\mathrm{e}^{-\omega\tau}}{1 + \mathrm{e}^{-\beta\omega}}, \tag{9.5}$$

we obtain the expression

$$G(\tau) = -\int_{-\infty}^{\infty} \mathrm{d}\omega\, K(\tau, \omega)\, A(\omega). \tag{9.6}$$

Note that the spectral function can also be obtained from either the retarded or advanced Green's function alone:

$$A(\omega) = \frac{G(\omega - \mathrm{i}0^+) - G(\omega + \mathrm{i}0^+)}{2\pi\mathrm{i}} = -\frac{1}{\pi}\,\mathrm{Im}\,G(\omega + \mathrm{i}0^+) = \frac{1}{\pi}\,\mathrm{Im}\,G(\omega - \mathrm{i}0^+), \quad (9.7)$$

since $G(\omega - \mathrm{i}0^+) = G^*(\omega + \mathrm{i}0^+)$ for real ω. Because $K(\tau, \omega)$ decays exponentially at large $|\omega|$, the high-frequency tail of $A(\omega)$ contributes weakly to $G(\tau)$, underscoring the ill-conditioned nature of the inverse problem. Similarly, an identity for the Matsubara Green's function can be derived,

$$G(\mathrm{i}\omega_n) = \frac{1}{2\pi\mathrm{i}} \oint_{\mathcal{C}} \mathrm{d}z\, \frac{G(z)}{z - \mathrm{i}\omega_n} = -\int_{-\infty}^{\infty} \mathrm{d}\omega\, \frac{A(\omega)}{\omega - \mathrm{i}\omega_n} = \int_{-\infty}^{\infty} \mathrm{d}\omega\, K(\mathrm{i}\omega_n, \omega)\, A(\omega), \quad (9.8)$$

with the kernel

$$K(\mathrm{i}\omega_n, \omega) = \frac{1}{\mathrm{i}\omega_n - \omega}, \quad (9.9)$$

which decays only algebraically at large $|\omega|$.

9.2 Padé approximants

One of the earliest and most straightforward methods for analytical continuation is the Padé approximant technique, which approximates the Green's function $G(z)$ by a rational polynomial. This analytic function can then be evaluated anywhere in the upper complex plane, including on the real axis. Its appeal is that rational functions can approximate analytic functions with branch cuts using dense interlacing poles and zeros, often yielding sharp features without explicit regularization [136, 137]. The Padé approximant is a ratio of two polynomials p and q of order N and M, respectively,

$$P_{N/M}(z) = \frac{p_N(z)}{q_M(z)} = \frac{a_0 + a_1 z + a_2 z^2 + \cdots + a_N z^N}{b_0 + b_1 z + b_2 z^2 + \cdots + b_M z^M} \approx G(z). \quad (9.10)$$

Since Green's functions typically decay as $1/z$ for $|z| \to \infty$, one usually chooses $M = N + 1$ to enforce the correct asymptotic behavior. The order M of the denominator polynomial determines the number of poles of the approximant, while the order N of the numerator polynomial determines the number of zeros. The coefficients a_i and b_i are determined by fitting the Padé approximant to the sampled Green's function values $G(z_i)$ at a chosen set of points z_i.

9.2.1 Thiele's reciprocal difference method

In 1909, Thiele introduced a continued-fraction construction for rational interpolation [141]. Given a set of K data points $\{(z_i, f_i)\}_{i=1}^{K}$, the Padé approximant $P_{N/M}(z)$ with $N + M + 1 = K$ that exactly matches the data at these points, $P_{N/M}(z_i) = f_i$, can be built as a continued fraction,

$$P_{N/M}(z) = \cfrac{c_1}{1 + \cfrac{c_2(z - z_1)}{1 + \cfrac{c_3(z - z_2)}{1 + \ddots}}}. \quad (9.11)$$

This construction is the basis for the reciprocal difference method [136, 137], which calculates an approximant of degrees $N = \frac{K}{2}$ and $M = \frac{K}{2} - 1$ interpolating the Green's function values exactly at K sample points z_i:

$$P_{N/M}(z_i) = G(z_i), \quad i = 1, 2, \ldots, K, \tag{9.12}$$

yielding a N-point Padé approximant. The coefficients a_i are computed recursively from the sampled values $G(z_i)$ via

$$a_n = g_n(z_n) \tag{9.13}$$

with the functions $g_n(z)$ defined recursively as

$$g_n(z) = \frac{g_{n-1}(z_{n-1}) - g_{n-1}(z)}{(z - z_{n-1})\, g_{n-1}(z)}, \tag{9.14}$$

and $g_0(z) = G(z)$. The rational polynomial fit $f_n(z)$ at iteration step n is then given by

$$f_n(z) = \frac{p_n(z)}{q_n(z)}, \tag{9.15}$$

where the polynomials $p_n(z)$ and $q_n(z)$ are defined recursively as

$$p_n(z) = p_{n-1}(z) + (z - z_{n-1}) a_n p_{n-2}(z), \tag{9.16a}$$
$$q_n(z) = q_{n-1}(z) + (z - z_{n-1}) a_n q_{n-2}(z), \tag{9.16b}$$

with initial conditions

$$p_{-1}(z) = 0, \quad p_0(z) = a_0, \quad q_{-1}(z) = 1, \quad q_0(z) = 1. \tag{9.17}$$

The fit function f_{2n+1} with an odd number of points is a Padé approximant of order $P_{n/n+1}$, while f_{2n} with an even number of points is of order $P_{n/n}$. For Green's functions, one typically uses an odd number of points to ensure the correct asymptotic behavior, as described above. Since the reciprocal difference method is an exact interpolation of the K data points, it is sensitive to noise in the sampled input data $G(z_i)$, which can lead to spurious poles and zeros.

9.2.2 Matrix formulation of Padé approximants

An alternative approach to constructing Padé approximants is to formulate the problem as a linear system of equations [136]. Given a rational polynomial function $f(z)$ approximating $G(z)$,

$$f(z) \approx \frac{p_N(z)}{q_M(z)}, \tag{9.18}$$

we can linearize the problem by multiplying both sides by the denominator,

$$f(z)\, q_M(z) \approx p_N(z). \tag{9.19}$$

Sampling this expression at K points z_i leads to a system of K equations, which can be written in matrix form as

$$\boldsymbol{FQ} = \boldsymbol{P}. \tag{9.20}$$

We write this matrix equation using diagonal matrices: The matrix $\boldsymbol{F}$ contains the function values $F_{ij} = f(z_i)\delta_{ij}$, and the matrices $\boldsymbol{P}$ and $\boldsymbol{Q}$ contain the polynomials $P_{ij} = p(z_i)\delta_{ij}$ and $Q_{ij} = q(z_i)\delta_{ij}$ evaluated at the sample points z_i. Introducing the Vandermonde matrices $\boldsymbol{V}$ for the polynomials, Eq. (9.20) can be rewritten as

$$\boldsymbol{F}\,\boldsymbol{V}_q\,\boldsymbol{q} = \boldsymbol{V}_p\,\boldsymbol{p}, \tag{9.21}$$

where the vectors $\boldsymbol{p} = (a_0, a_1, \ldots, a_N)^T$ and $\boldsymbol{q} = (b_0, b_1, \ldots, b_M)^T$ contain the polynomial coefficients. Vandermonde matrices contain powers of the sample points z_i as entries,

$$\boldsymbol{V} = \begin{pmatrix} 1 & z_1 & z_1^2 & \cdots & z_1^N \\ 1 & z_2 & z_2^2 & \cdots & z_2^N \\ 1 & z_3 & z_3^2 & \cdots & z_3^N \\ \vdots & \vdots & \vdots & \ddots & \vdots \\ 1 & z_K & z_K^2 & \cdots & z_K^N \end{pmatrix}, \qquad V_{ij} = z_i^{j-1}, \tag{9.22}$$

so that the polynomial evaluations can be expressed as matrix-vector products,

$$p(z_i) = \sum_{j=0}^{N} a_j z_i^j = (\boldsymbol{V}_p\,\boldsymbol{p})_i, \qquad q(z_i) = \sum_{j=0}^{M} b_j z_i^j = (\boldsymbol{V}_q\,\boldsymbol{q})_i. \tag{9.23}$$

Therefore, the matrices $\boldsymbol{V}_p$ and $\boldsymbol{V}_q$ have dimensions $K \times (N+1)$ and $K \times (M+1)$, respectively. Equation (9.21) can be rearranged to a homogeneous system of equations,

$$\boldsymbol{0} = \begin{pmatrix} \boldsymbol{F}\,\boldsymbol{V}_q & \boldsymbol{V}_p \end{pmatrix} \begin{pmatrix} \boldsymbol{q} \\ -\boldsymbol{p} \end{pmatrix} \equiv \boldsymbol{M}\,\boldsymbol{x}, \tag{9.24}$$

The homogeneous system $\boldsymbol{M}\,\boldsymbol{x} = \boldsymbol{0}$ in principle can be solved for the coefficient vector $\boldsymbol{x}$, which contains the coefficients $\{a_i\}$ and $\{b_i\}$ by finding the right null space of the matrix $\boldsymbol{M}$. Numerically, this can be achieved by computing the singular value decomposition (SVD) of $\boldsymbol{M}$

$$\boldsymbol{M} = \boldsymbol{U}\,\Sigma\,\boldsymbol{V}^\top, \tag{9.25}$$

and taking the right singular vector $\boldsymbol{V}_i^\top$ corresponding to the smallest singular value as the solution. Once the coefficient vector $\boldsymbol{x}_i = (\boldsymbol{q}, -\boldsymbol{p})_i^\top$ is determined, the Padé approximant can be evaluated as

$$f(z) = \frac{p_N(z)}{q_M(z)} = \frac{\sum_{j=0}^{N} a_j z^j}{\sum_{j=0}^{M} b_j z^j}, \qquad G(z) \approx f(z). \tag{9.26}$$

The matrix Padé fit trades analytic assumptions (rationality) for numerical stability and speed. On high-quality, low-noise Matsubara data it can resolve sharp structures that are often smoothed by other methods. On noisy data, weighting, symmetry constraints, and subset averaging are crucial to avoid spurious poles and zeros.

9.2.3 Padé continuation under controlled imaginary-axis noise

To assess how noise degrades the robustness of Padé analytic continuation, we adopt a controlled perturbation of the Matsubara Green's function. Let $G(\mathrm{i}\omega_n)$ denote the exact data and define the noisy inputs by

$$\tilde{G}(\mathrm{i}\omega_n) = G(\mathrm{i}\omega_n) + \delta G(\mathrm{i}\omega_n), \tag{9.27}$$

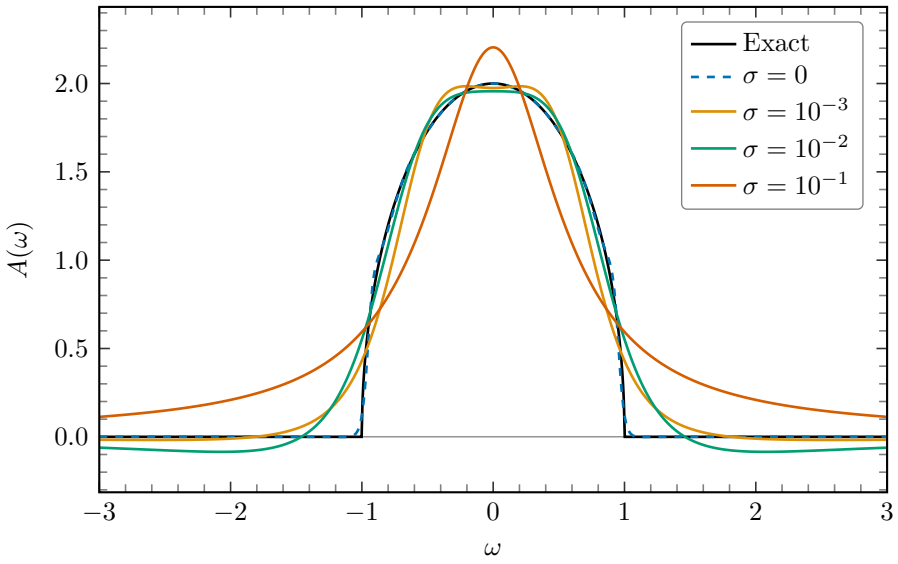

Figure 21: Spectral function $A(\omega) = -\operatorname{Im} G(\omega+\mathrm{i}\eta)$ obtained via Padé analytic continuation of Matsubara data for a semicircular density of states (Bethe lattice, half-bandwidth $D = 1$) at inverse temperature $\beta = 20$. The input Green's function is perturbed by zero-mean, Gaussian distributed complex noise with a standard deviation of σ. For comparison, the exact real-axis spectral function is shown. A uniform broadening $\eta = 10^{-4}$ is used both in the real-frequency evaluation and in the evaluation of the Padé approximants.

where δG is a zero-mean complex random variable at each Matsubara frequency, drawn from a normal (Gaussian) distribution with standard deviation σ, so that $\langle \delta G(\mathrm{i}\omega_n) \rangle = 0$ and σ sets the overall noise amplitude. Continuations are computed with the reciprocal-difference Padé scheme, and Fig. 21 reports results upon increasing σ. The underlying Matsubara Green's function corresponds to a semicircular density of states (Bethe lattice) with half-bandwidth $D = 1$ at inverse temperature $\beta = 20$, and Padé approximants are constructed from $K = 128$ Matsubara points using the implementation of the `TRIQS` library [C3].

As discussed earlier, Padé continuation notoriously amplifies noise: even small perturbations in $\tilde{G}$ can seed near-cancelling pole-zero pairs that manifest as spurious, narrow features on the real axis. With growing σ we observe characteristic signatures of this instability in the continued-fraction representation: additional peaks and dips emerge in the spectral function as spurious poles and zeros approach the real axis, causality violations appear in regions where $A(\omega) = -\operatorname{Im} G(\omega + \mathrm{i}0^+) < 0$ and deviations of spectral moments increase, indicating a progressive loss of high-frequency fidelity.

In the noise-free limit ($\sigma = 0$), the Padé reconstruction reproduces the target spectrum accurately (see dashed blue line in Fig. 21). Only a slight η-broadening and mild finite-K artifacts remain, reflecting the finite imaginary-axis sampling rather than genuine continuation errors.

9.3 The maximum entropy method

The Maximum Entropy Method (MaxEnt or MEM) is a widely used Bayesian framework for performing analytical continuation of noisy data, usually sampled from quantum Monte Carlo simulations. We will briefly outline the main concepts of MaxEnt following the pedagogical review by Jarrell [140]. For a more detailed discussion, we also refer the reader to Refs. [138, 139].

Given a set of $i = 1, \ldots, N$ noisy data points $\tilde{G}_l^i$ sampled at $l = 1, \ldots, L$ imaginary times τ_l or Matsubara frequencies $\mathrm{i}\omega_l$, the expectation value of the Green's function is given by

$$G_l \equiv \langle \tilde{G}_l \rangle = \frac{1}{N} \sum_{i=1}^{N} \tilde{G}_l^i. \tag{9.28}$$

Since many spectral functions $A(\omega)$ can reproduce the same $\tilde{G}_l$ via the integral equation (9.6) or its Matsubara counterpart (9.8), the MaxEnt method selects the most probable spectral function given the data by maximizing the probability given by Bayes' theorem,

$$P(A \,|\, G) = \frac{P(G \,|\, A)\, P(A)}{P(G)}, \tag{9.29}$$

where $P(G \,|\, A)$ is the likelihood of observing the data G given a spectral function A, $P(A)$ is the prior probability of the spectral function, and $P(G)$ is a normalization constant.

9.3.1 Prior probability and entropy

The prior probability $P(A)$ encodes any prior knowledge or assumptions about the spectral function. This probability is assumed to be proportional to the exponential of an entropy functional $S[A]$,

$$P(A) \propto \exp\Big(\alpha\, S[A]\Big), \tag{9.30}$$

where α is a regularization parameter that controls the relative weight of the entropy compared to the likelihood [142]. A common choice for the entropy is to use the Shannon-Jaynes entropy [143] to quantify the amount of information contained in the spectral function relative to a default model $m(\omega)$,

$$S[A,\, m] = \int_{-\infty}^{\infty} \mathrm{d}\omega \left[A(\omega) - m(\omega) - A(\omega) \ln \frac{A(\omega)}{m(\omega)} \right] \approx \sum_{j=1}^{N_\omega} \left[A_j - m_j - A_j \ln \frac{A_j}{m_j} \right], \tag{9.31}$$

where $A_i = A(\omega_i)\Delta\omega_i$. The default model $m(\omega) > 0$ represents our prior knowledge about the spectral function, such as its overall shape, width, or asymptotic behavior. Thus, the prior probability can be written as

$$P(A \,|\, m, \alpha) = \exp(\alpha\, S[A,\, m]). \tag{9.32}$$

This form implements a set of desirable and physically motivated properties for the prior over positive spectra $A(\omega) \geq 0$: $S[A, m]$ is maximized at $A(\omega) = m(\omega)$ and decreases when A departs from m. In the absence of informative data the posterior peaks at the default model. Because the functional is defined only for $A(\omega)$, $m(\omega) > 0$,

the prior assigns zero weight to non-physical (negative) spectra, enforcing the $A \geq 0$ constraint implicitly. Writing the entropy in terms of the measures $A(\omega)\mathrm{d}\omega$ and $m(\omega)\mathrm{d}\omega$ makes S invariant under smooth changes of variables and under rebinning of the frequency grid. If one merges or subdivides bins while preserving the integrated weights A_i, m_i, the discrete sum approximates the same continuum functional. If A and m are expressed in different but consistent units (common multiplicative factor), $S[A, m]$ changes only by an additive constant independent of A. The prior depends on the shape of A relative to m, not on arbitrary unit choices. If the frequency axis decomposes into disjoint windows with independent information, the total entropy is the sum of the entropies on each window. This ensures that independent pieces of the spectrum contribute independently to the prior.

The hyperparameter $\alpha > 0$ sets the trade-off between entropy (proximity to the default) and data fit (likelihood). Small α yields data-dominated, possibly noisy spectra, large α returns spectra close to $m(\omega)$. Practical choices of α (classic "historic" criterion vs. Bryan's evidence-based averaging) will be discussed later together with the stationarity equations and SVD implementation. For the present purpose, the form $P(A \,|\, m, \alpha) \propto \mathrm{e}^{\alpha S}$ is adopted because it encodes positivity, invariance, additivity, uniqueness, and a controlled, quadratic preference for simplicity – precisely the features one desires in regularizing the ill-posed continuation problem.

9.3.2 Likelihood function

The likelihood function $P(G \,|\, A)$ quantifies the probability of observing the data G given a spectral function A. Assuming that the data points $\tilde{G}_l$ are normally distributed around their expectation values G_l with covariance matrix $C_{ll'}$, the likelihood can be expressed as

$$P(G \,|\, A) = \exp\left(-\frac{1}{2}\chi^2[A]\right), \tag{9.33}$$

where the chi-squared functional $\chi^2[A]$ measures the discrepancy between the data and the model predictions,

$$\chi^2[A] = \sum_l \left(\frac{G_l - G_l[A]}{\sigma_l}\right)^2. \tag{9.34}$$

Here, $G_l[A]$ is the exact Green's function computed from the spectral function $A(\omega)$ via the integral equation (9.6) or (9.8). The variance σ_l is given by the diagonal elements of the covariance matrix, $\sigma_l^2 = C_{ll}$ with

$$C_{ll'} = \frac{1}{N(N-1)} \sum_{i=1}^{N} \left(\tilde{G}_l^i - G_l\right)\left(\tilde{G}_{l'}^i - G_{l'}\right). \tag{9.35}$$

In practice, the assumption of a Gaussian distribution is not valid, since the errors at adjacent imaginary times or frequencies are often correlated. Thus, the covariance matrix C is not diagonal, and the chi-squared functional must be generalized to

$$\chi^2[A] = \sum_{l,l'} \left(G_l - G_l[A]\right) C_{ll'}^{-1} \left(G_{l'} - G_{l'}[A]\right). \tag{9.36}$$

to measure the difference between the spectrum and the data.

9.3.3 Default model and regularization strength

The default model $m(\omega) > 0$ encodes prior knowledge about the spectrum before seeing the data and acts as the attractor when the data is uninformative. Its choice should reflect only robust information (normalizations, symmetries, asymptotics), avoiding prejudicial structure. Whenever possible, known moments should be enforced as constraints, e.g. the zeroth moment

$$\sum_j A_j \Delta\omega_j = \mu_0 \tag{9.37}$$

and, if available, the first/second moments (f-sum rules, high-frequency tails). Encoding these in m (and/or as linear constraints) avoids an otherwise unnecessary reduction of the entropy to fix trivial global properties. In general, the default model is restricted to the physically allowed region, e.g. a bandwidth window from the noninteracting DOS. A pragmatic workflow is to start from a minimally informative $m(\omega)$ satisfying the constraints above, for example a constant $m(\omega) = \mu_0/W$ on a window of width W, and then test robustness by moderately broadening/narrowing m or by using alternative smooth shapes. Stable features of $A(\omega)$ across such variations are more reliable [138, 140].

With the posterior

$$P(A \,|\, G,\, m,\, \alpha) = \exp\!\left(\alpha S[A,\, m] - \frac{1}{2}\chi^2[A]\right) \tag{9.38}$$

the spectrum $A^\star(\alpha)$ at fixed α is the maximizing function of the functional

$$Q_\alpha[A] = \frac{1}{2}\chi^2[A] - \alpha S[A,\, m]. \tag{9.39}$$

The hyperparameter $\alpha > 0$ balances fidelity to the data (χ^2) against entropy (closeness to m). Two standard strategies are commonly used [138, 139].

In the historic MaxEnt approach, α is chosen such that the fit quality is statistically acceptable,

$$\chi^2[A^\star] \approx N_{\text{eff}}, \tag{9.40}$$

with N_{eff} the effective number of independent data points. Operationally, $A^\star(\alpha)$ is computed for multiple α values, typically on a log-scale, and the smallest α for which χ^2 first reaches N_{eff} is selected. This avoids overfitting noise while not over-regularizing.

In Bryan's method [139], α is treated as a Bayesian hyperparameter and maximized (or averaged over) its posterior

$$P(\alpha \,|\, G,\, m) \approx \frac{\exp(-Q_\alpha(A^\star(\alpha)))}{\sqrt{\det(\nabla\nabla Q_\alpha|_{A^\star})}}. \tag{9.41}$$

where the denominator comes from a Laplace (Gaussian) approximation around $A^\star(\alpha)$ in the reduced SVD subspace of the kernel K, introduced in Eqs. (9.5) and (9.9). One then either picks α at the maximum of $P(\alpha \,|\, G,\, m)$ or forms the evidence-weighted average spectrum

$$\bar{A}(\omega) \propto \int \mathrm{d}\alpha\, A^\star(\omega;\, \alpha)\, P(\alpha \,|\, G,\, m) \tag{9.42}$$

This procedure reduces sensitivity to the exact choice of α.

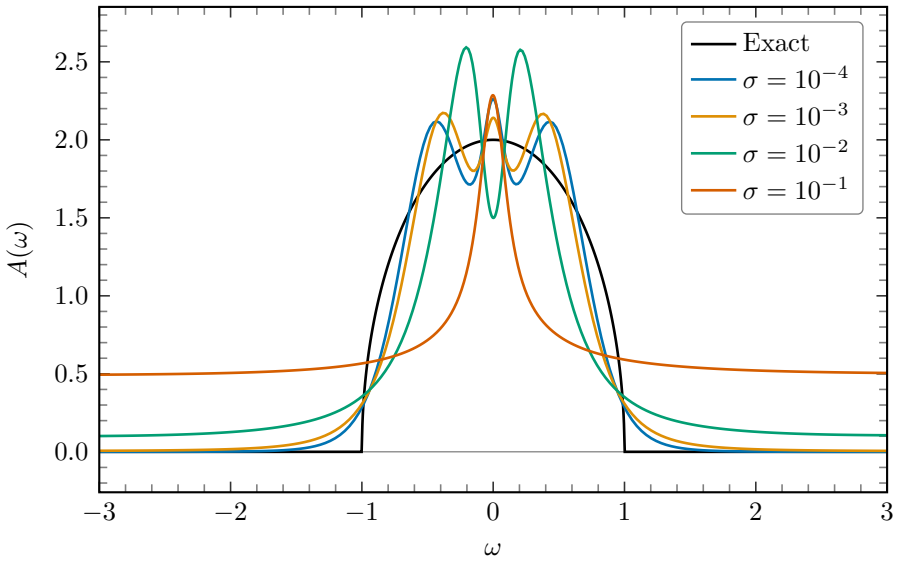

Figure 22: Spectral function $A(\omega)$ obtained via MaxEnt analytic continuation of Matsubara data for a semicircular density of states (Bethe lattice, half-bandwidth $D = 1$) at inverse temperature $\beta = 20$. The input Green's function is Fourier transformed to imaginary time data, where a Gaussian noise with standard deviation σ is added. For comparison, the exact real-axis spectral function is shown.

9.3.4 MaxEnt continuation example

Figure 22 illustrates a concrete MaxEnt continuation performed with the `TRIQS/maxent` implementation [C5] on the same semicircular benchmark (Bethe lattice, $D = 1$, $\beta = 20$) used above. The Matsubara Green's function is Fourier-transformed to imaginary time and perturbed by Gaussian of standard deviation σ, which is then supplied to MaxEnt as the per-time-slice error estimate. For small but finite noise in this example, the reconstruction follows the exact spectrum, but shows broadening of sharp features and oscillations due to the regularization. As σ is increased, the likelihood is down-weighted relative to the entropy and the spectrum correspondingly broadens, with sharp features progressively washed out. In the large-noise limit, the spectrum reverts to the default model (here chosen as a flat function over the bandwidth), as expected. By construction, MaxEnt enforces $A(\omega) \geq 0$: the entropy prior relative to a positive default model $m(\omega) > 0$ assigns zero weight to negative spectra. Thus, the reconstruction contains no unphysical regions with $A(\omega) < 0$.

We deliberately omit a "no-noise" curve: MaxEnt requires error bars (or a covariance) to define the likelihood and set the balance with the entropy. In the formal limit $\sigma \to 0$ the posterior collapses onto a hard constraint, the regularization ceases to play its intended role, and the procedure tends to overfit discretization artifacts rather than produce a controlled, Bayesian compromise with the default model [138].

10 Superconducting transition temperatures of V and TiV alloys [P1]

The superconducting critical temperature T_c provides a central link between a material's chemical composition and its crystal and electronic structure. At the same time, it serves as a quantitative fingerprint of the microscopic pairing mechanism responsible for superconductivity. For many elemental metals at ambient pressure, superconductivity is commonly described within the Bardeen-Cooper-Schrieffer (BCS) framework [144, 145], where an effective attractive interaction between electrons arises from phonon exchange in the weak-coupling limit. A key refinement beyond the original BCS picture is the retarded character of the electron–phonon interaction, which suppresses the impact of the bare Coulomb repulsion because electronic and phononic energy scales are widely separated [146]. These retardation effects lead to a frequency-dependent superconducting order parameter and are treated systematically within Eliashberg theory [147].

In Eliashberg theory, estimates of T_c are controlled by moments of the Eliashberg spectral function $\alpha^2F(\nu)$, which encodes both the relevant phonon excitations and their coupling to electronic states at the Fermi level. Conceptually, $\alpha^2F(\nu)$ can be viewed as the phonon density of states $F(\nu)$ weighted by a suitable Fermi-surface average of the squared electron–phonon matrix elements α^2. A commonly used microscopic representation is

$$\alpha^2F(\nu) = \frac{1}{N(E_F)} \sum_{\boldsymbol{k},\boldsymbol{q},\lambda} \left|g^{\lambda}_{\boldsymbol{k},\boldsymbol{k}+\boldsymbol{q}}\right|^2 \delta\left(\epsilon_{\boldsymbol{k}}\right) \delta\left(\epsilon_{\boldsymbol{k}+\boldsymbol{q}}\right) \delta\left(\nu - \omega_{\boldsymbol{q}\lambda}\right), \tag{10.1}$$

where $N(E_F)$ is the electronic density of states at the Fermi level, $g^{\lambda}_{\boldsymbol{k},\boldsymbol{k}+\boldsymbol{q}}$ denotes the electron–phonon coupling matrix element for phonon branch λ, and $\omega_{\boldsymbol{q}\lambda}$ is the corresponding phonon frequency [148]. The dimensionless electron–phonon coupling constant then follows directly as

$$\lambda = 2\int_0^{\infty} \mathrm{d}\nu \, \frac{\alpha^2F(\nu)}{\nu}, \tag{10.2}$$

and additional frequency moments of $\alpha^2F(\nu)$ enter compact estimates of T_c. In addition to the phonon-mediated attraction, Cooper pairing is opposed by the (screened) Coulomb repulsion between electrons. In Eliashberg theory this repulsion is commonly parameterized by the dimensionless quantity $\mu = N(E_F)\langle V_C\rangle$, where $\langle V_C\rangle$ denotes an appropriate Fermi-surface average of the screened Coulomb interaction. Because the Coulomb interaction acts on electronic energy scales while the pairing interaction is retarded on phononic scales, the effective Coulomb repulsion entering the pairing problem is reduced to the Morel–Anderson Coulomb pseudopotential μ^* [146].

While T_c can be obtained from a full numerical solution of the Eliashberg equations, it is often necessary to employ compact parametrizations that retain the dominant dependence on a few characteristic quantities, especially when the computation of phonon spectra and electron–phonon matrix elements is not possible. The McMillan expression offers a compact and widely used route to approximate T_c from a small set of material parameters [149], and it naturally introduces the electron–phonon mass

enhancement via $m^*/m \approx 1+\lambda$. This formula is widely used to obtain semi-quantitative estimates of T_c and to rationalize trends across materials.

Transition-metal alloys form a broad and technologically important class of superconductors, where disorder becomes an essential ingredient. The foundations of disordered superconductivity were laid by Abrikosov and Gor'kov [150]. In parallel, Anderson's theorem establishes that, for s-wave pairing, weak nonmagnetic disorder does not strongly affect superconductivity [151]. Nonetheless, experiments on strongly disordered systems show that superconductivity can be substantially suppressed, and sufficiently strong disorder may induce qualitative changes in the normal and superconducting states. These include disorder-driven metal-insulator transitions, pseudogap features in the excitation spectrum, enhanced spatial inhomogeneity of pairing, and an increased ratio Δ/T_c [152–158].

Random impurities and point defects offer a practical route to tune superconducting properties. By controlling the type and concentration of disorder, one can modify normal-state scattering and, in turn, influence the superconducting transition. A central difficulty is the characterization of impurity statistics, that is, the probability distribution over disorder realizations. In materials simulations, the coherent potential approximation (CPA) is widely used for this task. As a local effective-medium theory, CPA captures the average effect of different atomic species but does not resolve more delicate features such as short-range order. Extensions can partially remedy these limitations. The dynamical cluster approximation (DCA) [159], a cluster generalization of dynamical mean-field theory, incorporates short-range spatial correlations, while typical medium theory (TMT) [130, 160] targets localization-sensitive aspects of disorder. These developments have been applied to model Hamiltonians [161, 162] and, in concert with materials-specific first-principles calculations within density-functional theory (DFT), to realistic alloy problems [163, 164]. In a broader setting, comparative assessments of disorder modeling have also been carried out for complex alloys, for example in the high-entropy HfNbTaTiZr system where potential superconducting transition temperatures have been estimated [165].

Methodologically, this chapter builds on the framework established earlier in the thesis: DFT in a Green's-function, multiple-scattering formulation based on exact muffin-tin orbitals (EMTO, Ch. 3); DMFT for local, frequency-dependent electronic correlations (Ch. 4); and CPA for substitutional disorder (Sec. 7.6). We employ a charge and self-energy self-consistent EMTO+DMFT scheme with CPA averaging, as introduced in Sec. 8.2. In this setting, the interacting lattice Green's function $G(\boldsymbol{r}, \boldsymbol{r}', E)$ and the local self-energy $\Sigma(E)$ enter on the same footing as the EMTO scattering-path operator, while CPA provides the composition-dependent effective medium for substitutional randomness.

Within the conventional, phonon-mediated picture, McMillan's approach connects normal-state electronic input to the transition temperature. The DFT(CPA)+DMFT workflow delivers the correlated density of states $N(E_F)$ and the orbital-resolved scattering phase shifts needed to evaluate the Hopfield parameter η. Together with an appropriate phonon scale, this yields the electron–phonon coupling λ, from which we estimate T_c using McMillan's formula. The phonon frequency scale is taken from experimental Debye temperatures, and the Coulomb pseudopotential μ^* is varied in a narrow, physically motivated range. This strategy allows us to incorporate dynami-

cal electronic correlations consistently when assessing how disorder in V, and in V–Ti alloys, impacts η, λ, and ultimately T_c.

10.1 Methods

Density-functional theory (DFT) augmented by local, dynamical electronic correlations is required for d-band transition metals where narrow bands and on-site interactions influence low-energy properties [20, 75, 166]. In the presence of substitutional disorder, a Green's function formulation is advantageous because the one-particle propagator interfaces naturally with effective-medium treatments and with local many-body self-energies [163, 164, 167, 168]. In what follows we summarize the minimal ingredients of the charge and self-energy self-consistent LDA(CPA)+DMFT framework used here (cf. Ch. 4 and Secs. 7.6 and 8.2), and the evaluation of Hopfield parameters in the Gaspari–Györffy (GG) multiple-scattering formalism [169, 170] which, together with experimental Debye scales and a Coulomb pseudopotential μ^*, feed the McMillan estimate of T_c [149].

10.1.1 Combined disorder and dynamical electronic correlations

We employ a charge- and self-energy-self-consistent EMTO+DMFT scheme with CPA disorder averaging [64, 70, 171] using the `EMTO-CPA` code [C6], extended to include DMFT as in Refs. [164, 167, 168]. The interacting sector is a rotationally invariant on-site multiorbital Hamiltonian on the d shell,

$$H_U = \frac{1}{2}\sum_{im\sigma} U_{mm'm''m'''}\,\hat{c}^{\dagger}_{im\sigma}\,\hat{c}^{\dagger}_{im'\sigma'}\,\hat{c}_{im'''\sigma'}\,\hat{c}_{im''\sigma}\,, \tag{10.3}$$

with U and Hund's J parametrizing $U_{mm'm''m'''}$ [20]. Unless stated otherwise we scan $U \in [0,\,5]\,\mathrm{eV}$ and use $J = 0.6\,\mathrm{eV}$ (increasing J to $0.9\,\mathrm{eV}$ leaves conclusions unchanged). The impurity problem is solved with the spin-polarized T-matrix fluctuation-exchange (SPTF) approximation introduced in Ch. 5, yielding a local, frequency-dependent self-energy $\Sigma_\sigma(E)$ that corrects the EMTO Green's function [133, 167, 168]. Double counting is removed by a static shift, $\Sigma_\sigma(E) \to \Sigma_\sigma(E) - \Sigma_\sigma(0)$, and finite temperatures enter via $\omega_n = (2n{+}1)\pi T$. In addition to the standard LDA total energy, the Kohn-Sham band energy correction due to the DMFT is added together with the trace of the matrix product between the DMFT self-energy and the local Green's function (ΣG), the so-called Galitskii-Migdal contribution.

10.1.2 McMillan transition temperature

For conventional superconductors, an estimate of the transition temperature follows once the electron–phonon coupling strength λ and a characteristic phonon scale are specified; we adopt the McMillan expression [149] with retardation encoded by the Coulomb pseudopotential μ^* [146] and with mass enhancement $m^*/m \approx 1 + \lambda$ as in Eliashberg theory [147], namely

$$T_c = \frac{\theta_D}{1.45}\exp\left[-\frac{1.04(1+\lambda)}{\lambda - \mu^*(1+0.62\lambda)}\right]. \tag{10.4}$$

The coupling λ is assembled from purely electronic and lattice contributions,

$$\lambda = \frac{\eta}{M\,\langle\omega^2\rangle} = \frac{N(E_{\mathrm{F}})\,\langle I^2\rangle}{M\,\langle\omega^2\rangle}, \tag{10.5}$$

where $N(E_{\mathrm{F}})$ is the interacting DOS per spin at the Fermi level extracted from the LDA+DMFT Green's function, $\langle I^2\rangle$ is the Fermi-surface average of the squared electron–phonon matrix element, M is the ionic mass, and $\langle\omega^2\rangle$ is the phonon second moment. The electronic numerator $\eta \equiv N(E_{\mathrm{F}})\,\langle I^2\rangle$ is the Hopfield parameter [169]. To evaluate η we use the Gaspari–Györffy (GG) prescription in the multiple-scattering (rigid muffin-tin) formalism [170], which exploits the dominance of $l \to l \pm 1$ channels in a local-phonon representation and yields, in terms of single-site scattering phase shifts $\delta_l(E_{\mathrm{F}})$ and partial DOS $N_l(E_{\mathrm{F}})$ from the interacting EMTO+DMFT Green's function,

$$\eta \simeq \frac{E_{\mathrm{F}}}{\pi^2}\sum_l (2l+2)\sin^2\Big[\delta_{l+1}(E_{\mathrm{F}}) - \delta_l(E_{\mathrm{F}})\Big]\frac{N_l(E_{\mathrm{F}})N_{l+1}(E_{\mathrm{F}})}{N_l^{(1)}N_{l+1}^{(1)}}\,, \tag{10.6}$$

with $N_l^{(1)}$ the single-scatterer DOS normalizations. For transition metals the (p,d) and (d,f) channels typically dominate [169, 170]. The lattice factor is taken from the Debye scale via the standard estimate

$$\langle\omega^2\rangle \approx \frac{1}{2}\theta_D^2, \tag{10.7}$$

which reproduces isotope trends at the Debye level and provides reliable moments for elemental transition metals and their alloys [149, 170]. In disordered alloys $\mathrm{A}_{1-x}\mathrm{B}_x$, all site-resolved quantities entering Eqs. (10.5) to (10.6) are taken from the CPA-averaged EMTO+DMFT Green's function, and we use the disorder averages

$$\lambda = \frac{\langle\eta\rangle_d}{\langle M\rangle_d\,\langle\langle\omega^2\rangle\rangle_d}, \qquad \Big\langle\,\langle\omega^2\rangle\Big\rangle_d \approx \frac{1}{2}\Big\langle\theta_D^2\Big\rangle_d, \qquad \langle M\rangle_d = (1-x)M_{\mathrm{A}} + xM_{\mathrm{B}}, \tag{10.8}$$

while $\langle\theta_D^2\rangle_d$ is assembled from experimental Debye temperatures of the constituents or measured alloy values when available [172]. Equation (10.4) clarifies how electronic-structure changes propagate to T_{c}. Variations in the GG Hopfield factor η affect λ linearly, whereas μ^* enters through the retardation-corrected denominator. Logarithmic derivatives make these trends explicit,

$$\frac{\partial\ln T_{\mathrm{c}}}{\partial\lambda} = \frac{1.04[1+0.38\mu^*]}{\Big[\lambda-\mu^*(1+0.62\lambda)\Big]^2}, \qquad \frac{\partial\ln T_{\mathrm{c}}}{\partial\mu^*} = -\frac{1.04(1+\lambda)(1+0.62\lambda)}{\Big[\lambda-\mu^*(1+0.62\lambda)\Big]^2}. \tag{10.9}$$

In practice we treat μ^* as a parameter scanned within a narrow, physically motivated range for transition metals [146, 149], while λ is obtained directly from Eqs. (10.5) to (10.8) using EMTO+DMFT electronic inputs and experimental Debye scales. This provides a transparent, internally consistent route to T_{c} that incorporates dynamical correlations through $N(E_{\mathrm{F}})$ and the scattering phase shifts entering η, while treating substitutional disorder at the CPA level.

10.2 Vanadium and vanadium-titanium alloys

The physical properties of vanadium have been extensively investigated, for example in Ref. [173]. Elemental V is a type-II superconductor with $T_c = 5.38\,\mathrm{K}$, and its normal-state thermodynamics have been rationalized on the basis of phonon contributions [174]. On the theoretical side, electronic-structure calculations range from standard LDA to correlated extensions such as LDA+U [175], LDA+DMFT [176, 177], and schemes incorporating GW-like self-energies [178]. An alternative LDA+FLEX analysis for V [179] reported a sizeable, predominantly local ($\boldsymbol{k}$-independent) self-energy, underscoring the importance of local dynamical correlations for ground-state properties. In particular, LDA+DMFT captures substantial quantum fluctuations, improves agreement with the experimental Fermi surface [176], and accounts for the crossover from Pauli to Curie–Weiss behavior [177]. Computed T_c under pressure based on McMillan's estimate is likewise consistent with experiment [180].

For Ti_xV_{1-x} alloys, resistivity measurements reveal a relatively broad transition into the superconducting state over an appreciable composition range that cannot be assigned solely to a secondary phase [181]. This broadening motivated proposals of additional scattering channels beyond conventional electron–phonon coupling, in particular scenarios invoking spin fluctuations [182, 183]. At the same time, Ti substitution in bcc V enhances T_c beyond the elemental values of the constituents. Since dynamical electronic correlations already improve the description of pure V [176–178], it is natural to expect that they also matter in the disordered alloy. The objective here is therefore to explain the increase of T_c as a consequence of the combined effects of substitutional disorder and dynamical electronic correlations, with a particular focus on the dilute-Ti limit and the composition window where the enhancement is maximal.

10.2.1 Dynamic electronic correlation in the normal state of vanadium

We first present the LDA+DMFT results of the electronic structure for elemental vanadium. V crystallizes in the bcc (β) phase, space group $Im\bar{3}m$, with V on the Wyckoff $2a$ site and experimental lattice parameter $a_{\mathrm{exp}} = 3.02\,\text{Å}$. To obtain the equilibrium lattice constant a_{eq} within our computational framework, we computed the LDA+DMFT total energy $E(a)$ for several interaction strengths U and explicitly minimized $E(a)$ with respect to a (by fitting the near-minimum portion of $E(a)$), following Ref. [167]. This procedure ensures that the quoted a_{eq} corresponds to the energy minimum of our method, which could deviate from the experimental lattice parameter a_{exp}. The convergence of the LDA+DMFT calculations were checked on various $\boldsymbol{k}$-mesh sizes up to $57 \times 57 \times 57$ $\boldsymbol{k}$-points in the irreducible part of the first Brillouin zone, although the saturation of the results (no significant change in $N(E_F)$, or in the Hopfield parameters) was noticed for smaller number of $\boldsymbol{k}$-points.

Experimentally, the VB spectra display two broad maxima at approximately $-2.4\,\mathrm{eV}$ and $-0.7\,\mathrm{eV}$, while the unoccupied CB shows a shoulder near $0.7\,\mathrm{eV}$ and a more pronounced peak around $2.3\,\mathrm{eV}$ extending up to about $8\,\mathrm{eV}$ above E_F [184, 185], as shown in Fig. 23(a). For a direct comparison between theory and experiment, we construct simulated spectra from the LDA+DMFT total DOS by multiplying with the Fermi function $f(E,T)$ for the VB and with $1 - f(E,T)$ for the CB, and then convolving to mimic the experimental resolution: a Lorentzian of $0.1\,\mathrm{eV}$ followed by a Gaussian

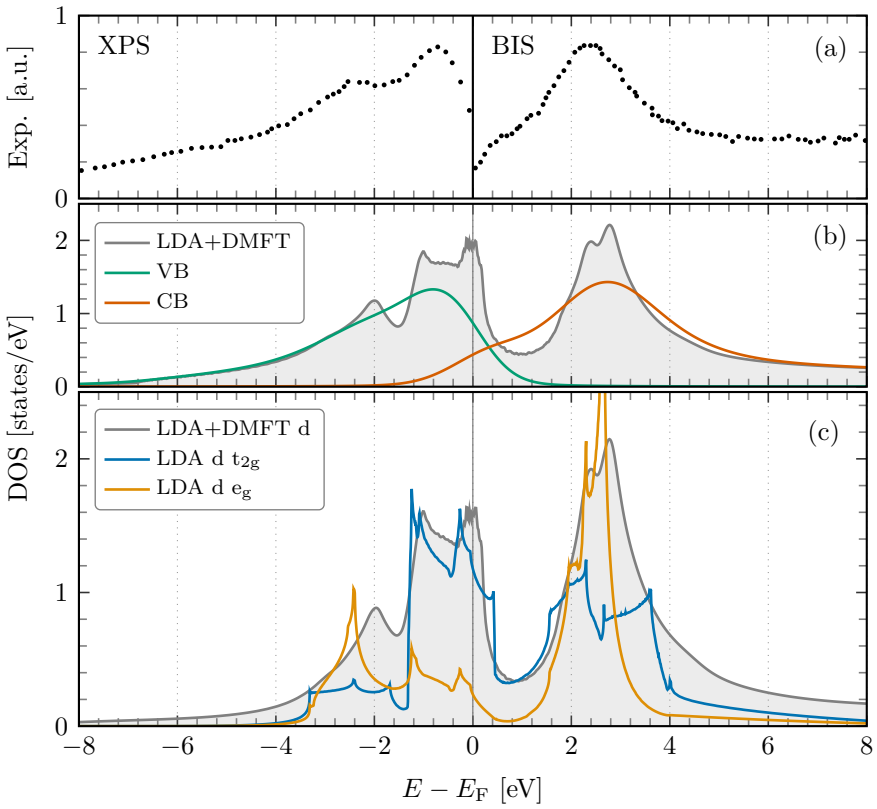

Figure 23: Vanadium spectral functions. (a) Experimental XPS [184] and BIS [185] spectra in arbitrary units. (b) Valence-band and conduction-band spectra obtained by convolving the total DOS with experimental resolution functions. (c) V d-orbital DOS from LDA and LDA+DMFT with $U = 2\,\mathrm{eV}$, $J = 0.6\,\mathrm{eV}$ at 300 K.

of 0.55 eV for XPS and 0.7 eV for BIS [178]. The energy scale is aligned at E_F without additional shifts. After this processing the theoretical spectra in Fig. 23(b) are smoothed, yet they reproduce the positions of the VB maxima and the CB shoulder/peak structure, including the shallow pseudo-gap just above E_F. In addition, the LDA+DMFT DOS exhibits high-binding-energy tails for $E - E_\mathrm{F} \in [-8, -4]\,\mathrm{eV}$, absent in plain LDA and characteristic of quantum fluctuations in transition metals, akin to the well-known −6 eV satellite in Ni [186–188]. Notably, the correlated DOS exhibits high-binding-energy tails for $E - E_\mathrm{F} \in [-8, -4]\,\mathrm{eV}$, absent in plain LDA and characteristic of quantum fluctuations in transition metals, akin to the well-known −6 eV satellite in Ni [186–188].

Figure 23(c) compares LDA and LDA+DMFT DOS. The gray area is the LDA+DMFT total d-DOS; blue/orange curves are LDA t_{2g}/e_g partial DOS. Within LDA, the t_{2g} and e_g bandwidths span similar energy ranges, with a dominant t_{2g} weight at E_F. In LDA+DMFT, the negative slope of $\mathrm{Re}\,\Sigma(E)$ near E_F slightly compresses the spectra toward the Fermi level – a hallmark of Fermi-liquid behavior-shifting, for example, the e_g peak from $\sim -2.5\,\mathrm{eV}$ to $\sim -2\,\mathrm{eV}$ and modestly enhancing the DOS at E_F. On the unoccupied CB, the e_g-dominated peak near 2.7 eV moves slightly away from E_F, consistent with a mean-field (Hartree-Fock-like) contribution dominating dynamic local correlations in that range. Remaining discrepancies between theory and experi-

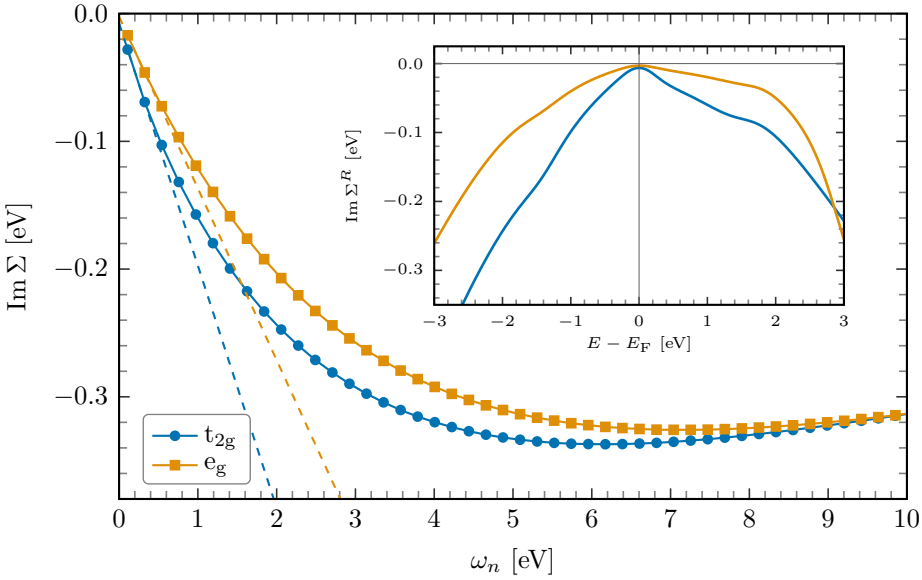

Figure 24: Imaginary parts of the t_{2g} and e_g self-energies vs. Matsubara frequency from LDA+DMFT with $U = 2\,\mathrm{eV}$ and $J = 0.6\,\mathrm{eV}$ at 400 K. Inset: parabolic $\mathrm{Im}\,\Sigma^R(E)$ near E_F, consistent with Fermi-liquid behavior.

ment in both occupied and unoccupied sectors have been discussed in Ref. [178], where LDA+U was shown to underestimate the inter-peak weight, while GW variants and LDA+DMFT bring the spectra into substantially better agreement.

Figure 24 shows the imaginary parts of the orbital-resolved self-energies; the inset presents the analytically continued retarded self-energies on the real axis exhibiting $\mathrm{Im}\,\Sigma^R(E) \propto -(E - E_\mathrm{F})^2$ near E_F, consistent with a Fermi liquid for both t_{2g} and e_g. The analytical continuation is performed with the Padé techniques [137, 189] introduced in Sec. 9.2, but to avoid continuation artifacts we interpret the results primarily on the Matsubara axis. In a Fermi liquid the low-frequency behavior of the self-energy on the Matsubara axis is linear,

$$\mathrm{Im}\,\Sigma(\mathrm{i}\omega_n) = -\Gamma(\omega_n) - (Z^{-1} - 1)\omega_n, \tag{10.10}$$

where Z is the quasiparticle weight ($Z^{-1} = m^*/m$ for a momentum-independent self-energy) and $\Gamma(\omega_n)$ denotes the quasiparticle damping.

For vanadium we find that $\mathrm{Im}\,\Sigma_{t_{2g}/e_g}(\mathrm{i}\omega_n)$ approaches zero linearly at small ω_n for both orbital manifolds, implying long-lived quasiparticles whose scattering rate vanishes on approaching the Fermi surface. This linear regime is preserved throughout the explored temperature range, $100\,\mathrm{K} \leq T \leq 600\,\mathrm{K}$, providing a clear and internally consistent indication of Fermi-liquid behavior in the normal state.

Within DMFT the quasiparticle mass enhancement m^*/m relative to the band mass m is local and can be estimated from Matsubara data in the zero-temperature limit as

$$m^*/m = 1 - \left.\frac{\mathrm{Im}\,\Sigma(i\omega_n)}{\omega_n}\right|_{\omega_n \to 0}. \tag{10.11}$$

In practice (e.g., in QMC) it is extracted from the slope of $\mathrm{Im}\,\Sigma(i\omega_n)$ at the lowest frequencies [74]. The dashed lines in Fig. 24 illustrate these slopes for t_{2g} and e_g.

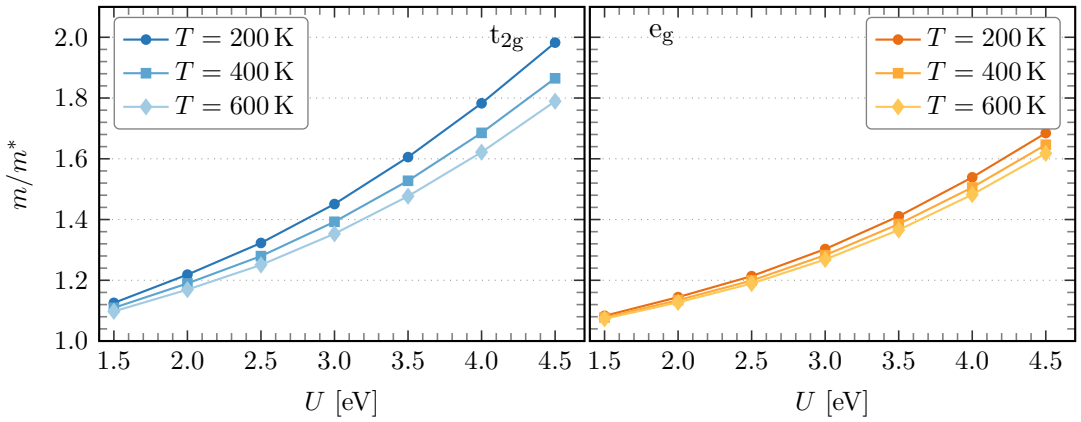

Figure 25: Effective-mass renormalization of V t_{2g} and e_g orbitals vs. interaction strength for several temperatures.

Figure 25 summarizes m^*/m for several U up to 5 eV. For $U > 2\,\mathrm{eV}$ we use $J = 0.6\,\mathrm{eV}$, for $U < 2\,\mathrm{eV}$ we keep $U/J = 2/0.6 \approx 3.33$ to ensure a positive $U-3J$. Increasing J up to 0.9 eV produces no significant changes in the spectra. For all T the effective masses grow with U; at higher T the estimates are slightly smaller. Overall, m^*/m lies in the range $1-2\,\mathrm{eV}$ with a monotonic increase versus U, characteristic of a moderately correlated metal rather than a heavy-fermion regime where m^*/m can reach 10^2-10^3 [190, 191]. The enhancement is weaker for e_g than for t_{2g}.

Deviations from Fermi-liquid behavior and non-analytic frequency dependences of the t_{2g} self-energies have been reported in Ref. [177] using continuous-time QMC impurity solvers. Our perturbative solver does not target the high-T or high-U regime, nevertheless, in the parameter window relevant for vanadium, $U \approx 2-3\,\mathrm{eV}$ and temperatures that correctly capture Fermi-surface properties [176], our results are consistent with the QMC findings and with earlier LDA+FLEX calculations [179].

10.2.2 McMillan estimates for the transition temperature of pure V

First-principles estimates of superconducting transition temperatures based on Eliashberg theory have achieved notable success in selected materials classes [192–194]. Those studies, however, typically assume a periodic crystal or employ simplified alloy treatments and therefore do not include the interplay of dynamical local electronic correlations with substitutional disorder. For transition-metal alloys where both ingredients are essential, a pragmatic and reliable route is to evaluate T_c within McMillan's framework, using correlated normal-state inputs and effective-medium disorder averages.

Figure 26 summarizes the LDA+DMFT-based inputs and outcomes entering the McMillan analysis. Panel (a) reports the equilibrium lattice parameter a_{eq} obtained by minimizing the total energy $E(a)$ within our scheme. Panel (b) shows the electron–phonon coupling $\lambda(U)$ as extracted from the Gaspari–Györffy Hopfield factor and the Debye moment, and panel (c) displays the corresponding transition temperature $T_c(U)$ evaluated from Eq. (10.4). Calculations were carried out for U up to 5 eV at fixed $J = 0.6\,\mathrm{eV}$. The $U = 0\,\mathrm{eV}$ point serves as the LDA baseline. For reference, panel (b) can also be read as the Eliashberg mass enhancement via $m^*/m \approx 1+\lambda$. Since θ_D and μ^* are treated as fixed inputs, the trends in T_c largely mirror those of $\lambda(U)$.

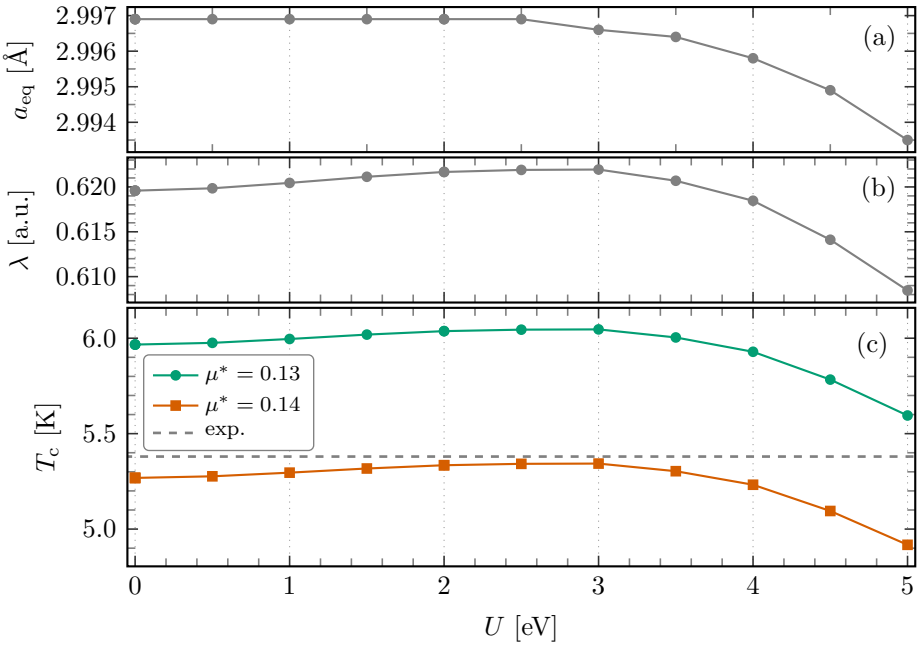

Figure 26: (a) Computed equilibrium lattice parameter a_{eq}, (b) electron–phonon coupling strength λ, and (c) the superconducting critical temperature T_{c} with respect to the interaction strength U of vanadium. The dashed line indicates the experimental T_c. The experimental lattice parameter is $a_{\mathrm{exp}} = 3.02\,\text{Å}$; it is not shown as it falls outside the shown scale.

All quantities in Fig. 26 vary only weakly with the on-site interaction U. The equilibrium lattice constant is essentially flat up to 3 eV and decreases for larger U. At $U = 5\,\text{eV}$ it is smaller by about 2 %. It is interesting to note that the mass enhancement factor λ reaches a maximum value of 0.622 for realistic U in the range $2 - 3\,\text{eV}$ and decreases beyond this interval.

With the first-principles inputs $N(E_{\mathrm{F}})$ from LDA+DMFT, the electron–phonon coupling λ, and experimental Debye temperatures θ_D we evaluate T_{c} using McMillan's expression and a physically motivated choice of the Coulomb pseudopotential μ^*. McMillan suggested $\mu^* \simeq 0.13$ for transition metals [149], but values reported in the literature vary: Ref. [195] finds $\mu^* \in [0.11, 0.14]$ depending on the local-field correction, while Ref. [181] employs $\mu^* \in [0.12, 0.175]$ to align calculated and measured transition temperatures. Figure 26(c) shows the resulting T_{c} estimates. For pristine V, using $\mu^* = 0.13$ yields a slight overestimate of the transition temperature, whereas $\mu^* = 0.14$ brings the calculation into near-quantitative agreement with experiment. While the absolute scale of T_c shifts with μ^* (as expected from the sensitivities in Eq. (10.9)), the U-dependence is robust: a mild increase at small U, a maximum coinciding with the peak of $\lambda(U)$, and a subsequent decrease at larger U. Adopting $\mu^* = 0.14$, realistic Hubbard interactions in the range $2 - 3\,\text{eV}$ reproduces the experimental benchmark $T_c = 5.73\,\text{K}$ (dashed line in Fig. 26(c)). We note that the same U interval also provides an excellent description of the Fermi surface of vanadium [176], ensuring the chosen correlation strength is consistent.

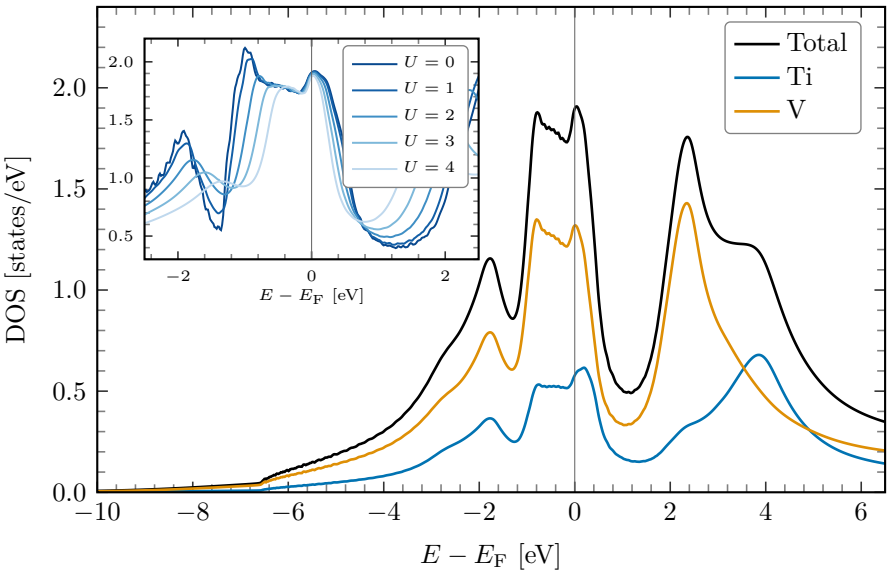

Figure 27: Total and sublattice DOS of $Ti_{0.35}V_{0.65}$ obtained using LDA+DMFT with $U = 2\,\text{eV}$ and $J = 0.6\,\text{eV}$ at 400 K. The inset shows the total DOS for different interaction strengths U around E_F.

10.2.3 Binary Ti–V alloys

The Ti_xV_{1-x} alloy exhibits several metallurgical phases as a function of composition. For $0 \leq x \leq 0.68$ the β phase with a bcc lattice is stable, whereas for high Ti contents, $0.86 \leq x \leq 1$, the α phase with an hcp structure is favorable. In the intermediate interval $0.67 < x < 0.86$, an additional hexagonal ω precipitate can form alongside the α and β phases [181]. The ω phase is a primitive hexagonal, commonly metastable structure in bcc metals and alloys, and in Ti–V it forms coherently with the bcc matrix with lattice-parameter relations $a_\omega = \sqrt{2}a_{\text{bcc}}$ and $c_\omega = \sqrt{3}/2a_{\text{bcc}}$. Mixed-phase samples containing ω precipitates display an anomalous increase of the electrical resistivity upon cooling [196]. The anomalous transport behavior has been discussed in terms of several mechanisms, including weak localization [196], Kondo (s-d) scattering, and localized spin fluctuations [197, 198]. In parallel, an enhancement of the superconducting transition temperature is observed for Ti concentrations $x \leq 0.5$ [181]. As emphasized in Ref. [181], this increase cannot be attributed to trivial changes of the Debye scale: Ti and V are adjacent in the periodic table, so mass and bonding trends imply only modest, largely monotonic variations of θ_D. Motivated by this, our goal is to assess whether *dynamical* electronic correlations – treated on equal footing with substitutional disorder – provide the missing electronic-structure lever that enhances T_c.

We focus on the bcc β phase, with Ti atoms randomly substituting V on the $2a$ site for compositions up to $x = 0.65$. For each pair (x, U) we computed the total energy as a function of the lattice parameter and determined the equilibrium value a_{eq} by minimizing $E(a)$ with respect to a. Over the investigated concentration range, a_{eq} exhibits an approximately linear dependence on x, consistent with Vegard's law [199]:

$$a_{\text{eq}}(x) = x\, a_{\text{eq}}^{\text{Ti}} + (1 - x)\, a_{\text{eq}}^{\text{V}}\,. \tag{10.12}$$

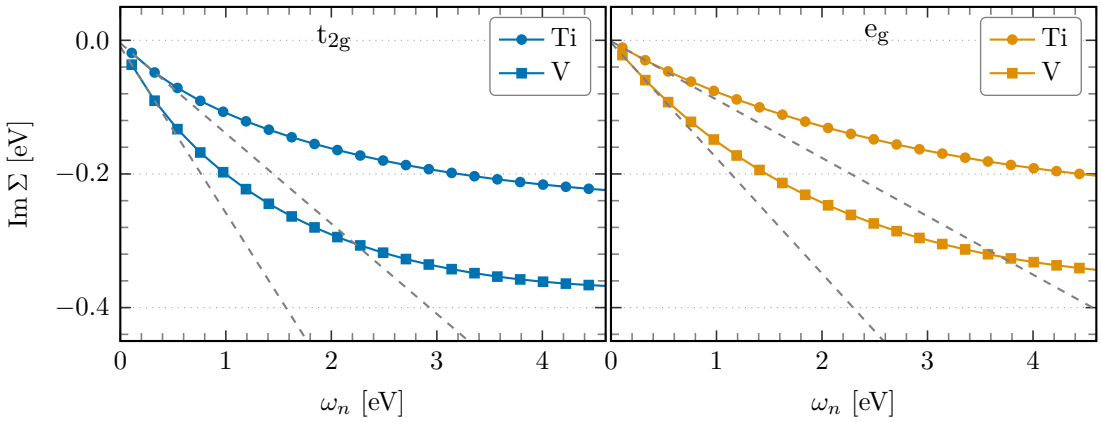

Figure 28: Imaginary part of the self-energies as a function of Matsubara frequencies of the t_{2g} and e_g orbitals of $Ti_{0.35}V_{0.65}$ for $U = 2\,\text{eV}$, $J = 0.6\,\text{eV}$ at 400 K.

Here, a_{eq}^{V} denotes the equilibrium lattice constant of pure V obtained from our calculations, while $a_{\text{eq}}^{\text{Ti}}$ is the corresponding (extrapolated) value for bcc Ti within the same computational framework. A linear fit yields $a_{\text{eq}}^{\text{Ti}} = 3.231\,\text{Å}$.

Figure 27 displays the total DOS for Ti_xV_{1-x} at $x \approx 0.35$, the composition at which the superconducting transition temperature attains its maximum within the series (see below). Across all concentrations the spectra are governed by broad d-electron manifolds and exhibit a characteristic bcc pseudo-gap in the vicinity of E_{F}. At $x = 0.35$ the states at the Fermi level are dominated by V-d character, with Ti-derived weight contributing mainly as a smooth background. The inset of Fig. 27 compares the LDA+DMFT DOS for several interaction strengths U. As for elemental V, we keep $J = 0.6\,\text{eV}$ for $U \geq 2\,\text{eV}$, while for $U < 2\,\text{eV}$ we maintain the ratio $U/J = 2/0.6 \approx 3.33$. DMFT is applied to both Ti and V sites using the same U, and the $U = 0$ curve corresponds to the LDA+CPA baseline. A systematic trend emerges with increasing U: a slight reduction of $N(E_{\text{F}})$ and a modest narrowing of the d-band features in the immediate vicinity of E_{F}, consistent with a quasiparticle weight $Z < 1$ and weak to moderate mass renormalization.

Figure 28 presents the low-energy Matsubara self-energies $\text{Im}\,\Sigma(\text{i}\omega_n)$ for the V and Ti components of Ti_xV_{1-x} at $x = 0.35$. In the small-ω_n regime both display a linear approach to zero, demonstrating that the Fermi-liquid character of the d electrons is preserved in the presence of substitutional disorder treated at the CPA level. The resulting quasi-particle weights for the different concentrations were extracted for both alloy components using the method outlined before.

A quantitative analysis of the concentration dependence of the effective masses at $T = 200\,\text{K}$, 400 K, and 600 K is shown in Fig. 29. For the e_g manifolds of both alloy components the renormalization $Z^{-1} = m^*/m$ exhibits only a very weak variation with x, clustering around $Z^{-1}_{\text{Ti-e}_g} \approx 1.07$ and $Z^{-1}_{\text{V-e}_g} \approx 1.16$. By contrast, the t_{2g} electrons display a slow, monotonic increase of Z^{-1} with Ti content, indicating a modest strengthening of correlations in that channel upon doping. Increasing the temperature reduces the magnitude of the effective masses for all cases, with the trend already visible in pristine V but less pronounced than in the alloys.

A characteristic feature of disordered, correlated metals is the gradual loss of quasi-

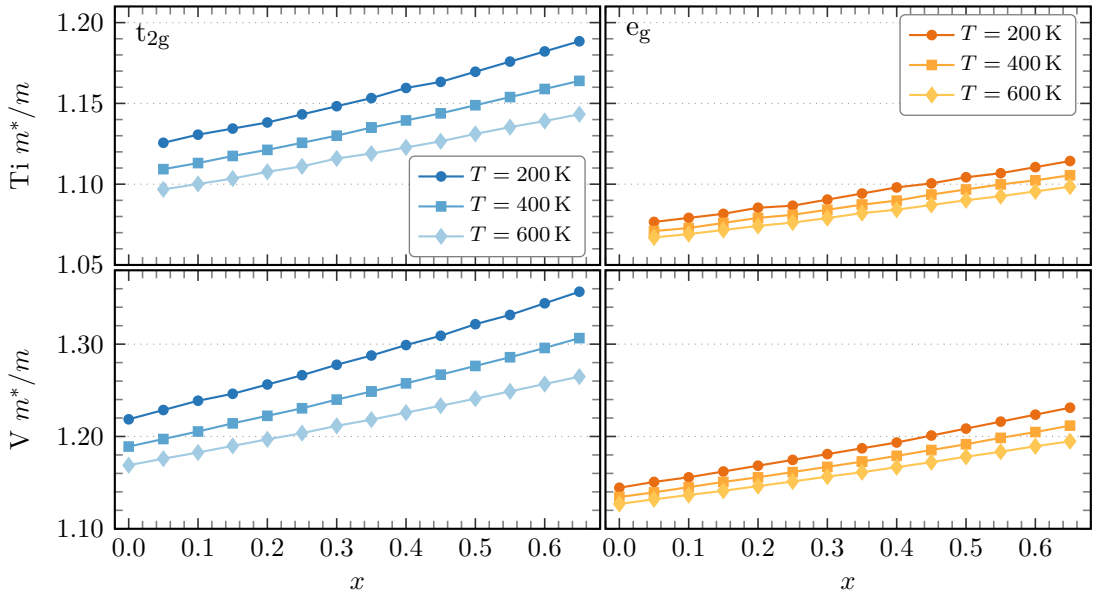

Figure 29: Concentration dependence of the effective mass renormalization of the t_{2g} and e_g orbitals for the alloy components Ti and V of Ti_xV_{1-x} with $U = 2\,\text{eV}$ and $J = 0.6\,\text{eV}$ at different temperatures.

particle coherence. Above a characteristic decoherence temperature, the resistivity increases with a reduction of the quasiparticle weight Z and enhanced scattering [200]. Dynamical mean-field calculations support this picture by linking the transport crossover to the frequency dependence of the self-energy in a disordered medium [201, 202]. We interpret our LDA+DMFT results for Ti_xV_{1-x} in the same framework: at low Ti concentrations, substitutional randomness produces random on-site potentials that are renormalized in the interacting problem by the real part of the self-energy,

$$\epsilon_{t_{2g}/e_g} \rightarrow \epsilon_{t_{2g}/e_g} + \mathrm{Re}\,\Sigma^R_{t_{2g}/e_g}(0), \tag{10.13}$$

shifting the d-level positions, modifying single-site scattering phase shifts, and altering the partial densities of states at E_F. At the same time, the linear low-ω_n behavior of $\mathrm{Im}\,\Sigma(i\omega_n)$ confirms well-defined quasiparticles with $Z < 1$; the extracted concentration and temperature trends of Z indicate a gentle loss of coherence rather than a breakdown of Fermi-liquid behavior over the composition range considered. For energies E close to E_F, screening of the random on-site potential is more effective on V-d states than on Ti-d states, consistent with the higher d occupancy and metallic background on the V sublattice. An orbital-resolved analysis of the real parts of the self-energies in Fig. 30 shows that on the occupied side ($E \leq E_F$) one finds $\mathrm{Re}\,\Sigma^R_{t_{2g}}(E) > \mathrm{Re}\,\Sigma^R_{e_g}(E)$, whereas for $E \geq E_F$ the trend reverses to $\mathrm{Re}\,\Sigma^R_{t_{2g}}(E) < \mathrm{Re}\,\Sigma^R_{e_g}(E)$. Consequently, screening is comparatively stronger for the t_{2g} channel below E_F and weaker above E_F, leading to a slight narrowing of the t_{2g} spectral window around the Fermi level and modifying the single-site phase shifts that enter the Hopfield analysis. Within numerical accuracy we do not observe a significant temperature dependence of the static screening, i.e., $\mathrm{Re}\,\Sigma^R(0)$ changes weakly with T. At the same time, the low-frequency slopes of $\mathrm{Im}\,\Sigma(i\omega_n)$ indicate that t_{2g} quasiparticles lose coherence somewhat more than their e_g counterparts as T increases; correspondingly, m^*/m for t_{2g} remains

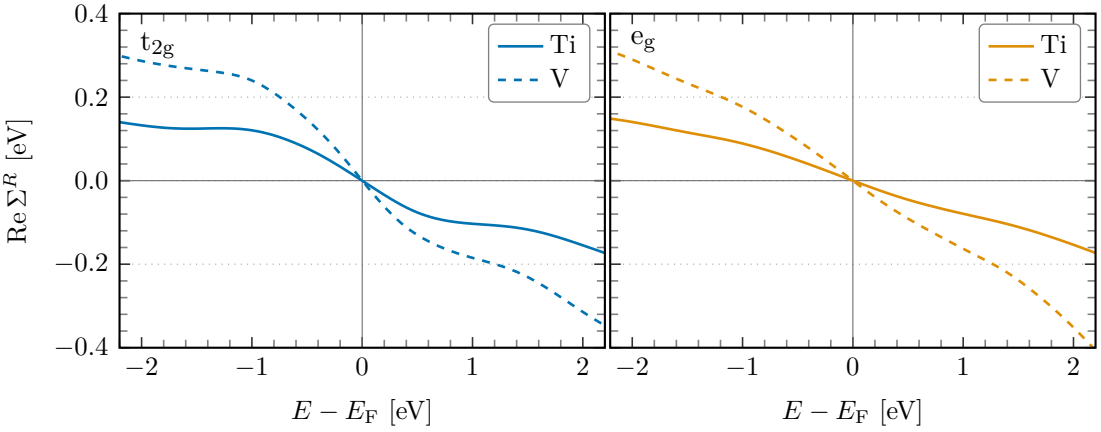

Figure 30: Real part of the retarded self-energies as a function of energy of the t_{2g} and e_g orbitals of $Ti_{0.35}V_{0.65}$ for $U = 2\,\text{eV}$, $J = 0.6\,\text{eV}$ at 400 K.

slightly larger than for e_g across the explored temperatures, while absolute changes with T are modest.

10.2.4 Enhanced critical temperatures in the pure β- and α-phases

To apply McMillan's formula (10.4) we use elemental atomic masses and Debye temperatures from Ref. [203]. For alloys, the phonon scale is interpolated as a concentration-weighted average of the elemental Debye temperatures,

$$\theta_D(x) = (1-x)\theta_D^{\text{V}} + x\theta_D^{\text{Ti}}, \tag{10.14}$$

and the mass entering λ, defined in Eq. (10.5), is taken as

$$M(x) = (1-x)M_{\text{V}} + xM_{\text{Ti}} \tag{10.15}$$

This provides a smooth, experimentally anchored input for the McMillan analysis without introducing additional adjustable parameters.

Figure 31 displays the composition dependence of the superconducting transition temperature in Ti_xV_{1-x}. The curve exhibits a broad maximum at $x \approx 0.33$, and the position of this maximum is essentially insensitive to the interaction strength U. The inset shows $T_c(U)$ for the composition at the peak and for two nearby concentrations. In all three cases T_c increases slightly with U at weak-to-intermediate coupling, reaches a maximum in the same U window where λ peaks, and then decreases once $U \gtrsim 3\,\text{eV}$. Thus, the U-driven trends mirror those of the Hopfield factor and remain robust across composition, while the primary x-dependence of T_c is controlled by the electronic-structure changes induced by Ti substitution and with the smooth variation of the phonon moment and average mass.

We also performed LDA+DMFT calculations for the α (hcp) phase of Ti_xV_{1-x}. For each composition we optimized the in-plane lattice parameter a of the close-packed structure while keeping the axial ratio c/a fixed, thereby ensuring that all subsequent quantities are evaluated at the energy minimum of our method for the hcp geometry. Using the correlated normal-state inputs (DOS and scattering phase shifts) together

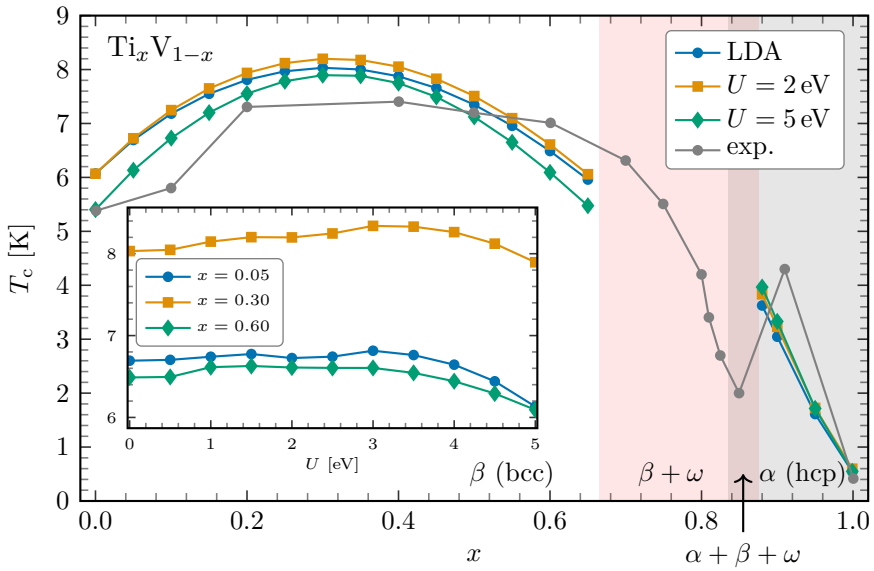

Figure 31: Concentration dependence of T_c in the β (bcc) and α (hcp) phases of Ti_xV_{1-x}. The maximal value for T_c can be observed at $x \approx 0.33$ and is independent of U. The inset shows the interaction strength dependence of T_c. The experimental data is taken from Ref. [204].

with the McMillan analysis, we reproduce the experimentally observed upward trend of the critical temperature for small vanadium contents $1 - x$ in the α phase [204]. By contrast, a quantitative treatment of the mixed $\beta+\omega$ and $\alpha+\beta+\omega$ regions would require explicit structural modeling of precipitate fractions, coherency strains, and short-range order, which lies beyond the present CPA-based framework. Accordingly, we restrict our analysis to the single-phase α and β regimes.

Within Eliashberg strong-coupling theory, the McMillan expression for the superconducting transition temperature T_c follows when the lattice is treated in the rigid-ion approximation and the electronic structure is described at the one-electron level, with retardation effects absorbed into the Coulomb pseudopotential μ^*. In this setting the central, materials-specific quantity accessible through the *ab-initio* computation is the electron–phonon mass-enhancement parameter λ, which contains the electron–phonon matrix element averaged over the Fermi surface (see the discussion in Sec. 10.1.2).

LDA+DMFT calculations for Ti_xV_{1-x} show a narrowing of the DOS around E_F (Fig. 27) together with an increased effective mass (Fig. 29). As a result, quasiparticles with energies near the d-resonance of the electron-ion interaction spend more time in the vicinity of the scatterer (the so-called Wigner delay-time). It is therefore reasonable to assume that electron scattering is governed by a screened local potential consisting of the ionic-displacement contribution and the real part of the local self-energy, i.e., $\Delta V_{\text{ion}} + \text{Re}\,\Sigma^R$. Thus, local dynamical correlations modify the electron–phonon coupling and can lead to an increase in T_c.

Figure 32 shows the surface $\lambda(U, x)$ at temperature $T = 400\,\text{K}$. For any fixed U, the electron–phonon coupling strength λ increases with Ti concentration, reaches a maximum near $x \approx 0.33$, and then decreases again. This trend provides a consistent picture of the concentration dependence of the critical temperature in Fig. 31, where

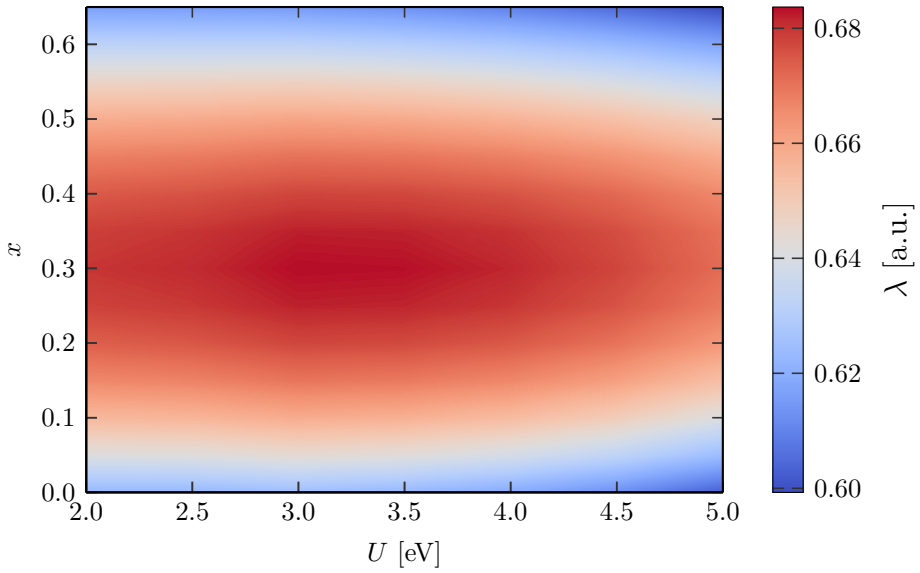

Figure 32: Surface plot of the electron–phonon coupling strength $\lambda(U, x)$ for Ti_xV_{1-x} alloys computed with LDA+DMFT at 400 K.

the maximum in $T_c(x)$ aligns with the maximum of $\lambda(x)$.

10.3 Summary

In this chapter we estimated superconducting transition temperatures of elemental V and Ti_xV_{1-x} alloys within a conventional phonon-mediated (BCS–Eliashberg) framework, with the specific aim of explaining the enhancement of T_c upon Ti substitution in bcc V. Methodologically, we treated substitutional disorder and local dynamical electronic correlations within a single, self-consistent electronic-structure workflow by combining CPA with charge- and self-energy self-consistent LDA(EMTO)+DMFT. Transition temperatures were then obtained from McMillan's expression, Eq. (10.4), using experimental Debye temperatures as the phonon scale and scanning a narrow, physically motivated range of Coulomb pseudopotentials μ^*. The electron–phonon coupling constant λ entering McMillan's formula was evaluated from electronic inputs through the Hopfield parameter η in the Gaspari–Györffy formalism, using correlated partial DOS and scattering phase shifts at E_F.

For pure bcc V, the LDA+DMFT self-energy exhibits clear Fermi-liquid behavior in the relevant temperature window: $\mathrm{Im}\,\Sigma(i\omega_n)$ approaches zero linearly for both t_{2g} and e_g channels, and $\mathrm{Im}\,\Sigma^R(E)$ is parabolic near E_F (Fig. 24), with moderate mass renormalizations (Fig. 25). Using an interaction window that provides a realistic normal-state description, $U \approx 2 - 3$ eV, the McMillan estimate reproduces the experimental scale of T_c for $\mu^* \approx 0.14$ (Fig. 26). The resulting U dependence of T_c is weak and mainly reflects the mild variation of $\lambda(U)$ obtained from the correlated Hopfield analysis.

For Ti_xV_{1-x} we focused on the single-phase bcc (β) and hcp (α) regimes. Within CPA+DMFT, both alloy components remain coherent correlated metals across the investigated compositions: Ti and V self-energies retain the low-frequency Fermi-liquid form (Fig. 28), and the extracted effective masses show only modest renormalization

with a weak concentration dependence (Fig. 29). Within this regime, the calculated $T_c(x)$ exhibits a broad maximum at $x \approx 0.33$ in the bcc phase (Fig. 31), consistent with experiment in the single-phase composition window. A central result is that the nonmonotonic $T_c(x)$ trend tracks the corresponding behavior of the electron–phonon coupling strength $\lambda(x)$ (Fig. 32): for fixed U, λ increases with Ti content, peaks near $x \approx 0.33$, and decreases again for larger x. Since the Debye scale and average mass vary smoothly with concentration, this identifies the T_c enhancement primarily with Ti-induced changes of the correlated electronic structure (through $N(E_F)$ and the scattering phase shifts entering the Hopfield factor), rather than with a purely lattice-driven effect.

Finally, let us emphasize the scope of the present description. CPA provides a local effective medium and therefore does not resolve short-range order, precipitates, or mixed-phase microstructures. Accordingly, our analysis is restricted to the single-phase α and β regimes and does not address the intermediate composition range where ω precipitates and phase coexistence can occur.

11 Quasiparticle Fermi surfaces of Nb and NbTi at high pressure [P2]

External pressure is a powerful control parameter for tuning interatomic distances, chemical bonding, and thus the electronic structure of solids. In the high-pressure regime, even modest volume reductions can induce substantial changes of material properties that are otherwise inaccessible at ambient conditions. This makes pressure a central tool in the ongoing search for conventional superconductors with enhanced critical temperatures T_c. On the theoretical side, progress in high-pressure superconductivity has been enabled by structure predictions and stability analyses within density functional theory (DFT), often combined with linear-response calculations of electron–phonon properties. Among transition-metal alloys, the Nb–Ti family is paradigmatic: it combines structural robustness with experimentally established superconductivity and thus offers a clean setting to interrogate the pressure evolution of the normal state and its implications for pairing.

For elemental and many alloy superconductors at low and moderate coupling, the Bardeen–Cooper–Schrieffer (BCS) framework describes pairing mediated by phonons, and its strong-coupling, retarded generalization due to Eliashberg incorporates the frequency dependence of the order parameter and quasiparticle self-energies, as described in the previous chapter 10.

In previous works, high-pressure crystal structures were obtained from first-principles DFT geometry optimizations [205, 206], and the electron–phonon coupling constant λ was evaluated within density-functional perturbation theory (DFPT) using linear-response calculations, for pressures up to 250 GPa [207]. In addition, the Fermi-level density of states $N(E_F)$ and screened Coulomb pseudopotential $\mu^\star$ within the Morel–Anderson framework [146] were analyzed [208].

Despite extensive phenomenological analyses, the microscopic origin and resilience of the superconducting phase at high pressures remain insufficiently resolved. One suggestion, proposed for Nb–Ti alloys in [209], attributes the persistence of superconductivity under compression to an almost pressure-independent e_g contribution to the Fermi-level density of states $N(E_F)$, while the t_{2g}-projected $N(E_F)$ decreases monotonically with pressure. A similar trend was reported in some multi-component high-entropy alloys, doping the Nb-Ti materials [209] with further impurities.

For the $Nb_{0.44}Ti_{0.56}$ alloy, X-ray diffraction measurements indicate that the *bcc* (β) phase is retained throughout the investigated pressure range up to 250 GPa. Disorder has been modeled by alternating atomic positions of Nb and Ti with uniform occupation in supercell calculations [208]. Namely, the atoms occupy the 1*a* and 1*b* Wyckoff positions of the $Pm\bar{3}m$ CsCl lattice.

A recent ab-initio study [210] of the ordered 1:1 composition, $Nb_{0.5}Ti_{0.5}$, reported state-of-the-art phonon and superconducting-gap calculations that explicitly include strong anharmonic lattice dynamics as well as an energy-dependent treatment of the Coulomb interaction. Nevertheless, the resulting T_c values remain significantly larger than experimental data: it was shown that, using a simple model based on Boltzmann-averaged supercells, the discrepancy can be qualitatively understood in terms of lattice

disorder.

The focus of this chapter is the pressure-dependent normal-state electronic structure of elemental Nb and Nb-Ti alloys, which we regard as a key prerequisite – though not the only ingredient – for understanding the robustness of superconductivity discussed above. Methodologically, we go beyond phenomenological pictures by combining, within a single self-consistent framework, substitutional disorder and local electronic correlations. Specifically, we make no *a priori* assumption about the spatial arrangement of Ti in the Nb *bcc* lattice: chemical randomness is treated using the coherent potential approximation (CPA), while local dynamical correlations are incorporated via dynamical mean-field theory (DMFT),

Within this setup, we analyze the evolution of the quasiparticle band structure and Fermi surface (FS) under compression up to 250 GPa. We extract orbital-resolved spectral functions and momentum-resolved FS maps, quantify disorder-induced broadening on the alloy FS sheets, and track correlation signatures such as the quasiparticle weight Z and effective-mass renormalizations. Together, these results provide the microscopic baseline needed to assess how pressure tunes the phase space and matrix elements relevant for conventional electron-phonon pairing in Nb and $Nb_{0.44}Ti_{0.56}$. Quite unexpectedly, we find that compression induces a pronounced evolution of the Fermi surface (FS) in elemental Nb, with substantial reshaping of individual sheets and momentum-dependent spectral-weight redistribution. In the disordered alloy $Nb_{0.44}Ti_{0.56}$, a CPA+DMFT treatment further reveals correlation- and disorder-driven modifications manifested as sheet-selective broadening in the spectral function and shifts of extremal orbits that persist up to 250 GPa.

11.1 Methods

The methodology employed in this section is similar to the previous chapter 10 on V and V–Ti alloys. We employ density functional theory with dynamical electronic correlations, a proven approach for materials with narrow d bands [20, 75, 166]. A Green's function formulation is used so that both dynamical correlations and substitutional disorder can be treated on equal footing: the one-particle Green's function is computed directly and averaged over disorder configurations within the electronic-structure loop [163, 164, 167, 168].

Our charge- and self-energy-self-consistent scheme uses the exact muffin-tin orbitals (EMTO) basis introduced in Ch. 3 with the local-density approximation (LDA) as starting point, extended by local dynamical correlations. Substitutional disorder at arbitrary concentrations is described by the coherent potential approximation (Sec. 7.6), without assuming any particular ordering of Ti in the Nb *bcc* lattice. The central object is the multiple-scattering (Korringa-Kohn-Rostoker) scattering-path operator, which enables (i) charge self-consistency in real space and (ii) the embedding of a local, frequency-dependent self-energy into the lattice Green's function [164, 211].

Local correlations are treated within dynamical mean-field theory (Ch. 4). The DMFT impurity problem is solved using the spin-polarized T-matrix fluctuation-exchange (SPTF) approximation (Ch. 5), yielding a complex, orbital- and spin-resolved self-energy $\Sigma_\sigma(\mathrm{i}\omega_n)$ that corrects the EMTO/LDA Green's function in a fully self-consistent CPA+DMFT cycle. The local electron-electron interaction is modeled by a rotationally

invariant multi-orbital Hubbard-Hund term as in the previous chapter:

$$H_U = \frac{1}{2} \sum_{im\sigma} U_{mm'm''m'''} \, \hat{c}^\dagger_{im\sigma} \, \hat{c}^\dagger_{im'\sigma'} \, \hat{c}_{im'''\sigma'} \, \hat{c}_{im''\sigma} \, , \tag{11.1}$$

with Coulomb matrix elements parameterized by average U and Hund's exchange J. Unless stated otherwise we use $U \in [0,5]\,\mathrm{eV}$ and $J = 0.6\,\mathrm{eV}$. Increasing J up to $0.9\,\mathrm{eV}$ leaves the qualitative trends unchanged. To remove double counting of interactions already implicit in LDA, we again replace $\Sigma_\sigma(E) \to \Sigma_\sigma(E) - \Sigma_\sigma(0)$ throughout the LDA+DMFT equations. Finite electronic temperatures enter via Matsubara frequencies $\omega_n = (2n+1)\pi T$, $n = 0, \pm 1, \pm 2, \ldots$.

Pressures up to 250 GPa are accessed through the DFT-relaxed crystal structures described in the preceding subsection; these volumes and atomic configurations are then used as input to the CPA+DMFT calculations. Total energies are evaluated with the LDA+DMFT functional using converged charge densities and local Green's functions, i.e., the standard LDA contribution plus the DMFT Kohn-Sham band-energy correction and the Galitskii-Migdal term ΣG. All remaining technical settings (basis partial waves, energy contour, $\boldsymbol{k}$-meshes, Matsubara grids) follow the previous chapter and are therefore not repeated here.

11.1.1 Computational details

Elemental Nb is treated in the β phase with space group $Im\bar{3}m$ (Wyckoff $2a$). The pressure-dependent lattice parameters used for Nb and $Nb_{0.44}Ti_{0.56}$ are listed in Tab. 1. Besides experimental values, the equilibrium lattice parameters a_{eq} were obtained by

	Nb		$Nb_{0.44}Ti_{0.56}$
P (GPa)	a_{exp} (Å)	a_{eq} (Å)	a_{exp}(Å)
0	3.3089	3.3045	3.2643
50	3.0932	3.0936	3.0111
100	2.9666	2.9665	2.8747
150	2.8801	2.8804	2.7767
200	2.8168	2.8155	2.7000
250	2.7642	2.7622	2.6412

Table 1: Experimental values of the lattice parameters are taken from [212]; the relaxed values are obtained using the DFT-GGA (PBE) [10] exchange-correlation functional.

relaxing the crystal at a series of fixed pressures using the projector-augmented-wave (PAW) method [213] as implemented in `VASP` [C7]. We tested several PAW datasets and exchange-correlation (XC) functionals; the best agreement with experiment was achieved with PBE [10] including semicore s and p states. Brillouin-zone integration in `VASP` employed a Γ-centered $12 \times 12 \times 12$ mesh, a plane-wave cutoff of 430 eV, and convergence thresholds of $10^{-8}\,\mathrm{eV}$ in total energy and $10^{-3}\,\mathrm{eV\,Å^{-1}}$ in residual forces. We find that treating s and p states as semi-core states together with the Perdew-Burke-Ernzerhof (PBE) [10] XC potential yields the structural parameters closest to the experimentally observed ones.

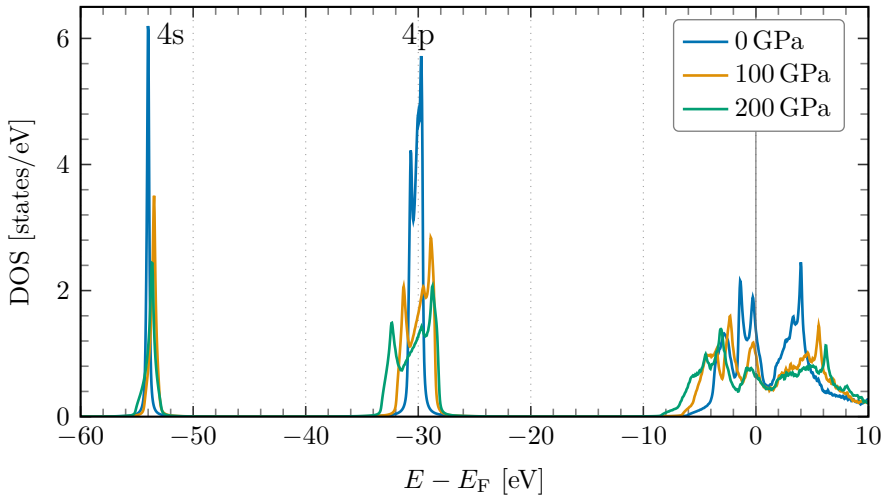

Figure 33: Total electronic density of states of pure Nb computed using LDA including the core 4s and semi-core 4p states.

To study pressure effects using multiple scattering type electronic structure techniques, such as EMTO, details of the Green's function computations are essential. We use an extended *spdf* basis set and a broad contour of 3.5 Ry, including $4s$, $4p$ states. At the same time 60 energy-points on the contour were chosen.

Unless stated otherwise, all calculations were performed using the same extended `EMTO-CPA` code [C6] already employed in the previous chapter.

11.2 Electronic structure of Nb under pressure

The electronic structure of elemental niobium has been analyzed since the early band-structure era [214, 215]. In these studies, Nb with its nominal electronic configuration $4d^4\,5s^1$ is described by five conduction electrons distributed over three d-derived bands: the lowest of these is essentially filled, the second is nearly filled, and the third is more than half filled [214, 215]. Under compression due to high pressure, the conduction manifold broadens substantially and hybridization increases, while semicore states (notably the $4p$ shell) exhibit a visible reshaping. This behavior is illustrated in Fig. 33. We emphasize that an explicit treatment of the semicore states stabilizes total-energy calculations at high pressure, even though these levels remain located at large binding energies (of order $-30\,\mathrm{eV}$) relative to E_F. This choice is consistent with the EMTO settings employed here (cf. Sec. 11.1.1).

The most relevant contributions to macroscopic properties originate from electronic states in the immediate vicinity of the Fermi level. Early photoemission on Nb reported three pronounced features at approximately 0.4 eV, 1.1 eV, and 2.3 eV below E_F [216]. These peaks are fairly well described by our electronic structure calculations. Figure 34 displays the orbital-resolved $4d$ densities of states, split into $\mathrm{t_{2g}}$ and $\mathrm{e_g}$ channels over an energy window $E_\mathrm{F} \pm 8\,\mathrm{eV}$. In the cubic *bcc* environment, $\mathrm{t_{2g}}$ and $\mathrm{e_g}$ belong to different irreducible representations and are orthogonal on site, so the projected DOS provides a clean decomposition of the local d manifold. Around (and below) E_F the total DOS is dominated by $\mathrm{t_{2g}}$ and $\mathrm{e_g}$ contributions; with increasing pressure their ratio decreases

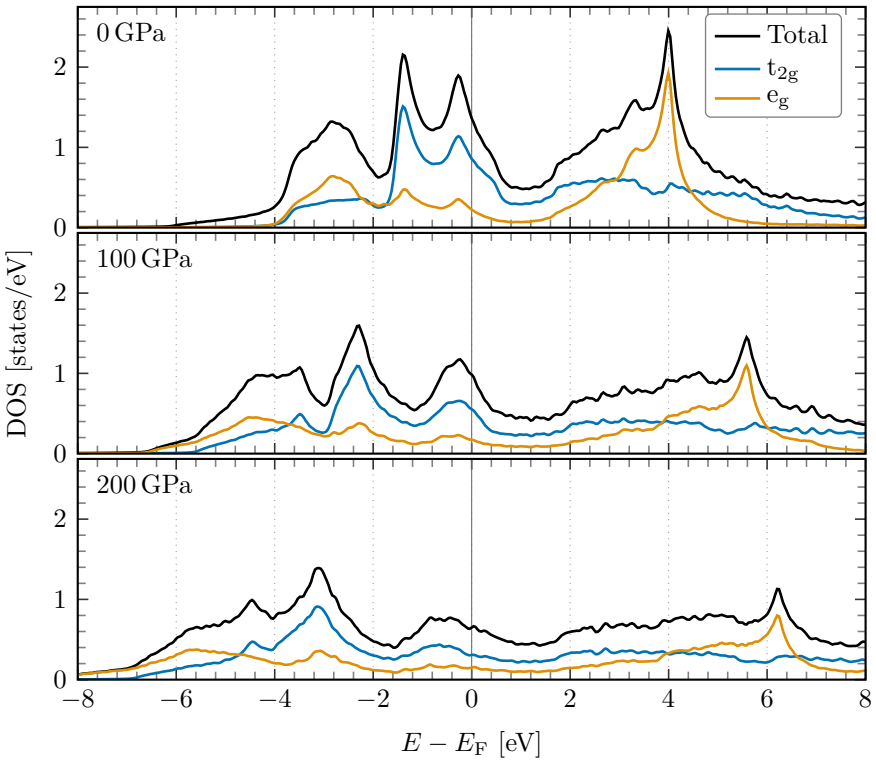

Figure 34: Orbital-resolved 4*d* (t_{2g}, e_g) electronic density of states of pure Nb in an energy window around E_F computed using LDA including the core 4s and semi-core 4p states. Note the decrease in magnitude with increasing pressure.

slightly, and a continuous suppression of the DOS in the immediate vicinity of E_F is observed. Within our accuracy, all *d* channels respond similarly to compression, and we do not find evidence for orbital selectivity.

Qualitatively, such a suppression of $N(E_F)$ with pressure is expected from increased hopping amplitudes and concomitant bandwidth growth upon volume reduction. Quantitatively, however, the trend reflects a nontrivial interplay of band-structure effects, substitutional disorder, and dynamical electronic correlations, which cannot be cleanly disentangled within a single-parameter picture.

11.3 Pressure and electronic correlation effects in $Nb_{0.44}Ti_{0.56}$

Due to the numerical challenges associated with DMFT computations, we adopt a reduced EMTO basis restricted to *spd* states and truncate the complex-energy contour used for evaluating the EMTO Green's function to 1 Ry. We validated this setup against the reference parameters of Sec. 11.1.1 (extended *spdf* basis, 3.5 Ry contour), keeping all other settings identical. The comparison shows no significant changes in the electronic density of states within an energy window of $E_F \pm 10$ eV, including $N(E_F)$ and the positions/intensities of the main spectral features. In particular, the near-E_F dispersions and Fermi-surface sheets are indistinguishable within our numerical resolution, confirming that the simplified setup is sufficient for the analysis presented below.

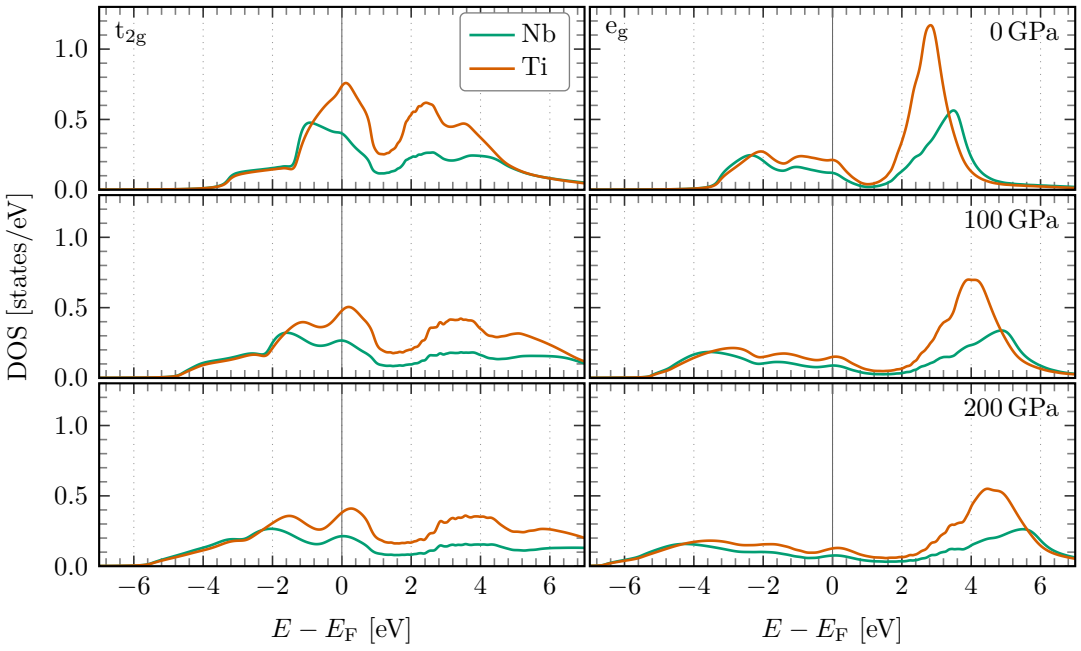

Figure 35: Orbital-resolved electronic densities of states of $Nb_{0.44}Ti_{0.56}$ at different pressures, for the non-interacting case, $U = J = 0$, computed using LDA with a reduced *spd* basis.

Figure 35 shows the orbital-projected densities of states of $Nb_{0.44}Ti_{0.56}$ up to 200 GPa in the non-interacting limit ($U = 0$, $J = 0$). Due to the cubic symmetry of the system, no mixture (hybridization) occurs between the t_{2g} and e_g orbitals, and accordingly, the local Green's function is diagonal in the orbital basis. Across all investigated pressures, the Ti-t_{2g} contribution dominates $N(E_F)$, with Nb-t_{2g} providing an additional, sizable weight in the energy window $E_F - 2\,\text{eV} \leq E \leq E_F + 1\,\text{eV}$. By contrast, the e_g weight at E_F remains at least a factor of four smaller than the t_{2g} weight at any pressure. These trends indicate that the low-energy carriers are predominantly of t_{2g} character on both Nb-4*d* and Ti-3*d* sites. While this points to t_{2g}-dominated states as the most relevant for superconductivity, a quantitative assessment ultimately depends on the electron-phonon matrix elements (e.g., via $\alpha^2F(\omega)$ or Hopfield parameters). Here we confine ourselves to the electronic-structure trends that set the stage for such analyses. At the non-interacting LDA level ($U = J = 0$), the spectral features of $Nb_{0.44}Ti_{0.56}$ are noticeably broader than in elemental Nb, reflecting finite-lifetime effects from substitutional disorder encoded in the imaginary part of the CPA self-energy.

Figure 36 compiles the total DOS at representative pressures, comparing calculations with and without DMFT corrections. For interaction parameters, we adopt the same parameters discussed in the previous chapter 10: For $U \geq 2\,\text{eV}$ we fix Hund's coupling to $J = 0.6\,\text{eV}$. For $U < 2\,\text{eV}$ we keep the ratio $U/J = 2/0.6 \approx 3.33$ so that the effective intra-orbital repulsion $U - 3J$ remains positive in the rotationally invariant multi-orbital interaction used in DMFT. Increasing J up to 0.9 eV leaves the calculated spectral functions essentially unchanged within our resolution, indicating a weak sensitivity to J in the pressure range considered.

Including local correlations within DMFT adds an additional finite-lifetime contri-

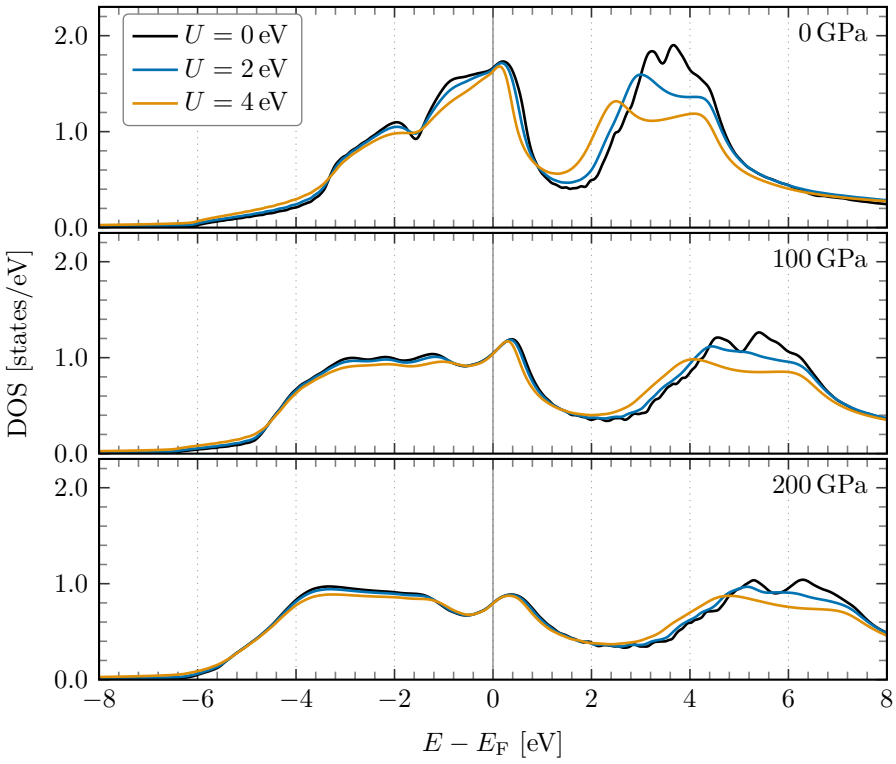

Figure 36: Total electronic densities of states of $Nb_{0.44}Ti_{0.56}$ computed using LDA+DMFT at different pressures and interaction strengths U, J as described above.

bution through the imaginary part of the self-energy, which broadens the alloy spectra beyond the CPA-only (LDA) case. Relative to the non-interacting limit, we observe a gradual suppression of the DOS in the immediate vicinity of E_F together with the development of longer tails near the band edges. Across the tested interaction range ($U \leq 5\,\mathrm{eV}$ with the J protocol specified above), the value of $N(E_F)$ remains essentially pinned within our numerical accuracy, consistent with a coherent Fermi-liquid regime of the low-energy quasiparticles. Overall, the total spectral functions change only weakly upon including correlations, with the most visible effects being a modest near-E_F depletion and disorder, plus correlation-induced broadening away from E_F (see Fig. 36).

To further characterize correlation effects, Fig. 37 shows the orbital-resolved imaginary parts of the self-energy. The inset shows analytically continued retarded self-energies on the real axis computed with Padé approximants discussed in Section 9.2, which display the expected quadratic behavior in the vicinity of the Fermi level, $\mathrm{Im}\,\Sigma(E) \propto -(E - E_F)^2$. Both t_{2g} and e_g channels exhibit indicators consistent with Fermi-liquid (FL) coherence. As anticipated, the corresponding mass enhancements differ between the two orbital sectors. Our quantitative discussion focuses again on the Matsubara axis to avoid possible artifacts of analytic continuation. In a Fermi-liquid, the low-frequency imaginary part of the self-energy is linear in ω_n,

$$\mathrm{Im}\,\Sigma^{\sigma}_{(l,m)}(\omega_n) \simeq -\Big[(Z^{\sigma}_{(l,m)})^{-1} - 1\Big]\omega_n, \tag{11.2}$$

where $Z^{\sigma}_{(l,m)}$ is the quasiparticle weight for orbital (l, m) and spin σ as we have already seen in Ch. 10, specifically in Eq. (10.10). At low ω_n, both $\mathrm{Im}\,\Sigma_{t_{2g}}(i\omega_n)$ and $\mathrm{Im}\,\Sigma_{e_g}(i\omega_n)$

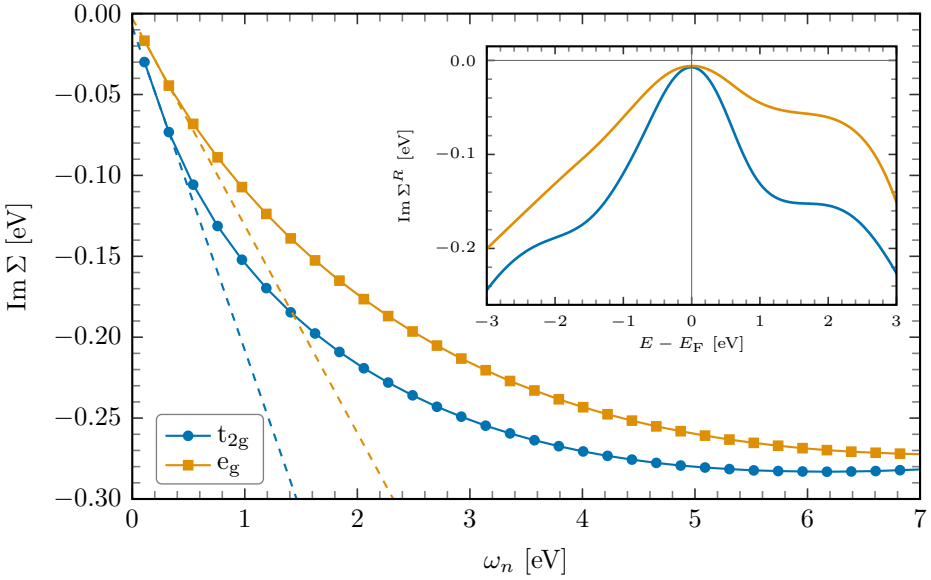

Figure 37: Imaginary part of the self-energies as a function of the Matsubara frequencies, ω_n, of the Ti t_{2g} and e_g orbitals in $Nb_{0.44}Ti_{0.56}$ as obtained from LDA+DMFT, with $U = 2\,\text{eV}$ and $J = 0.6\,\text{eV}$, at 400 K and ambient pressure (0 GPa). The inset shows the parabolic dependence of the imaginary part of the retarded self-energy on energy E around E_F, confirming the Fermi-liquid behavior. The non-zero (though tiny) value at $E = E_F$, seen in the inset, is due to the error inherent in the analytic continuation procedure.

extrapolate linearly to zero, indicating long-lived quasiparticles with a vanishing scattering rate at the Fermi surface. This linear low-ω_n behavior persists across the simulated temperature window $100\,\text{K} \leq T \leq 400\,\text{K}$, consistent with a coherent metallic regime.

Within DMFT the quasiparticle mass enhancement becomes a local quantity that can be estimated on the Matsubara axis. Analogously to Eq. (10.11) of the previous section, m^* can be determined in the zero-temperature limit as

$$\frac{m^*}{m} = 1 - \left.\frac{\text{Im}\,\Sigma(\text{i}\omega_n)}{\omega_n}\right|_{\omega_n \to 0} . \tag{11.3}$$

In practice, we follow the standard DMFT protocol and extract this slope using a linear fit to the first few Matsubara points [74]. The dashed lines in Fig. 37 indicate these fits for the t_{2g} and e_g channels.

The resulting mass enhancements m^*/m are compiled in Fig. 38 for interaction strengths up to $U = 5\,\text{eV}$. At all simulated temperatures, m^*/m increases monotonically with U for both orbital sectors. While the absolute values are slightly reduced at higher T, the overall U-dependence remains unchanged. Taken together with the pressure trends discussed above, this behavior supports the conclusion that correlation effects weaken under compression. We find no indications of an orbitally selective response: within our numerical resolution the t_{2g} and e_g effective masses track each other as functions of pressure and interaction strength. Consequently, at the highest pressures considered, sizable anisotropies in a prospective superconducting order parameter appear unlikely, and the anomalous Green's functions for t_{2g} and e_g sectors

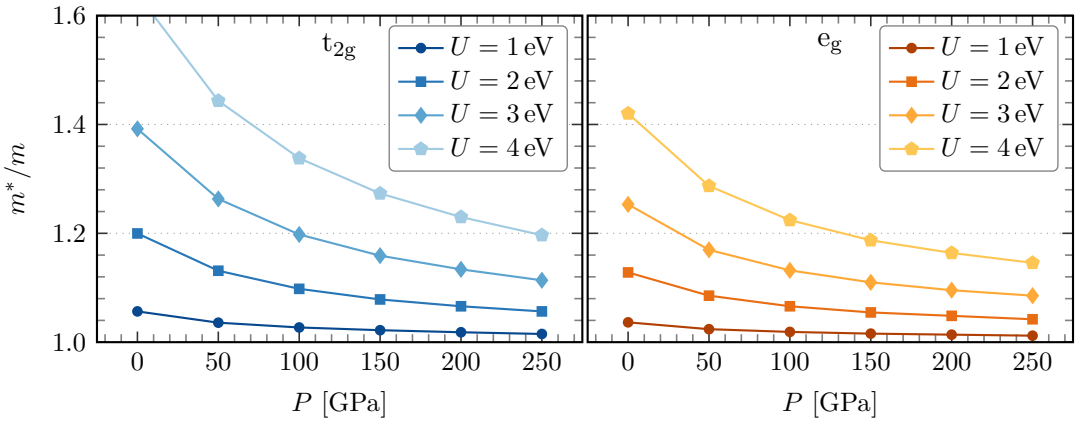

Figure 38: Pressure dependence of the effective mass renormalization of the t_{2g} and e_g orbitals for various interaction strengths U. For the choice of J, see text.

would be expected to display similar behavior. Inter-orbital pairing channels are not anticipated to play a significant role.

Additionally, the temperature dependence of the extracted quasiparticle masses is shown in Fig. 39. At fixed interaction strength, $m^\star/m$ decreases monotonically with increasing pressure and, by 250 GPa, approaches the band value within our numerical accuracy. This reduction of the many-body renormalization reflects the pressure-driven bandwidth growth W and the resulting decrease of the ratio U/W. Equivalently, the low-frequency slopes $\partial_\omega \operatorname{Re}\Sigma(\omega)\big|_{E_\mathrm{F}}$ and $\operatorname{Im}\Sigma(\mathrm{i}\omega_n)/\omega_n$ are diminished, indicating weaker local correlations. The trend is robust across all tested U and T: while higher temperatures yield slightly smaller absolute enhancements, the qualitative pressure dependence is unchanged. Throughout, we do not resolve any orbitally selective behavior – t_{2g} and e_g masses track each other – consistent with the absence of pronounced anisotropies suggested by the DOS and self-energy analyses above.

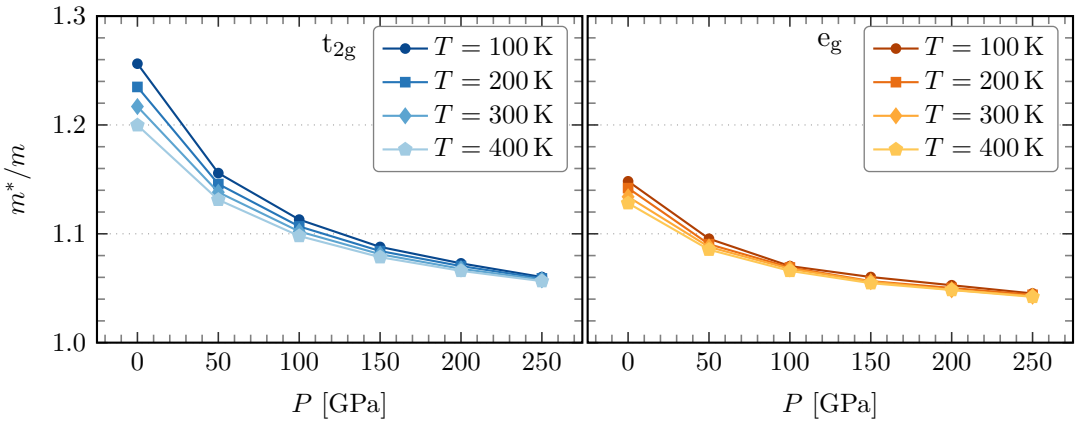

Figure 39: Pressure dependence of the effective mass renormalization of the t_{2g} and e_g orbitals for various temperatures T and fixed interaction strength $U = 2\,\mathrm{eV}$ and $J = 0.6\,\mathrm{eV}$.

11.4 Fermi surfaces of Nb and Nb–Ti alloys

Figure 40 displays central Fermi-surface (FS) cross-sections for elemental Nb and for $Nb_{0.44}Ti_{0.56}$ at selected pressures. The triangular sector ΓHN corresponds to the central (100) plane, while the rectangular region $\Gamma HNPN$ represents the central (110) plane. High-symmetry points are labeled following the standard bcc convention:

$$\Gamma = (0,\, 0,\, 0), \quad H = (1,\, 0,\, 0), \quad N = \left(\tfrac{1}{2},\, \tfrac{1}{2},\, 0\right), \quad P = \left(\tfrac{1}{2},\, \tfrac{1}{2},\, \tfrac{1}{2}\right) \tag{11.4}$$

given in units of $2\pi/a$ of the bcc reciprocal lattice. These two sections sample complementary Fermi-velocity directions – $\Gamma \to H$ ([100]), $\Gamma \to N$ ([110]), and $\Gamma \to P$ ([111]) – and thus capture the pressure evolution of the principal FS sheets with minimal redundancy.

The Fermi surfaces are constructed from the momentum-resolved spectral function at the Fermi level,

$$A_{l,m}(\boldsymbol{k},\, E_\mathrm{F}) = -\frac{1}{\pi}\,\mathrm{Im}\, G_{l,m}(\boldsymbol{k},\, E_\mathrm{F} + \mathrm{i}0^+)\,, \tag{11.5}$$

where $G(\boldsymbol{k},\, z)$ includes the CPA effective medium and the local DMFT self-energy. For reference, the (100) cut (ΓHN) emphasizes the Γ-centered sheet and its approach to the HN edge under compression, whereas the (110) cut ($\Gamma HNPN$) resolves features along Γ-H and Γ-N simultaneously and highlights possible changes near the P point. For a discussion of the band structure, the momentum-resolved spectral function $A(\boldsymbol{k},\, E)$ is shown in Appendix B.

The left column of Fig. 40 shows elemental Nb, with pressure increasing from top to bottom. A pronounced reshaping of the Fermi surface with compression is apparent. At ambient conditions ($P = 0$), the zone center (Γ) hosts a hole-like sheet with a distorted octahedral shape, commonly referred to as the "jack", while at the N points one finds a pair of distorted ellipsoids, together with additional hole sheets extending from Γ toward H along the $\langle 100\rangle$ directions, the so-called "jungle-gym" network [214]. Within the central (100) cut (ΓHN triangle), the jack and the jungle-gym touch at two symmetry-related locations. These high-intensity contact points lie along a direction perpendicular to the Σ line (i.e., normal to $\Gamma \to N$) and are symmetrically placed about ΓN at approximately

$$(0,\, -0.22,\, 0.62)\,\frac{\pi}{a} \quad \text{and} \quad (0,\, -0.62,\, 0.22)\,\frac{\pi}{a},$$

with the corresponding star of equivalent points generated by cubic symmetry. As pressure increases, these characteristic sheets deform continuously (see successive panels), while their connectivity within the (100) and (110) sections remains clearly identifiable across the investigated range. A further contact occurs along the Γ-P line (the Λ direction). In the central (110) section ($\Gamma HNPN$), this manifests as a high-intensity, quasi-linear feature extending toward P within the plane.

Earlier calculations at modest compression (6 GPa and 26 GPa) reported no substantial changes in the FS topology of Nb [217–219]. Augmented-plane-wave calculations further indicated that the N-H branch of the third band crosses the Fermi level only under pressure, which could account for the disappearance of the neck connecting the

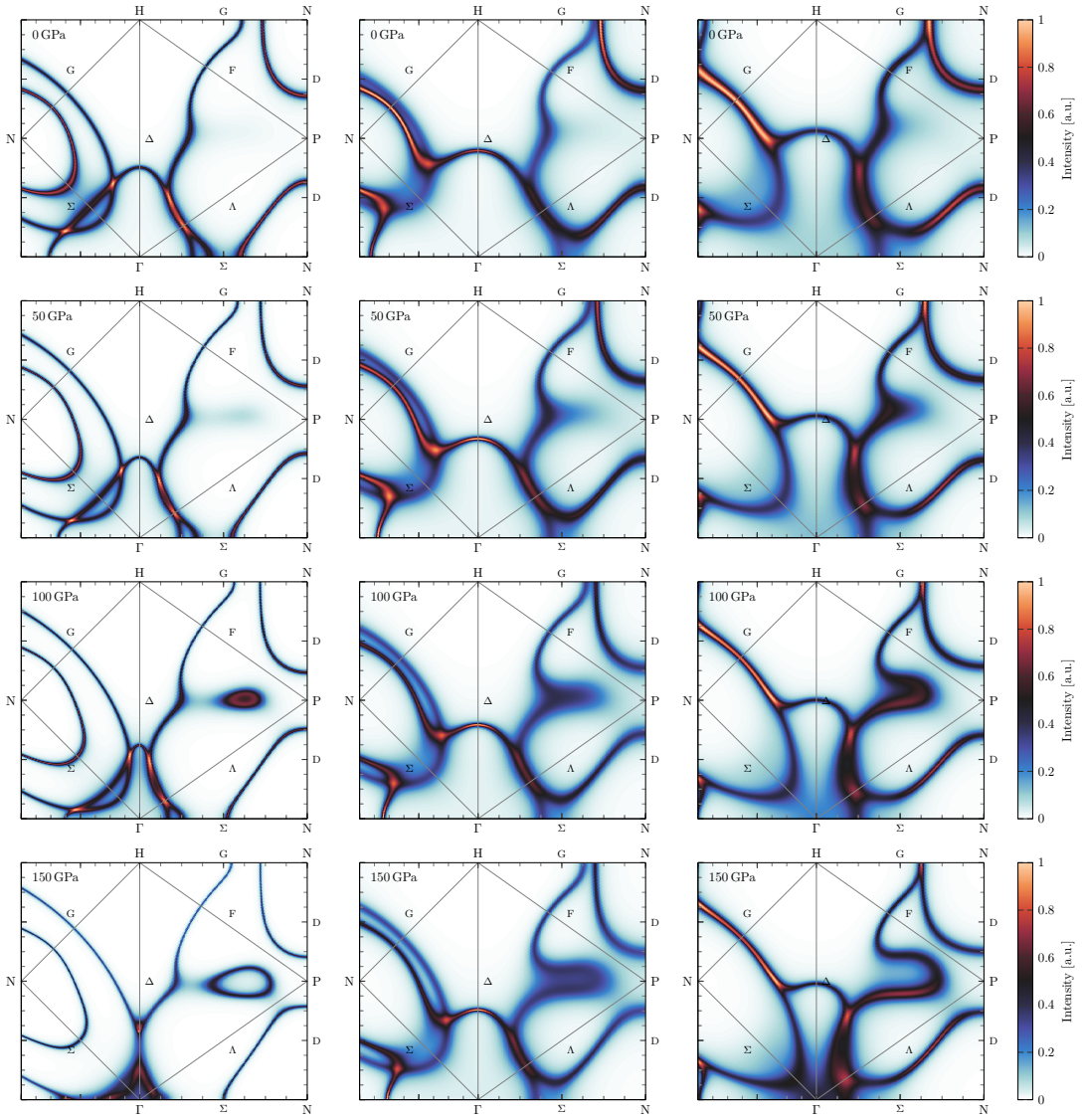

Figure 40: The evolution of the Fermi surface with pressure. The first column represents the LDA Fermi surface of bulk Nb at ambient pressure, 50 GPa, 100 GPa and 150 GPa. The second and the third column, respectively, show the Fermi surfaces for the $Nb_{0.44}Ti_{0.56}$ alloy using LDA(+CPA) and LDA(+CPA)+DMFT ($U = 2\,\text{eV}$, $J = 0.6\,\text{eV}$, $T = 400\,\text{K}$). The symmetry points in the first Brillouin zone of the body centered cubic (*bcc*) lattice are given by $\Gamma = (0,\, 0,\, 0)$, $H = (0,\, 0,\, 2\pi/a)$, $P = (\pi/a,\ \pi/a,\ \pi/a)$, and $N = (0,\ \pi/a,\ \pi/a)$, where a is the lattice constant.

N-centered ellipsoids to the jungle-gym network [220]. In parallel, the reduction of T_c observed above about 70 GPa was attributed to the Fermi level entering a region of reduced density of states [219, 221]. Our results reveal a clear and continuous pressure evolution of the salient FS features. Around Γ, the octahedral ("jack") sheet shrinks monotonically with increasing pressure. By 150 GPa its volume is significantly reduced. Within the (100) section, the pair of ellipsoids near N expands with pressure and their contact points with the jack separate progressively. In the rectangular (110) cut ($\Gamma HNPN$), a hole band first touches the Fermi level at 50 GPa; by 100 GPa it

develops into an oval pocket whose in-plane area continues to grow upon further compression. The center of this emerging hole pocket is located near (0.63, 0.63, 1.00) π/a in reciprocal-lattice units.

The central and right columns of Fig. 40 display the FS of $Nb_{0.44}Ti_{0.56}$ obtained from LDA(+CPA) (middle) and LDA(+CPA)+DMFT (right) at $U = 2\,\mathrm{eV}$, $J = 0.6\,\mathrm{eV}$, and $T = 400\,\mathrm{K}$. In contrast to elemental Nb, all alloy spectra are broadened: in the CPA panels the linewidth stems from the (complex) single-site disorder self-energy, while in the DMFT panels an additional broadening arises from the local, frequency-dependent many-body self-energy. As pressure increases, the Γ-centered octahedral sheet shrinks also in the alloy. However, the volume reduction is less pronounced than in pure Nb. The N-centered ellipsoids show a characteristic intensity redistribution: at ambient pressure the outer ellipsoid is comparatively diffuse while the inner one is sharp; with increasing pressure the two ellipsoids separate and spectral intensity shifts toward the outer sheet. Notably, the coordinates of the contact points between the Γ octahedron and the N-ellipsoids within the (100) cut remain nearly unchanged upon compression. Analogous to pure Nb, the jungle-gym features in the (110) rectangle ($\Gamma HNPN$) evolve once $P \gtrsim 50\,\mathrm{GPa}$. A previously occupied band is promoted toward E_F and becomes visible near (0.61, 0.61, 1.03) π/a. In the alloy, however, this band does not form a closed hole pocket: the lobes detach along the Λ and F directions, while the "neck" in the vicinity of P is reduced in cross-section. Overall, CPA lifetime effects dominate the broadening, with DMFT adding a modest, sheet-selective damping without altering the qualitative FS topology over the investigated pressure range.

Finally, we summarize the DMFT Fermi surfaces obtained for $U = 2\,\mathrm{eV}$, $J = 0.6\,\mathrm{eV}$, and $T = 400\,\mathrm{K}$. Within our resolution, varying U, J, or T in the tested ranges does not produce qualitative changes in the FS topology or connectivity. At $P = 0$, the most conspicuous DMFT-induced modification relative to the CPA result is the Γ-centered hole volume: it becomes more distorted and slightly larger. Upon compression, however, this feature shrinks monotonically, in line with the overall bandwidth increase. In the triangular ΓHN section (central (100) plane), the N-centered ellipsoids remain connected across the explored pressures and grow in size with increasing P, contributing to the progressive suppression of the Γ-octahedron. In the (110) plane ($\Gamma HNPN$ rectangle), correlation effects accentuate the jungle-gym distortions: FS boundaries acquire stronger intensity (reflecting enhanced spectral weight gradients), and the lobes along the Λ and F directions become more elongated with pressure. The contact feature along ΓP separates from the extended touching line within the (110) plane Its spectral intensity increases at higher pressures, while the neck near P is further reduced. Overall, DMFT adds sheet-selective damping and modest reshaping without altering the alloy's FS connectivity established at the CPA level.

We now turn to a discussion of the Fermi-liquid characteristics of the Fermi surface of $Nb_{0.44}Ti_{0.56}$. According to the Fermi-liquid picture, the low-energy behavior of electrons can be described in terms of interacting quasiparticles, and their collective excitations. The Landau phenomenological theory assumes a one-to-one correspondence between the quasiparticle excitations of the interacting system and the single-particle excitations of the non-interacting electron system. This correspondence implies that the volume of the FS of interacting quasiparticles is related to the electron density in the same manner as for non-interacting electrons [222]. Luttinger and Nozières [223–225] justified

the Landau assumption using many-body perturbation theory, establishing the relation between the Fermi surface volume and the electron density, commonly referred to as the Luttinger theorem or Luttinger sum rule. However, deviations from the Luttinger sum rule have been observed in impurity models [226], which lead to the distinction between Fermi and Luttinger surfaces. In our computations, we find that the Luttinger sum rule is satisfied. Technically, the total electron number is determined from the spectral function derived from the one-electron Green's function:

$$N = -\frac{1}{\pi} \sum_{(l,m),\sigma,\boldsymbol{k}} \int_{-\infty}^{E_\mathrm{F}} \mathrm{d}E \, \mathrm{Im}\, G^{\sigma}_{(l,m)}(\boldsymbol{k},\, E + \mathrm{i}\eta)\Big|_{\eta\to 0^+} \tag{11.6}$$

The interacting retarded Green's function $G^{\sigma}_{(l,m)}(\boldsymbol{k},\, z)$ is evaluated along the complex contour $z = E + \mathrm{i}0^+$, and incorporates the DMFT self-energy, $\Sigma^{\sigma}_{(l,m)}(z)$. The lattice Green's function includes the local, frequency-dependent DMFT self-energy,

$$G^{\sigma}_{(l,m)}(\boldsymbol{k},\, z) = \left[z - \epsilon^{\sigma}_{(l,m)}(\boldsymbol{k}) - \Sigma^{\sigma}_{(l,m)}(z)\right]^{-1}, \tag{11.7}$$

with $\epsilon^{\sigma}_{(l,m)}(\boldsymbol{k})$ the bare band dispersion of the CPA effective medium. Within Landau theory, quasiparticles are associated with poles of G,

$$G^{\sigma}_{(l,m)}(\boldsymbol{k},\, z) \simeq \frac{Z^{\sigma}_{(l,m)}(\boldsymbol{k},\, z)}{z - \tilde{\epsilon}^{\sigma}_{(l,m)}(\boldsymbol{k},\, z) + i\Gamma^{\sigma}_{(l,m)}(\boldsymbol{k},\, z)} + \text{incoh.}, \tag{11.8}$$

where $\tilde{\epsilon}^{\sigma}_{(l,m)}$ represents the quasiparticle energy, $Z^{\sigma}_{(l,m)}$ the quasiparticle weight, and $\Gamma^{\sigma}_{(l,m)}$ the scattering rate (broadening). In DMFT the self-energy is $\boldsymbol{k}$-independent, so Z and Γ are momentum independent (but orbital and spin dependent). As shown in Fig. 37, the self-energies satisfy the FL criteria near E_F across the simulated temperature and pressure ranges. Consistently, the effective-mass enhancements extracted from the low-Matsubara-frequency slopes (Sec. 11.1 and Fig. 38) are modest, decrease with pressure, and show no evidence for orbital selectivity, in line with the DOS and FS analyses presented above.

In the translationally invariant CPA medium and for the paramagnetic state, the lattice Green's function is diagonal in crystal momentum and spin, so that the quasiparticle dispersion may be written as

$$\tilde{\epsilon}^{\sigma}_{(l,m)}(\boldsymbol{k},\, z) = Z^{\sigma}_{(l,m)} \left[\epsilon^{\sigma}_{(l,m)}(\boldsymbol{k}) + \mathrm{Re}\, \Sigma^{\sigma}_{(l,m)}(z)\right]. \tag{11.9}$$

The corresponding quasiparticle density of states follows from integrating the spectral function over the Brillouin zone,

$$\tilde{N}^{\sigma}_{(l,m)}(E) = \frac{1}{V_{BZ}} Z^{\sigma}_{(l,m)} \sum_{\boldsymbol{k}} \delta\left(E - \tilde{\epsilon}^{\sigma}_{(l,m)}(\boldsymbol{k},\, E)\right), \tag{11.10}$$

such that the total electron count is, to leading order in the Fermi-liquid expansion,

$$N \simeq \sum_{(l,m),\sigma} \int_{-\infty}^{E_\mathrm{F}} \mathrm{d}E \; \tilde{N}^{\sigma}_{(l,m)}(E). \tag{11.11}$$

Figure 36 display the $(l,\, m)$- and σ-traced, $\boldsymbol{k}$-integrated spectral functions for the nonmagnetic, self-consistent solutions at representative U and T. Despite the locality of

DMFT and the perturbative character of the employed impurity solver, our calculations satisfy the Luttinger sum rule within numerical accuracy. Concretely, the electron number obtained from Eq. (11.6) matches the imposed filling at all pressures and interaction strengths, with the difference between the interacting and reference LDA chemical potentials bounded by

$$\Delta E_{\mathrm{F}} = \tilde{E}_F - E_{\mathrm{F}}^{\mathrm{LDA}} \approx 10^{-5}\,\mathrm{Ry} \tag{11.12}$$

for all U and P. The preservation of the Luttinger count is ensured by the fully charge- and self-energy-self-consistent LDA+DMFT cycle, which restores translational invariance to the impurity problem and guarantees a momentum-diagonal lattice Green's function. As shown in Fig. 37, the low-energy self-energies obey the Fermi-liquid constraints around E_{F}; correspondingly, the effective-mass enhancements extracted from the Matsubara slopes (Fig. 39) behave smoothly with pressure and temperature, without indications of orbital selectivity.

11.5 Summary

In this chapter we analyzed the pressure evolution of the *normal-state* electronic structure of elemental Nb and the disordered bcc alloy $Nb_{0.44}Ti_{0.56}$ up to $P = 250\,\mathrm{GPa}$ within a Green's-function LDA(CPA)+DMFT framework. The motivation is provided by the experimental contrast that T_{c} in pure Nb decreases under compression, whereas $Nb_{0.44}Ti_{0.56}$ shows an increasing $T_{\mathrm{c}}(P)$ [219]. While we do not compute T_{c} directly here, our results establish the pressure-dependent quasiparticle spectra and Fermi surfaces that underpin such superconducting trends.

For elemental Nb, compression leads to a continuous suppression of the $4d$ density of states at the Fermi level (Fig. 34), consistent with the established interpretation of the reduced T_{c} at high pressure in terms of a diminished $N(E_{\mathrm{F}})$ [219, 221]. At the same time, we find a pronounced reshaping of the Fermi surface (Fig. 40): the Γ-centered hole sheet ("jack") shrinks with increasing pressure, the N-centered ellipsoids expand and separate from the jack in the (100) cut, and, most notably, a hole band is promoted to the Fermi level in the (110) section and develops into a distinct pocket whose cross-section grows upon further compression.

For $Nb_{0.44}Ti_{0.56}$, CPA captures the dominant disorder-induced lifetime effects: already at the LDA(+CPA) level the spectral features are substantially broadened compared to pure Nb (Figs. 35 and 36). Including DMFT adds an additional (correlation-induced) damping and a modest near-E_{F} depletion, but the overall low-energy DOS scale remains essentially pinned within our numerical accuracy across the tested interaction range. Orbital-resolved spectra show that the low-energy carriers are predominantly of t_{2g} character on both Ti and Nb sites, while the e_g weight at E_{F} is comparatively small (Fig. 35). Within our resolution we find no orbitally selective response to pressure: t_{2g} and e_g channels display similar qualitative pressure trends in the DOS and self-energies. In momentum space, all alloy Fermi-surface sheets are broadened, with CPA providing the main contribution to the linewidth and DMFT adding a modest, sheet-dependent damping without changing the overall FS connectivity (Fig. 40). Under pressure the Γ-centered hole volume also decreases in the alloy,

but the additional band promoted toward E_{F} does not form a closed pocket in the same manner as in elemental Nb.

The CPA+DMFT solutions remain consistent with coherent Fermi-liquid quasiparticles throughout the explored pressure range. The Matsubara self-energies exhibit the low-frequency linear behavior expected for a Fermi liquid and the retarded self-energies show the corresponding quadratic dependence near E_{F} (Fig. 37). The extracted effective-mass enhancements are moderate (up to ~ 1.5), decrease monotonically with pressure, and track each other between $\mathrm{t_{2g}}$ and $\mathrm{e_g}$ sectors (Figs. 38 and 39), indicating a pressure-driven weakening of local correlations consistent with bandwidth growth. In addition, the fully self-consistent LDA+DMFT cycle preserves the Luttinger electron count within numerical accuracy (Sec. 11.4), i.e., the quasiparticle Fermi surfaces remain consistent with the imposed filling despite substantial substitutional disorder and finite lifetimes.

Finally, it is useful to relate these findings to the Ti–V alloys discussed in Ch. 10, which share the same β-phase (bcc) structural setting. There, an optimal Ti concentration of $x \approx 0.33$ produces an enhanced superconducting transition temperature, while the normal state remains a correlated Fermi liquid with moderate mass renormalization and well-defined quasiparticles. In the present Nb–Ti system we likewise find that, even under compression up to $P = 250\,\mathrm{GPa}$, the normal state remains within the Fermi-liquid regime and the Fermi-surface sheets retain coherent quasiparticle character, with disorder providing the dominant contribution to the linewidth and local correlation effects becoming weaker with increasing pressure. Taken together, the two studies underscore that a quantitative description of superconductivity in these bcc transition-metal alloys is tightly constrained by (and must be consistent with) the correlated, disorder-broadened normal-state quasiparticle structure.

12 Correlated electronic states at a ferromagnetic oxide interface [P3]

The appearance of magnetism at the interface between $LaAlO_3$ (LAO) and $SrTiO_3$ (STO) thin films is one of the most intriguing examples of emergent behavior in oxide heterostructures [227]. Experimentally, the magnetic signal is largely confined to the interface region, persists up to room temperature, and, at low temperature, it can coexist with superconductivity [228, 229]. A particularly striking phenomenology is the formation of μm-sized ferromagnetic domains which can align in an external magnetic field, giving rise to superparamagnetic response [228, 229]. These observations point to an electronic state at the n-type LAO/STO interface in which localized moments and itinerant carriers are simultaneously present and mutually coupled.

A growing body of evidence suggests that oxygen vacancies are central to this dual character [230–233]. As electron dopants, oxygen vacancies can bind two electrons each and thereby drive an otherwise band-insulating environment metallic. In STO-based surfaces and interfaces, a nontrivial interplay between localized and itinerant electrons is indeed suggested by scanning-tunneling spectroscopy [234, 235], magnetoresistance and anomalous Hall-effect measurements [236, 237], as well as angle-resolved photoelectron spectroscopy and photoemission experiments [238–241]. A consistent microscopic description must therefore account, at the same time, for (i) the local defect physics that generates moments and (ii) the correlated itinerant carriers that mediate long-wavelength transport and magnetic response.

From a theoretical perspective, realistic accounts of LAO/STO are challenging because correlation effects, multiorbital band structure, and interfacial structural reconstruction all enter on comparable energy scales. For the *stoichiometric* heterostructure, first-principles calculations typically find a metallic but non-magnetic state, with partially filled Ti t_{2g}-dominated bands at the Fermi level [231, 242, 243]. Hybrid-functional studies confirm this picture while improving control over the band gap as a function of LAO overlayer thickness [244]. At the same time, the analysis of tunneling spectroscopy has suggested early on that electronic interactions are strong enough for the interfacial electron system to be viewed as an electron liquid rather than a weakly interacting two-dimensional metal [234].

Introducing oxygen vacancies qualitatively changes the local electronic structure. DFT supercell studies indicate that, already for vacancy concentrations as low as 1/8, a multiorbital reconstruction occurs: Ti e_g-states in the vicinity of a vacancy become occupied and, together with the remaining O p-orbitals, form reconstructed $\tilde{e}_g$ molecular orbitals. The two electrons bound to a vacancy are found to form a triplet, implying a natural route to local-moment formation and suggesting a double-exchange-like mechanism for ferromagnetism at the interface [231]. Static correlation effects have been explored using effective Hubbard Hamiltonians at the Hartree–Fock level, yielding a defect- and carrier-concentration dependent magnetic phase diagram and robust magnetic states beyond a minimal vacancy concentration of order 0.1% [245]. For dilute disorder concentrations inaccessible to large supercells, single-band CPA studies support this conclusion and provide access to the low-impurity regime [246]. In

the dense-defect limit, the essential physics can be captured by a minimal two-orbital Hubbard model, and recent DFT+DMFT investigations have shown that ferromagnetic order in the interfacial TiO_2 layer can be understood in terms of an effective Zener double exchange between an $\tilde{e}_g$ orbital and an in-plane t_{2g} d_{xy}-orbital [243, 247, 248].

In the broader context of this thesis, LAO/STO provides a complementary testbed to the bulk transition-metal and alloy applications discussed earlier: here, reduced dimensionality and defect-induced inhomogeneity place the interplay of disorder and local dynamical correlations at center stage. Having established the methodological foundations of DMFT, CPA, and their combined DMFT+CPA framework in the preceding chapters (Chs. 4, 7 and 8), we now use this machinery in a minimal, interface-motivated model to address an emergent spectroscopic hallmark of correlated ferromagnets at oxide interfaces. Specifically, we formulate a tight-binding description for oxygen-vacancy induced magnetism at the LAO/STO interface and treat configurational disorder by the Coherent Potential Approximation (CPA), while including local electronic correlations via Dynamical Mean Field Theory (DMFT). The CPA is exact for non-interacting fermions with diagonal (local) disorder in the limit $Z \to \infty$ (with appropriate scaling of the hopping), making it a natural extension to DMFT, which becomes exact in the same limit for local interactions [249]. Within this combined CPA+DMFT scheme we investigate correlated itinerant fermions subject to the effective Zeeman field induced by magnetic impurities at the interface.

Electronic correlations in strongly spin-polarized systems are well known to generate qualitatively new spectral features beyond a simple quasiparticle description [250, 251]. In particular, half-metallic ferromagnets host incoherent non-quasiparticle (NQP) states: spectral weight appears in the gapped spin channel close to the Fermi level, while the corresponding density of NQP states vanishes at the Fermi level and is enhanced on an energy scale set by characteristic magnon frequencies (or, more generally, by low-energy spin excitations) [252–254]. First-principles studies have identified such NQP features in prototypical half-metals including NiMnSb [255], various Heusler alloys [256], zinc-blende compounds [257, 258], and CrO_2 [259]. Microscopically, NQP states originate from "spin-polaron" processes in which minority-spin excitations are entangled with collective spin fluctuations [253, 254]; intriguingly, related polaronic effects have also been discussed for LAO/STO interfaces [241]. In this chapter, we analyze a possible departure from the Fermi-liquid theory that may form at the LAO/STO interface in the presence of magnetic impurities.

12.1 Metallic magnetism at the interface: A simple model

To illustrate the real-space partitioning underlying the effective description of the interfacial TiO_2 layer, Fig. 41 (left) shows the interface plane containing an oxygen vacancy (OV) located between two nearest-neighbor Ti sites. Motivated by this local geometry, we decompose the interface plane (right) into elementary $O-Ti-O$ units (green) and vacancy-containing $O-Ti-OV$ units (red). At finite vacancy concentration, the number of $O-Ti-OV$ units increases accordingly. This decomposition suggests a natural "host–guest" viewpoint: the intact $O-Ti-O$ units form the "host" background of the interface, while $O-Ti-OV$ units act as embedded "guest" defect.

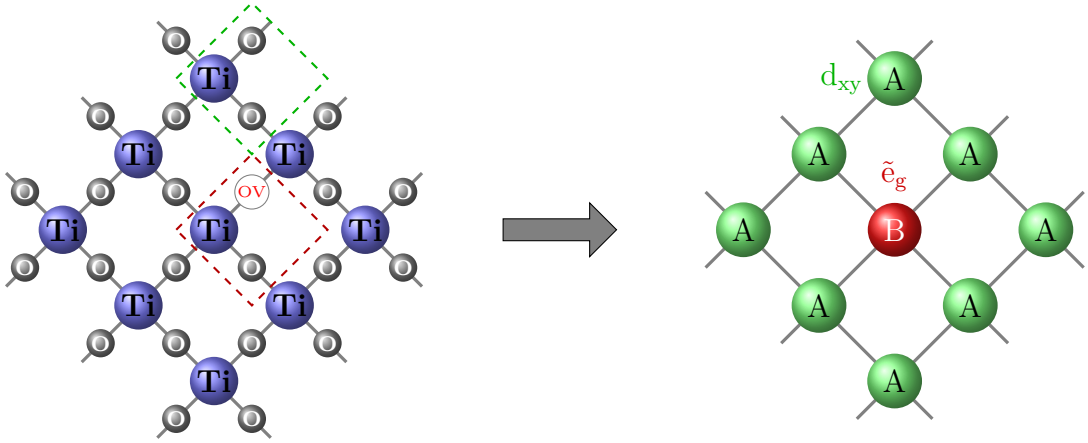

Figure 41: Left: The interface TiO_2-layer containing randomly distributed oxygen vacancies (OV). Right: Mapping onto an effective model of the molecular d_{xy} (A) $\equiv$ O − Ti − O (green) and $\tilde{e}_g$ (B) $\equiv$ O − Ti − OV (red) orbitals. A "local moment" is induced by oxygen vacancies at the B-sites.

Introducing A to denote a host unit O − Ti − O and B to denote a vacancy-containing unit O − Ti − OV, the interface plane can be mapped onto a substitutional binary-alloy problem of type $A_{1-c}B_c$, where c is the oxygen vacancy (OV) concentration.

Within this alloy representation, the local electronic structure depends on the component. For A sites, the relevant low-energy states are well captured by "molecular" orbitals associated with an intact TiO_2 unit, whereas for B sites the corresponding states are of TiO-molecular-orbital character due to the oxygen vacancy. For both local environments, the interfacial symmetry breaking lifts the bulk t_{2g} degeneracy and lowers the Ti d_{xy} level relative to the d_{xz} and d_{yz} orbitals. In the low-filling regime of interest here, the d_{xz} and d_{yz} orbitals remain essentially unoccupied, so that a single partially filled band of predominant d_{xy} character describes the itinerant degrees of freedom on the Ti sites. In contrast, the vacancy-bearing B units host additional, more localized states: hybridization between Ti e_g levels and the remaining oxygen p orbitals forms reconstructed $\tilde{e}_g$ orbitals [243, 245], which act as randomly distributed magnetic impurities embedded in the itinerant d_{xy} background.

Most material-specific descriptions of the LAO/STO interfacial electronic liquid take the DFT band structure as a starting point and construct a low-energy effective Hamiltonian by downfolding to a minimal two-orbital subspace, typically (d_{xy}, $\tilde{e}_g$). Local interaction terms are then added in Hubbard–Kanamori form, parameterized by U, U' and J, and the resulting two-band Hubbard model is treated with many-body techniques such as DMFT. Notably, the range of validity of this Hubbard-type formulation in the presence of a spin-polarized ground state and strong inhomogeneity due to vacancies is rarely addressed explicitly. A commonly invoked physical rationale is a Zener-type double-exchange mechanism, in which localized moments associated with OV-induced magnetic regions couple to itinerant d_{xy} carriers and thereby promote ferromagnetic correlations at the interface [243, 247, 248]. As an alternative perspective, it is worth recalling that ferromagnetic solutions can in fact be stabilized already within Hubbard-type models provided that (i) the noninteracting density of states carries substantial spectral weight near the band edges [260], and (ii) Hund's-rule coupling favors

spin polarization in the orbitally degenerate case [261].

In this chapter we concentrate on the dilute-defect regime, where a sparse distribution of vacancy-induced magnetic regions generates a stable ferromagnetic background via a Zener-type double-exchange mechanism. Within the minimal "alloy" picture introduced above, the itinerant carriers reside in a single effective band (predominantly of d_{xy} character), while vacancy-bearing units act as randomly distributed magnetic scatterers. This motivates an Anderson–Hubbard Hamiltonian with binary (A/B) local parameters and an additional spin-dependent potential on the B sites, treated as an effective Zeeman field.

Our numerical analysis starts from a simple Hubbard Hamiltonian of the form

$$\begin{aligned} \hat{H} &= \sum_{i,\sigma} v_{i,\sigma}\hat{n}_{i\sigma} - \sum_{\langle ij\rangle,\sigma} t_{ij}\hat{c}^{\dagger}_{i\sigma}\hat{c}_{j\sigma} + \sum_{i} U_i \hat{n}_{i\uparrow}\hat{n}_{i\downarrow}\,, \\ v_{i,\sigma} &= \varepsilon_i - \mu - \delta_{i,\mathrm{B}}\mathcal{B}\sum_{a,b}\hat{c}^{\dagger}_{ia}\sigma_z^{ab}\hat{c}_{ib}\,, \\ U_i &= U_{\mathrm{A}}\delta_{i,\mathrm{A}} + U_{\mathrm{B}}\delta_{i,\mathrm{B}}\,, \end{aligned} \tag{12.1}$$

where $\hat{n}_{i,\sigma} = \hat{c}^{\dagger}_{i,\sigma}\hat{c}_{i,\sigma}$ is the local number operator for an electron with spin σ on site i, μ is the chemical potential controlling the filling of the system, and the kinetic term describes nearest-neighbor hopping with amplitude t_{ij}. Within our simplified model, we neglect spatial and orbital dependence of the hopping, $t_{ij} \equiv t$, which is consistent with restricting to a single effective itinerant orbital per Ti site. The binary (A/B) character enters through the site-dependent on-site energies $\varepsilon_i = \varepsilon_{\mathrm{A/B}}$ and local interactions $U_i = U_{\mathrm{A/B}}$, where A denotes an intact $\mathrm{O-Ti-O}$ unit and B a vacancy-bearing $\mathrm{O-Ti-OV}$ unit. The delta functions $\delta_{i,\mathrm{A}}$ and $\delta_{i,\mathrm{B}}$ select whether site i belongs to the host or impurity component, respectively (with probabilities $1-c$ and c in the substitutional alloy $\mathrm{A}_{1-c}\mathrm{B}_c$). Local correlations are retained via the Hubbard term $U_i\hat{n}_{i,\uparrow}\hat{n}_{i,\downarrow}$ and are treated at the DMFT level. The spin-dependent contribution in $v_{i,\sigma}$ represents the exchange coupling between the itinerant d_{xy} carriers and the localized moments residing on the vacancy-related degrees of freedom. In practice, we treat these local moments in a mean-field spirit and replace their dynamics by a static Zeeman field $\mathcal{B}$ acting only on B sites. Equivalently, for $\delta_{i,\mathrm{B}} = 1$ the term $-\mathcal{B}\,\hat{c}^{\dagger}_{ia}\sigma_z^{ab}\hat{c}_{ib}$ induces a local spin splitting of the itinerant spectrum on the impurity sites. In principle, $\mathcal{B}$ may be determined self-consistently from the occupation and polarization of the vacancy-derived $\tilde{e}_g$ states; in the present minimal model it is taken as an effective input parameter that encodes the strength of the vacancy-induced exchange field. The label z on σ_z in Eq. (12.1) defines the quantization axis of the local moments that generate the field; experimentally, these moments are typically oriented in-plane [228, 229]. Since the impurity units are randomly distributed, configurational averaging is required. We perform this disorder average within a combined CPA+DMFT framework, in which the CPA accounts for the substitutional A/B randomness while DMFT captures the local dynamical correlations of the itinerant carriers. Within this realization of the interface physics, Kondo singlet formation is not included: the localized degrees of freedom are represented by an effective (classical) exchange field rather than a quantum spin that can be fully screened and, in the vacancy scenario, the underlying impurity moment is naturally closer to a spin-one object, for which screening would be incomplete.

12.2 CPA+DMFT computations for the Hubbard model

The computational strategy adopted here follows directly the methodological framework introduced earlier in this thesis: the DMFT mapping for local correlations (Ch. 4), the effective-medium description of substitutional disorder within CPA (Ch. 7), and their combined self-consistency in the CPA+DMFT scheme (Ch. 8). In our approach, we simplify the model by representing the effective impurity spins as a homogeneous external magnetic field acting only at the impurity sites. Furthermore, we consider a square lattice with the energy scale set to $4dt^2 = t^{*2}$ required for the non-trivial result as $d \to \infty$ and with the half-bandwidth $D = 2t^* = 2\,\mathrm{eV}$.

Within the binary-alloy representation, the A-type $\mathrm{d_{xy}}$ orbitals with on-site energy $\varepsilon_\mathrm{A} = 0.6D$ model the host, while a concentration $c = 20\%$ of magnetic impurities[1] is modeled by B-type $\tilde{\mathrm{e}}_\mathrm{g}$ orbitals with on-site energy $\varepsilon_\mathrm{B} = -0.6D$ and a Zeeman splitting parameter $\mathcal{B} = 0.4D$. This value of $\mathcal{B}$ is estimated from DFT results: the magnetic splitting of the $\mathrm{d_{xy}}$ bands is approximately 1.04 eV [231].

In the absence of the interaction term ($U = 0$), the magnetic field $\mathcal{B}$ in Eq. (12.1) can be included into the random potential $v_{i,\sigma}$ and treated within CPA. According to standard multiple scattering theory [122] (see also Ch. 7), the Hamiltonian can be divided into an unperturbed reference part and a perturbative term, $\hat{H}_\mathrm{ref} + \hat{H}_\mathrm{per}$. The reference Hamiltonian is

$$\hat{H}_\mathrm{ref}(z) = \sum_{\boldsymbol{k},\sigma} \left[\varepsilon_{\boldsymbol{k}} + \Sigma_\sigma^\mathrm{coh}(z)\right] \hat{c}^\dagger_{\boldsymbol{k}\sigma}\hat{c}_{\boldsymbol{k}\sigma} \tag{12.2}$$

in reciprocal space for an electron with dispersion $\varepsilon_{\boldsymbol{k}}$, moving in the energy-dependent effective medium described by a spin-dependent complex coherent potential $\Sigma_\sigma^\mathrm{coh}(z)$. The perturbative term containing the substitutional disorder is written as sum over all lattice sites,

$$\hat{H}_\mathrm{per} = \sum_{i,\sigma} w_{i,\sigma} \tag{12.3}$$

with

$$w_{i,\sigma} = -\delta_{i,\mathrm{B}}\mathcal{B}\sum_{a,b} \hat{c}^\dagger_{ia}\sigma_z^{ab}\hat{c}_{ib} + \left[\varepsilon_i - \mu - \Sigma_\sigma^\mathrm{coh}(z)\right]\hat{n}_{i\sigma}. \tag{12.4}$$

Given the coherent reference Green's function $G_{\mathrm{coh},\sigma}(z)$, the single-site t-matrix describing the scattering of an embedded alloy component at site i is

$$t_{i,\sigma}(z) = v_{i,\sigma}\left[1 - G_{\mathrm{coh},\sigma}(z)v_{i,\sigma}\right]^{-1}. \tag{12.5}$$

Note that $t_{i,\sigma}$ describes the complete scattering associated with the isolated potential in the effective medium and the reference system, and thus the reference Green's function does not contain the magnetic field contribution. The total scattering operator is then expressed in the usual multiple-scattering expansion,

$$T_\sigma(z) = \sum_i t_{i,\sigma}(z) + \sum_i t_{i,\sigma}(z)G_{\mathrm{coh},\sigma}(z)\sum_{j\neq i} t_{j,\sigma}(z) + \ldots. \tag{12.6}$$

[1] This amount of impurities is related to an approximate concentration of oxygen vacancies, which itself depends on sample preparation. Here we assume a low concentration of oxygen vacancies in order to keep a low filling consistent with most experiments.

Within the single-site approximation, the condition of $\langle t_{i,\sigma}\rangle = 0$ for any site i and spin σ leads to $\langle T_\sigma\rangle = 0$ and thus $\langle G_\sigma\rangle \approx G_{\mathrm{coh},\sigma}$, representing the CPA solution.

The local part of the coherent (spin-polarized) reference Green's function is given by the Hilbert transform of the non-interacting (and disorder-free) density of states $\rho(\epsilon)$:

$$G_{\mathrm{coh},\sigma}(z) = \frac{1}{N_k}\sum_{\boldsymbol{k}} \frac{1}{z - \varepsilon_{\boldsymbol{k}} - \Sigma_{\mathrm{coh},\sigma}(z)} = \int_{-D}^{D} \frac{\rho(\epsilon)}{z - \varepsilon - \Sigma_{\mathrm{coh},\sigma}(z)} \mathrm{d}\varepsilon. \tag{12.7}$$

Next, we incorporate local electronic correlations via a Hubbard interaction $U = U_{\mathrm{A}}$ acting on the host ($\mathrm{d_{xy}}$) orbitals only. For most evaluations we choose $U = t^*$, consistent with tunneling spectroscopy data [234]. In the combined CPA+DMFT self-consistency loop, we start from an initial guess for the coherent self-energy $\Sigma_{\mathrm{coh},\sigma}$. The local Green's function is computed from the electronic dispersion $\varepsilon_{\boldsymbol{k}}$ (eigenstates of the lattice Hamiltonian in the absence of disorder and electronic correlations) and the self-energy $\Sigma_{\mathrm{coh},\sigma}$ (Eq. 12.7). From the coherent (local) Green's function $G_{\mathrm{coh},\sigma}$, the alloy-component Green's functions are obtained as

$$G_{\alpha,\sigma}(z) = G_{\mathrm{coh},\sigma}(z)\left[1 - \Big(v_{\alpha,\sigma} + \Sigma_{\alpha,\sigma}(z) - \Sigma_{\mathrm{coh},\sigma}(z)\Big)G_{\mathrm{coh},\sigma}(z)\right]^{-1} \tag{12.8}$$

for $\alpha \in \{\mathrm{A}, \mathrm{B}\}$, where $v_{\alpha,\sigma}$ is the local potential of the alloy component α. The corresponding DMFT bath Green's function is then constructed according to

$$\mathcal{G}^{-1}_{\alpha,\sigma}(z) = G^{-1}_{\alpha,\sigma}(z) + \Sigma_{\alpha,\sigma}(z), \tag{12.9}$$

or, equivalently, via the hybridization function $\Delta_{\alpha,\sigma}$ as

$$\Delta_{\alpha,\sigma}(z) = z + v_{\alpha,\sigma} - \Sigma_{\mathrm{coh},\sigma}(z) - G^{-1}_{\alpha}(z). \tag{12.10}$$

Note that the chemical potential μ is included in the local potential $v_{\alpha,\sigma}$ and thus not explicitly shown in Eq. (12.10). Given $\Delta_{\alpha,\sigma}$ (or $\mathcal{G}_{\alpha,\sigma}$), the impurity problem is solved to obtain the component self-energy $\Sigma_{\alpha,\sigma}[\Delta_{\alpha,\sigma}]$. Note that the DMFT self-energy $\Sigma_{\alpha,\sigma}$ encodes only local correlation effects of the alloy component α, while the coherent self-energy $\Sigma_{\mathrm{coh},\sigma}$ contains both disorder and correlation contributions. The updated component Green's functions must satisfy the CPA condition $G_{\mathrm{coh},\sigma} = \sum_\alpha c_\alpha G_{\alpha,\sigma}$. From the newly obtained $G_{\mathrm{coh},\sigma}$, the coherent self-energy $\Sigma_{\mathrm{coh},\sigma}$ follows, and $G_{\mathrm{coh},\sigma}$ together with $\Sigma_{\mathrm{coh},\sigma}$ are returned into Eq. (12.8) to generate new component Green's functions, closing the self-consistency cycle.

The calculations in this chapter were performed using the `model-dmft` library [C2], a versatile framework based on `TRIQS` [C3] I have developed for CPA+DMFT calculations. We solve the DMFT impurity problem using the CT-HYB quantum Monte Carlo impurity solver as implemented in `TRIQS/cthyb` [C4]. Since Monte-Carlo based impurity solvers can produce noisy self-energies when evaluated via a direct Dyson equation, we employ the constrained residual minimization (CRM) method [110] to stabilize the impurity self-energy $\Sigma_{\alpha,\sigma}$, as described in Sec. 6.6.3. We also tested alternative noise-mitigation strategies, including the previously discussed high-frequency tail fitting and the orthogonal polynomial (Legendre) representation of the self-energy. However, for the parameter range relevant to this chapter, the CRM procedure yielded the most stable high-frequency behavior and the most consistent convergence of the CPA+DMFT loop. On a more formal level, the combined CPA+DMFT algorithm used here is discussed in Refs. [129, 168] and in the general presentation of Ch. 8.

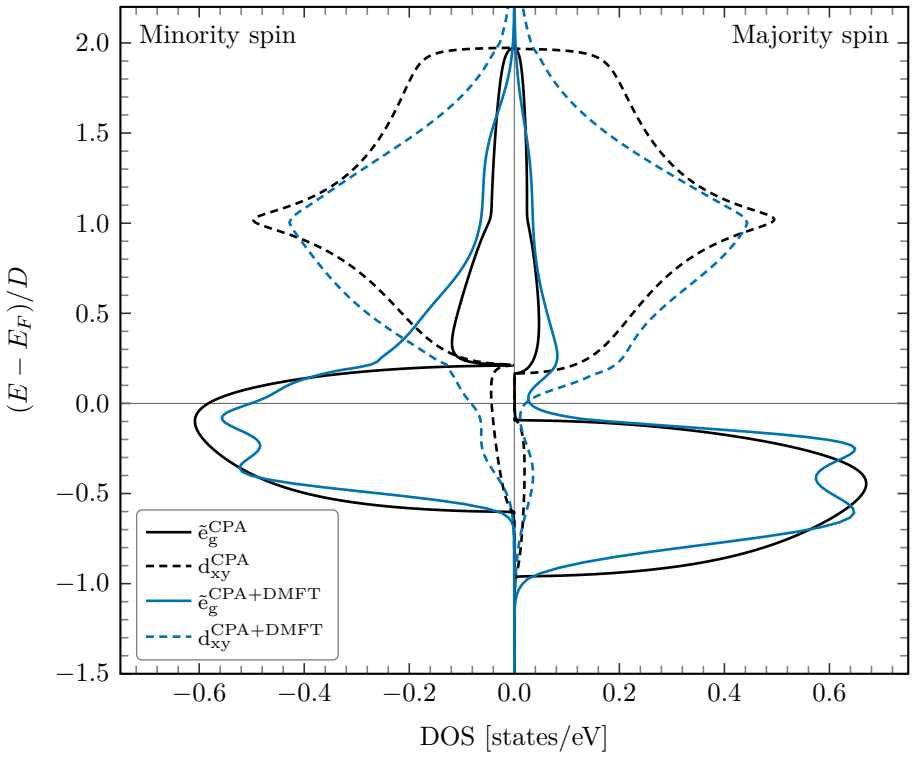

Figure 42: Alloy component density of states of the host d_{xy} (dashed lines) and impurity $\tilde{e}_g$ (solid lines) orbitals for the non-interacting $U = 0$ (black) and interacting $U = 0.5D = t^*$ (blue) case at the inverse temperature $\beta = 20/D$. The concentration of the magnetic impurities is $c = 20\%$.

12.3 Results

We now present the results of our CPA+DMFT calculations for the model defined in Eq. (12.1). The main focus is on the spectral properties of the system, in particular the alloy component density of states and the self-energies, which provide insight into the nature of the electronic excitations and the possible emergence of non-quasiparticle states in the minority spin channel.

12.3.1 Spectral functions and self-energies

Figure 42 shows the spin-resolved density of states (DOS) for the dilute impurity case with $c = 20\%$ of $\tilde{e}_g$ orbitals, computed for the model Hamiltonian Eq. (12.1) in the non-interacting limit $U = 0$ (black curves). Since the CPA does not require a many-body impurity solver, the spectral functions are obtained directly on the real-frequency (energy) axis. For the present parameter set, the CPA yields a fully spin-polarized ground state, often referred to as a majority-spin half-metallic ferromagnetic state [250, 262]. The majority-spin $\tilde{e}_g$ spectral function forms a split-off band, effectively separated from the main d_{xy} host band. The Fermi energy E_F lies in the minority-spin channel and is located close to the maximum of the split-off impurity-band DOS. Consequently, the CPA solution corresponds to a minority-spin metallic state with magnetic bands. Note that the CPA effective medium has a finite energy support, limited by the common

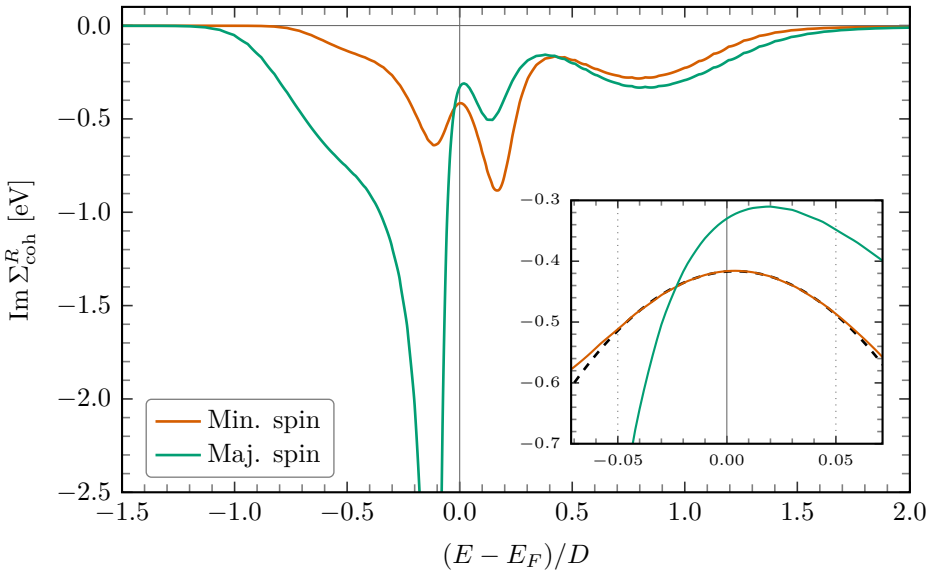

Figure 43: Imaginary part of the retarded self-energy Σ^R_{coh} computed using CPA+DMFT with $U = 0.5D$ and $\beta = 20/D$ for the minority and majority spin channel. The inset shows the self-energy around the Fermi level, where the minority spin channel clearly shows the Fermi-liquid behavior $\mathrm{Im}\,\Sigma^R_{\mathrm{coh}} \propto (E - E_F)^2$ (dashed line).

bandwidth [162], in accordance with the Gershgorin theorem [263].

Including electronic correlations on the host $\mathrm{d_{xy}}$ orbitals leads to a pronounced broadening of the host DOS (blue curves) in both spin channels. In particular, the minority-spin host spectral function gains weight at E_F. The spectral functions of both the majority- and minority-spin $\tilde{\mathrm{e}}_\mathrm{g}$ orbitals are slightly shifted towards the Fermi level. Moreover, in the vicinity of the $\mathrm{d_{xy}}$ majority-spin band edge, a shoulder develops whose tail crosses the Fermi energy, thereby contributing to depolarization. Because the DMFT impurity problem is solved using a QMC solver (yielding Green's functions on the Matsubara axis), we perform the analytical continuation from Matsubara frequencies to real frequencies using the Maximum Entropy (MaxEnt) method as implemented in `TRIQS/maxent` [C5]. It is important to emphasize that, although only the host $\mathrm{d_{xy}}$ orbitals are subject to explicit electronic correlations, the (nominally) non-correlated $\tilde{\mathrm{e}}_\mathrm{g}$ spectra are nevertheless significantly modified through the combined CPA+DMFT self-consistency.

In the following, we analyze the self-energy, which provides a self-consistently determined homogeneous, complex, and energy-dependent effective medium that contains information about both disorder and correlations. The analytical continuation of the self-energy is performed using the same MaxEnt procedure as for the spectral functions. The main panel of Fig. 43 displays the imaginary part of the CPA+DMFT coherent self-energy, while the inset zooms into the low-energy window $E_F \pm k_B T$. Close to the Fermi level, the minority-spin channel exhibits an imaginary part that is very well described by a quadratic energy dependence, $\mathrm{Im}\,\Sigma^R_{\mathrm{coh}} \propto (E - E_F)^2$ (dashed curve in the inset of Fig. 43). This behavior is consistent with a Fermi-liquid description of the minority-spin electrons. At the same time, $\mathrm{Im}\,\Sigma^R_{\mathrm{coh}}$ does not vanish at E_F; its finite value reflects the residual scattering rate in the combined disordered and correlated

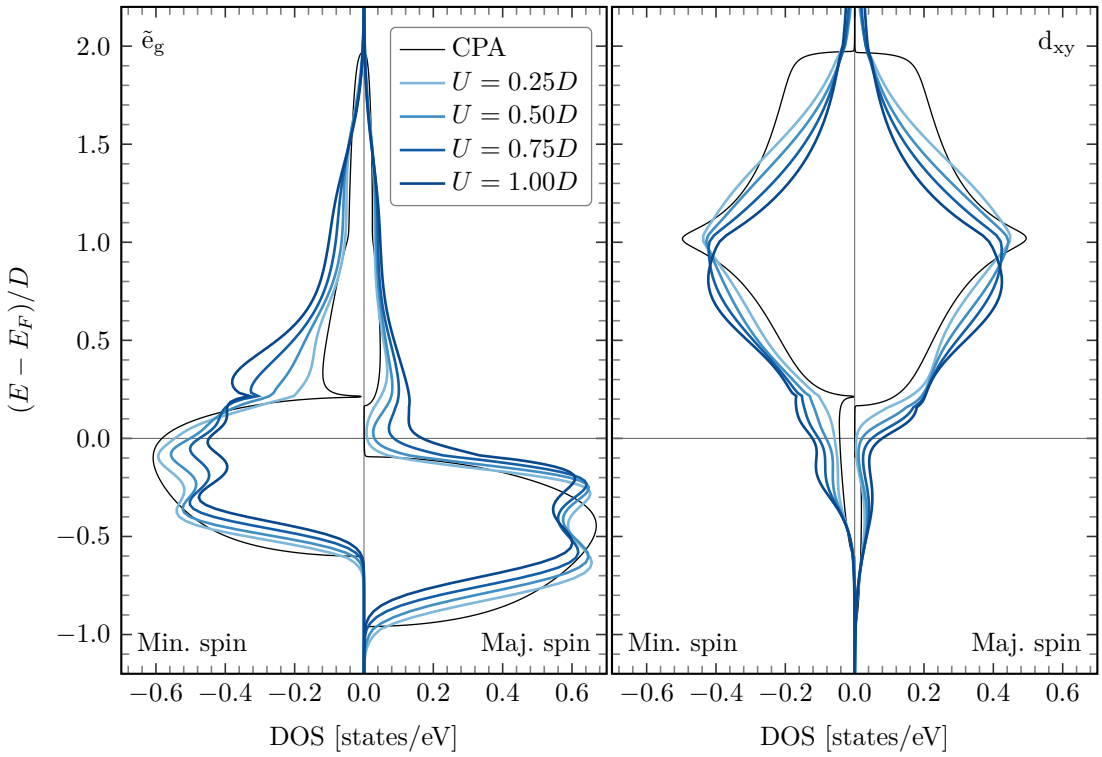

Figure 44: Alloy component density of states of the impurity $\tilde{e}_g$ (left) and host d_{xy} (right) orbitals for various values of U computed with CPA+DMFT at the inverse temperature $\beta = 20/D$.

medium and results in an energy-dependent broadening of the minority-spin bands. In the majority-spin channel, the deviation from the conventional clean Fermi-liquid behavior is more apparent: the inset reveals a shift relative to E_F. Nevertheless, within the shown energy window the majority-spin self-energy can still be approximated by an approximately parabolic dependence.

Figure 44 shows the spin- and orbital-resolved spectral functions for increasing interaction strengths, starting from the uncorrelated CPA limit and extending to the strongest-coupling case where the local interaction equals the half-bandwidth ($U = D = 2\,\mathrm{eV}$). With increasing U we observe a continuous filling of the majority-spin CPA gap. Most notably, the interacting majority-spin band-edge states move towards the Fermi level, which enhances the spectral weight at E_F and strengthens depolarization effects.

12.3.2 Impurity state conductivity

The single-particle spectra and the associated coherent self-energies were discussed in the previous section. In particular, the appearance of spectral weight in the majority-spin channel of the host d_{xy} orbital constitutes a clear signature of correlation effects and reflects the progressive closure of the CPA gap. Here, we turn to the corresponding implications for charge transport and focus explicitly on the (dc) resistivity, i.e. on how the combined effects of configurational disorder (CPA, Ch. 7) and local dynamical correlations (DMFT, Ch. 4) manifest in the transport response within the CPA+DMFT

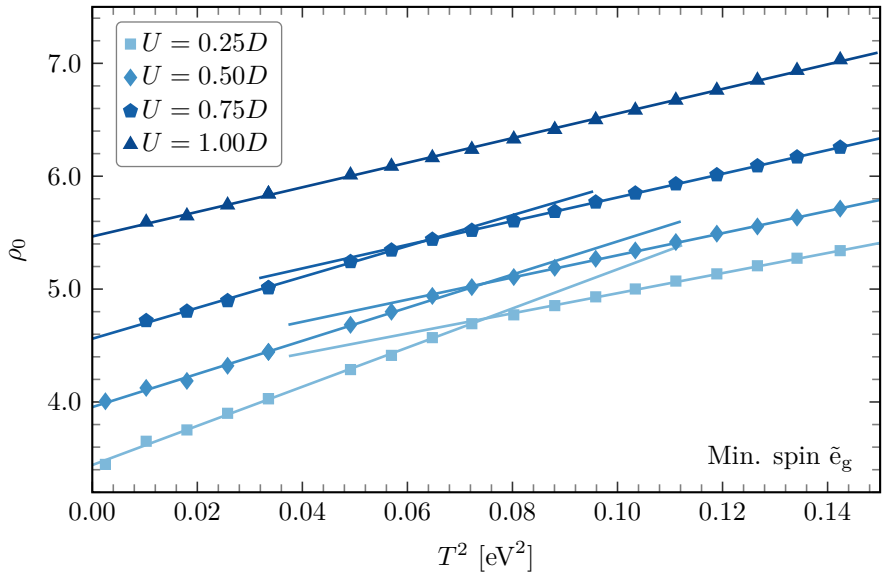

Figure 45: The inverse of the Drude peak $\rho_0 = 1/\sigma(0, T)$ in dependence on temperature T^2 for the minority spin channel of the guest $\tilde{e}_g$ (B) orbital computed with CPA+DMFT. The solid lines are linear fits of ρ_0.

framework.

Our analysis is restricted to the impurity-induced $\tilde{e}_g$ orbitals. The motivation is that the host electrons retain well-defined Fermi-liquid quasiparticles even in the presence of disorder and correlations, whereas the impurity-derived states provide the most direct window into the correlation-induced renormalization and disorder-enhanced scattering in the spin-polarized regime. The resulting resistivity therefore acts as a sensitive probe of changes in the quasiparticle properties of these impurity states.

To this end, we compute the optical conductivity in the limit of infinite coordination [74]. In this simplified setup, the conductivity associated with the $\tilde{e}_g$ band is expressed as a convolution of interacting spectral functions [264–266]:

$$\frac{\sigma(\omega)}{\sigma_0} = \int_{-\infty}^{\infty} \mathrm{d}E \, \frac{f(E) - f(E+\omega)}{\omega} A_{\tilde{e}_g}(E) \, A_{\tilde{e}_g}(E+\omega), \tag{12.11}$$

where $A_{\tilde{e}_g}(E)$ denotes the interacting spectral function of the impurity orbital $\tilde{e}_g$ and $f(E)$ is the Fermi-Dirac distribution function.

Figure 45 shows the computed dc resistivity $\rho_0(T)$ as a function of temperature for several values of the interaction strength U. These trends can be related directly to the evolution of the $\tilde{e}_g$ spectral function. In particular, the spectral weight at the Fermi level, $A_{\tilde{e}_g}(E_F)$ (cf. Fig. 44), decreases as U is increased. As long as the system remains metallic, this reduction is naturally associated with a decreasing quasiparticle weight Z, while at the same time the spectral function develops Hubbard-band features. In correlated metals, the dc conductivity generically scales as $\sigma_0 \propto Z\tau$ [74, 264–266], where τ is the quasiparticle lifetime. Here, the presence of disorder further enhances scattering processes, i.e. correlation-induced scattering acts on top of impurity scattering. Consequently, the quasiparticle lifetime τ is reduced, leading to a suppressed σ_0 and therefore an increased dc resistivity, consistent with the behavior

observed in Fig. 45. Strictly speaking, at $T = 0$ the DMFT contribution to $\mathrm{Im}\,\Sigma$ vanishes, implying a zero scattering rate from electron–electron interactions. However, the disorder-induced CPA contribution to the total effective-medium self-energy (Fig. 43) is expected to remain finite, providing a residual broadening even as $T \to 0$.

We now comment on the temperature dependence of $\rho_0(T) = 1/\sigma(0, T)$. The quadratic relation $\rho_0(T) \propto T^2$ is characteristic of a Fermi liquid at low temperatures. For the minority-spin $\tilde{e}_g$ states, we clearly identify a kink in the otherwise linear dependence of $\rho_0(T)$ on T^2 for interaction strengths below the half-bandwidth, $U < D$. At $U = D = 2t^*$, this kink disappears and ρ_0 follows an essentially straight line down to the lowest numerically accessible temperatures. The change in slope indicates the presence of an additional low-energy scale affecting the low-temperature transport of the minority carriers. This scale, $k_B T^\star$, is controlled by the frequency-dependent self-energy at the Fermi level (i.e. the effective scattering amplitudes), the bandwidth, and the magnitude of the exchange parameter $|\mathcal{B}|$. A more detailed analysis would be required to clarify the microscopic origin and robustness of this scale, which is beyond the scope of the present discussion.

12.4 Summary

In this chapter we studied a minimal interface-motivated model for LAO/STO in which oxygen-vacancy related $\tilde{e}_g$ states act as magnetic impurities embedded in an itinerant d_{xy} host. Configurational disorder was treated within CPA and local dynamical correlations were included via DMFT, combined self-consistently in the CPA+DMFT framework (see Chs. 4, 7 and 8). The vacancy-induced moments were modeled in the ferromagnetic regime by an effective exchange field $\mathcal{B}$ acting only on impurity sites, motivated by experimentally observed ferromagnetic domains that can be aligned by weak external fields [228, 229].

On the single-particle level, the non-interacting CPA solution yields a fully spin-polarized state with a split-off majority-spin $\tilde{e}_g$ band and a metallic minority-spin channel. Upon switching on correlations on the host ($U > 0$), the majority-spin CPA gap is progressively filled: spectral weight appears near E_F in the majority channel, leading to depolarization, even though only the d_{xy} orbitals are explicitly correlated. The coherent self-energy shows that minority-spin carriers retain Fermi-liquid characteristics ($\mathrm{Im}\,\Sigma^R_{\mathrm{coh}} \propto (E - E_F)^2$ near E_F), while a finite residual scattering rate persists due to disorder. The majority-spin sector is best characterized as a *disordered Fermi-liquid* regime in which quasiparticles are broadened but remain well-defined, consistent with correlation-induced spectral weight in an otherwise suppressed spin channel (akin in spirit to non-quasiparticle phenomenology in strongly spin-polarized systems) [250].

On the transport side, focusing on impurity-derived $\tilde{e}_g$ states, the dc resistivity $\rho_0(T)$ displays a kink in its T^2 dependence for intermediate interactions $U < D$, signaling a crossover between two low-temperature relaxation regimes. For stronger correlations ($U \sim D$) this kink disappears and a single quadratic regime is recovered down to the lowest accessible temperatures. The kink therefore indicates an additional low-energy scale $k_{\mathrm{B}} T^\star$ governed by the frequency-dependent self-energy at E_F, the bandwidth, and the effective exchange field $|\mathcal{B}|$, which could be probed in transport measurements.

13 Conclusion

The electronic structure theory of metals and alloys with local electronic correlations is based on the successful combination of DFT and DMFT. Using numerically exact QMC, solutions of effective DMFT quantum impurity problems provide a reliable description of electronic structure and finite-temperature magnetic properties. Within the same Green's function language, substitutional disorder can be included through effective medium theories such as the CPA, leading to the CPA+DMFT framework used throughout this thesis.

In the theoretical part, I presented the DFT framework and introduced DMFT from the effective-action point of view. Two impurity-solvers for DMFT were discussed and used: a simplified perturbative solver (SPTF) suitable for realistic materials input and fully self-consistent electronic-structure cycles, and the state-of-the-art CT-HYB QMC solver for the SIAM. Since QMC produces noisy high-frequency data, practical aspects such as stabilizing self-energies (tail constraints, CRM/Legendre ideas, smooth splicing) are not technical side notes, but central for robust self-consistency and continuation.

In the first two applications of this thesis, I applied the combined DFT(CPA)+DMFT approach within an existing Green's-function electronic-structure method based on EMTO. In this setting, the CPA+DMFT loop is naturally implemented in the multiple-scattering basis, and a non-stochastic, perturbative solver (SPTF) is particularly practical because continuation steps are not required within the self-consistency cycle. For V and Ti_xV_{1-x}, this approach provides correlated input for a McMillan analysis and yields a broad maximum of $T_c(x)$ around $x \approx 0.33$ in the bcc phase, with the nonmonotonic trend tracking the corresponding behavior of $\lambda(x)$ and the correlated electronic structure. For Nb and $Nb_{0.44}Ti_{0.56}$ under pressure, the same methodology resolves a pronounced reshaping of the Fermi surface in elemental Nb, while in the alloy the dominant linewidth comes from CPA lifetime effects and DMFT adds a modest, sheet-selective damping without changing the qualitative connectivity over the explored pressure range.

A central goal of the thesis, however, was to implement CPA+DMFT with modern tools and frameworks and to make it usable beyond a single electronic-structure backend. This is the motivation behind the software `TRIQS/CPA` and `model-dmft`. `TRIQS/CPA` provides single-site disorder solvers in the `TRIQS` ecosystem, while `model-dmft` was developed as a practical framework to run CPA+DMFT calculations in a modular way. A large part of this work concerns the numerically critical steps: consistent high-frequency handling, stabilization of QMC self-energies, and a robust two-stage workflow that ports self-energies between the disorder and many-body parts of the linked self-consistency.

The new implementation is demonstrated in the theoretical analysis of disorder and correlation effects at a low-density oxide interface (LAO/STO), modeled as a dilute alloy problem with vacancy-related $\tilde{e}_g$ impurity states embedded in an itinerant host. In this CPA+DMFT setting, correlations fill the majority-spin CPA gap and induce depolarization, and the transport analysis of impurity-derived states reveals a kink in the low-temperature T^2 resistivity for intermediate interactions, indicating an additional

low-energy scale in the correlated disordered medium.

The framework developed here also points beyond single-site CPA. Understanding the limitations of CPA (in particular the absence of nonlocal scattering correlations and localization physics) motivates extensions based on alternative configurational averages (typical-medium ideas or cluster generalizations) that can be combined with DMFT in a systematic way.

Finally, besides the published and submitted works discussed above, I also contributed to an ongoing study of the pressure-dependent electronic and magneto-optical properties of a topologically relevant kagome-type material.

A Legendre polynomials

We summarize the basic properties of Legendre polynomials. They are defined by Rodrigues' formula

$$P_\ell(x) = \frac{1}{2^\ell \ell!} \frac{\mathrm{d}^\ell}{\mathrm{d}x^\ell}\Big[(x^2-1)^\ell\Big], \qquad \ell = 0, 1, 2, \ldots \tag{A.1}$$

They are orthogonal with unit weight on $[-1, 1]$,

$$\int_{-1}^{1} \mathrm{d}x P_\ell(x) P_m(x) = \frac{2}{2\ell+1}\delta_{\ell m}, \tag{A.2}$$

so that the coefficients in a Legendre expansion $f(x) = \sum_{\ell\geq 0} f_\ell P_\ell(x)$ are

$$f_\ell = \frac{2\ell+1}{2}\int_{-1}^{1} \mathrm{d}x P_\ell(x) f(x). \tag{A.3}$$

Legendre polynomials obey the three-term recurrence

$$(\ell+1)\,P_{\ell+1}(x) = (2\ell+1)xP_\ell(x) - \ell P_{\ell-1}(x), \qquad \ell \geq 1, \tag{A.4}$$

with initial conditions $P_0(x) = 1$ and $P_1(x) = x$. The generating function is

$$\frac{1}{\sqrt{1-2xt+t^2}} = \sum_{\ell=0}^{\infty} P_\ell(x) t^\ell, \qquad |t| < 1, \tag{A.5}$$

and the parity relation reads

$$P_\ell(-x) = (-1)^\ell P_\ell(x). \tag{A.6}$$

At the endpoints of the interval $x \in [-1, 1]$ one has $P_\ell(1) = 1$ and $P_\ell(-1) = (-1)^\ell$. Useful derivatives are

$$P'_\ell(1) = \frac{\ell(\ell+1)}{2}, \qquad P'_\ell(-1) = \frac{(-1)^{\ell+1}\ell(\ell+1)}{2}. \tag{A.7}$$

The Fourier transform of the Legendre polynomials on the interval $[-1, 1]$ is given by

$$\int_{-1}^{1} \mathrm{d}x\, e^{ikx} P_\ell(x) = i^\ell \sqrt{\frac{2\pi}{k}} J_{\ell+\frac{1}{2}}(k) = 2i^\ell j_\ell(k), \tag{A.8}$$

where $J_\nu(k)$ is the Bessel function of the first kind and $j_\ell(k)$ the spherical Bessel function [108].

B Band structure of Nb and NbTi

A complementary representation of the electronic structure, beyond Fermi-surface cuts, is provided by the momentum-resolved spectral function $A(\boldsymbol{k}, E)$ along a high-symmetry path. Within a Green's-function framework, it is obtained directly from the retarded one-particle Green's function as

$$A_{l,m}(\boldsymbol{k}, E) = -\frac{1}{\pi} \operatorname{Im} G_{l,m}(\boldsymbol{k}, E + \mathrm{i}0^{+}) \,, \tag{B.1}$$

In a weakly scattered metal, the maxima of $A(\boldsymbol{k}, E)$ form narrow, band-like ridges. Any finite scattering mechanism produces a linewidth governed by the imaginary part of the relevant self-energy contributions. In the present context, substitutional disorder yields a coherent (CPA) self-energy, while local electronic correlations add a dynamical (DMFT) self-energy. Both enter $G(\boldsymbol{k}, z)$ and therefore broaden the spectral features in a natural, parameter-free manner once the self-energies are determined self-consistently.

Figure 46 shows $A(\boldsymbol{k}, E)$ at ambient pressure (0 GPa, left column) and at 100 GPa (right column) for bulk Nb (top row), $Nb_{0.44}Ti_{0.56}$ within CPA (middle row), and $Nb_{0.44}Ti_{0.56}$ within combined CPA+DMFT (bottom row). For the correlated alloy, local Coulomb interactions were included on Ti with $U = 2\,\mathrm{eV}$ and $J = 0.6\,\mathrm{eV}$. The first row serves as a benchmark of the Green's function based method: for elemental Nb, a Hamiltonian-based band-structure calculation (LMTO) [59] computed with `TB-LMTO-ASA` [C8] is overlaid as solid lines, and an excellent agreement of the two methods is observed. This consistency is in line with established electronic-structure results for Nb reported, for instance, by Mattheiss [214]. The Hamiltonian-based method is not applicable to the disordered alloy, thus the second and third rows show only the Green's-function results.

The effect of disorder is immediately visible when comparing the first and second rows. Within CPA, sharp dispersions acquire a finite linewidth that varies across the Brillouin zone and with energy, reflecting the fact that alloy scattering depends on orbital character and on the local band velocities. Consequently, near-degeneracies and crossings that appear sharp in pure Nb turn into broadened intensity patches in $Nb_{0.44}Ti_{0.56}$, while the overall dispersive structure remains clearly identifiable. Adding DMFT (third row) introduces an additional, dynamical broadening on top of the CPA background. In the present parameter regime, the spectra remain metallic with pronounced low-energy quasiparticle features, but with reduced coherence compared to the CPA-only case. The pressure dependence follows the expected trend for d-electron systems: at elevated pressure the overall bandwidth increases, and the correlated spectra tend to become closer to the disorder-only spectra, consistent with a reduced relative importance of local correlations under compression.

Finally, it is worth noting that the intensity distribution in $A(\boldsymbol{k}, E)$ is strongly structured: different $(\boldsymbol{k}, E)$ regions exhibit markedly different spectral weights and linewidths, indicating a nontrivial interplay of disorder- and correlation-induced scattering across the relevant band manifold. A fully quantitative analysis would naturally involve an orbital-resolved decomposition and a detailed discussion of how the CPA and DMFT self-energies shape specific dispersive features. Since such an analysis would

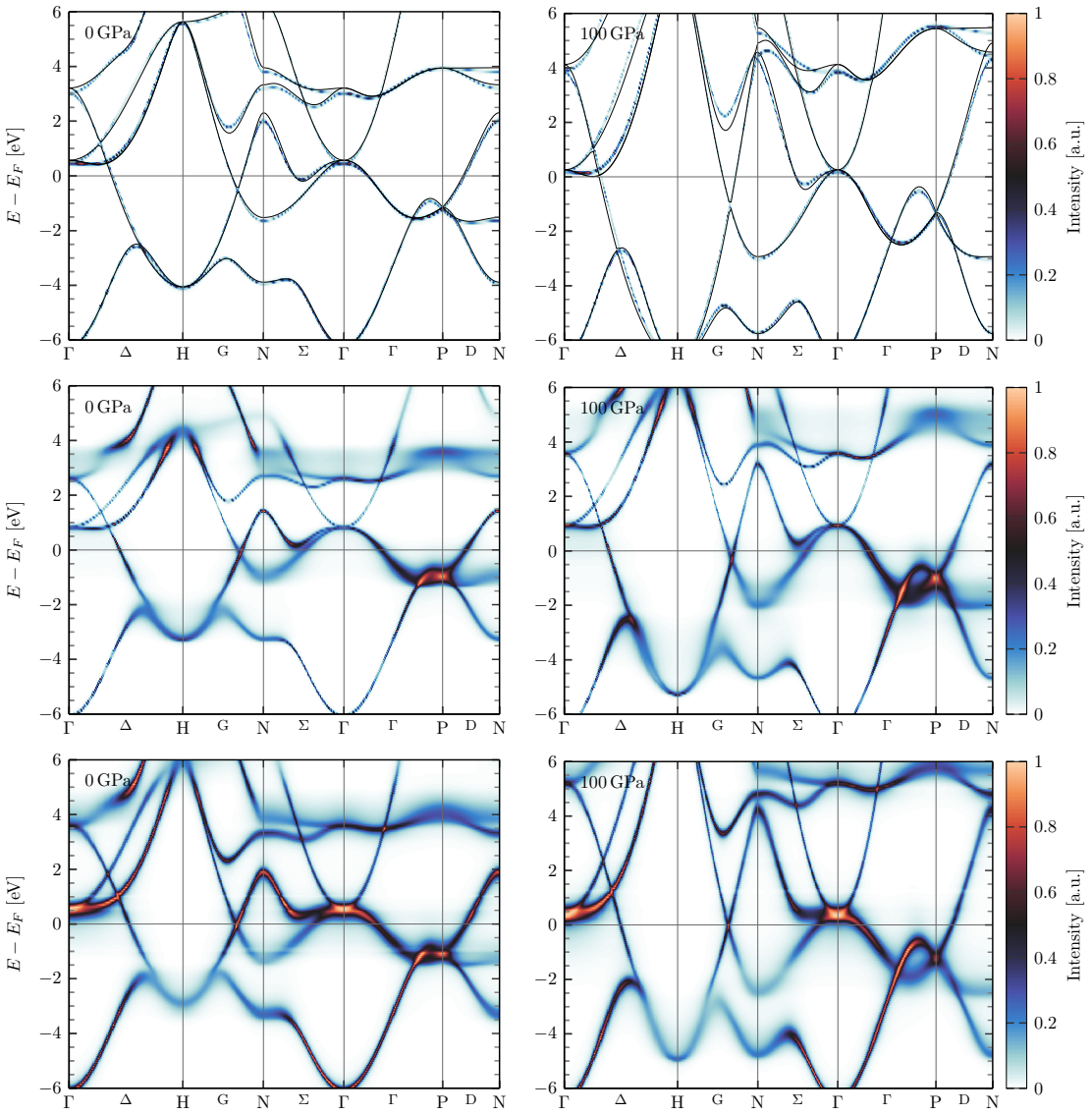

Figure 46: Band structure of bulk Nb (top), $Nb_{0.44}Ti_{0.56}$ (center) and $Nb_{0.44}Ti_{0.56}$ with correlations (bottom), at ambient pressure (left column) and 100 GPa (right column). The DMFT results were computed with $U = 2\,\text{eV}$ and $J = 0.6\,\text{eV}$. The solid lines are the exact results using Hamiltonian based methods (LMTO) for bulk Nb.

require substantial additional material, Fig. 46 is primarily used here to document the momentum-resolved spectra and to illustrate, in a band-structure-like visualization, the progressive broadening induced by disorder and correlations.

Publications

[P1] **D. Jones**, A. Östlin, et al., "Superconducting transition temperatures of pure vanadium and vanadium–titanium alloys in the presence of dynamical electronic correlations", Phys. Rev. B **109**, 165107 (2024).

[P2] **D. Jones**, A. Östlin, et al., "Quasiparticle Fermi surfaces of niobium and niobium–titanium alloys at high pressure", Phys. Rev. B **111**, 165152 (2025).

[P3] **D. Jones**, A. Weh, et al., "Correlated electronic states at a ferromagnetic oxide interface", 2026, `10.48550/arXiv.2602.15774`, preprint.

[P4] A. Chmeruk, **D. Jones**, et al., "Suppression of magnetism in $Co_3Sn_2S_2$ under external pressure", 2025, `10.48550/arXiv.2511.08141`, under review.

Codes

[C1] **D. Jones**, *TRIQS/CPA: single site disorder solvers for TRIQS*, version 3.3.x, 2025, `https://github.com/dylanljones/triqs_cpa`.

[C2] **D. Jones**, *model-dmft: A framework to perform CPA+DMFT calculations*, version 0.4.x, 2025, `https://github.com/dylanljones/model_dmft`.

[C3] O. Parcollet, M. Ferrero, et al., "TRIQS: a toolbox for research on interacting quantum systems", Comput. Phys. Commun. **196**, 398 (2015), Version 3.3.x, `https://github.com/TRIQS/triqs`.

[C4] P. Seth, I. Krivenko, M. Ferrero, and O. Parcollet, "TRIQS/CTHYB: a continuous-time quantum monte carlo hybridisation expansion solver for quantum impurity problems", Comput. Phys. Commun. **200**, 274 (2016), Version 3.3.x, `https://github.com/TRIQS/cthyb`.

[C5] G. J. Kraberger, R. Triebl, M. Zingl, and M. Aichhorn, "Maximum entropy formalism for the analytic continuation of matrix-valued green's functions", Phys. Rev. B **96**, 155128 (2017), Version 3.3.x, `https://github.com/TRIQS/maxent`.

[C6] L. Vitos, *EMTO-CPA: Exact muffin-tin orbitals with coherent potential approximation*, version 5.8, `https://emto.gitlab.io/`.

[C7] G. Kresse and J. Furthmüller, "Efficiency of ab-initio total energy calculations for metals and semiconductors using a plane-wave basis set", Comput. Mater. Sci. **6**, 15 (1996), Version 6.5.x, `https://www.vasp.at/`.

[C8] G. Krier, O. Jepsen, A. Burkhardt, and O. K. Andersen, *The TB-LMTO-ASA program*, version 4.5, 1994, `https://www2.fkf.mpg.de/andersen/LMTODOC/LMTODOC.html`.

References

[1] R. W. Hamming, *Numerical methods for scientists and engineers* (McGraw-Hill, 1962).

[2] L. H. Thomas, "The calculation of atomic fields", Proc. Cambridge Philos. Soc. **23**, 542 (1927).

[3] E. Fermi, "Eine statistische Methode zur Bestimmung einiger Eigenschaften des Atoms und ihre Anwendung auf die Theorie des periodischen Systems der Elemente", Z. Phys. **48**, 73 (1928).

[4] P. A. M. Dirac, "Note on exchange phenomena in the Thomas atom", Proc. Cambridge Philos. Soc. **26**, 376 (1930).

[5] C. F. von Weizsäcker, "Zur Theorie der Kernmassen", Z. Phys. **96**, 431 (1935).

[6] P. Hohenberg and W. Kohn, "Inhomogeneous electron gas", Phys. Rev. **136**, B864 (1964).

[7] W. Kohn and L. J. Sham, "Self-consistent equations including exchange and correlation effects", Phys. Rev. **140**, A1133 (1965).

[8] D. M. Ceperley and B. J. Alder, "Ground state of the electron gas by a stochastic method", Phys. Rev. Lett. **45**, 566 (1980).

[9] J. P. Perdew and A. Zunger, "Self-interaction correction to density-functional approximations for many-electron systems", Phys. Rev. B **23**, 5048 (1981).

[10] J. P. Perdew, K. Burke, and M. Ernzerhof, "Generalized Gradient Approximation Made Simple", Physical Review Letters **77**, Publisher: American Physical Society, 3865 (1996).

[11] J. Sun, A. Ruzsinszky, and J. P. Perdew, "Strongly constrained and appropriately normed semilocal density functional", Phys. Rev. Lett. **115**, 036402 (2015).

[12] A. D. Becke, "Density-functional thermochemistry. III. the role of exact exchange", J. Chem. Phys. **98**, 5648 (1993).

[13] J. Heyd, G. E. Scuseria, and M. Ernzerhof, "Hybrid functionals based on a screened coulomb potential", J. Chem. Phys. **118**, 8207 (2003).

[14] M. Dion, H. Rydberg, et al., "Van der waals density functional for general geometries", Phys. Rev. Lett. **92**, 246401 (2004).

[15] S. Grimme, "Semiempirical GGA-type density functional constructed with a long-range dispersion correction", J. Comput. Chem. **27**, 1787 (2006).

[16] R. O. Jones, "Density functional theory: its origins, rise to prominence, and future", Rev. Mod. Phys. **87**, 897 (2015).

[17] R. M. Martin, *Electronic structure: basic theory and practical methods* (Cambridge University Press, Cambridge, 2004), ISBN: 9780521782852.

[18] K. Burke, "Perspective on density functional theory", J. Chem. Phys. **136**, 150901 (2012).

[19] S. L. Dudarev, G. A. Botton, et al., "Electron-energy-loss spectra and the structural stability of nickel oxide: an LSDA+U study", Phys. Rev. B **57**, 1505 (1998).

[20] G. Kotliar, S. Y. Savrasov, et al., "Electronic structure calculations with dynamical mean-field theory", Rev. Mod. Phys. **78**, 865 (2006).

[21] A. Karolewski, "Describing Charge Transfer in Extended Donor-Acceptor Systems with Density Functional Theory", PhD thesis (Universität Bayreuth, 2013).

[22] T. Schmidt, "Constraint-Guided Construction of Exchange-Correlation Approximations in Density-Functional Theory", PhD thesis (Universität Bayreuth, 2016).

[23] H. Brezis and E. Lieb, "A relation between pointwise convergence of functions and convergence of functionals", Proc. Am. Math. Soc. **88**, 486 (1983).

[24] J. P. Perdew, R. G. Parr, M. Levy, and J. L. Balduz, "Density-functional theory for fractional particle number: derivative discontinuities of the energy", Phys. Rev. Lett. **49**, 1691 (1982).

[25] M. Levy, "Universal variational functionals of electron densities, first-order density matrices, and natural spin-orbitals and solution of the v-representability problem", Proc. Natl. Acad. Sci. U.S.A. **76**, 6062 (1979).

[26] M. Levy, "Electron densities in search of hamiltonians", Phys. Rev. A **26**, 1200 (1982).

[27] G. Czycholl, *Theoretische Festkörperphysik: Von den klassischen Modellen zu modernen Forschungsthemen* (Springer-Verlag, 2007), ISBN: 978-3-540-74790-1.

[28] R. G. Parr and W. Yang, *Density-functional theory of atoms and molecules* (Oxford University Press, 1989).

[29] J. P. Perdew and K. Schmidt, "Jacob's ladder of density functional approximations for the exchange-correlation energy", AIP Conf. Proc. **577**, 1 (2001).

[30] M. T. Czyyk and G. A. Sawatzky, "Local-density functional and on-site correlations: the LDA+U method", Phys. Rev. B **49**, 14211 (1994).

[31] V. I. Anisimov, F. Aryasetiawan, and A. I. Lichtenstein, "First-principles calculations of the electronic structure and spectra of strongly correlated systems: the LDA+U method", J. Phys.: Condens. Matter **9**, 767 (1997).

[32] K. Haule, "Exact double counting in combining the dynamical mean field theory and the density functional theory", Phys. Rev. Lett. **115**, 196403 (2015).

[33] J. P. Perdew and Y. Wang, "Accurate and simple analytic representation of the electron-gas correlation energy", Phys. Rev. B **45**, 13244 (1992).

[34] A. J. Cohen, P. Mori-Sánchez, and W. Yang, "Insights into current limitations of density functional theory", Science **321**, 792 (2008).

[35] J. P. Perdew and Y. Wang, "Pair-distribution function and its coupling-constant average for the spin-polarized electron gas", Phys. Rev. B **46**, 12947 (1992).

[36] J. P. Perdew, A. Ruzsinszky, et al., "Restoring the density-gradient expansion for exchange in solids and surfaces", Phys. Rev. Lett. **100**, 136406 (2008).

[37] L. J. Sham and M. Schlüter, "Density-functional theory of the energy gap", Phys. Rev. Lett. **51**, 1888 (1983).

[38] J. Tao, J. P. Perdew, V. N. Staroverov, and G. E. Scuseria, "Climbing the density functional ladder: nonempirical meta–GGA designed for molecules and solids", Phys. Rev. Lett. **91**, 146401 (2003).

[39] J. Sun, A. Ruzsinszky, and J. P. Perdew, "Strongly constrained and appropriately normed semilocal density functional", Phys. Rev. Lett. **115**, 036402 (2015).

[40] R. Sabatini, T. Gorni, and S. de Gironcoli, "Nonlocal van der Waals density functional made simple and efficient", Phys. Rev. B **87**, 041108 (2013).

[41] C. Adamo and V. Barone, "Toward reliable density functional methods without adjustable parameters: the PBE0 model", J. Chem. Phys. **110**, 6158 (1999).

[42] J. Heyd, G. E. Scuseria, and M. Ernzerhof, "Erratum: hybrid functionals based on a screened coulomb potential", J. Chem. Phys. **124**, 219906 (2006).

[43] S. Grimme, "Density functional theory with london dispersion corrections", WIREs Comput. Mol. Sci. **1**, 211 (2011).

[44] O. A. Vydrov and T. Van Voorhis, "Nonlocal van der Waals density functional: the simpler the better", J. Chem. Phys. **133**, 244103 (2010).

[45] X. Ren, P. Rinke, C. Joas, and M. Scheffler, "Random-phase approximation and its applications in computational chemistry and materials science", J. Mater. Sci. **47**, 7447 (2012).

[46] H. Eshuis, J. E. Bates, and F. Furche, "Electron correlation methods based on the random phase approximation", Theor. Chem. Acc. **131**, 1084 (2012).

[47] L. Hedin, "New method for calculating the one-particle Green's function with application to the electron-gas problem", Phys. Rev. **139**, A796 (1965).

[48] G. Onida, L. Reining, and A. Rubio, "Electronic excitations: density-functional versus many-body Green's-function approaches", Rev. Mod. Phys. **74**, 601 (2002).

[49] M. C. Payne, M. P. Teter, et al., "Iterative minimization techniques for ab initio total-energy calculations: molecular dynamics and conjugate gradients", Rev. Mod. Phys. **64**, 1045 (1992).

[50] G. P. Kerker, "Efficient iteration scheme for self-consistent pseudopotential calculations", Phys. Rev. B **23**, 3082 (1981).

[51] D. G. Anderson, "Iterative procedures for nonlinear integral equations", J. Assoc. Comput. Mach. **12**, 547 (1965).

[52] P. Pulay, "Convergence acceleration of iterative sequences. the case of SCF iteration", Chem. Phys. Lett. **73**, 393 (1980).

[53] P. Pulay, "Improved SCF convergence acceleration", J. Comput. Chem. **3**, 556 (1982).

[54] C. G. Broyden, "A class of methods for solving nonlinear simultaneous equations", Math. Comp. **19**, 577 (1965).

[55] D. D. Johnson, "Modified Broyden's method for accelerating convergence in self-consistent calculations", Phys. Rev. B **38**, 12807 (1988).

[56] J. Korringa, "On the calculation of the energy of a bloch wave in a metal", Physica **13**, 392 (1947).

[57] W. Kohn and N. Rostoker, "Solution of the Schrödinger equation in periodic lattices with an application to metallic lithium", Phys. Rev. **94**, 1111 (1954).

[58] O. K. Andersen, "Linear methods in band theory", Phys. Rev. B **12**, 3060 (1975).

[59] O. K. Andersen and O. Jepsen, "Explicit, first-principles tight-binding theory", Phys. Rev. Lett. **53**, 2571 (1984).

[60] R. Zeller, P. H. Dederichs, and et al., "The screened Korringa–Kohn–Rostoker method", J. Phys.: Condens. Matter **7**, 9947 (1995).

[61] N. Papanikolaou, R. Zeller, and P. H. Dederichs, "Conceptual improvements of the KKR method", J. Phys.: Condens. Matter **14**, 2799 (2002).

[62] L. Vitos, I. A. Abrikosov, and B. Johansson, "Total-energy method based on the exact muffin-tin orbitals theory", Phys. Rev. B **64**, 014107 (2001).

[63] L. Vitos, *Computational quantum mechanics of materials* (Springer, London, 2007), ISBN: 978-1-84628-950-7.

[64] L. Vitos, H. L. Skriver, J. Kollár, and B. Johansson, "Full charge-density technique within the exact muffin-tin orbitals method", Phys. Rev. B **62**, 10046 (2000).

[65] J. C. Slater, "Wave functions in a periodic potential", Phys. Rev. **51**, 846 (1937).

[66] A. Östlin, "Electronic structure studies and method development for complex materials", PhD thesis (KTH Royal Institute of Technology, 2013).

[67] L. Vitos, H. Skriver, B. Johansson, and J. Kollár, "Application of the exact muffin-tin orbitals theory: the spherical cell approximation", Computational Materials Science **18**, 24 (2000).

[68] V. Kumar, O. K. Andersen, and A. Mookerjee, *Lectures on methods of electronic structure calculations* (World Scientific, 1995), ISBN: 978-981-02-1485-2.

[69] O. K. Andersen, O. Jepsen, and D. Glötzel, "Canonical description of the band structure of metals", in *Highlights of condensed-matter theory*, Vol. 89, edited by F. Bassani, F. Fumi, and M. P. Tosi, Proceedings of the International School of Physics "Enrico Fermi" (North-Holland, Amsterdam, 1985), pp. 59–176, ISBN: 9780444869760.

[70] L. Vitos, "Total-energy method based on the exact muffin-tin orbitals theory", Phys. Rev. B **64**, 014107 (2001).

[71] P. Lloyd, "Wave propagation through an ordered alloy", Proc. Phys. Soc. **90**, 207 (1967).

[72] M. Weinert, E. Wimmer, and A. J. Freeman, "Total-energy all-electron density functional method for bulk solids and surfaces", Phys. Rev. B **26**, 4571 (1982).

[73] W. Metzner and D. Vollhardt, "Correlated lattice fermions in $d = \infty$ dimensions", Phys. Rev. Lett. **62**, 324 (1989).

[74] A. Georges, G. Kotliar, W. Krauth, and M. J. Rozenberg, "Dynamical mean-field theory of strongly correlated fermion systems and the limit of infinite dimensions", Rev. Mod. Phys. **68**, 13 (1996).

[75] K. Held, "Electronic structure calculations using dynamical mean-field theory", Adv. Phys. **56**, 829 (2007).

[76] T. Maier, M. Jarrell, T. Pruschke, and M. H. Hettler, "Quantum cluster theories", Rev. Mod. Phys. **77**, 1027 (2005).

[77] J. Hubbard, "Electron correlations in narrow energy bands", Proc. R. Soc. Lond. A **276**, 238 (1963).

[78] M. C. Gutzwiller, "Effect of correlation on the ferromagnetism of transition metals", Phys. Rev. Lett. **10**, 159 (1963).

[79] J. Kanamori, "Electron correlation and ferromagnetism of transition metals", Prog. Theor. Phys. **30**, 275 (1963).

[80] D. Vollhardt, "Dynamical meanfield theory of electronic correlations in models and materials", AIP Conf. Proc. **1297**, 339 (2010).

[81] A. Weh, "Electronic correlations in inhomogeneous model systems: numerical simulation of spectra and transmission", PhD thesis (Universität Augsburg, 2022).

[82] A. Altland and B. D. Simons, *Condensed matter field theory*, 2nd ed. (Cambridge University Press, 2010), ISBN: 9780511789984.

[83] J. W. Negele and H. Orland, *Quantum many-particle systems* (Westview Press, Nov. 1998), ISBN: 0738200522.

[84] W. Metzner, "Linked-cluster expansion around the atomic limit of the Hubbard model", Phys. Rev. B **43**, 8549 (1991).

[85] E. Müller-Hartmann, "Correlated fermions on a lattice in high dimensions", Z. Phys. B: Condens. Matter **74**, 507 (1989).

[86] P. W. Anderson, "Localized magnetic states in metals", Phys. Rev. **124**, 41 (1961).

[87] N. E. Bickers, D. J. Scalapino, and S. R. White, "Conserving approximations for strongly fluctuating electron systems. i. formalism and calculational approach", Phys. Rev. Lett. **62**, 961 (1989).

[88] A. I. Lichtenstein and M. I. Katsnelson, "Ab initio calculations of quasiparticle band structure in ferromagnetic Ni", Phys. Rev. B **57**, 6884 (1998).

[89] M. I. Katsnelson and A. I. Lichtenstein, "Quantum theory of magnetism and the problem of the calculation of exchange interactions in metals", J. Phys.: Condens. Matter **14**, L537 (2002).

[90] A. N. Rubtsov, V. V. Savkin, and A. I. Lichtenstein, "Continuous-time quantum Monte Carlo method for fermions", Phys. Rev. B **72**, 035122 (2005).

[91] P. Werner and A. J. Millis, "Hybridization expansion impurity solver: General formulation and application to Kondo lattice and two-orbital models", Phys. Rev. B **74**, 155107 (2006).

[92] E. Gull, A. J. Millis, et al., "Continuous-time Monte Carlo methods for quantum impurity models", Rev. Mod. Phys. **83**, 349 (2011).

[93] G. Baym and L. P. Kadanoff, "Conservation laws and correlation functions", Phys. Rev. **124**, 287 (1961).

[94] G. Baym, "Self-consistent approximations in many-body systems", Phys. Rev. **127**, 1391 (1962).

[95] J. M. Luttinger and J. C. Ward, "Ground-state energy of a many-fermion system. II", Phys. Rev. **118**, 1417 (1960).

[96] A. I. Lichtenstein and M. I. Katsnelson, "Ab initio calculations of quasiparticle band structure in correlated systems: LDA++ approach", Phys. Rev. B **57**, 6884 (1998).

[97] J. E. Hirsch and R. M. Fye, "Monte Carlo method for magnetic impurities in metals", Phys. Rev. Lett. **56**, 2521 (1986).

[98] P. Werner, A. Comanac, et al., "Continuous-time solver for quantum impurity models", Phys. Rev. Lett. **97**, 076405 (2006).

[99] E. Gull, P. Werner, et al., "Continuous-time auxiliary-field Monte Carlo for quantum impurity models", Phys. Rev. B **80**, 245102 (2009).

[100] N. Metropolis, A. W. Rosenbluth, et al., "Equation of state calculations by fast computing machines", J. Chem. Phys. **21**, 1087 (1953).

[101] W. K. Hastings, "Monte Carlo sampling methods using Markov chains and their applications", Biometrika **57**, 97 (1970).

[102] P. Werner, "Continuous-time impurity solvers", in *The LDA+DMFT approach to strongly correlated materials*, Vol. 1, edited by E. Pavarini, E. Koch, A. Lichtenstein, and D. Vollhardt, Schriften des Forschungszentrums Jülich. Modeling and Simulation (Forschungszentrum Jülich GmbH, Zentralbibliothek, Verlag, Jülich, 2011) Chap. 10.

[103] H. Shinaoka, E. Gull, and P. Werner, "Continuous-time hybridization expansion quantum impurity solver for multi-orbital systems with complex hybridizations", Comput. Phys. Commun. **215**, 128 (2017).

[104] G. H. Golub and C. F. Van Loan, *Matrix computations*, 4th (Johns Hopkins University Press, 2013), pp. 19–20.

[105] M. Troyer and U.-J. Wiese, "Computational complexity and fundamental limitations to fermionic quantum Monte Carlo simulations", Phys. Rev. Lett. **94**, 170201 (2005).

[106] E. Y. Loh, J. E. Gubernatis, et al., "Sign problem in the numerical simulation of many-electron systems", Phys. Rev. B **41**, 9301 (1990).

[107] A. Sokal, "Monte Carlo methods in statistical mechanics: foundations and new algorithms", in *Functional integration: basics and applications*, edited by C. DeWitt-Morette, P. Cartier, and A. Folacci (Springer US, Boston, MA, 1997), pp. 131–192, ISBN: 978-1-4899-0319-8.

[108] L. Boehnke, H. Hafermann, et al., "Orthogonal polynomial representation of imaginary-time Green's functions", Phys. Rev. B **84**, 075145 (2011).

[109] J. Kaye, K. Chen, and O. Parcollet, "Discrete Lehmann representation of imaginary time Green's functions", Phys. Rev. B **105**, 235115 (2022).

[110] H. LaBollita, J. Kaye, and A. Hampel, "Stabilizing the calculation of the self-energy in dynamical mean-field theory using constrained residual minimization", Phys. Rev. B **111**, 115155 (2025).

[111] H. Shinaoka, D. Geffroy, et al., "Sparse sampling and tensor network representation of two-particle Green's functions", SciPost Phys. **8**, 012 (2020).

[112] H. Shinaoka, J. Otsuki, M. Ohzeki, and K. Yoshimi, "Compressing Green's function using intermediate representation between imaginary-time and real-frequency domains", Phys. Rev. B **96**, 035147 (2017).

[113] J. Otsuki, M. Ohzeki, H. Shinaoka, and K. Yoshimi, "Sparse modeling approach to analytical continuation of imaginary-time quantum Monte Carlo data", Phys. Rev. E **95**, 061302 (2017).

[114] P. W. Anderson, "Absence of diffusion in certain random lattices", Phys. Rev. **109**, 1492 (1958).

[115] A. A. Abrikosov and L. P. Gor'kov, "Contribution to the theory of superconducting alloys with paramagnetic impurities", Zhur. Eksptl'. i Teoret. Fiz. **Vol: 39** (1960).

[116] P. Soven, "Coherent-Potential Model of Substitutional Disordered Alloys", Phys. Rev. **156**, 809 (1967).

[117] D. W. Taylor, "Vibrational properties of imperfect crystals with large defect concentrations", Proc. Phys. Soc. **91**, 755 (1967).

[118] B. Velický, "Theory of electronic transport in disordered solids", Phys. Rev. **184**, 614 (1968).

[119] B. L. Gyorffy, "Coherent-potential approximation for a nonoverlapping-muffin-tin-potential model of random substitutional alloys", Phys. Rev. B **5**, 2382 (1972).

[120] R. J. Elliott, J. A. Krumhansl, and P. L. Leath, "The theory and properties of randomly disordered crystals", Rev. Mod. Phys. **46**, 465 (1974).

[121] F. Yonezawa and K. Morigaki, "Electronic properties of the liquid and amorphous states", Prog. Theor. Phys. Suppl. **53**, 1 (1968).

[122] A. Gonis, *Green functions for ordered and disordered systems*, Studies in Mathematical Physics (North-Holland, Amsterdam, 1992), ISBN: 978-0-444-88471-1.

[123] J. A. Nelder and R. Mead, "A simplex method for function minimization", Com. J. **7**, 308 (1965).

[124] C. G. Broyden, "The convergence of a class of double-rank minimization algorithms", IMA J. Appl. Math. **6**, 76 (1970).

[125] R. Fletcher, "A new approach to variable metric algorithms", Com. J. **13**, 317 (1970).

[126] D. Goldfarb, "A family of variable-metric methods derived by variational means", Math. Comp. **24**, 23 (1970).

[127] D. F. Shanno, "Conditioning of quasi-Newton methods for function minimization", Math. Comp. **24**, 647 (1970).

[128] V. Janis and D. Vollhardt, "Coupling of quantum degrees of freedom in strongly interacting disordered electron systems", Phys. Rev. B **46**, 15712 (1992).

[129] M. Ulmke, V. Janis, and D. Vollhardt, "Anderson-Hubbard model in infinite dimensions", Phys. Rev. B **51**, 10411 (1995).

[130] V. Dobrosavljevi, A. A. Pastor, and B. K. Nikoli, "Typical medium theory of Anderson localization: a local order parameter approach to strong disorder effects", Europhys. Lett. **62**, 76 (2003).

[131] M. C. O. Aguiar, V. Dobrosavljevi, E. Abrahams, and G. Kotliar, "Critical behavior at the Mott-Anderson transition: a typical-medium theory perspective", Phys. Rev. Lett. **102**, 156402 (2009).

[132] E. Miranda and V. Dobrosavljevi, "Dynamical mean-field theories of correlation and disorder", in *Conductor-insulator quantum phase transitions* (Oxford University Press, 2012).

[133] L. Chioncel, L. Vitos, et al., "Ab initio electronic structure calculation of correlated systems: EMTO-DMFT approach", Phys. Rev. B **67**, 235106 (2003).

[134] J. Minár, L. Chioncel, et al., "Multiple scattering formalism for correlated systems: a KKR+DMFT approach", Phys. Rev. B **72**, 045125 (2005).

[135] A. Östlin, L. Vitos, and L. Chioncel, "Correlated electronic structure with uncorrelated disorder", Phys. Rev. B **98**, 235135 (2018).

[136] G. A. Baker and P. Graves-Morris, *Padé approximants*, 2nd (Cambridge University Press, Cambridge, 1996), ISBN: 978-0-521-48184-1.

[137] H. J. Vidberg and J. W. Serene, "Solving the Eliashberg equations by means of Pade approximants", J. Low Temp. Phys. **29**, 179 (1977).

[138] M. Jarrell and J. E. Gubernatis, "Bayesian inference and the analytic continuation of imaginary-time quantum Monte Carlo data", Phys. Rep. **269**, 133 (1996).

[139] R. K. Bryan, "Maximum entropy analysis of oversampled data problems", Eur. Biophys. J. **18**, 165 (1990).

[140] M. Jarrell, "The maximum entropy method: analytic continuation of QMC data", in *Correlated electrons: from models to materials*, Vol. 2, edited by E. Pavarini, Schriften des Forschungszentrums Jülich (Forschungszentrum Jülich GmbH, Zentralbibliothek, Verlag, Jülich, 2012) Chap. 13.

[141] T. N. Thiele, *Interpolationsrechnung*, Nineteenth Century Collections Online: Science, Technology, and Medicine, Part I (B.G. Teubner, Leipzig, 1909).

[142] J. Skilling, "Classic maximum entropy", in *Maximum entropy and Bayesian methods*, edited by J. Skilling (Kluwer Academic, Dordrecht, 1989), pp. 45–52.

[143] E. T. Jaynes, "Information theory and statistical mechanics", Phys. Rev. **106**, 620 (1957).

[144] J. Bardeen, L. N. Cooper, and J. R. Schrieffer, "Microscopic theory of superconductivity", Phys. Rev. **106**, 162 (1957).

[145] J. Bardeen, L. N. Cooper, and J. R. Schrieffer, "Theory of superconductivity", Phys. Rev. **108**, 1175 (1957).

[146] P. Morel and P. W. Anderson, "Calculation of the superconducting state parameters with retarded electron-phonon interaction", Phys. Rev. **125**, 1263 (1962).

[147] G. Eliashberg, "Interactions between electrons and lattice vibrations in a superconductor", Sov. Phys. JETP **11**, 696 (1960).

[148] G. A. Ummarino, "Eliashberg theory", in *Emergent Phenomena in Correlated Matter*, Vol. 1, edited by E. Pavarini, E. Koch, and U. Schollwöck, Schriften des Forschungszentrums Jülich. Modeling and Simulation (Forschungszentrum Jülich GmbH, Zentralbibliothek, Verlag, Jülich, 2013) Chap. 13, pp–pp, ISBN: 978-3-89336-884-6.

[149] W. L. McMillan, "Transition temperature of strong-coupled superconductors", Phys. Rev. **167**, 331 (1968).

[150] A. Abrikosov and L. Gor'kov, "Superconducting alloys at finite temperatures", Sov. Phys. JETP **9**, 220 (1959).

[151] P. W. Anderson, "Theory of dirty superconductors", J. Phys. Chem. Solids **11**, 26 (1959).

[152] D. Shahar and Z. Ovadyahu, "Superconductivity near the mobility edge", Phys. Rev. B **46**, 10917 (1992).

[153] M. V. Sadovskii, "Superconductivity and localization", Phys. Rep. **282**, 225 (1997).

[154] A. Ghosal, M. Randeria, and N. Trivedi, "Role of spatial amplitude fluctuations in highly disordered *s*-wave superconductors", Phys. Rev. Lett. **81**, 3940 (1998).

[155] A. Ghosal, M. Randeria, and N. Trivedi, "Inhomogeneous pairing in highly disordered s-wave superconductors", Phys. Rev. B **65**, 014501 (2001).

[156] M. A. Steiner, N. P. Breznay, and A. Kapitulnik, "Approach to a superconductor-to-Bose-insulator transition in disordered films", Phys. Rev. B **77**, 212501 (2008).

[157] B. Sacépé, C. Chapelier, et al., "Disorder-induced inhomogeneities of the superconducting state close to the superconductor-insulator transition", Phys. Rev. Lett. **101**, 157006 (2008).

[158] V. F. Gantmakher and V. T. Dolgopolov, "Superconductor–insulator quantum phase transition", Phys. Usp. **53**, 1 (2010).

[159] M. Jarrell and H. R. Krishnamurthy, "Systematic and causal corrections to the coherent potential approximation", Phys. Rev. B **63**, 125102 (2001).

[160] V. Dobrosavljevi, "Typical medium theory of Mott-Anderson localization", Int. J. Mod. Phys. B **24**, 1680 (2010).

[161] H. Terletska, Y. Zhang, et al., "Typical-medium multiple-scattering theory for disordered systems with Anderson localization", Phys. Rev. B **95**, 134204 (2017).

[162] A. Weh, Y. Zhang, et al., "Dynamical mean-field theory of the Anderson-Hubbard model with local and nonlocal disorder in tensor formulation", Phys. Rev. B **104**, 045127 (2021).

[163] J. Minár, H. Ebert, and L. Chioncel, "A self-consistent, relativistic implementation of the LSDA+DMFT method", Eur. Phys. J. Special Topics **226**, 2477 (2017).

[164] A. Östlin, Y. Zhang, et al., "Ab initio typical medium theory of substitutional disorder", Phys. Rev. B **101**, 014210 (2020).

[165] M. Karabin, W. R. Mondal, et al., "Ab initio approaches to high-entropy alloys: a comparison of CPA, SQS, and supercell methods", J. Mater. Sci. **57**, 10677 (2022).

[166] G. Kotliar and D. Vollhardt, "Strongly correlated materials: insights from dynamical mean-field theory", Phys. Today **57**, 53 (2004).

[167] A. Östlin, L. Vitos, and L. Chioncel, "Analytic continuation-free Green's function approach to correlated electronic structure calculations", Phys. Rev. B **96**, 125156 (2017).

[168] A. Östlin, L. Vitos, and L. Chioncel, "Correlated electronic structure with uncorrelated disorder", Phys. Rev. B **98**, 235135 (2018).

[169] J. J. Hopfield, "Angular momentum and transition-metal superconductivity", Phys. Rev. **186**, 443 (1969).

[170] G. D. Gaspari and B. L. Gyorffy, "Electron-phonon interactions, d resonances, and superconductivity in transition metals", Phys. Rev. Lett. **28**, 801 (1972).

[171] O. K. Andersen, O. Jepsen, and G. Krier, *Lectures on methods of electronic structure calculation* (World Scientific, Singapore, 1994), p. 63.

[172] I. R. Gomersall and B. L. Gyorffy, "A simple theory of the electron-phonon mass enhancement in transition metal compounds", J. Phys. F: Met. Phys. **4**, 1204 (1974).

[173] S. Vonsovsky, E. Brandt, et al., *Superconductivity of transition metals: their alloys and compounds*, Springer Series in Solid-State Sciences (Springer Berlin Heidelberg, 2011), ISBN: 9783642618215.

[174] D. Westlake and L. Alfred, "Determination of the debye characteristic temperature of vanadium from the Bloch-Grüneisen relation", J. Phys. Chem. Solids **29**, 1931 (1968).

[175] M. Tokii and S. Wakoh, "An effective potential of metallic vanadium and chromium", J. Phys. Soc. Jpn. **72**, 1476 (2003).

[176] J. A. Weber, D. Benea, et al., "Electronic correlations in vanadium revealed by electron-positron annihilation measurements", Phys. Rev. B **95**, 075119 (2017).

[177] A. S. Belozerov, A. A. Katanin, and V. I. Anisimov, "Transition from Pauli paramagnetism to Curie-Weiss behavior in vanadium", Phys. Rev. B **107**, 035116 (2023).

[178] A. Sihi and S. K. Pandey, "A detailed electronic structure study of vanadium metal by using different beyond-DFT methods", Eur. Phys. J. B **93**, 10.1140/epjb/e2019-100500-8 (2020).

[179] S. Y. Savrasov, G. Resta, and X. Wan, "Local self-energies for V and Pd emergent from a nonlocal LDA+FLEX implementation", Phys. Rev. B **97**, 155128 (2018).

[180] C. N. Louis and K. Iyakutti, "Electronic phase transition and superconductivity of vanadium under high pressure", Phys. Rev. B **67**, 094509 (2003).

[181] M. Matin, L. S. Sharath Chandra, et al., "The influence of electron-phonon coupling and spin fluctuations on the superconductivity of the Ti-V alloys", Eur. Phys. J. B **87**, 131, 131 (2014).

[182] N. F. Berk and J. R. Schrieffer, "Effect of ferromagnetic spin correlations on superconductivity", Phys. Rev. Lett. **17**, 433 (1966).

[183] H. Rietschel and H. Winter, "Role of spin fluctuations in the superconductors Nb and V", Phys. Rev. Lett. **43**, 1256 (1979).

[184] L. Ley, O. B. Dabbousi, et al., "X-ray photoemission spectra of the valence bands of the 3*d* transition metals, Sc to Fe", Phys. Rev. B **16**, 5372 (1977).

[185] W. Speier, J. C. Fuggle, et al., "Bremsstrahlung isochromat spectra and density-of-states calculations for the 3*d* and 4*d* transition metals", Phys. Rev. B **30**, 6921 (1984).

[186] A. I. Lichtenstein, M. I. Katsnelson, and G. Kotliar, "Finite-temperature magnetism of transition metals: an ab initio dynamical mean-field theory", Phys. Rev. Lett. **87**, 067205 (2001).

[187] J. Braun, J. Minár, et al., "Spectral function of ferromagnetic 3*d* metals: a self-consistent LSDA + DMFT approach combined with the one-step model of photoemission", Phys. Rev. Lett. **97**, 227601 (2006).

[188] J. Kolorenc, A. I. Poteryaev, and A. I. Lichtenstein, "Valence-band satellite in ferromagnetic nickel: LDA+DMFT study with exact diagonalization", Phys. Rev. B **85**, 235136 (2012).

[189] A. Weh, J. Otsuki, et al., "Spectral properties of heterostructures containing half-metallic ferromagnets in the presence of local many-body correlations", Phys. Rev. Res. **2**, 043263 (2020).

[190] D. Pines and P. Nozieres, *Quantum liquids* (Benjamin, New York, 1966).

[191] J. Negele and H. Orland, *Quantum many-body systems* (Frontiers in physics (Addison-Wesley, Redwood City, Calif. ua, 1988), 1988).

[192] M. A. L. Marques, M. Lüders, et al., "Ab initio theory of superconductivity. II. application to elemental metals", Phys. Rev. B **72**, 024546 (2005).

[193] X. Gonze, B. Amadon, et al., "ABINIT: first-principles approach to material and nanosystem properties", Comput. Phys. Commun. **180**, 2582 (2009).

[194] J. Noffsinger, F. Giustino, et al., "EPW: a program for calculating the electron-phonon coupling using maximally localized Wannier functions", Comput. Phys. Commun. **181**, 2140 (2010).

[195] A. M. Vora, "Superconducting state parameters of binary alloys", Physica C Supercond. **470**, 475 (2010).

[196] T. Sasaki and Y. Muto, "Low temperature resistivity anomaly in tinb and tiv alloys", Physica B Condens. Matter **165-166**, 291 (1990).

[197] A. F. Prekul, V. A. Rassokhin, and N. V. Volkenshtein, "Effect of spin fluctuations on the superconducting and normal properties of alloys of Ti containing V, Nb, or Ta", Sov. Phys. JETP **40**, 1134 (1975).

[198] A. F. Prekul, V. A. Rassokhin, and N. V. Volkenshtein, "Cause of low-temperature resistance maximum in titanium alloys", JETP Lett. **22**, 209 (1975).

[199] A. R. Denton and N. W. Ashcroft, "Vegard's law", Phys. Rev. A **43**, 3161 (1991).

[200] G. T. Zimanyi and E. Abrahams, "Disorder and interactions in the Hubbard model", Phys. Rev. Lett. **64**, 2719 (1990).

[201] V. Dobrosavljevi and G. Kotliar, "Hubbard models with random hopping in $d = \infty$", Phys. Rev. Lett. **71**, 3218 (1993).

[202] V. Dobrosavljevic and G. Kotliar, "Strong correlations and disorder in $d = \infty$ and beyond", Phys. Rev. B **50**, 1430 (1994).

[203] K. Clusius, P. Franzosini, and U. Piesbergen, "Ergebnisse der tieftemperaturforschung xxxii. die atom - und elektronenwärme des vanadins und niobs zwischen 10° und 273° k", Z. Naturforsch. **15 a**, 728 (1960).

[204] P. Upton, P. Upton, and J. Ho, "Low-temperature-calorimetric studies of superconductivity and microstructure in titanium-vanadium alloys", J. Less Common Met. **42**, 285 (1975).

[205] S. Y. Savrasov and D. Y. Savrasov, "Electron-phonon interactions and related physical properties of metals from linear-response theory", Phys. Rev. B **54**, 16487 (1996).

[206] S. Baroni, S. de Gironcoli, A. Dal Corso, and P. Giannozzi, "Phonons and related crystal properties from density-functional perturbation theory", Rev. Mod. Phys. **73**, 515 (2001).

[207] F. Giustino, "Electron-phonon interactions from first principles", Rev. Mod. Phys. **89**, 015003 (2017).

[208] J.-F. Zhang, M. Gao, K. Liu, and Z.-Y. Lu, "First-principles study of the robust superconducting state of NbTi alloys under ultrahigh pressures", Phys. Rev. B **102**, 195140 (2020).

[209] C. Huang, J. Guo, et al., "RSAVS superconductors: materials with a superconducting state that is robust against large volume shrinkage", Phys. Rev. Mater. **4**, 071801 (2020).

[210] A. Cucciari, D. Naddeo, S. Di Cataldo, and L. Boeri, "NbTi: a nontrivial puzzle for the conventional theory of superconductivity", Phys. Rev. B **110**, L140502 (2024).

[211] A. Östlin and L. Chioncel, "Electronic correlations and Fermi liquid behavior of intermediate-band states in titanium-doped silicon", Phys. Rev. B **104**, L201201 (2021).

[212] J. Guo, G. Lin, et al., "Record-high superconductivity in niobium-titanium alloy", Advanced Materials **31**, 1807240 (2019).

[213] P. E. Blöchl, "Projector augmented-wave method", Phys. Rev. B **50**, 17953 (1994).

[214] L. F. Mattheiss, "Electronic structure of niobium and tantalum", Phys. Rev. B **1**, 373 (1970).

[215] W. H. Butler, H. G. Smith, and N. Wakabayashi, "Electron-phonon contribution to the phonon linewidth in Nb: theory and experiment", Phys. Rev. Lett. **39**, 1004 (1977).

[216] D. Eastman, "Photoemission studies of d-band structure in Sc, Y, Gd, Ti, Zr, Hf, V, Nb, Cr and Mo", Solid State Commun. **7**, 1697 (1969).

[217] J. R. Anderson, D. A. Papaconstantopoulos, J. W. McCaffrey, and J. E. Schirber, "Self-consistent band structure of niobium at normal and reduced lattice spacings", Phys. Rev. B **7**, 5115 (1973).

[218] J. R. Anderson, D. A. Papaconstantopoulos, and J. E. Schirber, "Influence of pressure on the Fermi surface of niobium", Phys. Rev. B **24**, 6790 (1981).

[219] V. V. Struzhkin, Y. A. Timofeev, R. J. Hemley, and H.-k. Mao, "Superconducting T_c and electron-phonon coupling in Nb to 132 GPa: magnetic susceptibility at megabar pressures", Phys. Rev. Lett. **79**, 4262 (1997).

[220] N. Elyashar and D. D. Koelling, "Self-consistent relativistic APW calculation of the electronic structure of niobium with a non-muffin-tin potential", Phys. Rev. B **15**, 3620 (1977).

[221] L. L. Boyer, D. A. Papaconstantopoulos, and B. M. Klein, "Effect of self-consistency and exchange on the electronic structure of the transition metals, V, Nb, and Ta", Phys. Rev. B **15**, 3685 (1977).

[222] L. D. Landau, "The theory of a Fermi liquid", Sov. Phys. JETP **3**, 920 (1957).

[223] J. M. Luttinger, "Fermi surface and some simple equilibrium properties of a system of interacting fermions", Phys. Rev. **119**, 1153 (1960).

[224] P. Nozières and J. M. Luttinger, "Derivation of the Landau theory of Fermi liquids. I. Formal preliminaries", Phys. Rev. **127**, 1423 (1962).

[225] J. M. Luttinger and P. Nozières, "Derivation of the Landau theory of Fermi liquids. II. Equilibrium properties and transport equation", Phys. Rev. **127**, 1431 (1962).

[226] O. J. Curtin, Y. Nishikawa, A. C. Hewson, and D. J. G. Crow, "Fermi liquids and the Luttinger integral", J. Phys. Commun. **2**, 031001 (2018).

[227] A. Brinkman, M. Huijben, et al., "Magnetic effects at the interface between non-magnetic oxides", Nature Mater. **6**, 493 (2007).

[228] L. Li, C. Richter, J. Mannhart, and R. Ashoori, "Coexistence of magnetic order and two-dimensional superconductivity at LaAlO3/SrTiO3 interfaces", Nature Phys. **7**, 762 (2011).

[229] J. A. Bert, B. Kalisky, et al., "Direct imaging of the coexistence of ferromagnetism and superconductivity at the LaAlO3/SrTiO3 interface", Nature Phys. **7**, 767 (2011).

[230] N. Pavlenko, T. Kopp, et al., "Magnetic and superconducting phases at the laalo$_3$/srtio$_3$ interface: the role of interfacial ti 3*d* electrons", Phys. Rev. B **85**, 020407(R) (2012).

[231] N. Pavlenko, T. Kopp, et al., "Oxygen vacancies at titanate interfaces: Two-dimensional magnetism and orbital reconstruction", Phys. Rev. B **86**, 064431 (2012).

[232] J. Park, B.-G. Cho, et al., "Oxygen-vacancy-induced orbital reconstruction of Ti ions at the interface of LaAlO3/SrTiO3 Heterostructures: A resonant soft-X-ray scattering study", Phys. Rev. Lett. **110**, 017401 (2013).

[233] M. Salluzzo, S. Gariglio, et al., "Origin of Interface Magnetism in $BiMnO_3/SrTiO_3$ and $LaAlO_3$ Heterostructures", Phys. Rev. Lett. **111**, 087204 (2013).

[234] M. Breitschaft, V. Tinkl, et al., "Two-dimensional electron liquid state at $LaAlO_3$-$SrTiO_3$ interfaces", Phys. Rev. B **81**, 153414 (2010).

[235] R. Di Capua, M. Radovic, et al., "Observation of a two-dimensional electron gas at the surface of annealed SrTiO3 single crystals by scanning tunneling spectroscopy", Phys. Rev. B **86**, 155425 (2012).

[236] Ariando, X. Wang, et al., "Electronic phase separation at the LaAlO3/SrTiO3 interface", Nat. Commun. **2**, 188 (2011).

[237] P. Seiler, J. Zabaleta, et al., "Antilocalization at an oxide interface", Phys. Rev. B **97**, 075136 (2018).

[238] G. Berner, M. Sing, et al., "Direct *k*-space mapping of the electronic structure in an oxide-oxide interface", Phys. Rev. Lett. **110**, 247601 (2013).

[239] G. Berner, A. Müller, et al., "Band alignment in $LaAlO_3/SrTiO_3$ oxide heterostructures inferred from hard X-ray photoelectron spectroscopy", Phys. Rev. B **88**, 115111 (2013).

[240] V. N. Strocov, C. Cancellieri, and A. S. Mishchenko, "Electrons and polarons at oxide interfaces explored by soft-X-ray ARPES", in *Spectroscopy of complex oxide interfaces*, edited by C. Cancellieri and V. N. Strocov (Springer International Publishing, Cham, 2018), pp. 107–151, ISBN: 9783319749884, 9783319749891.

[241] V. Strocov, A. Chikina, et al., "Electronic phase separation at $LaAlO_3/SrTiO_3$ interfaces tunable by oxygen deficiency", Phys. Rev. Mater. **3**, 106001 (2019).

[242] N. Pavlenko and T. Kopp, "Structural relaxation and metal-insulator transition at the interface between $SrTiO_3$ and $LaAlO_3$", Surf. Sci. **605**, 1114 (2011).

[243] F. Lechermann, L. Boehnke, D. Grieger, and C. Piefke, "Electron correlation and magnetism at the $LaAlO_3/SrTiO_3$ interface: a DFT+DMFT investigation", Phys. Rev. B **90**, 085125 (2014).

[244] F. Cossu, U. Schwingenschlögl, and V. Eyert, "Metal-insulator transition at the $LaAlO_3/SrTiO_3$ interface revisited: a hybrid functional study", Phys. Rev. B **88**, 045119 (2013).

[245] N. Pavlenko, T. Kopp, and J. Mannhart, "Emerging magnetism and electronic phase separation at titanate interfaces", Phys. Rev. B **88**, 201104(R) (2013).

[246] N. Pavlenko and T. Kopp, "Magnetically ordered state at correlated oxide interfaces: the role of random oxygen defects", J. Supercond. Nov. Magn. **26**, 1175 (2013).

[247] M. Sing, H. O. Jeschke, et al., "Influence of oxygen vacancies on two-dimensional electron systems at SrTiO3-based interfaces and surfaces", Eur. Phys. J. Spec. Top. **226**, 2457 (2017).

[248] M. Behrmann and F. Lechermann, "Interface exchange processes in $LaAlO_3/SrTiO_3$ induced by oxygen vacancies", Phys. Rev. B **92**, 125148 (2015).

[249] R. Vlaming and D. Vollhardt, "Controlled mean-field theory for disordered electronic systems: Single-particle properties", Phys. Rev. B **45**, 4637 (1992).

[250] M. Katsnelson, V. Irkhin, et al., "Half-metallic ferromagnets: From band structure to many-body effects", Rev. Mod. Phys. **80**, 315 (2008).

[251] T. Moriya, *Spin fluctuations in itinerant electron magnetism*, Springer Series in Solid-State Sciences (Springer Berlin Heidelberg, 1985), ISBN: 9783642825019.

[252] D. M. Edwards and J. A. Hertz, "Electron-magnon interactions in itinerant ferromagnetism. II. strong ferromagnetism", J. Phys. F: Met. Phys. **3**, 2191 (1973).

[253] V. Y. Irkhin and M. Katsnelson, "Charge-carriers in the narrow-band Hubbard ferromagnet in the spin-wave temperature-range", Fiz. Tverd. Tela. **25**, 3383 (1983).

[254] V. Y. Irkhin and M. I. Katsnel'son, "Half-metallic ferromagnets", Phys. Usp. **37**, 659 (1994).

[255] L. Chioncel, M. Katsnelson, R. de Groot, and A. Lichtenstein, "Nonquasiparticle states in the half-metallic ferromagnet NiMnSb", Phys. Rev. B **68**, 144425 (2003).

[256] L. Chioncel, E. Arrigoni, M. Katsnelson, and A. Lichtenstein, "Electron correlations and the minority-spin band gap in half-metallic Heusler alloys", Phys. Rev. Lett. **96**, 137203 (2006).

[257] L. Chioncel, M. Katsnelson, et al., "Tunable spin transport in CrAs: Role of correlation effects", Phys. Rev. B **71**, 085111 (2005).

[258] L. Chioncel, P. Mavropoulos, et al., "Half-metallic ferromagnetism induced by dynamic electron correlations in VAs", Phys. Rev. Lett. **96**, 197203 (2006).

[259] L. Chioncel, H. Allmaier, et al., "Half-metallic ferromagnetism and spin polarization in CrO_2", Phys. Rev. B **75**, 140406 (2007).

[260] Ulmke, M., "Ferromagnetism in the hubbard model on fcc-type lattices", Eur. Phys. J. B **1**, 301 (1998).

[261] D. Vollhardt, N. Blümer, et al., "Metallic ferromagnetism: progress in our understanding of an old strong-coupling problem", in Advances in solid state physics 38, edited by B. Kramer (1999), pp. 383–396, ISBN: 978-3-540-44558-6.

[262] L. Chioncel, E. Arrigoni, M. Katsnelson, and A. Lichtenstein, "Majority-spin nonquasiparticle states in half-metallic ferrimagnet Mn_2VAl", Phys. Rev. B **79**, 125123 (2009).

[263] S. Gergorin, "Über die abgrenzung der eigenwerte einer matrix", Izv. Akad. Nauk SSSR Ser. Mat., 749 (1931).

[264] T. Pruschke, M. Jarrell, and J. Freericks, "Anomalous normal-state properties of high-T_c superconductors: intrinsic properties of strongly correlated electron systems", Adv. Phys. **44**, 187 (1995).

[265] T. Pruschke, D. L. Cox, and M. Jarrell, "Hubbard model at infinite dimensions: thermodynamic and transport properties", Phys. Rev. B **47**, 3553 (1993).

[266] M. Jarrell, J. K. Freericks, and T. Pruschke, "Optical conductivity of the infinite-dimensional hubbard model", Phys. Rev. B **51**, 11704 (1995).

Acknowledgements

I would like to use the opportunity to thank everyone who supported me on the journey to this point and the colleagues and friends I have met along the way.

First and foremost, I would like to thank Prof. Dr. Liviu Chioncel and Prof. Dr. Ulrich Eckern, who have supported me all the way since my time as bachelor student. Ulrich Eckern inspired me to pursue theoretical physics, and it was always a pleasure – and truly inspiring – to work with him. Liviu Chioncel introduced me to the world of computational physics and numerical methods, a field that I have genuinely fallen in love with. His supervision during my PhD was extremely valuable: he always pushed me beyond what I thought I could achieve. Working with him is always fun, even in stressful times, and I am very grateful for his support and guidance and all the memorable moments we shared during the last years.

I gratefully acknowledge financial support from the Augsburg Centre for Innovative Technologies (ACIT) and from the Collaborative Research Center/Transregio projects TRR80 and TRR360. Their funding provided the resources and research environment that made this work possible. Additionally, I would like to thank the TRIQS team for the summer school and meetings I attended, where I had the opportunity to learn from and collaborate with many talented researchers and developers in the field of computational physics.

I am very grateful for all the colleagues and friends I have met at the University of Augsburg, who made my time here very enjoyable: Maxi Metzner, Simon Haugg, Rosa Balducci, Nico Unglert, Luca Leone, Fabian Ballar, Vighnesh Naik, Dr. Artem Chmeruk, Dr. Marcus Kollar and Prof. Dr. Markus Heyl just to name a few. A special thanks goes to my office mates – Tobias Wiener, Laurin Brunner and Kaiqian Huang – with whom I shared the good and the bad times, and who always had a good joke to share. I also want to thank Dr. Andreas Weh and Dr. Andreas Östlin, who have left the university by now, but have taught me a lot during my time here. Many thanks also to my mother and Dushyant Sukhija for proofreading parts of this thesis and giving me valuable feedback. Furthermore, I want to thank my friends outside the university, especially my best friend Dennis Egerer, who have always been there for me and supported me in all aspects of life. I am also very grateful for my girlfriend Anna Lappler, who has been a great support and motivation for me during the last years, and endured the stress of the last months with me. I love you!

Finally, I want to dedicate this thesis to my mother and my father, who have supported me throughout my life and have been my constant source of love, encouragement, and strength.

My mom, an accomplished medical doctor, always taught me critical thinking and, from a very young age, inspired me to keep learning more about the world. She helped me stay focused on school, even during the tough years. After I realized my interest in physics, I can recall countless evenings where we talked about it over dinner. When I started my academic career, she was always genuinely interested in what I was learning – no matter the topic – and she kept me motivated even in hard times. Without her,

I would not be where I am today.

I also want to thank my dad, who sadly passed away at the beginning of my time as a PhD student. My dad and I always talked about science and other interesting topics, and he first sparked my interest in computers. As an artist with an academic background, he was creative and open-minded, and I learned a lot from him about how to think outside the box. We had many great conversations about physics during my bachelor's and master's, and he couldn't wait to hear what interesting new things I could tell him. I always enjoyed our time together and wish he could celebrate this moment with me. Miss you, Dad!